


Doctoral Dissertation
Doctoral Program in Aerospace Enginering (XXXIII cycle)

Planning and Control Strategies for Collaborative Aerial Autonomous Vehicles

Luca Spanò Cuomo

* * * * * *

Supervisor
Prof. Giorgio Guglieri

Doctoral Examination Committee:
Prof. Kimon Valavanis, University of Denver
Prof. Giancarmine Fasano, University Naples Federico II
Prof. Carlo Riboldi, Polytechnic University of Milan
Ph.D. Andrea Vilardi, Eurac Research

Politecnico di Torino

I hereby declare that, the contents and organisation of this dissertation constitute my own original work and does not compromise in any way the rights of third parties, including those relating to the security of personal data.

. . . . . .

Luca Spanò Cuomo

Turin,

Summary

Drones or UAVs have long entered everyday language. They were born to achieve particular tasks whose requirements were difficult to obtain from crewed aircraft (e.g., very long flight time, overflight of areas dangerous to health, low cost). They are today increasingly widespread also in the civil sector. A rapid spread and the introduction of low-performance models marked the drone introduction to the civil environment, leading to some accidents. These incidents prompted the need for appropriate legislation, which often resulted in a practically absolute ban on the use of drones, even outside the urban environment.
This work analyzes the technical and legislative challenges that need to be overcome for drones to be fully exploited, even in the urban environment, offering a valid and realistic solution. The present work, therefore, has a dual purpose. On the one hand, to overcome the legislative problem by introducing an original drone risk assessment, on the other, to propose an architecture that uses the novelty introduced, allowing drones to carry out their task independently of the human.
The original risk assessment formula proposed in this work would enable expanding the use of drones considerably, allowing a much more profitable way than today.

Contents

Chapter 1

Introduction

This chapter introduces the thesis's purpose and a series of helpful information for the reader to understand clearly what a drone is and the problems related to its introduction in the national airspace. The first part introduces the main drone topics and features, where their use is more promising, and their typically available payloads. It will mainly deal with an analysis of electric drones, explaining why they are the most common ones. The second part is about the drone-related legislation in several countries. A conspicuous part of this chapter deals with the various drones on the market, grouping them into macro-categories. The purpose of the market analysis is to evaluate the technological reached level that is economically accessible. A hypothetical model with the most common characteristics will be extrapolated for each category, representing the archetype for future analysis. This chapter also correlates drone-based services with other options, highlighting their pros and cons.

1.1 Purpose of the Thesis

The purpose of the thesis is twofold. The former is to offer an alternative drone-related risk assessment. The latter is to propose a new architecture that uses drones.
The governments have to face the following problem: most drones are carelessly used by unqualified people who use low-performance drones that inevitably caused property and people damage. The control bodies have introduced restrictions to drone usage to prevent further accidents by virtually comparing drones to airplanes and using the same risk assessment. This legislative condition is common in almost all countries. The prevailing airplane-related risk assessments used by air traffic control bodies and available in the literature are too conservative if applied to drones, overestimating the related risk. As explored in section 1.5, by imposing too stringent limits, the legislative aspect blocks the diffusion of many services that rely on drones. Also, the urban context, which is the most economically profitable environment, is affected by these restrictions. The urban environment turns out to be the environment the author has chosen to test

his original introduction about the risk assessment and the drone-based architecture.

Chapter 2 demonstrates how the current risk assessments for flying objects are not suitable for drones, and therefore an original drone risk assessment is introduced. Based on an original drone risk assessment, a new legislation introduction would be less prohibitive, allowing a wider diffusion of drones, making possible a series of services just hypothesized in the literature to date.

The other purpose of the thesis, which is the new architecture that uses drones, is the topic of chapter 3; the architecture is simulated, using the original drone-related risk assessment, and exploiting drones for missions in the urban environment. The primary purpose of the proposed architecture is to lighten the drone from calculus, exploiting the internet and an off-board computer. The simulation uses the original risk assessment and all the tools proposed in chapter 2, demonstrating the practical side of the novelty introduced. The author paid much attention to simulate the models and the communication system in the most reliable way, using the drone market-based data, cadastral data, and verifying the goodness of some of the exploited libraries.

1.2 What Unmanned Vehicles are

An unmanned vehicle can be either remote-controlled or an autonomous vehicle capable of sensing its environment and navigating independently. Also, the degree of automation and the tools necessary to perform its task are different. The dynamic models that many enthusiasts use have an automation level that typically stops at finding the horizontal attitude; the pilot must manage almost everything. The automation level is undoubtedly higher in war drones, where the pilot provides very high-level commands, entrusting most of the low-level work to the drone. Therefore, the term 'unmanned vehicles' includes various objects with few characteristics familiar with each other. In the current language and in this thesis, the term drone refers to a relatively small aerodyne (MTOW less than 5 kilograms) that moves without an onboard pilot. So the term drone is appropriately used only for small remote-piloted fixed-wing, rotary-wing, or airships. The level of automation does not result in a classification parameter, and for this reason, the author does not take it into account.
Drones, as said, are tools. They are more or less suitable for a specific context. There are areas where they result in a practical, safe, and economical solution. However, it is good to anticipate that in the civilian field (but also in the military one that we will not deal with), we notice, more and more, a trend of integration of drone and crewed solutions. There still exist, and probably will always exist, situations where the crewed solutions better fit over the drone. The design phase can't foresee all problems, and man's intuition is still indispensable in many missions [38]. According to several economic studies [152] and scientific papers [281], the following has been quite clear. If the

goal is to cover a large area quickly, not being too detailed (a classic example is mapping a region), then the crewed aircraft is the preferred choice. Even today, human-crewed aircraft can stay in the air for a more significant amount of time than commercial-grade drones.
The military-grade drones also have, usually, better performances than the civil-grade ones. The reasons for this disparity in range or endurance of civil-grade drones compared to crewed-aircraft or some military drones are manifold. Among the reasons, we can include the difficulty of selling drones with good performance to the public due to purchase or maintenance cost reasons. About the first reason, we can declare that, for the same size, military drones can cost tens of times more than a civil-grade drone. For example, the Raven RQ-11B [20] costs around 35 thousand dollars, while the Foxyslim [133] of similar dimensions costs about 700 US dollars. About the predominance, in the civil environment, of totally electric devices, we can declare, as explained in section 1.2.1, that this dramatically reduces the maintenance and operating costs, but greatly limits performance compared to non-electric powered drones, for example, jet engines-propelled drones. Regarding the crewed-aircraft, their costs are much higher than the previous choices. However, there are missions where drones are much more advantageous than crewed alternatives. For example, in areas difficult to fly over by large aerodynes (noise problems) or when the flight must be at a very low altitude or very close to the analyzed object (high accuracy analysis is required), the crewed alternative is not compatible with the mission specifications, and the drone one performs better. The cooperation is to be preferred in the situation like the control of oil pipelines or powerlines, where crewed aircraft are used for the overview, while drones for detail work [152]. The reader should not forget the legislative aspect; the above is an analysis of the practicality and economics, not considering the legislation. Drones cannot fly over some areas due to legislative reasons, as explained in section 1.5. In this thesis work, however, we want to offer a service involving drones that can hardly be performed by crewed aircraft.

1.2.1 Why electrical propulsed drones

This section wants to explain why electric drones are the types of drones considered in this thesis work and, more generally, why battery-powered drones are the most used ones. In choosing the kind of tool to use, the first action in the civil-commercial field is to investigate the market offer. Currently, battery-powered drones are the most common, and theirs is a virtual monopoly [110]. This section wants to clarify the kind of benefits battery-powered drones offer over not-battery-powered ones.
The amount of energy that a kilogram of fuel such as gasoline can carry is about 50 times greater than the energy provided by a lithium-ion battery (the most used battery type in the drone propulsion) of equal weight [238]. One might think that the reason for choosing electric propulsion drones is their safety, but it is not a valid reason. There are

many circumstances in which battery results dangerous by catching fire or even exploding [89]. Not optimal conditions of use or charging, or impacts, make a battery certainly vulnerable [45], and they can enormously decrease the battery lifetime. Furthermore, the battery's weight does not change with the time of service, unlike an alternative power supply, which further reduces the operating range of a battery-powered moving device. The reason almost all civilian drones are battery-powered, as can be guessed, is economical and practical. Although the disadvantages are many, battery-powered solution has the significant advantage of having a lower number of high-priced pieces and the maintenance costs reduced to a minimum.
The main alternative to electric motors, as regards small weights, are the jet, the piston, and the Wankel engine.
The jet engines are small and light devices composed of a few pieces and generate thrust directly, not needing additional propellers or gear. However, jet engines have a value of thousands of euros (compared to a few dozen for electric ones), are quite challenging to start, and need, even if simple to obtain, constant and costly maintenance [195]. The performances that jet-powered drones can offer are sought only in areas where speed and extended range are essential. Also the piston and the Wankel engines are solutions that turn out to be not suited for small drones for a number of reasons. For the piston engines, these reasons include the high number of parts they are composed of, while for the Wankel engines, their fast wear and the subsequent high maintenance cost. Furthermore, the low-pressure ratio in their combustion chamber degrades the efficiency of these two types of engines, and, in order for the drone to move, they need a gearbox and a propeller, dramatically increasing the weight of the propulsion system. For very small drones so, piston engines are, typically, not chosen while they are a valid alternatives for drones weighing more than 25 Kilograms [6].
As previously introduced, in the civil field, the purchase and maintenance cost is a starkly important factor, leading to the choice of electric-powered drones. That is why the author has analyzed only battery-powered drones, confident that other power sources will not be competitive in the short term.

1.3 Characteristics of electric drones on the market

This paragraph analyzes some on-market drone calculable characteristics. The author has divided the drone market into categories according to their propulsion features, scilicet, fixed-wing, rotary-wing, and lither-than-air (also called LTA or airship) drones. This analysis was necessary due to the lack of such data in the literature. The goal is to better evaluate the available material on the market to offer the best solution to a specific scenario or mission and provide the most appropriate possible values to the simulations the thesis will show. Market analysis is necessary if the aim is to offer a commercially viable product, one of the goals of the present work. A more holistic concept of optimization would include also cost. The author of this work has only relied on manufacturers' drone data. The various analyzed quantities were divided into small ranges, indicating how many models have the characteristics falling within them to evaluate the most probable range. Section 1.3.1 analyzes the characteristics of 38 fixed-wing drone models by examinating the various launch methods, the wingspan, the MTOW, cruising speed, communication range, and flight endurance. Section 1.3.1 analyzes 45 rotary-wing drone models checking their maximum size, MTOW, cruising speed, communication range, and flight endurance. Section 1.3.3 focuses on 35 lither-than-air drone models analyzing their maximum length, maximum diameter, payload, cruising speed, communication range, and flight endurance. Table 1.1 shows the most common crucial drone characteristics for the analyzed types; the thesis will later exploit these values.

Table 1.1: drone type and their average characteristics on the market.

Type	Maximum Length	Speed	Weight	Flight Endurance	Turning Radius
Fixed wing	1.5 m	15 m/s	2 kg	45 min	13 m (n_{max}=2)
Rotary wing	0.5 m	7 m/s	2 kg	25 min	3 m (n_{max}=2)
LTA	7 m	5 m/s	6 kg	90 min	23 m (n_{max}=2)

1.3.1 Fixed wing

This section analyzes the main features of 38 commercial fixed-wing remote-controlled systems. Almost all the on-market fixed-wing drones have a conventional tailplane configuration, straight cantilevered wings, one motor, and one fixed pitch propeller. Fixed-wing drones can rapidly explore vast territories (like cropped fields), being the fastest choice among the types of drones. They can fly for a long time and distance for each battery charge cycle compared to rotary-wing drones, their major competitors. Also, fixed-wing drones are little affected by the wind proving to be generally stable.
On the other hand, fixed-wing drones can't analyze a particular area carefully; they have an image resolution equal to a tenth than a rotary-wing model for a comparable market segment [284]. Fixed-wing drones can't hover since they need to move into the air to generate lift. They are not VTOL (Vertical Take-Off and Landing), requiring a runway or other complicated device to take off (human hand as in Fig.1.2a, or catapults as in Figg.1.2c and 1.2d) or landing (drone net, Fig.1.2b). These problems are severe disincentives, especially in the civil field, which needs practicality rather than high performance.
Consequently, the commercial drone market has moved to rotary-wing models that have worse both speed and operating time range features but have the advantage of being able to land and take off vertically in a straightforward way. Fixed-wing drones are less than 10% of the total commercial drone market [158], while rotary-wing ones are near 90%. The market also offers hybrid drone models to take advantage of both fixed and rotary-wing model characteristics, as in Fig.1.3.

(a) (b)

Figure 1.1: soldier mounting a *Raven RQ-11B* [20] taking parts from the briefcase where the drone is carried, Fig.1.1a completely disassembled as in Fig.1.1b.

Tables 1.3 and 1.4 list the essential features of the analyzed fixed-wing drones, while figure 1.4 represents the distribution of their most common attributes. Figure 1.4a

(a)

(b)

(c)

(d)

Figure 1.2: manual launch of *'Raven RQ-11B'* [20] in Fig.1.2a, a recovery net on the stern of a battleship catches a *Pioneer I* [243] in Fig.1.2b, the launch catapult of the *'Orbiter'* [18] in Fig.1.2c, and the manual launch catapult of the *'BlueBird'* [53] in Fig.1.2d.

(a)

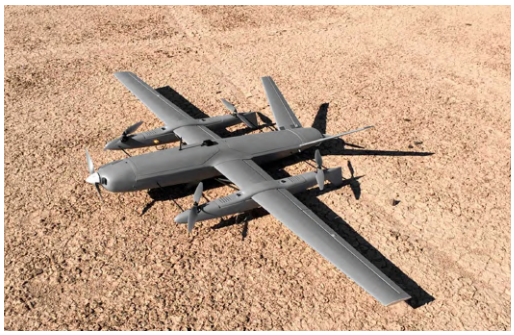

(b)

Figure 1.3: hybrid VTOL-fixed wing drones *Foxyslim* [133] in Fig.1.3a and *Pelican* [67] in Fig.1.3b.

shows that the most common wing-span drone value lies between 1.5 and 2 meters with 31% of the analyzed models. For this reason, the author suggests as drone fixed-wing wing-span, the value 1.5 meters. The path planner uses the wing-span value to

determine the casualty area covered in section 2.3.4. Figure 1.4b shows the distribution of the maximum take-off weight (MTOW) value. The range between 1 and 2 kilograms contains the most considerable portion, with 21% of the analyzed models; the author suggests the 2 kilograms as MTOW value. The drone's dynamics and the probability of fatality given the exposure, discussed in section 2.3.2, are linked to the MTOW. Figure 1.4c shows the cruising speed value distribution; almost 45% of the analyzed models have a speed between 15 and 20 m/s. The writer suggests 15 m/s as cruising speed value, used to evaluate the buffer zone, discussed in section 2.4.3, and the probability of fatality given the exposure, discussed in section 2.3.2. Figure 1.4d suggests that the majority of the fixed-wing drones fly less than 90 minutes, and a significant part less than 60, but more than 30 minutes. That means that these kinds of drones can be used for a relatively long mission that can cover great distances. In choosing the best drone for the mission, the mission requirement turns out to be decisive.

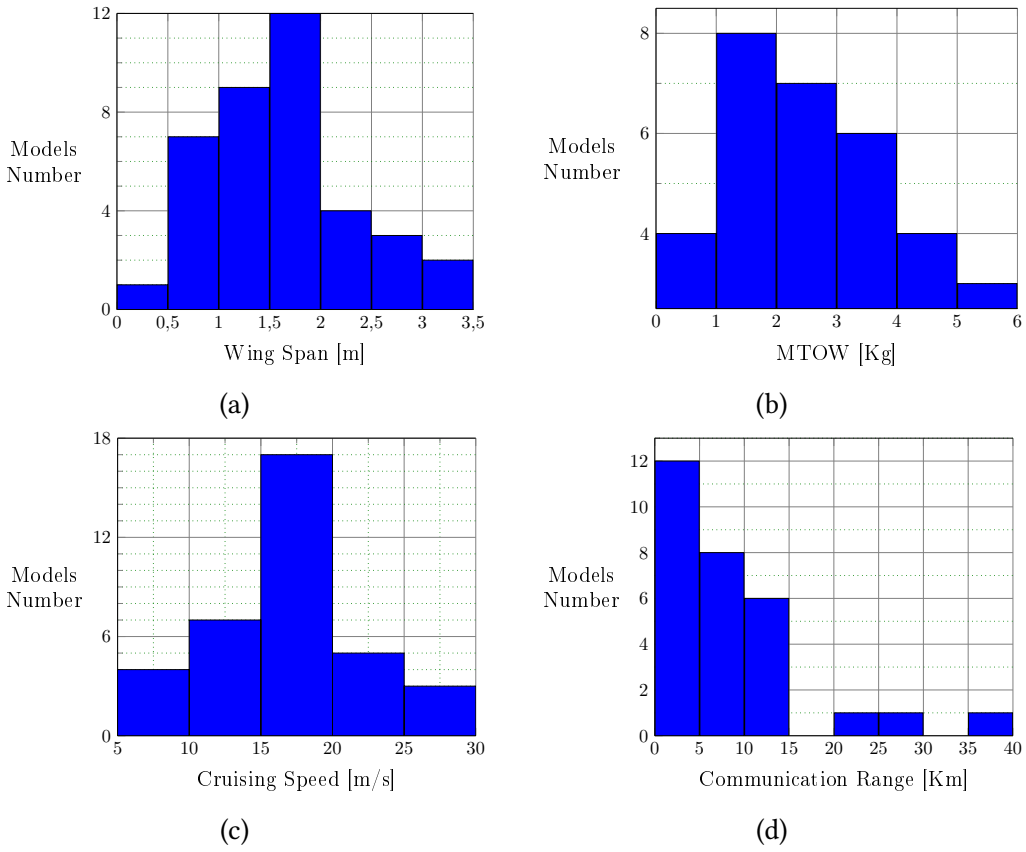

Figure 1.4: distribution of the wing-span 1.4a, maximum take-off weight 1.4b, cruising speed 1.4c, and flight endurance 1.4d for the fixed-wing analyzed models.

Table 1.2: fixed-wing aircraft – main pros and cons [131]

• Long endurance: the fixed-wing allows greater efficiency compared to rotary-wing solutions, which means, with the same batteries used, a longer endurance than rotary-wing drones. • Large area coverage: fixed-wing drones are characterized by both higher speed and higher endurance compared to other solutions. These features allow the analysis of large surfaces in a single mission. • Fast flight speed: the fixed-wing allows flying at high speeds without degrading efficiency, as with rotary-wing drones or lighter than air solutions. When you need to fly at high speeds, the choice falls on the use of the fixed-wing drones. • No VTOL/hover: Fixed-wing drones need minimal airflow around the wings to generate lift. This fact does not allow fixed-wing drones to fly below a certain speed or hover. If you need to over-analyze an area, fixed-wing drones are not the solution to choose. • Launch and recovery are not practical. The previous point also involves another result: the need for help to speed up the drone during take-off and slow down the drone during landing. For take-off, in the case of small drones, the human force can be used to hurl the drone, but it is necessary to use catapults in the case of larger drones. For landing, if runways cannot be used, a net can be used instead. These methods always presuppose the presence of some type of infrastructure, and the use of fixed-wing drones can therefore be impractical. • Harder to fly, more training needed: fixed-wing drones have some critical issues compared to other types of drones. They need to fly at high speeds to have a lift, and this fact forces the pilot to have quick reflexes and to analyze a large volume simultaneously. In case of problems, there is no possibility of hovering, and therefore an emergency plan is mandatory. Ultimately a fixed-wing drone pilot does a more difficult job than a rotary-wing drone pilot.

Table 1.3: fixed-wing remote-controlled systems analyzed characteristics part 1 of 2.

Model	Manufacturer	Wing Span	Length	Weight	Cruising speed
Raven RQ-11B [20]	AeroVironment	1.4 m	0.9 m	1.9 Kg	8.5 m/s
Puma RQ-20B [19]	AeroVironment	2.8 m	1.4 m	5.9 Kg	21 m/s
Dragon Eye RQ-14 [35]	AeroVironment	1.1 m	0.9 m	2.7 Kg	18 m/s
Wasp [21]	AeroVironment	1 m	0.76 m	1.3 Kg	10 m/s
Wasp III [263]	AeroVironment	0.7 m	0.4 m	0.4 Kg	11 m/s
Skate [270]	Aurora Flight Sc.	0.6 m	0.5 m	1 Kg	23 m/s
Orbiter [18]	A.D.O.	2.2 m	1 m	6.5 Kg	30 m/s
Mosquito [140]	I.A.I.	0.35 m	0.35 m	0.5 Kg	13 m/s
Micro Falcon [143]	Innocon	2 m	0.7 m	5 Kg	18 m/s
Spider [144]	Innacon	1.75 m	0.8 m	3.5 Kg	21 m/s
Foxyslim [133]	Heliceo	1.5 m	1 m	2 Kg	33 m/s
Foxypro [132]	Heliceo	3.2 m	1 m	11 Kg	33 m/s
RemoEye-002B [271]	UconSystem	1.8 m	1.4 m	3.5 Kg	23 m/s
Atmos7 [62]	CATUAV	1.3 m	1 m	2.6 Kg	8 m/s
MicroB[53]	BlueBird AeroSys.	1 m	0. 75 m	1.5 kg	23 m/s
SB4 Phoenix[250]	Sunbird	3 m	1.3 m	3 Kg	8 m/s
Rx60 [26]	AgEagle	1.4 m	0.7 m	3.2 Kg	15 m/s
Rx48 [25]	AgEagle	1.2 m	0.7 m	2 Kg	15 m/s
Avem [17]	Aeromapper	2.1 m	1.5 m	2 Kg	16 m/s
F7200[273]	Altavian	2.7 m	1.7 m	6.8 Kg	15 m/s
Tracker [28]	Cassidian	3.6 m	1.7 m	8.5 Kg	17 m/s
Bramor C4EYE [59]	C-Astral	2.3 m	1.8 m	4.5 Kg	23 m/s
Goshhawk[9]	Aeraccess	2 m	1.5 m	6 Kg	25 m/s
MH850 [182]	MAVTech	0.85 m	0.5 m	1 Kg	12.5 m/s
Agri1900 [180]	MAVTech	1.9 m	1.1 m	2.5 Kg	12.5 m/s
Agri2000 [181]	MAVTech	2.2 m	1 m	4 Kg	15 m/s
LA500-AG[167]	Lehman A.	1.6 m	0.7 m	1.2 Kg	19 m/s
Desert Hawk III[173]	Lokheed Martin	1.5 m	0.7 m	3.7 Kg	12 m/s
Sirius[179]	MAVinci	1.6 m	1.2 m	2.7 Kg	18 m/s
ZALA 421-08[166]	ZALA	0.8 m	0.4 m	1.7 Kg	28 m/s
ZALA 421-16EM[165]	ZALA	1.8 m	0.9 m	6.5 Kg	28 m/s
Bayraktar Mini A [118]	Baykar	1.6 m	1.2 m	3.5 Kg	19 m/s
Bayraktar Mini B[119]	Baykar	1.9 m	1.2 m	4.5 Kg	15 m/s
Avian-RTK[266]	Uaver	1.9 m	1 m	5.2 Kg	19 m/s
Besra[267]	Uaver	1.5 m	0.8 m	2.6 Kg	17 m/s
Avian-S [265]	Uaver	1.9 m	1 m	5.2 Kg	19 m/s
Avian-P[264]	Uaver	1.6 m	0.8 m	4.7 Kg	19 m/s
Swallow-P[268]	Uaver	1 m 0.4 m	2.5 Kg	25 m/s	

Table 1.4: fixed-wing remote-controlled systems analyzed characteristics part 2 of 2.

Model	Manufacturer	Range	Endurance	Launch	Payload
Raven RQ-11B [20]	AeroVironment	10 Km	90’	manual	0.18 Kg
Puma RQ-20B [19]	AeroVironment	15 Km	120’	manual	0.2 Kg
Dragon Eye RQ-14 [35]	AeroVironment	10 Km	60’	manual	0.3 Kg
Wasp [21]	AeroVironment	5 Km	50’	manual	0.2 Kg
Wasp III [263]	AeroVironment	5 Km	45’	manual	0.1 Kg
Skate [270]	Aurora Flight Sc.	3 Km	40’	manual	0.2 Kg
Orbiter [18]	A.D.O.	15 Km	90’	catapult	2 Kg
Mosquito [140]	I.A.I.	3Km	40’	manual	undefined
Micro Falcon [143]	Innocon	30 Km	180’	manual	0.6 Kg
Spider [144]	Innacon	10 Km	120’	manual	1 Kg
Foxyslim [133]	Heliceo	5 Km	45’	VTOL	0.2 Kg
Foxypro [132]	Heliceo	5 Km	60’	VTOL	1 Kg
RemoEye-002B [271]	UconSystem	10 Km	60’	manual	0.3 Kg
Atmos7 [62]	CATUAV	undefined	80’	manual	0.6 Kg
MicroB[53]	BlueBird AeroSys.	10 Km	60’	port. catap.	0.5 Kg
SB4 Phoenix[250]	Sunbird	12 Km	sunlight	manual	0.5 Kg
Rx60 [26]	AgEagle	2 Km	60’	catapult	0.3 Kg
Rx48 [25]	AgEagle	2 Km	40’	maual	0.1 Kg
Avem [17]	Aeromapper	15 Km	120’	manual	0.5 Kg
F7200[273]	Altavian	80 Km	90’	manual	2 Kg
Tracker [28]	Cassidian	10 Km	90’	manual	1 Kg
Bramor C4EYE [59]	C-Astral	40 Km	180’	catapult	0.5 Kg
Goshhawk[9]	Aeraccess	undefined	120’	catapult	1 Kg
MH850 [182]	MAVTech	5 Km	45’	manual	0.1 Kg
Agri1900 [180]	MAVTech	1 Km	30’	manual	0.3 Kg
Agri2000 [181]	MAVTech	7.5 Km	60’	manual	1 Kg
LA500-AG[167]	Lehman A.	3 Km	45’	manual	0.3 Kg
Desert Hawk III[173]	Lokheed Martin	undefined	90’	bungee cord	1 Kg
Sirius[179]	MAVinci	2.5 Km	50’	manual	0.2 Kg
ZALA 421-08[166]	ZALA	15 Km	90’	manual	0.2 Kg
ZALA 421-16EM[165]	ZALA	25 Km	90’	manual	0.5 Kg
Bayraktar Mini A [118]	Baykar	10 Km	60’	manual	0.4 Kg
Bayraktar Mini B[119]	Baykar	15 Km	60’	manual	0.7 Kg
Avian-RTK[266]	Uaver	undefined	90’	bungee cord	0.7 Kg
Besra[267]	Uaver	undefined	40’	manual	0.3 Kg
Avian-S [265]	Uaver	undefined	95’	bungee cord	0.7 Kg
Avian-P[264]	Uaver	undefined	90’	bungee cord	0.4 Kg
Swallow-P[268]	Uaver	undefined	50’	bungee cord	0.3 Kg

1.3.2 Rotary Wing

This paragraph analyzes the main features of 45 commercial rotary-wing remote-controlled systems. Rotary-wing models have features that are often complementary to those of fixed-wings. They are VTOL, which is why they are breaking into the market; as mentioned in the previous paragraph, the most widespread configuration in the civil market is the quadrotor with about 90% of the market share [158]. They don't need any device, runway, or human intervention to take off or land. Rotary-wing models can hover, on the contrary of the fixed-wing ones, allowing them to sift through a specific area since they can analyze closer than other solutions, thanks to a ten times better resolution than the ones offered by the fixed-wing drone's model [284]. Since the rotary-wing propulsion is less efficient than the fixed-wing, compared to fixed-wing drones, rotary-wing drones are slower (compare Figg.1.4c and 1.6c), noisier, and can fly for a lower amount of time (the reader can compare Figg.1.4d and 1.6d). They also typically have larger engines and propellers like the helicopter-like *Vapor* by Aeroenvironment [16] in Fig.1.5a, or a more significant number of engines; the classic rotary-wing drone configuration is the quadrotor with four fixed-pitch propellers as the *Phantom 4* by DJI [95] in Fig.1.5b. Rotary-wing drones can carry a wider variety of payloads, typically larger and heavier than those installed onboard fixed-wing models, presenting no encumbrance problems. Their characteristics make them suitable for various missions; they are usually used for aerial photography and video aerial inspection, and delivery purposes. However, these devices present a practical problem that is slowing down their use in some contexts or countries, especially for the delivery purposes [148], and has totally prohibited their use in many environments, such as over the animal feeding structures [194], and protected natural areas [36]: these devices are very noisy. The solution to this problem is not trivial, but some studies [285] suggest that a different propeller design could greatly improve the problem by letting the noise produced enter within acceptable ranges. Noise-related problems, however, are not addressed in the thesis, which aims to offer a different risk formulation and simulate an operational scenario in which the original risk assessment is used. The data extrapolated in this section were tabulated in Tables 1.6-1.9 and represented in figure 1.6.
Figure 1.6a shows the drones' maximum size values distribution; 31% of models analyzed belong to the range between 0 and 0.5 meters, while 58% of the models surveyed belong to the range between 0 and 1 meter. In the calculations, this magnitude influences the path planner that uses it to determine the *casualty area* covered in section 2.3.4. The author of this thesis proposes as the maximum size of rotary-wing drones, one-half meter. Figure 1.6b shows the distribution of the rotary-wing maximum take-off weight (MTOW) value. Again, the range between 1 and 2 kilograms contains the most considerable portion, with 17% of the analyzed models, not very far from the other MTOW ranges. The author also suggests, in this case, 2 kilograms as MTOW value; the drone's dynamics and the probability of fatality given the exposure, discussed in section 2.3.2, are linked to the MTOW. Figure 1.6c shows the rotary-wing cruising speed

value distribution; how one can imagine, this value is much lower than one related to the fixed-wing models previously analyzed. Almost 23% of the analyzed values lie in the range between 5 and 7 m/s, while 38% lie in the 5 to 9 m/s range. The author of this thesis suggests the value 7 m/s as cruising speed in the calculation of this thesis. As said in the previous section, cruising speed is used to evaluate the buffer zone, discussed in section 2.4.3, and the probability of fatality given the exposure, discussed in section 2.3.2. Graph 1.6d suggests that most rotary-wing models have a flight endurance in the range between 15 and 30 minutes; that is a characteristic that the mission analysts have to consider.

Table 1.5: rotary-wing aircraft main pros and cons [131]

• Vertical take-off and landing (VTOL): the rotary-wing drones need no extra devices or help for take-off and landing.
• Hovering capability: it is possible to hover on a spot allowing more accurate analysis.
• Easy to use: since they are slower than fixed-wing drones and since they are more stable not having stall problems, rotary-wing drones are considered easier to fly.
• Greater maneuverability: since the slower allowed speed, even the hoovering is allowed, the rotary-wing drones have a very small turning-radius.
• Can operate in a confined area: the rotary-wing drones can operate in small and spaces.
• Good camera data quality: the ability to hover can produce better camera data compared to the one obtained from a fixed-wing drone.
• Lower speeds on more power: due to the intrinsic characteristics, these drones are typically slow.
• Short flight times constrained by batteries: rotary-wing is a very uneffi-cient way to fly thus consuming more battery power.

(a) (b)

Figure 1.5: two different types of rotary-wing drone; Fig.1.5a shows the helycopter-like *Vapor* [16] while Fig.1.5b shows the quadrotor *Phantom 4* [95].

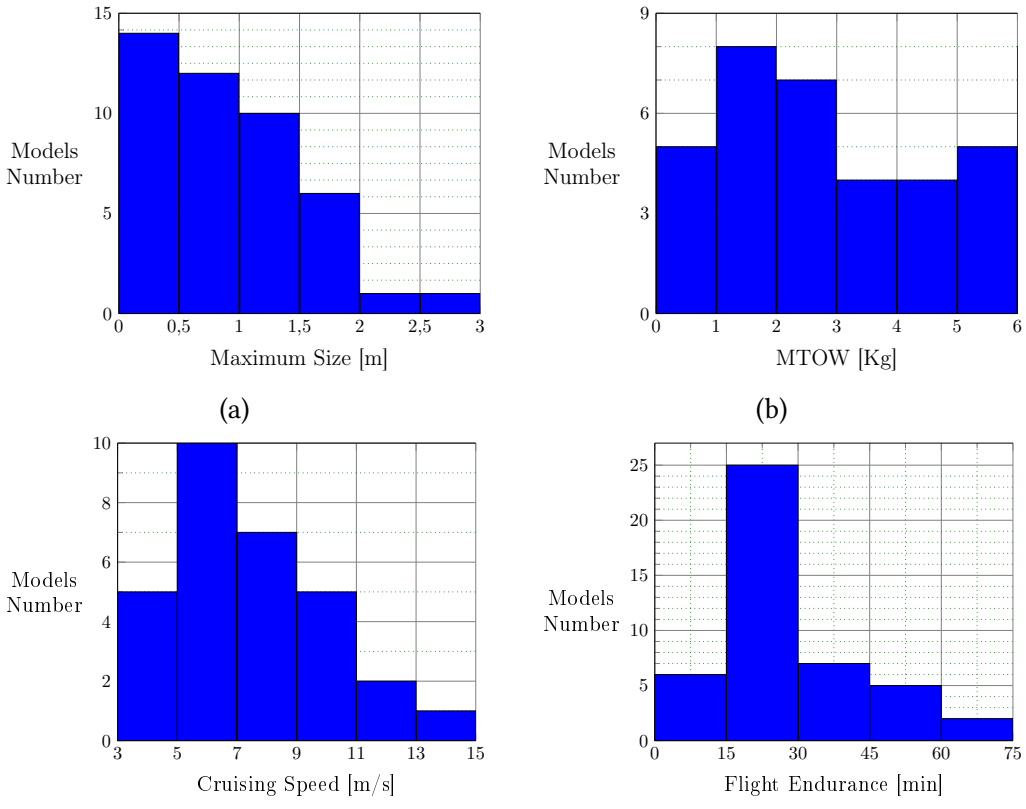

(a) (b) (c) (d)

Figure 1.6: maximum size 1.6a, maximum takeoff weight 1.6b, cruising speed in horizontal direction 1.6c, and flight endurance 1.6d for the analyzed rotary-wing models.

Table 1.6: rotary-wing remote-controlled systems analyzed characteristics part 1 of 4.

Model	Manufacturer	Max. Size	Weight	Cruising speed
Scout[23]	Aeryon	0.8 m	1.7 Kg	11 m/s
SkyRanger[24]	Aeryon	1 m	2.5 Kg	14 m/s
Fox6[135]	Hélicéo	1.5 m	7.5 Kg	8 m/s
Fox4[134]	Hélicéo	1.2 m	5 Kg	8 m/s
Q4L [183]	MAVTech	1 m	1.8 Kg	5 m/s
Q4P[184]	MAVTech	1.9 m	7.5 Kg	4 m/s
Titan4HSE[147]	Italdron	1.7 m	5.5 Kg	8 m/s
4HSE EVO[147]	Italdron	0.7 m	9 Kg	8 m/s
Inspire 2[92]	DJI	1.5 m	4 Kg	22 m/s
Inspire 1 PRO[91]	DJI	1.5 m	3.5 Kg	16 m/s
Mavic[93]	DJI	0.4 m	0.75 Kg	18 m/s
Phantom 4 adv[95]	DJI	0.4 m	1.4 Kg	16 m/s
MK8-3500 S[191]	Mikrokopter	1.2 m	4.6 Kg	undefined
BE 4000[287]	Xamen	0.3 m	2 Kg	15 m/s
LE4-8X[288]	Xamen	0.3 m	6.7 Kg	11 m/s
Pelican[67]	Clearpathrobotics	0.7 m	1.2 Kg	8 m/s
Hummingbird[66]	Clearpathrobotics	0.5 m	0.7 Kg	14 m/s
Galaxy R8700[31]	Altavian	1.3 m	12 Kg	7 m/s
Q800XE[8]	Aeraccess	1.3 m	6 Kg	7 m/s
Typhoon H[292]	Yuneec	0.5 m	2 Kg	16 m/s
Breeze[290]	Yuneec	0.2 m	0.4 Kg	4 m/s
Typhoon 4K[292]	Yuneec	0.4m	1.7 Kg	6 m/s
H920[291]	Yuneec	1 m	5 Kg	10 m/s

Table 1.7: rotary-wing remote-controlled systems analyzed characteristics part 2 of 4.

Model	Manufacturer	Max. Size	Weight	Cruising speed
Neo[1]	AceCore Tech.	1.1 m	19 Kg	10 m/s
Zoe[2]	AceCore Tech.	0.7 m	12 Kg	10 m/s
OH8200[213]	Origin Hobby	2.7 m	30 Kg	6 m/s
OH6061[212]	Origin Hobby	2.3 m	20 Kg	11 m/s
OH6086[211]	Origin Hobby	1.3 m	4 Kg	6 m/s
OH4100[214]	Origin Hobby	1.8 m	8 Kg	6 m/s
R4 Roller LM[232]	R4robotics	0.5 m	1.7 Kg	6 m/s
R4 Roller SM[233]	R4robotics	0.3 m	0.5 Kg	4 m/s
R4 IMSQC[234]	R4robotics	1.4 m	3 Kg	11 m/s
R4 IMSHC[231]	R4robotics	1 m	2.5 Kg	11 m/s
R4 IMLEHPQC[230]	R4robotics	2 m	2.8 Kg	11 m/s
Snipe[22]	Aerovironment	0. 3m	0.15 Kg	8 m/s
MD4-1000[189]	Microdrones	1 m	6 Kg	13 m/s
Splash Drone 3 Auto[251]	Swellpro	0.5 m	5 Kg	13 m/s
Quadrotor [269]	Uaver	1.7 m	8 Kg	13 m/s
D800[261]	Pentax	0.5 m	5 Kg	8 m/s
Guardian[15]	Draganfly	0.6 m	1.5 Kg	13 m/s
X4-P[244]	Draganfly	0.9 m	2.5 Kg	13 m/s
Commander [98]	Draganfly	1.1 m	3.8 Kg	13 m/s
AD1[3]	Action Drone USA	0.6 m	2.2 Kg	8 m/s
AD2[4]	Action Drone USA	1 m	5.5 Kg	8 m/s
IA-3 Colibrì [141]	IDS Corp.	0.8	5 Kg	16 m/s

Table 1.8: rotary-wing remote-controlled systems analyzed characteristics part 3 of 4.

Model	Manufacturer	Range	Endurance	Payload
Scout[23]	Aeryon	3 Km	25’	0.3 Kg
SkyRanger[24]	Aeryon	5 Km	50’	0.3 Kg
Fox6[135]	Hélicéo	2 Km	25’	1 Kg
Fox4[134]	Hélicéo	2 Km	25’	0.3 Kg
Q4L [183]	MAVTech	1.2 Km	25’	0.3 Kg
Q4P[184]	MAVTech	1.2 Km	60’	2 Kg
Titan4HSE[147]	Italdron	1.5 Km	30’	1 Kg
4HSE EVO[147]	Italdron	1.5 Km	30’	2.5 Kg
Inspire 2[92]	DJI	7 Km	25’	0.8 Kg
Inspire 1 PRO[91]	DJI	5 Km	15’	0.4 Kg
Mavic[93]	DJI	7 Km	21’	0.05 Kg
Phantom 4 adv[95]	DJI	4 Km	30’	0.3Kg
MK8-3500 S[191]	Mikrokopter	4 Km	30’	2 Kg
BE 4000[287]	Xamen	1 Km	15’	0.3 Kg
LE4-8X[288]	Xamen	4 Km	20’	1 Kg
Pelican[67]	Clearpathrobotics	1 Km	20’	0.6 IKg
Hummingbird[66]	Clearpathrobotics	1 Km	20’	0.2 Kg
Galaxy R8700[31]	Altavian	6 Km	25’	1.5 Kg
Q800XE[8]	Aeraccess	3 Km	25’	1 Kg
Typhoon H[292]	Yuneec	1.6 Km	25’	0.3 Kg
Breeze[290]	Yuneec	0.3 Km	12’	0.05 Kg
Typhoon 4K[292]	Yuneec	0.4 Km	25’	0.3 Kg
H920[291]	Yuneec	1.6 Km	25’	0.7 Kg

Table 1.9: rotary-wing remote-controlled systems analyzed characteristics part 4 of 4.

Model	Manufacturer	Range	Endurance	Payload
Neo[1]	AceCore Tech.	1.6 Km	25’	9 Kg
Zoe[2]	AceCore Tech.	1.5 Km	40’	6.5 Kg
OH8200[213]	Origin Hobby	5 Km	70’	8 Kg
OH6061[212]	Origin Hobby	5 Km	70’	5 Kg
OH6086[211]	Origin Hobby	5 Km	60’	1 Kg
OH4100[214]	Origin Hobby	6 Km	60’	1 Kg
R4 Roller LM[232]	R4robotics	1 Km	20’	0.2 Kg
R4 Roller SM[233]	R4robotics	0.2 Km	10’	0.1 Kg
R4 IMSQC[234]	R4robotics	2 Km	45’	1 Kg
R4 IMSHC[231]	R4robotics	2 Km	45’	0.5 Kg
R4 IMLEHPQC[230]	R4robotics	2 Km	60’	0.3 Kg
Snipe[22]	Aerovironment	1 Km	15’	0.05 Kg
MD4-1000[189]	Microdrones	20Km	35’	1.2 Kg
Splash Drone 3 Auto[251]	Swellpro	1Km	16’	1 Kg
Quadrotor [269]	Uaver	1.5Km	30’	0.5 Kg
D800[261]	Pentax	2Km	15’	4 Kg
Guardian[15]	Draganfly	1Km	15’	0.4 Kg
X4-P[244]	Draganfly	1Km	16’	0.8 Kg
Commander [98]	Draganfly	1Km	16’	1 Kg
AD1[3]	Action Drone USA	1.6Km	20’	0.6 Kg
AD2[4]	Action Drone USA	1.6Km	45’	0.7 Kg
IA-3 Colibrì [141]	IDS Corp.	1 Km	40’	1 Kg

1.3.3 Airship

Lither-than-air drones are an interesting alternative to the two types of drones previously seen. They are machines that exploit Archimedes's principle to stay in the air, typically using helium as lifting gas. Since they don't need any moving parts to generate lift, they could float in the air for a very long time. Many disadvantages limit their usages, such as their great inertia and the large surface that makes them vulnerable to wind and difficult to maneuver on many occasions. In this section, the author focused on electric, non-tethered LTA drones. This section analyzes 35 commercial lither-than-air drones characteristics as previously did.
Figure 1.7a shows one of the two main lither-than-air drone dimensions; the length (the other one is the maximum radius). It's hard to find LTA drones below 3 meters in length, and most of the analyzed LTA drones fall within the range between 5 and 7 meters, with 26% of the analyzed models, while 43% of them have a diameter between 1.5 and 2 meters, shown in Fig.1.7b. These dimensions are related to the significant volume of lifting gas the lither-than-air drones need to exploit Archimedes's principle properly. LTA risk evaluation should exploit the LTA drones length in the same role as the wing-span for the fixed-wing drones; the path planner uses this value to determine the casualty area covered in section 2.3.4. This thesis's author proposes 7 meters as LTA drone length for the further simulations.
The LTA MTOW value is not easy to obtain, because it is not provided in the datasheets, but the LTA manufacturers provide the related payload. From the human carrying LTA ship data [84] and [37], it has emerged that the really small LTA drones, MTOW is about three times its payload. Therefore, looking at graph 1.7a, it appears that the range between 1 and 2 kilograms is the most likely payload mass, with 31% of the analyzed models, i.e., the most probable commercial LTA drone mass is in the range between 3 and 6 kilograms. The author suggests, for the LTA drones, 6 kilograms as MTOW value for the calculation; the drone's dynamics and the probability of fatality given the exposure, discussed in section 2.3.2, are linked to the MTOW.
Figure 1.7d shows the cruising speed value distribution; this value is even competitive to the fixed-wing drones one; 45% of the analyzed values lie in the range between 4 and 8 m/s, while more than 77% lie in the 4 to 12 m/s one. For the calculation, the author suggests the value 5m/s as speed value. The buffer zone, discussed in section 2.4.3, and the probability of fatality given the exposure, discussed in section 2.3.2, exploit the cruising speed.
Graphs 1.7e describes the flight endurance distribution (intended as the amount of time the LTA drone can move at cruising speed), that could be useful data for the mission analysis, but it is not exploited in this thesis.
On paper, these devices seem to have some good features. However, as will become clear later in the thesis, their size makes the associated risk simply unacceptable for any use in an urban environment.

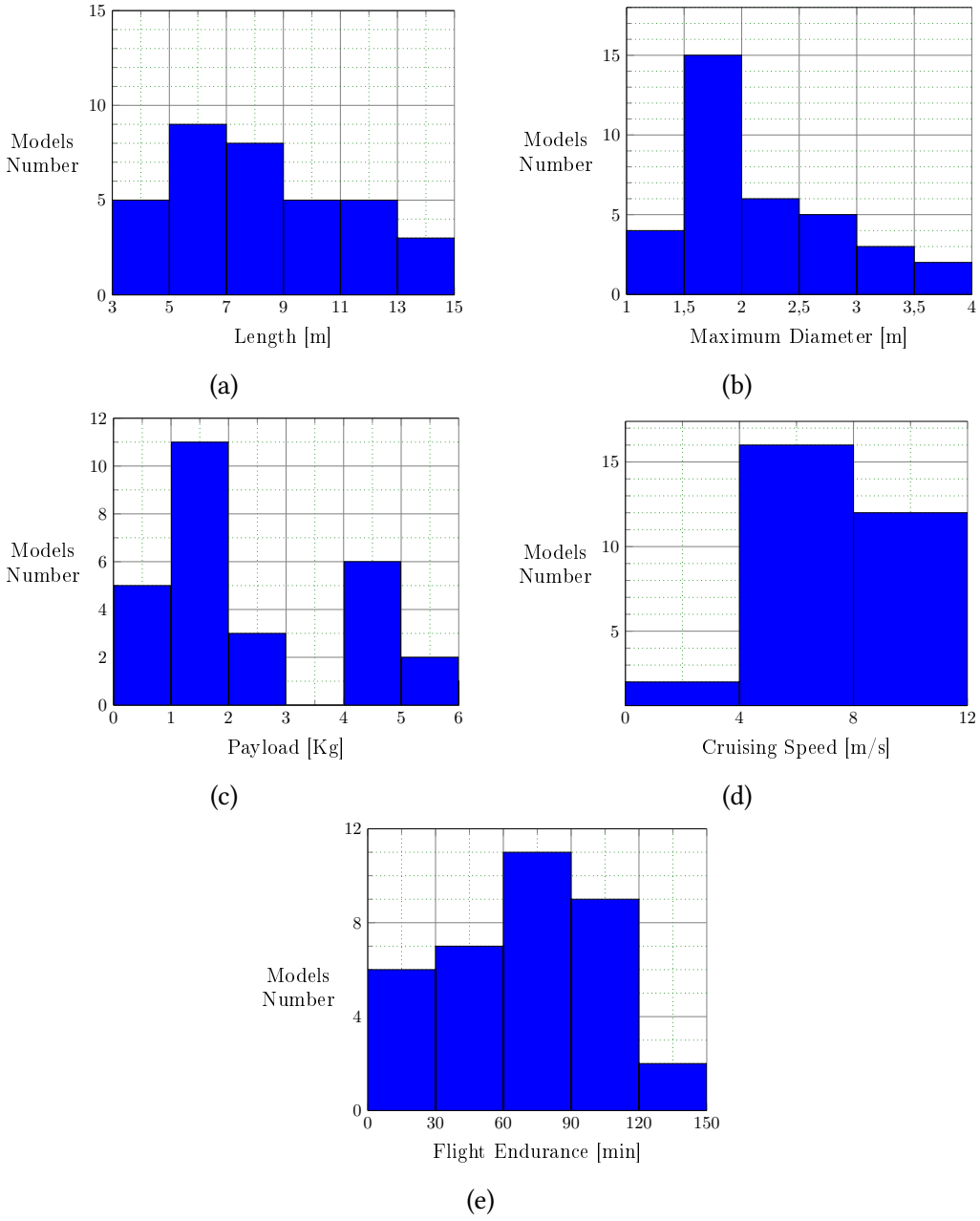

Figure 1.7: distribution of the length 1.7a, diameter 1.7b, payload weight 1.7c, cruising speed 1.7d, and endurance 1.7e for the lighter-than-air anlyzed models.

Table 1.10: lither-than-air remote-controlled systems analyzed characteristics part 1 of 2.

Model	Manufacturer	Length	Diameter	Payload
13 ft Elec. Air.[51]	Blimpguys	4 m	1.3 m	0.5 Kg
20 ft Elec. Air. [52]	Blimpguys	6 m	1.8 m	1.4 Kg
5m ORC [12]	RC-Zeppelin	5m	1.7 m	1.2 Kg
6m ORC [13]	RC-Zeppelin	6 m	1.7 m	2 Kg
7m ORC [14]	RC-Zzeppelin	7 m	2 m	2 Kg
10m ORC [10]	RC-Zeppelin	10 m	2.2 m	5 Kg
12m ORC [11]	RC-Zeppelin	12 m	2.2 m	5 Kg
MZ4000 I [32]	Anabatic Aero	4 m	1.4m	0.5 Kg
MZ4500 I [32]	Anabatic Aero	4.5 m	1.4 m	1 Kg
MZ5000 I[32]	Anabatic Aero	5 m	1.5 m	1.5 Kg
MZ6000 I [32]	Anabatic Aero	6 m	1.6 m	1.5 Kg
MZ7000 I [32]	Anabatic Aero	7 m	1.7 m	2.8 Kg
MZ8000 I [32]	Anabatic Aero	8 m	1.9m	4.5 Kg
MZ6000 Outdoor SE[33]	Anabatic Aero	6 m	1.7 m	1.5 Kg
MZ7000 Outdoor SE [33]	Anabatic Aero	7 m	1.8 m	1.5 Kg
MZ8000 Outdoor SE [33]	Anabatic Aero	8 m	1.9m	2.8 Kg
MZ9000 Outdoor SE ADV [33]	Anabatic Aero	9 m	1.7 m	0.4 Kg
MZ9000 Outdoor SE [33]	Anabatic Aero	9 m	2.2 m	4.5 Kg
MZ10'000 Outdoor SE[33]	Anabatic Aero	10 m	2.3 m	6 Kg
MZ11'000 Outdoor SE[33]	Anabatic Aero	11 m	2.6 m	10 Kg
MZ12'000 Outdoor SE[33]	Anabatic Aero	12 m	3 m	15 Kg
MZ13'000 Outdoor SE[33]	Anabatic Aero	13 m	3.5 m	20 Kg
MZ14'000 Outdoor SE[33]	Anabatic Aero	14 m	3.5 m	22 Kg
MZ6000 Outdoor TE[34]	Anabatic Aero	6 m	1.7 m	1.5 Kg
MZ7000 Outdoor TE[34]	Anabatic Aero	7 m	1.8 m	1.5 Kg
MZ8000 Outdoor TE[34]	Anabatic Aero	8 m	1.9 m	2.8 Kg
MZ9000 Outdoor TE ADV [34]	Anabatic Aero	9 m	1.7m	0.4 Kg
MZ9000 Outdoor TE [34]	Anabatic Aero	9 m	2.2 m	4.5 Kg
MZ10'000 Outdoor TE[34]	Anabatic Aero	10 m	2.3 m	6 Kg
MZ11'000 Outdoor TE[34]	Anabatic Aero	11 m	2.6 m	10 Kg
MZ12'000 Outdoor TE[34]	Anabatic Aero	12 m	3 m	15 Kg
MZ13'000 Outdoor TE[34]	Anabatic Aero	13 m	3.5 m	20 Kg
MZ14'000 Outdoor TE[34]	Anabatic Aero	14 m	3.5 m	22 Kg
UAS EM T1 [58]	BVPService	8.7 m	2.6m	1.5 Kg
UAS EM T2 [58]	BVPService	12.7m	3.2m	5 Kg

Table 1.11: lither-than-air remote-controlled systems analyzed characteristics part 2 of 2.

Model	Manufacturer	Cruising Speed	Range	End.
13 ft Elec. Air.[51]	Blimpguys	2 m/s	0.5 Km	25’
20 ft Elec. Air. [52]	Blimpguys	3 m/s	0.5 Km	25’
5m ORC [12]	RC-Zeppelin	undefined	0.5 Km	60’
6m ORC [13]	RC-Zeppelin	undefined	0.5 Km	60 ’
7m ORC [14]	RC-Zzeppelin	undefined	undefined	60 ’
10m ORC [10]	RC-Zeppelin	undefined	undefined	60’
12m ORC [11]	RC-Zeppelin	undefined	undefined	70’
MZ4000 I [32]	Anabatic Aero	7 m/s	3 Km	25’
MZ4500 I [32]	Anabatic Aero	7 m/s	3 Km	25’
MZ5000 I[32]	Anabatic Aero	7 m/s	3 Km	25’
MZ6000 I [32]	Anabatic Aero	7 m/s	3 Km	90’
MZ7000 I [32]	Anabatic Aero	7 m/s	3 Km	90’
MZ8000 I [32]	Anabatic Aero	7 m/s	3 Km	90’
MZ6000 Outdoor SE[33]	Anabatic Aero	8 m/s	3 Km	25’
MZ7000 Outdoor SE [33]	Anabatic Aero	8 m/s	3 Km	60’
MZ8000 Outdoor SE [33]	Anabatic Aero	7 m/s	3 Km	60’
MZ9000 Outdoor SE ADV [33]	Anabatic Aero	7 m/s	3 Km	90’
MZ9000 Outdoor SE [33]	Anabatic Aero	7 m/s	3 Km	90’
MZ10’000 Outdoor SE[33]	Anabatic Aero	10 m/s	3 Km	120’
MZ11’000 Outdoor SE[33]	Anabatic Aero	10 m/s	3 Km	120’
MZ12’000 Outdoor SE[33]	Anabatic Aero	10 m/s	3 Km	120’
MZ13’000 Outdoor SE[33]	Anabatic Aero	10 m/s	3 km	120’
MZ14’000 Outdoor SE[33]	Anabatic Aero	10 m/s	3 Km	120’
MZ6000 Outdoor TE[34]	Anabatic Aero	7 m/s	3 Km	25’
MZ7000 Outdoor TE[34]	Anabatic Aero	7 m/s	3 Km	60’
MZ8000 Outdoor TE[34]	Anabatic Aero	7 m/s	3 Km	60’
MZ9000 Outdoor TE ADV [34]	Anabatic Aero	7 m/s	3 Km	90’
MZ9000 Outdoor TE [34]	Anabatic Aero	7 m/s	3 Km	90’
MZ10’000 Outdoor TE[34]	Anabatic Aero	10 m/s	3 Km	120’
MZ11’000 Outdoor TE[34]	Anabatic Aero	10 m/s	3 Km	120’
MZ12’000 Outdoor TE[34]	Anabatic Aero	10 m/s	3 Km	120’
MZ13’000 Outdoor TE[34]	Anabatic Aero	10 m/s	3 Km	120’
MZ14’000 Outdoor TE[34]	Anabatic Aero	10 m/s	3 Km	120’
UAS EM T1 [58]	BVPService	10 m/s	undefined	240’
UAS EM T2 [58]	BVPService	10 m/s	undefined	360’

1.4 Advantage of using drones compared to other solutions

This paragraph analyzes all the alternatives to drones or drone networks by assessing their pros&cons. It investigates a series of scenarios declaring which solution suits better since drones are not always the best solution. Small drones' growing reliability, increasing performances, and more accessible prices led them to conquer more market niches. Until there is a technological leap, drone limits will remain. Their limits are linked to the commercial drone's intrinsic characteristics to be small and fly at relatively low altitude and speed. Ultimately, the drones have features that are unlikely to change with technological advancement. For example, the range could increase in adopting extremely efficient batteries but never reaching those of the crewed aircraft as the low number of Reynolds at which they fly limit their efficiency [202].

1.4.1 Ground-sensing network

This section analyzes the ground-sensing network advantages and disadvantages compared to a drone-sensing network, the closest drone alternative. The ground-sensing network comprises a number of sensors placed in strategic points connected in a wired or wireless way to each other or the main station. Table 1.12 shows the ground-sensing network characteristics that are virtually opposite to those the drone-sensing network offers. Installing a ground sensors network can be expensive (depending on the field's size), but the maintenance and operating costs are almost negligible. In contrast, drones' operating and maintenance costs can be high as a pilot is typically needed.
Capillary control of ground characteristics used to [72] widely apply ground-sensing networks. The typical scenarios where ground-sensing networks are employed are two. The former is the cropped field, where there are large spaces to explore with relatively little information to study, i.e., little data and a relatively low refresh rate, for example, daily.
The latter is the urban environment, which poses very different challenges; the data to be analyzed and transmitted are many, while the refresh rate can greatly vary depending on the data to be studied. Video surveillance services need a refresh rate greater than one hertz, while the air quality measurement can use a much lower refresh rate.
Let's compare the use of a ground sensors network to a drone network for these two scenarios.
Sample data can serve as important information in a cropped field, and farmers have used ground sensing networks for a long time. It is impossible to rely only on sample information even in the cropped field anymore [262]; the farmers increasingly require the better approach of a complete field analysis even with just a daily update; drones are perfect for this purpose. We are witnessing a collaboration between the already installed ground solutions and drones, [277] and [294], but examples of the exclusive use of drones in cropped fields are increasingly common. Many scientific article authors

and companies, indeed, claim that it is possible to rely only on drones' information to monitor in a proper way the cropped areas, [256] and [39]. This claim is due to the improved batteries' autonomy and the onboard drone sensors quality. Consequently, farmers who don't have an installed ground-sensing network rely only on drone analysis.

The urban environment, the scenario studied in this thesis, instead, poses different challenges [252]. Let's assume that there are no legislative limitations to drones' overflight in an urban environment; the legislative aspect is the topic of section 1.5. The following only analyzes the technical point of view for drone-sensing networks. The urban environment is characterized by a multitude of data to be investigated and various sources, very different challenges than a cropped field. The urban environments require good quality, excellent resolution (spatial and temporal), and continuous data acquisition. Ground-sensing networks are a more practical solution in monitoring people, traffic, and air quality in high population density areas where drones usage can't offer the same quality. In contrast, the use of drones is more competitive in monitoring these magnitudes in low population density urban areas or obtaining timely information in exceptional circumstances. For these reasons, the trend that has been coming up lately in the urban environment as well, is a collaboration between drones and ground sensors networks [208].

Table 1.12: ground-sensing network main characteristics

• Limited environmental impact: the sensor network, if properly placed, does not bother the fauna, flora, or any people observed as it can happen with unmanned or manned solutions, which are very noisy.
• Continuous data acquisition: ground-sensing network continuously provides information of the analyzed area. This feature can be handy in cases where sample data is not sufficient.
• No weight problems: the weight of the sensors used is not a problem as it happens for unmanned solutions. This feature allows the use of sensors with better performances or less expensive as they are not miniaturized.
• Low hour cost: the cost of running the ground-sensing network is limited to the cost of electricity and communication. There is no need for any external support as a pilot, and maintenance can be inexpensive due to the lack of moving parts. These features allow a much lower cost of these solutions than the manned or unmanned ones and, therefore, their continuous use for prolonged periods.
• Modularity: the user can exploit a specific sensor to perform a particular task. There is no need to be redundant in choosing which sensors to use.
• Can cover a limited area: the sensors used can analyze a limited area. If placed at a very high height, the sensors can analyze larger areas but not in an urban environment where obstacles severely limit the analyzed surface.
• Each net-node needs a sensor: as easily understood, each node in the network must be associated with at least one sensor, and this leads to a high number of sensors used with the increase of the surface to be analyzed.

1.4.2 Manned aircraft

There is a clarification to be made in the use of the terms. Drones are typically associated with smaller aircraft, while larger, self-flying planes - like air-taxis - are generally associated with the term "urban air mobility" vehicles. Currently, airplanes for transporting people autonomous in every phase of the mission have been tested in the civil field. These models have also passed air traffic authority certification, such as the converted *Cessna Grand Caravan* by Xwing that has secured FAA Part 135 air carrier certification [289]. It is a matter of time for autonomous airplanes to achieve full and worldwide regulatory approval, public confidence, and usage. However, this thesis focuses on small drones, and this section wants to compare drones and manned solutions. There are many areas where drones, with appropriate payloads, result in competition or better than a piloted aircraft solution in the civil fields. Crewed aircraft turn out still essential in all those situations where a relatively long-distance, high payload mass or a particular mission is required. The civil market has focused on creating and distributing relatively small, slow, and limited autonomy drone models (see the related drone-type Tables in section 1.3). Technologically, current batteries' energy and power density make it impossible to create higher-performance electric-powered drones. The present technology reached a performance limit of the most common batteries, namely Li-Po and Li-Ion [257]. The other electrical power sources are not mature enough [7]. In the civil field, with the currently available technology, it is tough to rely upon drones to cover long distances (> 15 km), fly at high speeds (> 30 m/s), or have a payload more massive than 15 kilograms, Table 1.13 shows a comparison between these two solutions. Some research groups, in recent years, have been trying to overcome these limitations with generous funds for years and still have not reached satisfactory solutions since related technical problems persist. Furthermore, the fixed-pitch quadrotor configuration has the advantage of being cheaper to build and easier to control than the single pitch-controlled propeller, but is not very efficient; as the required power increases, it becomes a less and less economical alternative. When you need to transport large masses, such as carrying passengers, it is preferred to use a single pitch-controlled propeller; since the mechanism allowing it is expensive, it is better to have the least possible rotors to reduce the cost. Ultimately, an electrical quadrotor's real advantage over a single-rotor helicopter in people transportation does not exist.
For various other services, such as photo shootings, the inspection of electricity pylons, or precision agriculture, the drones present an alternative widely exploiting today, mostly in VLOS mode [226]. In the cases just described, being able to count on light but functional quality payloads is a significant advantage over crewed aircraft that stays in the air, moves much more air, and presents a series of problems that the drone's use dramatically reduces. Drones operating costs are meager, and in a lot of cases, the crewed alternative is impractical. In many fields where crewed solutions were widely used, for example, the inspection of power lines or oil pipelines, we are witnessing more and more often, at the cooperative use of drones and crewed aircraft. As explained in

[293] and [282], cooperation reduces costs, exploiting the multiple systems' peculiar advantages.

Table 1.13: comparision between unmanned and manned solutions.

	Drone	Manned
Coverage	m^2-km^2	several km^2
Image resolution	mm-cm	cm-dm
Geo registration accuracy	meter level	centimeter-level
Operating cost	low-moderate	high
Flexibility	can work in hazardous areas	pilot needed

1.4.3 Satellite network

A satellite network is a constellation of artificial satellites orbiting around the Earth. Each satellite can be equipped with image sensors (in different bandwidths for a complete mapping service) or communication devices (high-speed satellite-provide internet is now widespread). It can provide a broad series of services, from mapping to communication. These satellites generally orbit in LEO (Low Earth Orbit), providing no equal service-quality coverage on the Earth's surface; furthermore, they can hardly change their orbit. This section analyzes the fields where the drone and satellite sensing network can compete, showing their advantages and disadvantages, which Table 1.14 sums up. Current technology has significantly lowered satellites' construction and their placing in orbit price and improved payload quality and reliability: this significantly reduced their service cost [204], allowing better and better civil services. Satellite service's low price paved the way for a whole range of services that, until recently, was unthinkable to offer, such as distributing the internet to large areas [83] or mapping services at an affordable price [114].
Mapping is the field where satellite and drone-provided services can offer similar both quality and price solutions. Each data source has advantages and disadvantages. The main disadvantages of the satellite-provided mapping services are the low update rate and resolution, and the decreasing data quality for areas farther and farther from the satellite's orbit. Furthermore, not all Earth's surface is equally covered. Let's analyze some specific satellite-provided services.
Landsat and Sentinel are satellite-provided services that make their data available for free. Landsat is a Nasa-provided service [236]. It captures data in seven bands at a resolution of almost 30 square meters per pixel, having a revisit time of about 16 days. Sentinel is an EASA-provided service [111]. It captures data in ten bands with an almost ten square meters per pixel resolution (depending on the band). Its revisit time is five days. Other satellites provided services exist, but they are still not global or free. GaoJing/SuperView is a five-band, two-day revisit time, at 2 square meter resolution Chinese-provided service, but it only has four satellites [127].
In mapping, drones can allow a resolution <0.05m, times better than satellite-provided data, having no problems in flying over an area all the times needed; the quality of the two sources' information is incomparable.
Still, there are scenarios where the surface data obtained from satellites is enough, for example, assessing the forests' growth or health, or checking an environment before and after a seismic event or the process of erosion due to river overflows. Therefore, these cases analyze large surfaces, a process that would be too expensive and time-consuming to carry out with drones.
This market is witnessing the cooperative use of drones and satellites: the amount of data extrapolated using both sources combined is way more than those from a single source ([153] and [185]). There are geographical areas that are not well or not at all covered by the satellite mapping service, and therefore, the drone-provided one is the

only available.

Communication service in remote or rural places is another field that can use both satellites and drones. Even in this field, drones and satellites can be comparable choices [97] at first glance, mainly regarding the overall price. Still, a satellite network's reliability is much higher [223], and in the end, the satellite-based service proved to be better; drone-provided internet service has been unable to build a long-term sustainable business. To date, all the drone-based communication services have been abandoned, like Loon by Alphabet Inc. [275] or Aquila by Facebook Inc. [5].
Ultimately, the purpose determines the convenience of using the drone or satellites or both.

Table 1.14: comparision between unmanned and satellite solutions.

	Drone	Satellite
Coverage	m^2-km^2	unlimited
Image resolution	mm-cm	m-dam
Geo registration accuracy	meter level	centimeter level
Operating cost	low-moderate	data could be available for free
Flexibility	can work in hazardous areas	orbit-depending
Updating rate	seconds	days-weeks

1.5 Legislative situation in various countries

This second part of the chapter deals with the laws regarding the introduction of drones in the national civil airspace for a list of national or supranational entities of interest. The author of the thesis only analyzed countries with specific drone legislation within the nations with a significant market share. The paragraph will assess the various drones' requirements and what is allowed or forbidden to them. Two main philosophies accompany drones' legislations; the former is aimed at innovation, the latter is conservative. The innovative philosophy encourages the technological progress that drones can offer in the various civil and economic fields encouraging their use in the most diverse architectures. The other philosophy, by far the most used, focuses on human safety, making it very difficult to introduce innovations in this area, virtually preventing the use of drones with a few exceptions. In the following, the text introduces specific terminologies about the drone flight mode

- Visual Line of Sight, VLOS; in this flight mode, the pilot must always see the drone, which cannot go behind clouds, trees, or buildings. The only aids allowed to the pilot are eyeglasses and sunglasses. The maximum distance between pilot and drone is about 500 meters in almost all the legislations. VLOS is the most common flight mode among simple enthusiasts or professionals. The various legislations do not require the drone to have particular precautions in an accident, and no backup or sense and avoidance systems are needed. While this is the most common flight mode, it severely limits the usefulness of drones. No special permissions are typically required when the drone flies in VLS mode over sparsely populated areas. The competent authorities apply several restrictions to drones flying in VLOS mode in urban areas, requiring, if allowed, special permission.

- Extended Visual Line of Sight, EVLOS; this drone flight mode arises from the need to fly a drone more than 500 meters from the pilot. Navigating in this mode requires certification and an additional permit compared to the previous case. In this mode, the pilot can use aids such as binoculars or monoculars. Other subjects, called ”observers” or ”secondary pilots,” can also help the pilot; their task is to have visual contact with the drone and continuously update the pilot. The pilot remains responsible for any damage to things or people. It persists the obligation of visual contact between the pilot (or observer) and the drone, which cannot enter in clouds or hide behind buildings or trees. This flight mode is more useful than VLOS in almost all circumstances.

- Beyond Visual Line of Sight BVLOS; this is the most exciting drone flight mode and the one that drone companies are pushing for the most. Its implementation could enable service providers to conduct complex drone operations and facilitate drones to fly without human intervention. This flight mode consists of monitoring a drone mainly through the data provided by on-board instruments, which,

through a reliable connection, transmits all the necessary information to the pilot. BVLOS requires the pilot to equip the drone with some unnecessary safety systems for other flight modes. Typically, the legislation requires the pilot to provide drones with a sufficient Sense&Avoidance system. The infrastructure needed to fly the drone can also be based on the mobile network, as many tests have shown [54]. This type of flight is still not very widespread today due to legislative impediments, and when it is allowed, it is permitted only in sparsely populated areas. Many states are actively collaborating with some large companies (like Amazon.com Inc. or Alphabet Inc.) to develop a more permissive regulatory framework, evaluating the real risks that this type of flight entails.

In the drone sector, the regulation of BVLOS is a much-discussed topic, and at the moment, it is not effortless to obtain permission to fly in this mode. It would also allow drones' flight not managed by human beings, promoting a series of services not yet implemented, with essential impacts from a commercial and social perspective. Many drone-based service companies are pushing for this mode to be easier to obtain. The problems related to people's safety are still unsolved, and few countries have made it easier to obtain authorization to fly in this mode. The simulation of chapter 3 assumes the drone management in BVLOS flight mode from a remote computer.
For the thesis, the legislative aspect linked to the BVLOS is of particular interest; this section analyzes the situation exclusively about the BVLOS legislation in the countries of interest.

1.5.1 USA

In the USA, BVLOS mode is a rare exception that must be allowed, via a hard-to-get *Certificate of Waiver* (CoW), on a case-by-case basis by the body in charge, the *Federal Aviation Administration* of the United States (FAA), that has assessed the security requirements needed. Among the submitted applications, there are very few accepted. As the first one to be accepted, the most famous is an experimental test in Kansas [227]. The conditions to fly in BVLOS mode are so restrictive that most companies or universities that need to test BVLOS mode technologies prefer to move to other countries where the rules are less stringent. The push from companies that would benefit from BVLOS is strong. In 2017, the FAA Administrator Michael Huerta said that BVLOS flight regulation was the first target for the year [186]. Alphabet Inc. (an American multinational conglomerate that owns Google) has been the first company to receive the FAA approval for commercial drone deliveries. It has tested the delivery drone-based service completely in BVLOS mode in Virginia [151], in sparsely populated areas. Another company that had received FAA approval is Amazon.com Inc. that offers a delivery service using drones; Amazon.com Inc. can, at the moment, only operate in some sparsely populated areas.

1.5.2 China

China is among the most advanced countries in the introduction of drones into the national airspace. The Civil Aviation Administration of China (CAAC) is very active and at the forefront of introducing drones into the national airspace. Drone operations in BVLOS are allowed, and it is not difficult to obtain compulsory permission [117]. The limits to be respected are very generous as regards the maximum weight and speed of the drones. Limiting the weight also limits the drone's usefulness; typically, a low weight involves low autonomy and low payload quality. The Chinese legislation provides operations in BVLOS mode for drones weighing up to 150 kg, speeding up to 100 km/h (27.8 m/s), without particular restrictions on the operation site or mission. It is only necessary for the pilot to be responsible for every damage the drone makes and the drone to be connected to the Unmanned Aircraft Control Station (UACS), reporting its flight data once per second if in a high densely-populated area or once per thirty seconds otherwise. Flying in BVLOS also implies the drone to fly autonomously; this is explicitly allowed, with the obligation of the pilot to take control of the drone at any time. As often happens, the drone, in any flight mode, must always give precedence to crewed airplanes, not enter unauthorized airspace (for example, private or near airports), and terminating the flight if uncooperative drones appear. An emergency plan must be in place in the event of an out-of-control drone. China has become the privileged testing benchmark for new technologies that include drones. Having access to the BVLOS flight mode has now become indispensable for offering new drone-based services. Many US companies that test drones in BVLOS mode, since the difficulty of operating in the USA, use to carry out their tests in China.

1.5.3 European Union

EASA (European Union Aviation Safety Agency) is the European body that deals with drones' legislation in the European community's airspace. From January 1^{st}, 2021, the agencies that legislate and control the airspace of the various nations of the union have adopted the rules imposed by EASA. In September 2019, EASA provided very detailed drone rules [100]. A drone pilot must always be associated with only one drone, but there is the possibility of piloting a drone in BVLOS mode over a controlled ground area and in a sparsely populated environment. EASA has not yet expressed its opinion on using BVLOS in a populated environment and over an assembly of people, hinting a future updating. Fully autonomous operations are not allowed, except in case of a lost link. For these reasons, the European legislation forbids the drone architecture proposed in this thesis work.
The European approach is safety-first. Analyzing the EASA legislation in a more detailed way is useful because it introduces innovative concepts and because it will be applied to a vast audience, more than 300 million inhabitants. EASA regulations do not distinguish between occasional amateur use and professional use. The things to

consider are the drone, the environment in which it operates, and the pilot's flight certification. Apart from cases that fall within the sporadic amateur use in uninhabited areas, the drone pilot needs to obtain a permit from the national air traffic authority, which must assess on a case-by-case basis whether the risk associated with the mission is adequate or not. The process to follow to evaluate the risk is called *Specific Operations Risk Assessment* (SORA). The SORA process is iterative, and possible risk mitigation, as the adoption of airbags, soft frames, or parachutes, must also be taken into account to increase the probability of obtaining authorization to fly.

1.5.4 Italy

ENAC (Italian National Agency for Civil Aviation) is the Italian Civil Aviation Authority and promotes the introduction of drones in the airspace to encourage progress related to the use of drones ([103]). BVLOS architectures are favored by a generally lean bureaucracy, introducing specific test areas, the *'Innovation Hubs.'* There are currently many BVLOS related projects sponsored by ENAC [104]. Flying in BVLOS mode is possible in civil airspace even at night time from 2017. Potentially, the architecture proposed in this work is at least testable in a likely environment in Italy. In Italy, many service providers use the BVLOS mode intensively. One of the most active companies in this field is SNAM S.p.A. (National Pipeline Company). Through this flying mode, SNAM S.p.A. monitors some kilometers of Italian oil pipelines. In Italy, as in all the European Union countries, ENAC had adapted to the legislation dictated by the EASA (European Union Aviation Safety Agency) from January 1^{st}, 2021.

1.5.5 Great Britain

The British bureau that oversees and regulates all the aspects of civil aviation, including those concerning drones, is the Civil Aviation Authority, CAA. Great Britain is among the most avant-garde countries in terms of drone legislation, and its philosophy is to encourage their introduction and drone-based services as much as possible. For this reason, as done in Italy, a series of *Innovation Hubs* were born, aware that it is only a mandatory step to generate a better infrastructure, also involving on the ground sensors [65]. Some drone-provided BVLOS mode services are also available outside the Innovation Hubs and are, in any case, tests to examine the hardware and software exploited. Those services are provided in sparsely populated and not authorized to fly third-party drone areas, i.e., areas where there is no collision risk with other aircraft. Those restrictions have made testing a series of innovations in the drone field possible, but the need to lower the drone-associated risk is still alive today. In Great Britain, some delivery parcel services have been available for a long time. The most famous of them is the Amazon Prime Air (powered by Amazon.com Inc.) that has started the delivery service in the Cambridge country area in 2016. It introduced many innovations that should demonstrate the goodness of its delivery service to the CAA [102]. This service

is now available only in some sparsely populated areas.

1.5.6 France

In France, the Direction Générale de Aviation Civile (DGAC) is the body that deals with regulating the legislative aspects of civil aviation, and therefore, drones. The French government is pushing hard to encourage more productive use of drones. BVLOS is possible in the scenarios called S2 and S4 [193], where the drone has to fly at a maximum height of 150 m and in the countryside. The S2 scenario sets a 1 km distance limit drone from the pilot. S4 has an unlimited maximum distance from the pilot but 2 kg as the maximum drone weight. The overflight of urban areas is not covered by the legislation, effectively preventing drone-based services in the cities. License to fly in S4 mode, the most useful for commercial and scientific purposes, is difficult to obtain. Still, many companies have got it and use or offer monitoring services via drones in BVLOS mode. For the communication between drones and Ground Stations, these companies often use the mobile network. By now, the proposed services have been available for a long time, and already in 2017, DGAC authorized the company RTE (Electricity Transmission Network) to maintain its electricity network through the drone company Delair, completing a 30 miles BVLOS flight via 3G cell network [85]. As in all countries that are part of the European Union, DGAC had adapted to the legislation dictated by the EASA (European Union Aviation Safety Agency) from January 1st, 2021.

1.5.7 Spain

Spain is also among the countries that have legislated drones with specific regulations. The legislation is edited by the Ministry of Development (Ministerio de Fomento) and the national agency of aviation safety AESA (Agencia Estatal de Seguridad Aerea). The legislation also provides rules for drones in BVLOS mode. The conditions to be respected to fly in BVLOS mode without AESA authorization exist and are clear. They are: to fly during the day in weather conditions that allow visibility, have a drone weighing less than two kg, not to fly either in urban areas, inhabited places, aggregation of people, or segregated air spaces [27]. These conditions are quite restrictive and do not allow the profitable commercial use of drones; these limits can be overcome with an authorization from AESA. To obtain this kind of authorization, a drone company had to demonstrate an effective Sense and Avoidance system, the quality of the ground station-drone connection, and the presence of a frontal camera that transmits images of adequate quality. The first flight in BVLOS mode with commercial characteristics, authorized in Spain, was developed in 2020 by the SCR, a company engaged in defense and security [142]. Being part of the European Union, Spain had adapted to the legislation dictated by the EASA (European Union Aviation Safety Agency) from January 1st, 2021.

1.5.8 Conclusions

As seen, the regulation of drones' use has essentially limited their use, especially in the urban environment. The foresee of rapid introduction and diffusion of drones (Fig.1.8a from [240] and Fig.1.8b from [225]) and the use of these tools by non-expert personnel has increased the number of drone-related accidents, Fig. 1.8c from [99]. None of these incidents were fatal, but severe personal or property damage was reported [259]. Furthermore, these products' market value is proportional to their diffusion, and the numbers involved are becoming very high, Fig.1.8d from [225]. These facts have prompted the various nations to legislate; most countries adopted the human safety-first philosophy, which resulted in an almost total drone ban from cities, relegating them only to tasks in remote areas or test sites. Nations do not consider the introduction of drone-based services in urban contexts to be of primary importance. China seems to be, among the developed countries, the one that sets the least severe limits on drones, even in urban contexts and in BVLOS flight mode. These are essential incentives to test drone-based technologies eventually, and in fact, China is becoming the selected country to test new drone-based technologies and services. For countries that have introduced the most severe restrictions, adopting the risk assessment proposed in this thesis can prove very useful. Demonstrating that a specific mission presents a low risk would bring many advantages, and it is ultimately the only way to make these imposed prohibitions less rigid.
As already mentioned, the author of the thesis only analyzed countries with specific drone legislation within the nations with a significant drone market share. Many countries do not have drone-related legislation. In such countries, researchers could theoretically test drone-based solutions without any ban. Unfortunately, these countries are also poor or dangerous. They are not suitable countries to test new technologies due to the lack of telecommunication infrastructures or unattractive economic or social situations. Research teams prefer to validate their solutions in high-wealth countries, where the environment is as similar as possible to the ideal one where they want to operate in.

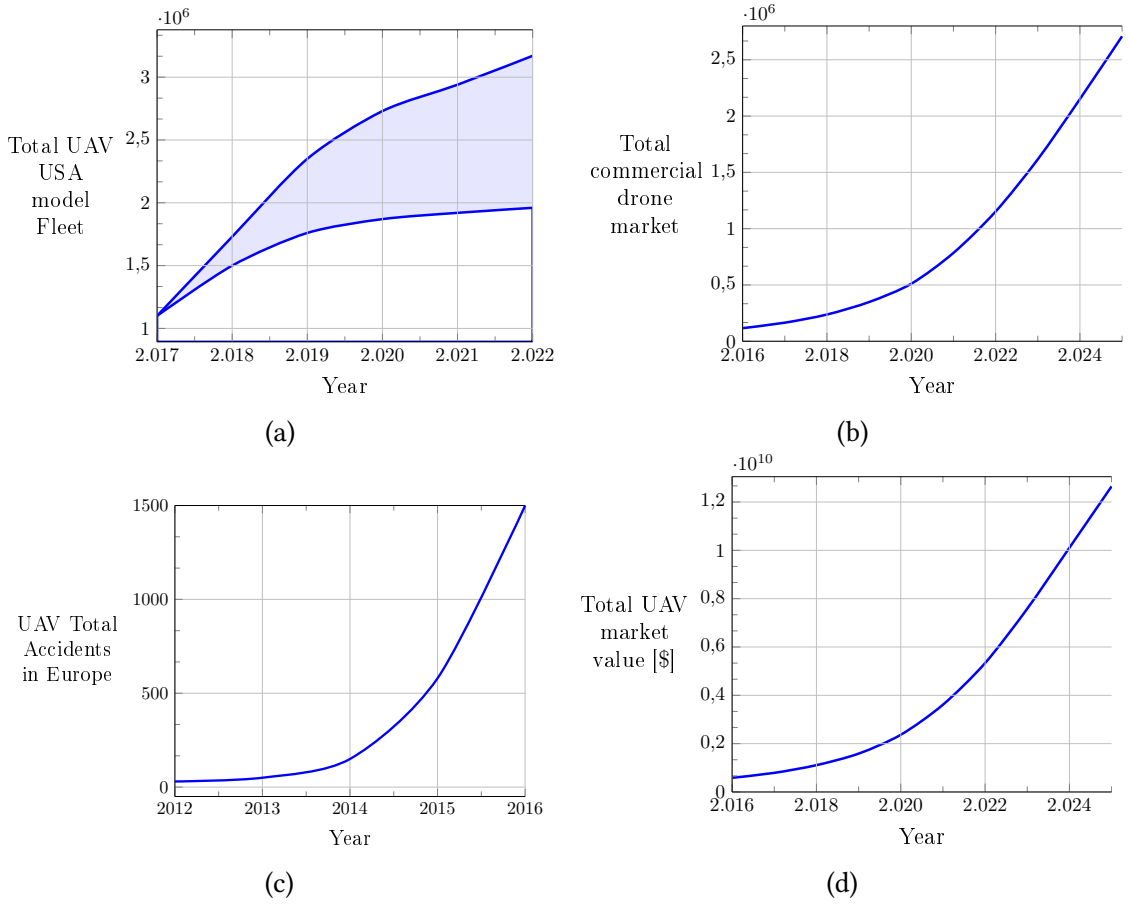

Figure 1.8: forecasts of the total number of drones on the US market in Fig.1.8a and globally Fig.1.8b. Total drone-related accident in Europe in Fig.1.8c and total UAV market value forecast in Fig.1.8d.

Chapter 2

Novelty introduction

This chapter represents the central part of the thesis and is divided into two parts. The first part introduces the path planner tool, showing the path planner adopted in this thesis. The second part of the chapter illustrates all the original introductions that the author of the thesis has proposed. The novelties mainly concern a new formulation of risk, justified in all its parts. The author also provides all the necessary tools useful to obtain a quantitative and not a qualitative result of the solutions. The original introductions will then be applied to likely cases.

2.1 Path planner typology

The physical place where UAVs have to operate is the urban environment. According to this thesis's aim, many UAVs will move simultaneously for different tasks in this environment. A path planner finds a suitable collision-free path for a mobile robot to move from a start to a target location in an environment with obstacles or boundary conditions.

The path planners used for drones don't consider the travel directions; the drones can travel in any order in the allowed airspace. Moreover, the map is not a priori schematized as a graph (a set of edges and vertices with a sense). It is, therefore, necessary to find an algorithm that creates graphs. Among the available path planner algorithms, we focus on those that both generate a graph and find a path. The path the drone has to follow is often highly desirable to be optimal or near-optimal concerning time, distance, or energy consumption. This thesis work proposes a minimum of both distance and risk path planner. An original risk assessment (treated in section 2.2) helps to find the risk map, where each point on the map is related to a risk value; according to the author's original risk assessment, the risk is associated with the map, drone, and risk characteristics. In this thesis, the path planner manages the risk adding it to the length of the path, forming a quantity called *'expected cost,'* indicated in equation 2.1 with 'Par.' The task of the path planner is to find, among the various paths generated,

the one that minimizes the *'expected cost.'*

Robot path planning has been an active research area, and researchers have developed many methods to tackle this problem. The most used drone-related path planner does not directly generate trajectories. Commonly, a list of GPS-based points, called waypoints, is generated. The drone autopilot generates a trajectory that takes these waypoints into account, approaching a specific waypoint and then moving on to the next. The most common approach is the fly-by-waypoints, where the airplane or drone moves toward the (n+1)-th waypoint when it is close enough to the n-th waypoint.
In addition to the map, the waypoint generation considers the vehicle constraints. The most important of them is the minimum turning radius, better described in section 2.4.3, while the maximum drone dimension, better described in section 1.3, even in the urban environment, for small drones, has little influence. There are several methods used to take these two constraints into account. The most used approach -also adopted in this thesis- assumes that the robots are points, while the obstacles are enlarged by a quantity called buffer zone, whose evaluation is the topic of section 2.4. Considering the drone as a point and shifting the drone's dimensions to the obstacles has another significant advantage; the drone space state is only the position.
Having introduced these simplifications, we identified the path planner's requirements by analyzing the classical mission's request. They are as follows:

- able to control a multitude of UAVs simultaneously;
- able to refresh the path in real-time when a new obstacle appears, i.e., an online path planner;
- as little computational calculation as possible.

The next section presents bibliographic research to evaluate which type of path planner fits the needs of the drone-based service proposed in the thesis.

2.1.1 Motion planning for multiple UAVs

The motion planning for multiple UAVs, moving simultaneously, is a significantly more challenging problem than the single UAV path planning. However, researchers have been studying this problem for a long time, and the solutions are specialized for specific operating scenarios and boundary conditions.
The existing methods for solving the problem of motion planning for multiple robots can be divided into the *centralized* or *decoupled* approach, according to Latombe ([162] and [160]). The *centralized* approach combines the individual robot's state-spaces into a composite and more complex one. The path planner exploits this whole state-space to search the solution paths for the entire system. The *decoupled* approach (reviewed by Bullo et al. in [56] and Van et al. in [87]), instead first computes separate paths for

the individual robots and then tries to solve possible conflicts of the generated routes. Centralized approaches can find, theoretically, the optimal solution to any planning problem with an existing one (as stated by Sanchez et al. in [239], van Den Berg et al. in [87], and Karaman et al. in [155]). In some circumstances, the centralized approach is the only possible approach; for example, when coordination between the various robots is fundamental as in the factories.
The most crucial downside of the centralized approach is the computational time that increases when drone configuration space and map size increase. The configuration space grows exponentially with the number of drones (as pointed out by Barraquand et al. in [43] and [44], and Latombe in [161]). For many centralized approach-based path planner algorithms, this means an exponential increase in computation time as the number of drones increases.
The typical scenario addressed in the thesis comprises an entire city or district and a few dozen drones working simultaneously but independently. In this scenario, drones perform tasks that do not involve other drones, such as delivering or controlling certain areas with specific payloads. Using a *centralized* approach, the high number of drones and the map's extension increase the calculation time in an unmanageable way, not fulfilling the online path planner requirement. Furthermore, drones are not dependent on each other, making the centralized approach unnecessary since a coordination among them is not mandatory.
For the thesis, the best method to adopt turns out to be the decoupled one that often [87] is the fastest, especially in operational scenarios such as those analyzed in this thesis. This approach, as said, also has drawbacks. The solutions known for a single robot system cannot directly be transferred to a multi-robot system, as shown by Gautam et al. In [113] and Parker in [217]. The reason is the possible incompatibility of the paths, i.e., paths where two or more drones are at the same point simultaneously. Researchers have solved this problem by using the *priority scheme* (Lemaire et al. in [168]), that assigns a priority number to each drone that has to operate in a specific area. The centralized path planner continuously monitors the drones' position and speed, evaluating the actions to be taken to prevent crashes.
The priority scheme method suggested for this thesis is now introduced. All rotary-wing drones have a lower priority than fixed-wing drones. The rationale is that it is relatively easy for a rotary-wing drone to change course or hover.
When two or more rotary-wing drones are about to crash, and they are collaborative, the drones with low priority remain stationary in hovering and allow those with higher priority to pass. When a fixed-wing drone is about to cross a rotary-wing drone (or group), the first keeps going undisturbed while the other(s) wait (the drones in the group pass according to their priority). Figure 2.1 shows this process when the red dot represents a fixed-wing drone or a higher priority rotary-wing compared to the green dot representing a low-priority rotary-wing drone.
The thesis doesn't consider the case of more than one fixed-wing drone.
The author of this thesis has chosen the decoupled approach, so it is necessary to find

the best single-drone path planner. The suitable path planner must refresh the path in real-time with as little computational calculation as possible. At the same time, the proposed solution doesn't need to be the optimal one. The need to have a solution, even not optimal, in the shortest possible time led the researchers to introduce methods known as heuristics in the path planner field. These methods yield a good-enough solution if enough time is given (Studied by Pearl in [219]). Some heuristics methods propose improvements to the found solution when more computation time is provided. They also have another significant advantage; the computation time grows less than exponentially as the configuration space increases, unlike in the 'exact' method cases.
The centralized approach can also use the heuristic methods. Due to the exponential computational time amount vs. the number of UAVs, only groups of up to three UAVs with similar characteristics can apply these last methods (as stated by Burgard in [57] and Bennewitz et al. in [47]).
As mentioned in the previous section, the space the drones can move is not a priori schematized as a graph. Among the Eurisics single-drone path planner algorithms, we focus on those that both generate a graph and find a path. RRT*, Rapidly-exploring Random Trees Star [155] has the sought characteristics; also it enhances the solution's quality as the computation time increases, converging towards an optimal solution. RRT* is the path planner algorithm used in this thesis.
The academic environment has been widely used to employ RRT* for a long time; now, it is very well-established, and some libraries make its implementation easy. Matlab provides an RRT*-based path planner in the 'Navigation Toolbox' that makes the generation of the waypoints, the occupancy map's loading, the evaluation of the drone's parameters, and the surrounding environment straightforward. The speed offered by RRT* also allows its use as an online path planner.
RRT*, like all path planners, requires a map that indicates the obstacles and the weights related to each point of the flyover area. The greater the weight of a specific area, the more crossing it increases the *'expected cost,'* which the path planner must decrease. The original introduction of this thesis is to use the risk as weight in the map. Other approaches that the author judged not suitable are *Dynamic-Window Approaches* (studied by Fox et al. in [109]), *Nearness Diagram Navigation* (analyzed by Minguez et al. in [192]), *Vector-Field-Histogram* (used for mobile robots by Borenstein et al. in [55]), and *Extended Potential Fields* (Khatib et al. [156]); they are less efficient for the particular characteristics of the environment studied in this thesis (Parker in [218]).
The best approach turns out to be the decoupled one using a priority scheme and the RRT* path planner from the just carried out analysis.
For simplification, the author of the thesis assumed that the drones travel at a constant speed; thus, the drone's probability of failure, that is, time depending, is proportional to the traveled distance; this aspect will be more evident in section 2.3. The path planner has to minimize, as is common for all the path planner that consider a gain map (that

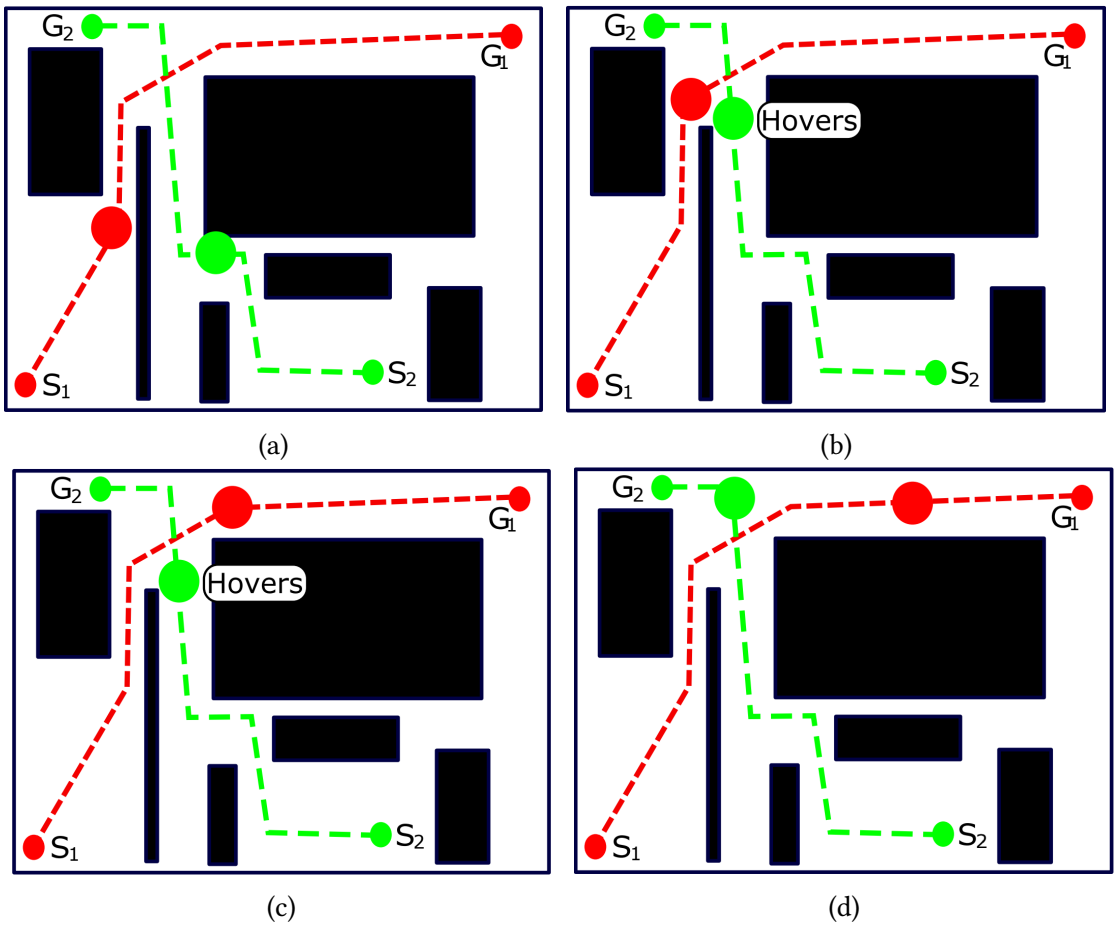

Figure 2.1: simulation of two UAVs crossing their paths using the priority scheme; the red dot represents a fixed-wing or a rotary-wing drone while the green dot represents a lower priority rotary-wing drone. In fig 2.1a the two drones are proceeding before crossing each other's paths. Near their path intersection, the UAV path planner orders the green-dot UAV to hover until the other one is far enough 2.1b and 2.1c, while the red-dot drone goes on undisturbed. In 2.1d, the green-dot drone resumes its path.

is in ths thesis the risk map), the following function, clearer if you look at Fig.2.2:

$$\text{Par} = \sum_{j=1}^{n} \left[\sum_{i=1}^{m} (\text{E}_{C_{ij}} \cdot \text{d}_{ij} \cdot \text{W}) + \text{D}_j \right] \tag{2.1}$$

where

- Par is the expected cost, the quantity path planner has to minimize
- n is the number of segments of the path

- m is the number of parts a segment can be divided into due to the different risk areas
- $E_{C_{ij}}$ is the risk associated with the area ij
- d_{ij} is the distance traveled on the area ij
- W is the risk weight coefficient
- $D_j$euclidean is the distance between two consecutive way-points

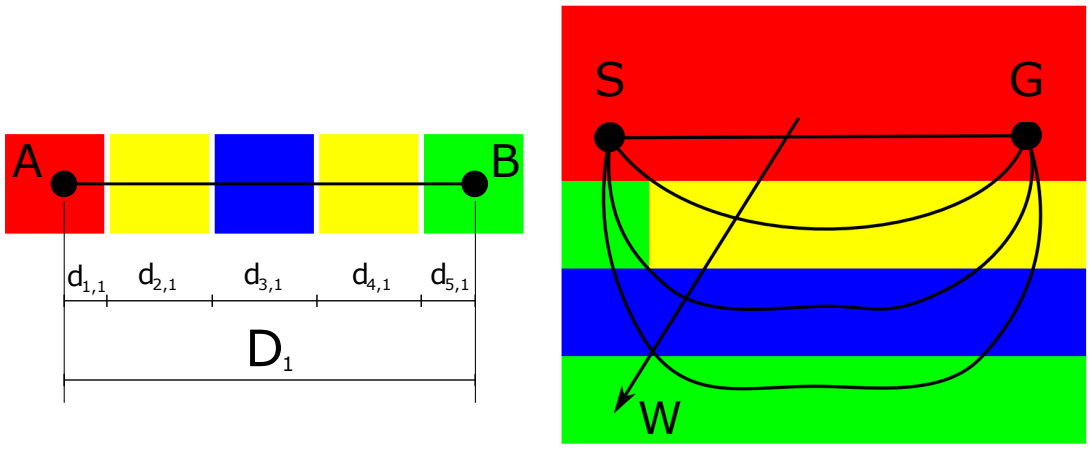

(a) (b)

Figure 2.2: Fig.2.2a shows the two consecutive waypoints A and B; 'D' represents the Euclidean distance between the points 'A' and 'B;' 'd' is the distance covered by the segment 'A-B' in an area with the same risk. Fig.2.2b shows the effect on the path planner waypoints generation of different values of the weight coefficients 'W' in the Eq.2.1. The areas red, yellow, blue and green, have respectively decreasing risk values. The more 'W' increases, the more the path lies on low-risk areas.

The 'W' parameter allows to choose whether to favor safety or distance; the author of the thesis chose 'W 'equal to 50, to have the same magnitude for the two addends of the function 2.2b. The rest of the chapter will explain what risk is, how to calculate it and what it mostly depends on, evaluating likely cases.

2.2 Risk assessment state of the art

Table 2.1: authors and their risk assessment models

Authors	Formula
RCC [78]	$ELS = P(E_{Failure}) \cdot \sigma \cdot A_C \cdot P(F\|E) \cdot p_S$
Weibel et al. [286]	$E_C = \frac{1}{MTBF} \cdot \sigma \cdot A_c \cdot P_{pen} \cdot (1 - P_{mit})$
Dalamagkidis et al.[81]	$E_C = f_{GIA} \cdot \sigma \cdot A_C \cdot P(F\|E)$

This section introduces the risk assessment state of the art. There are different risk definitions in the literature. In this work, the risk is the probability that a flying object will cause at least one death in the affected area. Other authors provide a different risk definition. This section analyzes and compares the most influential small-scale UAVs risk formulations in the literature, based on the number of scientific papers citing them. The risk formulations that introduce low-impact novelties or those too simplistic, having no practical use, will not be analyzed.
The flying object-related fatality, whose probability is the risk, occurs when a series of events happen in a row, as stated by Weibel and Hansman in [286]. Their fatality event-chain is the following:

1. UAV is out of control;
2. the debris penetrates the shelter (if there is one);
3. the UAV impacts a person;
4. the hit is fatal.

All the authors that studied the risk associated with flying objects analyzed this event-chain. Some of them have proposed methods for evaluating one or more of these quantities. While the probability that the first link in the chain, UAV is out of control, happens depends on the examined drone (related to the main time to failure -MTTF- of all its parts), the probabilities that the other links of the chain occur are challenging to evaluate. The probabilities that the points 2, 3, and 4 of the chain occur in a row are proportional to the number of potential people hit by a drone (if no shelter is supposed), to a quantity called in this text the *'probability of fatality given exposure,'* (section 2.3.2) and to the protection offered by the occupation on the ground, related to the so-called *'sheltering parameter'* (section 2.3.1).
The evaluation of the number of potential people hit by a drone fall is not a trivial problem. It increases as both the population density of the affected area or the drone's size increase. In the most influential risk formulations (Table 2.1), the number of potential people hit by a drone fall is the product of the population's density of the overflown area and a surface, commonly, but not by all, called *casualty area*, mainly depending on the drone characteristics (discussed in section 2.3.4).

The influence of the shelter and the probability that the eventual impact will be fatal is not defined in the same way by the analyzed authors. Few authors in the literature have developed the whole risk assessment methodologies. Simultaneously, many other authors have developed evaluation methods for the different quantities exploited in the risk assessment, such as the *casualty area*, or the *probability of fatality given the exposure*.
In the following, the section analyzes the risk formulations provided by RCC, Weibel et al., and Dalamagkidis et al., which are the most cited in the scientific world.

2.2.1 Risk assessment according to RCC

The first practical risk evaluation methodology was the one introduced by RCC (Range Command Council [77] and [76]), with the following equation:

$$E_C = P(E_{Failure}) \cdot \sigma(x, y) \cdot A_c \cdot P(F|E) \cdot p_S \tag{2.2}$$

where

- E_C = risk, measured as casualty expected related to the drone mission
- $P(E_{Failure})$ = probability of a drone failure over the entire mission
- σ = population density [inhabitants/m^2]
- A_c = casualty area [m^2], deepened in section 2.3.4
- P(F|E) = probability of a fatality given the exposure (considered constant by RCC) deepened in section 2.3.2;
- p_S = sheltering parameter, further detailed in section 2.3.1

According to RCC, the risk represents the number of deaths linked to the drone's mission. RCC introduced a probabilistic setting in which two probabilities appear; the former, $P(E_{Failure})$, is the probability that an event causes the drone to lose control over a mission. The latter, P(F|E), is the probability that the drone fall will cause a casualty. This probabilistic approach will also be adopted by other authors but not by all. RCC does not provide a methodology for evaluating these parameters, suggesting labeled drone-related values as $P(E_{Failure})$, and the worst possible scenario, i.e., the value one, as the P(F|E). RCC risk evaluation also considers the shelter to the drone fall offered by the overflown area via the p_S value acting linearly. RCC provides no further guidelines on how to calculate p_S, suggesting, also in this case, the worst possible scenario, i.e., everything is exposed, so p_S is equal to one.

σ and A_c are values common to all risk formulas, and their product indicates the number of people involved in the accident; RCC also provides its A_c assessment, see

section 2.3.4, and Table 2.5.
This risk assessment is not suitable to be exploited by a path planner which decreases both the risk and the distance of the path, being the risk related to the mission and not to a covered space or time. Furthermore, RCC does not provide precise methodologies for evaluating all elements composing the equation 2.2. This assessment provides qualitative, not quantitative results.

2.2.2 Risk assessment according to Weibel and Hansman

Weibel and Hansman in [286] proposed their own risk assessment method via the following equation:

$$E_C(x, y) = \frac{1}{MTBF} \cdot A_c \cdot \sigma(x, y) \cdot P_{pen} \cdot (1 - P_{mit}) \tag{2.3}$$

where

- E_C = risk, measured as casualty expectation on the ground per unity of time
- MTBF = time between failures resulting in ground impact [s]
- σ = population density [inhabitants/m^2]
- A_c = casualty area [m^2], deepened in section 2.3.4
- P_{pen} = probability of debris' penetration
- P_{mit} = probability of mitigation preventing a ground fatality

In this formula, the risk E_C represents the casualty expectation on the ground per unity of time, and it varies for each point of the map. $MTBF^{-1}$ indicates the drone failure rate, depending on the on-board adopted technology. However, the probability of failure, which appears in formula 2.2, in 2.3 is missing, as the drone's flight time is missing; the risk is, therefore, a value associated with the overflown area, not with the mission; the same happens as to formula 2.4. This risk assessment is suitable to be adopted by path planners, decreasing both distance and the total mission risk, as expanded in section 2.3. The product between σ and A_c indicates the number of people involved in the accident; in their work, Weibel and Hansman have perfected the *'casualty area'* formulation used in their risk assessment, introducing an original one, see section 2.3.4 and Table 2.5. P_{pen} indicates the probability that a drone will penetrate the shelter; in [286], Weibel and Hansman only linked it to the type of aircraft, not the overflown area's characteristics. The P_{mit} is a value related to all the mitigation events; Weibel and Hansman do not indicate how to evaluate it, suggesting to adopt the most dangerous case possible, namely P_{mit} equal to zero. This risk assessment has the advantage over formula 2.2 by RCC, to better be adopted by a path planner that considers the risk.

However, formula 2.3 is not practical as its authors do not propose methodologies for its components evaluation; the author of this formula had not chosen it as the starting point for the thesis.

2.2.3 Risk assessment according to Dalamagkidis

Dalamagkidis et al. in [81] proposed an original risk assessment methodology via formula 2.4. This formula is currently the most advanced for assessing the risk related to the drone overflight. The author of this thesis exploits it, even modifying some elements of it. The Dalamagkidis' formula is the following:

$$E_C(x, y) = f_{GIA} \cdot \sigma(x, y) \cdot A_c \cdot P(F|E)(x, y) \tag{2.4}$$

where the variables are defined as

- $E_C(x, y)$ = risk, measured in casualty expectation on the ground per unity of time
- f_{GIA} = rate of ground impact accident, supposed to be constant and equal to 10^{-7} Hz
- $\sigma(x, y)$ = population density [inhabitants/m^2]
- A_c = casualty area [m^2], deepened in section 2.3.4
- $P(F|E)(x, y)$ = probability of a fatality given the exposure, expanded in section 2.3.2

E_C is a value related to each point of the map. f_{GIA} indicates the drone failure rate, depending on the on-board adopted technology, and has the same role as $MTBF^{-1}$ in formula 2.3. The product between σ and A_c indicates the number of people involved in the accident, while $P(F|E)$ (x, y), the probability of fatality given the exposure (detailed in section 2.3.2), represents an instrumental novelty. $P(F|E)$ (x, y) takes into account the kinetic energy of the drone and the shelter offered by the overflown area. Dalamagkidis et al. have also introduced methods to evaluate these magnitudes, making formula 2.4 practical, which is the reason the author of the thesis exploits it.
The risk value related to all the points of a specific area produces the *risk map*, deepened in section 2.3.5. Among the elements used in the risk calculation, f_{GIA} and A_C depend on the drone and its mission.
In contrast, $\sigma(x, y)$ and $P(F|E)(x, y)$ are map-related; their evaluation for all the points of a given area produces the relative maps, see section 2.3.3 and 2.3.2.
As said, the thesis exploited formula 2.4 but introducing some changes. They concern the use of an original *casualty area* developed by the author of the thesis (deepened in section 2.3.4) and a different range of the sheltering parameter (deepened in section 2.3.1).

2.3 Evaluation of the Risk

The drones' path evaluation considers both the obstacles (or not allowed areas) on the map and the risk for the population on the ground. The former's magnitude appraisal is the subject of section 2.4, while the latter is virtually based on formula 2.4 provided by Dalamagkidis et al. in [81], and it is the subject of this section. The differences between the assessment proposed by Dalamagkidis and the one exploited in this thesis are in the evaluation of the casualty area, A_C (where an original formulation was introduced), and in the range of the shelter parameter p_S, for the evaluation of the probability of a fatality given the exposure, also known as P(F|E).
The risk assessment, as apparent in section 2.3.5, leads to the so-called risk map. The evaluation of it requires the preliminary calculation of the other quantities that appear in formula 2.4 that are the subject of this paragraph. The quantities P(F|E)(x, y) and $\sigma(x, y)$, dealt with respectively in sections 2.3.2 and 2.3.3, are also values that then produce maps. The f_{GIA} value is constant for each type of drone, as suggested by Dalamagkidis et al. in [81], while the A_C value, analyzed in section 2.3.4, varies for each drone. In the following, we will better explain these quantities and offer practical methods for their evaluation in real cases, highlighting the improvements introduced in this thesis to the literature's solutions.

2.3.1 Sheltering parameter

The *sheltering* parameter, denoted as p_s, is a value introduced in the risk assessment. It provides information about the shelter offered by the environment when objects fall from the sky. The environment sheltering has no more meaning when the debris has very high kinetic energy, such as an asteroid or a large aircraft. The *sheltering* parameter is a value exploited by many authors writing about risk, as RCC in [78], Weibel et al. [286], and Dalamagkidis et al. in [80] and [81] (see Table 2.2). For all these authors, this value is related to the ground characteristics (like trees, buildings, or streets) and determines the shelter offered by the overflowed environment; the safer the protection provided, the lower is the risk associated with a flying object possible fall, such as a drone. Although many authors have dealt with it, the *sheltering* parameter evaluation remains a problem. All the authors, but Dalamagkidis et al., suggest a constant p_s value since the complication in its assessment. That is not acceptable anymore. This thesis starts from the work of Dalamagkidis et al. (in [81]), the most cited work in this field, to face the evaluation of the *sheltering* parameter offering a new evaluation scale and an original assessment method. This assessment method will help to evaluate the *sheltering* parameter map (analyzed in section 2.3.1), i.e., the set of all the *sheltering* parameters of an area of interest; the *sheltering* parameter map is one of the inputs the path planner needs.

As mentioned previously, the *sheltering* parameter influences the risk assessment (deepened in section 2.2) via the *probability of fatality given the exposure* value (heightened in section 2.3.2). However, the way it does so varies from author to author, tables 2.1 and 2.2. Assuming constant sheltering parameter leads to the impossibility to discriminate different ground characteristics, preventing changes in the risk to the ground, based on the shelter offered by the overflowed ground characteristics.

Table 2.2: authors and dependences of the *sheltering* parameter in their risk assessment.

Authors	Dependance	Lower	Upper
RCC [78]	Linear	0, all sheltered	1, all exposed
Weibel et al. [286]	Linear	0, all sheltered	1, all exposed
Dalamagkidis et al. [80]	Exponential	0, no shelter	1, best shelter
Dalamagkidis et al.[81]	Exponential	0, no shelter	∞ best shelter

According to the most accreditated risk evaluation methodology, the one by Dalamagkidis et al. in [81], the sheltering parameter is not constant and acts in a non-linear manner in the risk evaluation (via the probability of fatality given the exposure value, Eq.2.5). The range p_s belongs to is between zero and infinite; this makes its attribution not practical, since it is impossible to correlate a p_s value to a land occupation. Moreover, in the literature, there are no guidelines (or criteria) on its connections to the ground characteristics.

Table 2.3: relationship between sheltering parameter value and land occupation according to the author of the thesis.

Sheltering Parameter Values	Ground Occupancy
0	No shelter
2.5	Sparse trees
5	Trees and low buildings
7	Tall buildings

The author of this thesis adopted the same risk assessment methodology proposed by Dalamagkidis et al. in [81] but presenting some changes, in particular, as analyzed in this section, introducing a finite sheltering parameter range. He set the sheltering parameter range arbitrarily from 0 to 7, where '0' indicates the most dangerous scenario, while '7' the safest one. The rationale behind this choice was the following: the author of the thesis has chosen the highest p_s value so that the probability of fatality given the exposure (deepened in section 2.3.2) in the case of a drone with kinetic energy at impact equal to 1000J is about 5% (precisely 5.7%, Fig.2.6b). Table 2.3 and Fig.2.3 show some values of the *sheltering* parameter and the relative land occupation. The area to which attribute a p_s value may have a non-homogeneous nature; in this case, the weighted value is taken, that is, the risk proportional to the occupation (see Fig.2.3). The original attribution method is, therefore, visual: there are no precise formulae but guidelines. This methodology is not perfect and has many criticalities starting from choosing the range and the distribution of the values, but it is a necessary step to attribute the *sheltering* parameter to the surface. In the p_s evaluation, the author has developed and exploited a neural network; it can attribute a p_s value thanks to satellite images in order to create a *sheltering* parameter map. The development of the neural network and the evaluation of the *sheltering* parameter map are topics covered in this section.

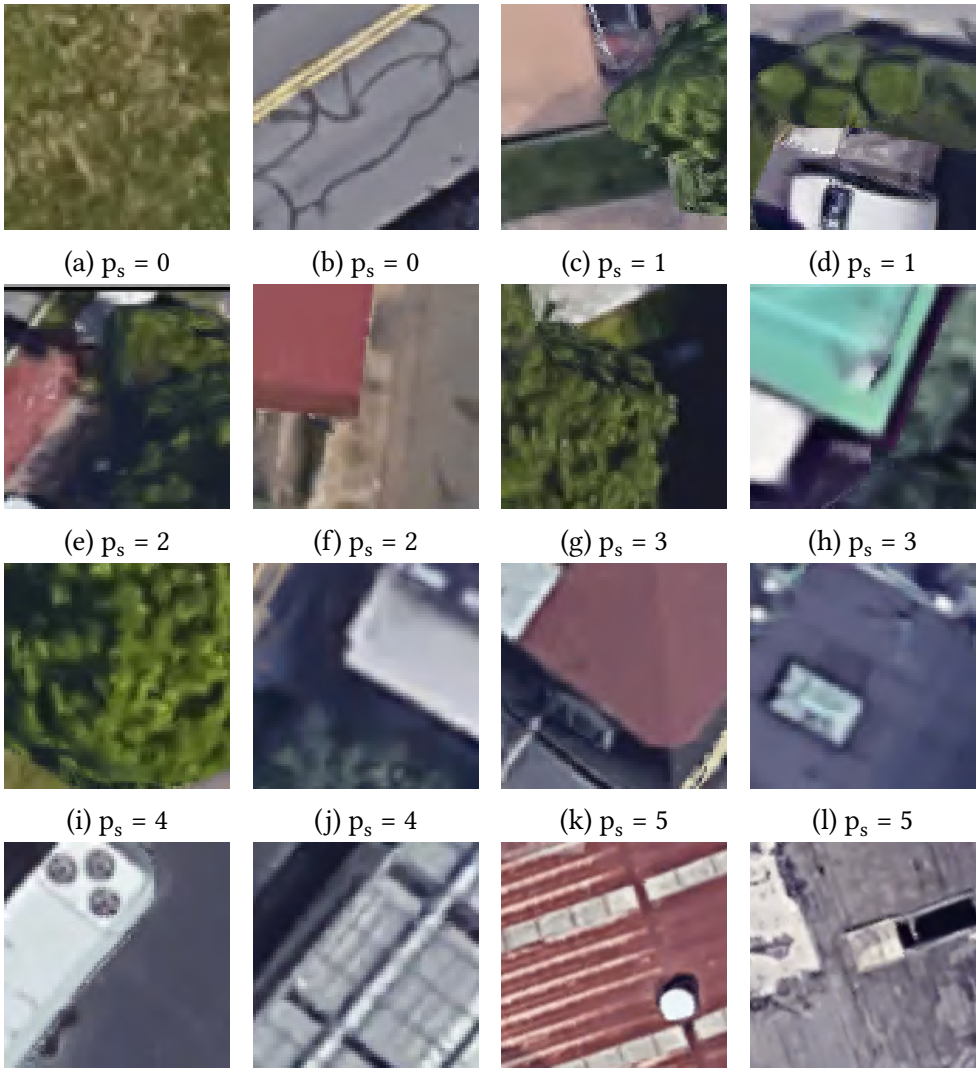

(a) $p_s = 0$ (b) $p_s = 0$ (c) $p_s = 1$ (d) $p_s = 1$

(e) $p_s = 2$ (f) $p_s = 2$ (g) $p_s = 3$ (h) $p_s = 3$

(i) $p_s = 4$ (j) $p_s = 4$ (k) $p_s = 5$ (l) $p_s = 5$

(m) $p_s = 6$ (n) $p_s = 6$ (o) $p_s = 7$ (p) $p_s = 7$

Figure 2.3: examples of attribution of p_s proposed in this thesis The values are completely arbitrary but they have allowed for the first time to define a sheltering parameter map as in section 2.3.1.

Sheltering Parameter Map Evaluation

The *sheltering* parameter map is an indispensable map for the risk assessment and consequently for the path evaluation. It represents the distribution of the *sheltering* parameter in a given zone. The proposed methodology assigns a *sheltering* parameter value to each meter square surface, and thanks to its evaluation, the path planner can choose the minimum risk path. This thesis work proposes a scale for evaluating the *sheltering* parameter, among the many novelties. The limits of this scale are many, being subjective both in the range and in the definition. However, this scale made it possible to create a risk-based path planner, like the one used in this thesis. The *sheltering* parameter, and therefore the *sheltering* parameter map evaluation, in the thesis work, were possible by exploiting the Neural Network *'AlexNet'* (in Matlab version) appropriately trained. To train this CNN, the author used a database of about 5000 aerial images divided into 8 'classes' (as in Fig.2.3). That database represents all the possible values of the *sheltering* parameter, which has values from zero - the lowest potential value, which corresponds to 'none shelter at all'- to seven -the highest possible value corresponding to the roof of a tall building, the safest area in a city-.
The exploited CNN needs only the aerial image of the affected area with a sufficient number of pixels (Matlab allows to extrapolate information even from 5x5 pixels images providing fairly accurate results) and outputs an integer value representing the *sheltering* factor of each section of the analyzed area, or the *sheltering* parameter map.

The famous web mapping service Google Maps [30] provided the aerial images used to train the network and determine the *sheltering* parameter map.
The complete analysis of the aerial photography of the area of interest was sufficient to evaluate the *sheltering* parameter map. The sites analyzed for the thesis are two. The former is nearby the 'Medaglie d'oro' square, in Naples, Italy, Fig.2.4a, 472x624 meters wide. The latter is in the East Village, in New York City, (NY), Fig.2.5a, 1200x1600 meters wide. The exploited image resolution was about 100x100 pixels for each square meter, a value much greater than the Matlab program's minimum to offer accurate analyzes, and the corresponding image is 30 Mb. The computation time on an i5 6200 2.3 GHz processor to evaluate the *sheltering* parameter maps, Fig.2.4b and Fig.2.5b, was about 20 hours for both the cases. Since the *sheltering* parameter is a value that varies very slowly over time, it is plausible to calculate the *sheltering* parameter map once a week. During the training, the adopted CNN returned the exact value more than 70% of the times while it produced a very distant value (with a difference of 2 or more from the precise value) less than 1% of the times.

The trained CNN seems suitable for the thesis purposes. However, the CNN method is not a perfect one, and then it is mandatory to evaluate the acceptable accuracy value for each purpose. However, with modern algorithms, it is hard to exceed 97 % of accuracy, that is incredibly high, and that results suitable for commercial purposes. To obtain better accuracy, the developed CNN needs some more train; however, it is difficult to say in advance how many images are required in order to achieve the desired

accuracy. The computational cost of the CNN usage is not an obstacle with modern computers; the difficulty, therefore, is the training of CNN, not its use.

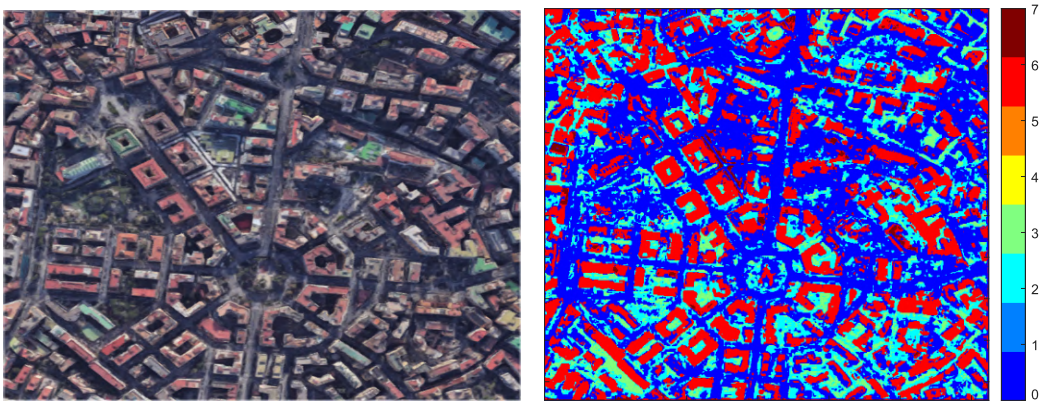

(a) 'Medaglie d'oro' square, aerial view.

(b) *sheltering* parameter map of the area in Fig.2.4a.

Figure 2.4: aerial view of the area near Medaglie d'Oro square, Naples, Italy, Fig.2.4a, and the related *sheltering* parameter map Fig.2.4b, obtained through a neural network.

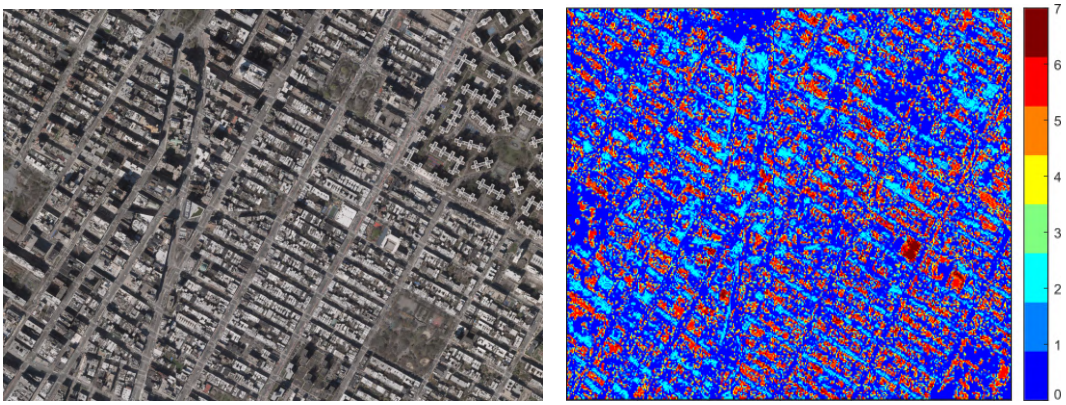

(a) East Village, New York City (NY), aerial view.

(b) *sheltering* parameter map of the area in Fig.2.5a.

Figure 2.5: aerial view of East Village, New York City (NY), Fig.2.5a, and the related *sheltering* parameter map Fig.2.5b, obtained through a neural network.

Sheltering Parameter refreshing methodologies

Sheltering parameter variation reasons are the growth (or demolition) of vegetation, building, streets, and so on. Pruning can change the canopy (and thus the related *sheltering* parameter) within a few minutes. The pruning of large municipal green areas requires pruning companies or municipal employees. It is, in fact, one of the municipality tasks in almost all the countries of the world, as legislated in Netherlands [122], Italy [86], USA [276], Cina [64], South Africa [123], and Australia [41]. In this case, it is possible to receive such information in advance and lower the affected zones' sheltering parameters. The spring canopy growth and the fall of the leaves during the autumn are slower processes, in the order of weeks ([224], [68], and [222]).
The construction or demolition of buildings must be communicated to the municipality, in most of the nations of the world, for example, the United Kingdom [246], Italy [70], South Africa [228], Australia [124], USA [235], China [221], and in other countries of the world as stated by Harwood in [129]. During the construction or demolition of a building, the sheltering parameter will be reasonably equivalent to the lowest possible one (with the risk evaluation methodology adopted in this work, p_s equal to zero) until the process completion; these phases cannot guarantee an adequate shelter. During buildings or infrastructures maintenance work (obligatorily communicated to the municipality, for example, New York State [206], United Kingdom [101], South Africa [210], and Australia [40]), the sheltering parameter value must be equal to that offered by the scaffolding, approximately p_s equal to three. In any case, an analysis obtained with optical instruments of the area of interest can evaluate any not communicated p_s variations. For the just analyzed reasons, the author of this thesis proposes a data refreshing rate of once a day. The flyover, with the appropriate equipment, above the operating area, can allow the *sheltering* parameter map refreshing. Typical equipment, in this case, is a multispectral camera capable of seeing in visible and near-infrared wavelength. The multispectral cameras for drones are performing and lightweight. To date, a lot of drone companies are proposing their drone with native multispectral devices, like DJI with its P4 Multispectral [94] that have characteristics in line with the ones found in Paragraph 1.3; virtually every drone analyzed in this thesis can carry these types of payloads.

2.3.2 Probability of fatality given the exposure

The *'probability of fatality given the exposure'* indicates the likelihood of a fatality if a drone hits a person. RCC in [78] (equation 2.2) and Dalamagkidis et al. in [81] (formula 2.4) adopt this probability in a very similar way in their risk assessment, while Weibel and Hansman in [286] (formula 2.3) to evaluate this quantity use a combination of P_{pen} e P_{mit}, not exploited or analyzed in this thesis work. The *'probability of fatality given the exposure,'* also indicated with P(F|E), depends on several variables as the shelter offered by buildings or vegetation, the UAV's debris kinetic energy at the impact, the hit part of the body, the age, and the health of the person, the amount of energy transferred to the person, and so on.
RCC in [78] proposes a constant value for the *probability of fatality given the exposure*, the highest possible, i.e., one; every time a piece of debris hits a person, it results in a fatality. When contextualized, this value makes sense; RCC had tailored its risk assessment to space debris, not to drones.

Dalamagkidis et al. in [80] and [81] proposed a computational methodology based on statistical considerations in the assessment of P(F|E). The computational method proposed by Dalamagkidis et al. (equation 2.5) takes into account many quantities evaluable in a reasonably simple way; it has been exploited by the author of this thesis without any modification, except for the different range of the sheltering parameter, better detailed in section 2.3.1.
According to Dalamagkidis et al. in [81], the probability of fatality given the exposure depends on the kinetic energy of the debris and the sheltering parameter (discussed in section 2.3.1):

$$P(F|E)(x,y) = \frac{1 - k(x,y)}{1 - 2k(x,y) + \sqrt{\frac{\alpha}{\beta}}\left[\frac{\beta}{E_{imp}}\right]^{\frac{3}{p_s(x,y)}}} \tag{2.5}$$

where

- α = impact energy required for a fatality probability of 50% with p_s = 0.5, the value suggested in [81] and used in the present work, is 100 kJ;
- β = parameter is the impact energy threshold required to cause a fatality as p_s goes to zero, a value suggested in [81], and used in this work, is 34 J;
- E_{imp} = energy of the debris at the impact, assumed equal to sum of the kinetic energy and the gravitational potential energy of the debris at the beginning of the fall, to be conservative;
- $p_s(x,y)$ = sheltering parameter for each point of the analyzed map $\in(0, \infty)$ according to [81], while $\in [0, 7]$, in this thesis (discussed in section 2.3.1);

- $k(x, y)$ = correction factor for each point of the analyzed map, evaluated as $\min\left[1,\left(\frac{\beta}{E_{imp}}\right)^{\overline{p_s(x,y)}^{3}}\right]$.

E_{imp} can be assumed to be constant for each drone in the calculations, identified by the cruising speed, altitude, and mass of the aircraft; P(F|E) will only depend on p_s.

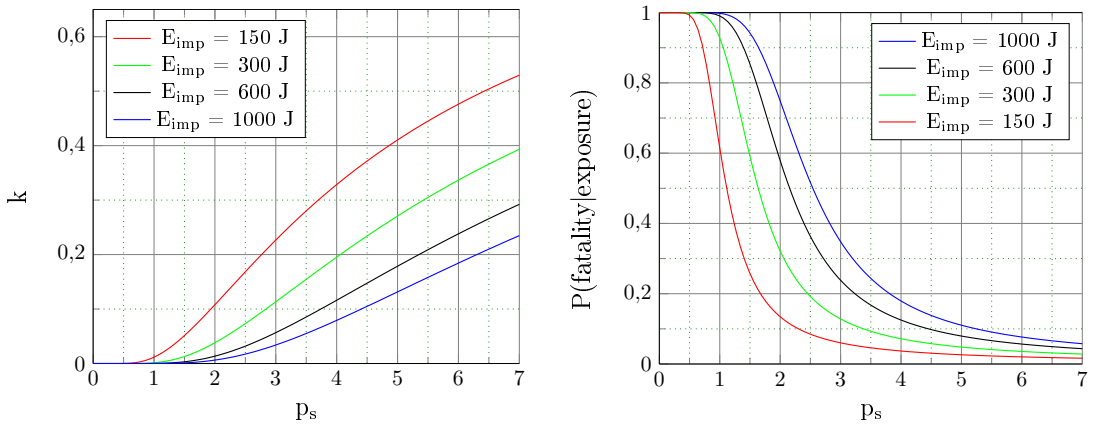

(a) (b)

Figure 2.6: correction factor vs. sheltering parameter in Fig.2.6a and probability of fatality given the exposure vs. sheltering parameter in Fig.2.6b, both for several kinetic energy at the impact.

The probability of fatality given the exposure exploited in this thesis is, as said previously, a value that varies for each point of the map as the sheltering parameter does. The evaluation of P(F|E) for each point on the map provides the probability of fatality given the exposure map, one of the needed parameters to the risk map, deepened in section 2.3.5. Figures 2.7 and 2.8 show some P(F|E) maps, which vary in kinetic energy at the impact of the drone.
In the figures related to the case E_{imp} equals to 100 J, the P(F|E) values seem to be more polarized towards the extreme ones of the scale. On the other hand, the figures related to the case of E_{imp} equals to 1000 J, P(F|E) seems to be more uniformly distributed over the scale.

This behavior arises from that of the curves P(F|E) vs. p_s, as shown in Figure 2.6b. For meager E_{imp} values, P(F|E) tends to zero much faster than for higher E_{imp} values whose curve is less steep. If E_{imp} equals to 150 J, the red curve in Fig.2.6b, P(F|E) is 1 when p_s is around 2.5, then slowly decreasing till p_s equals 7. When E_{imp} equals 1000 J, the blue curve in 2.6b, P(F|E) is 1 for ps around 6.5; the values decrease slower than the former case. This behavior leads to a smoother P(F|E) values variation in the blue curve than in the red one.

Figs.2.7 and 2.8 show the P(F|E) maps for the two scenarios analyzed in this thesis, i.e., an area near 'Medaglie d'oro' square in Naples, Italy Fig2.7a and an area in the East

Village, New York City (NY), Fig.2.8a. The sheltering parameter maps, Figs.2.7b-2.7f and Figs.2.8b-2.8f show that even small drones can be very dangerous. The highest P(F|E) levels occur where the sheltering parameter, as in roads or areas with lawn cases. E_{imp} equal to 150 J (approximately the potential energy of a 1.5 kg drone falling from a height of 10 meters), as in Figs.2.7c and 2.8c, is enough to obtain values of $P(F|E) \approx 1$. As it is intuitive, as the energy on impact of the drone increases, the dangerous areas increase. It can be seen that the areas with high p_s, corresponding to the roofs of the houses, remain safe when E_{imp} increases.

(a) 'Medaglie d'oro' square, Naples, Italy aerial view.

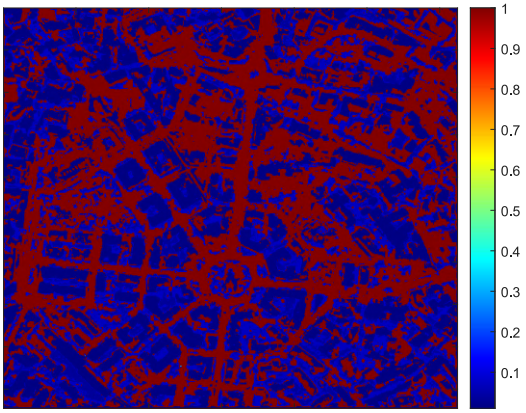

(b) P(F|E) map, E_{imp}=100 J.

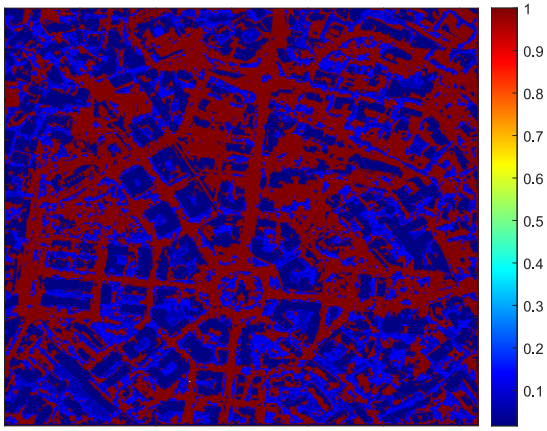

(c) P(F|E) map, E_{imp}=150 J.

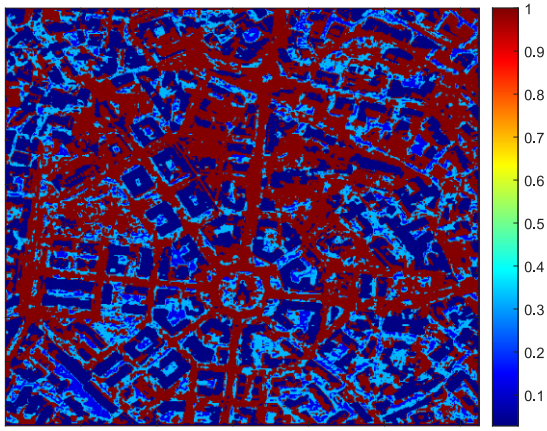

(d) P(F|E) map, E_{imp}=300 J.

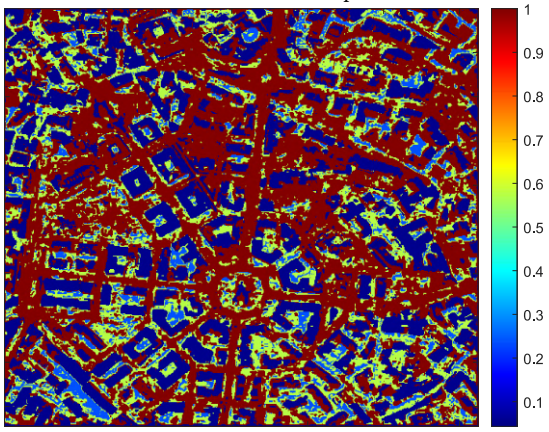

(e) P(F|E) map, E_{imp}=600 J.

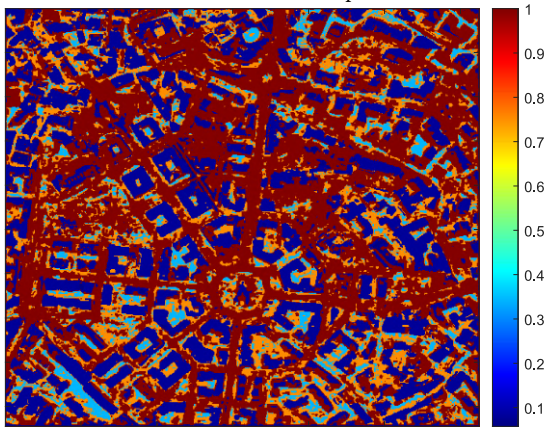

(f) P(F|E) map, E_{imp}=1000 J.

Figure 2.7: P(F|E) maps as the drone E_{imp} varies related to the area in Naples, Italy, Fig.2.7a. These maps will then be used in the evaluation of the risk map.

(a) East Village (NY), aerial view.

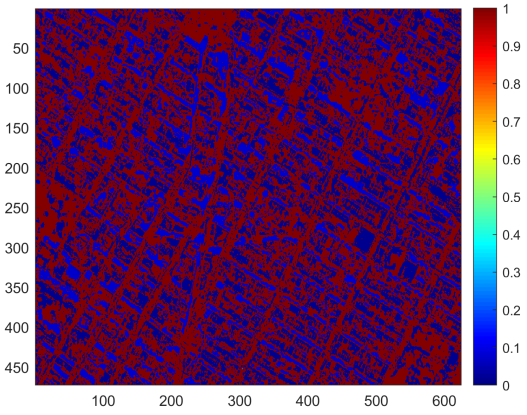

(b) P(F|E) map, E_{imp}=100 J.

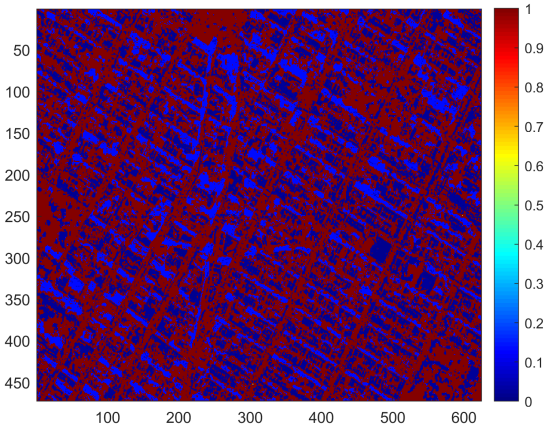

(c) P(F|E) map, E_{imp}=150 J.

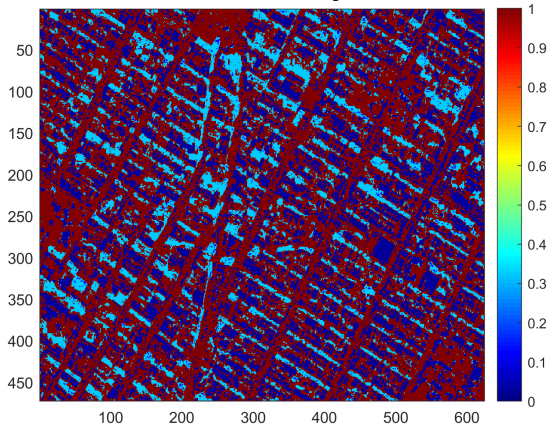

(d) P(F|E) map, E_{imp}=300 J.

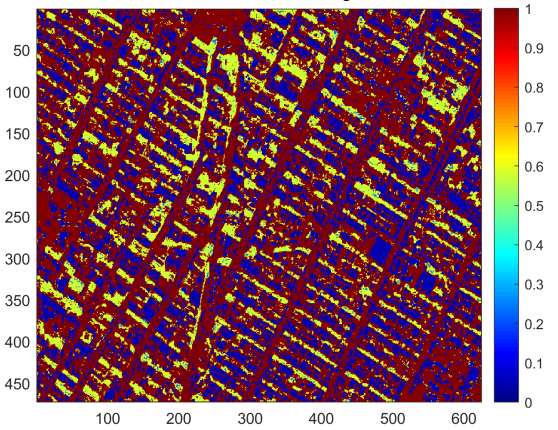

(e) P(F|E) map, E_{imp}=600 J.

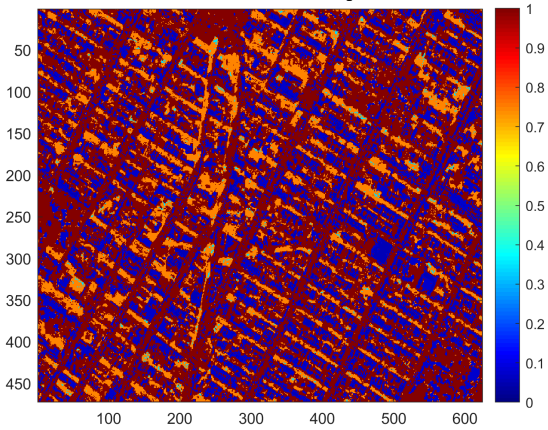

(f) P(F|E) map, E_{imp}=1000 J.

Figure 2.8: P(F|E) maps as the drone E_{imp} varies. These maps will then be used in the evaluation of the risk map.

2.3.3 Population density evaluation

This section analyzes the currently available methods for population density evaluation. The risk map assessment (section 2.3.5), an essential path planner input, needs it. As indicated in the risk formula 2.4 in section 2.2, σ is a coordinates dependent value; it varies for each point of the overflown area and produces a population density map. By its nature, it is tough to associate the population density to any point on a map; it needs a minimum size area. The exploited methodology defines the minimum size for which it is possible to determine the population density.
There are several methods for assessing σ. At least from a theoretical point of view, they are available and differ in their accuracy and data updating frequency. Some are not available for practical or legislative reasons. In the following, the section will introduce the most discussed population density assessments in the literature. This section will evaluate their characteristics, finding out the best for the thesis, which also has practical purposes.
A possible solution for assessing the population density is to use national entities' statistical data. Examples of such institutions are ISTAT (Italian National Institute of Statistics [146]) in Italy, DESTATIS (German Federal Statistical Office [247]) in Germany, the United States Census Bureau [272] in the USA, etc. This method's disadvantage is the low refreshing rate (less than once per year) and the relatively low spatial resolution (in the order of 0,01 square kilometers).
Researchers have developed different methodologies to evaluate real-time *population density*; the most widespread literature techniques are analyzed below.
The *social media data analysis* (analyzed by Gonzales et al. in [121], Liben-Nowell et al. in [170], and Song et al. in [245]) is a promising methodology to forecast urban activity in a relatively simple way. It derives the *population density* by analyzing metadata from social media sponsored events participation. It is mostly applicable to large event monitoring, where many social media users are sending event-specific activities; the event organizers can access these data forecasting the number of participants in a significant public event. This approach is less useful for routine day-to-day urban activity monitoring; moreover, it can only estimate the people's number involved in an event. For these reasons, this thesis work cannot exploit it.
The *mobile phone location data* exploits the number of SIM-provided devices connected to each cell tower evaluating the average population density in the area it covers. Each cell tower's related area varies according to many factors as the communication protocol (and therefore the frequency), the number of people to be served, the obstacles, etc. Typically, in an urban environment, cell towers cover a 200 up to 400 meters radius circle like-area. A cell phone could not be connected to the nearest cell tower, but this does not significantly vary the obtained information's quality [48]. This methodology does not require ad hoc devices and would, therefore, have low costs. Its refresh rate is in minutes order, depending on the metadata acquisition methodology (examples of experiments are available in the papers of Calabrese et al. [60], Pei et al. [220], Candia

et al. [61], and Khodabandelou et al. [157]). The downside of this methodology lies in the opposition by telephone operators to make such metadata available. Only the telephone company *Sonatel Orange* has made this data available for scientific purposes for some areas of Senegal, Africa, [149] and [197]; the thesis cannot exploit this method. The *optical flow analysis* can count people entering and leaving a circumscribed area (see Fig.2.9). Data from the camera network on the ground, arranged on entry and exit gates or streets, are analyzed. There are lots of available software, and the process requires a limited number of simple cameras (as demonstrated by Teixeira et al. in [258]), determined by their resolution and the characteristics of the surface to be analyzed (see works of Velipasar et al. [279]). In this case, the refreshing data rate in the order of 1 ms (date obtained by the work of Cong et al. in [71], Benabbas et al. [46], and Cutler et al.[79]). This method is excellent for counting people in squares, stadiums, universities, and any space where it is easy to analyze all the entry and exit routes. However, it is not a valid method to evaluate σ for an entire city, as it requires infrastructures that do not exist at the moment. It is not suitable for the thesis.

Another method of exploiting cameras is the *crowd counting people* (studied by Loy

(a) (b) (c)

Figure 2.9: *optical flow analysis* is used to count people entering and leaving an access point. Data from camera network on the ground, arranged on entry and exit points, are analyzed. Many are the available software and the process requires a limited number of simple cameras.

et al. in [174]). This methodology differs from the previous one because the exploited camera focuses on analyzing the whole area (see Fig.2.10). The software counts the people in the framed area. This methodology requires a calculation time in the order of 1ds, and no particular cameras are required, as stated by Li et al. in [169]. This methodology can also be applied to a camera mounted on the drone (as tested by Al-Sheray et al. in [241]); in this case, only the population density of the overflown area will be available, making the online path planner less effective.

In choosing which tool to use for the thesis, it is necessary to evaluate both legislative and economic feasibility. The *crowd counting people* but even more the *optical flow analysis*, need, to have accurate data and high refresh rate, of a vast number of cameras; The larger and more complex the extension of the place to be analyzed, the more the

number of cameras increases. From a legal perspective, as the recorded images are not made public, these analyzes are not considered a crime. The high number of cameras could make this tool economically probable if used only by one company, while it would be a valid proposal if the data obtained from the camera network were used by multiple service providers, as would happen in smart cities projects. No real experiments are using camera-based methods on a large scale. It is not clear how many cameras are needed to offer a reliable service; this methodology does not fulfill the requirements of this thesis, and it is not exploited.

Figure 2.10: *'crowd counting people'* (studied by Loy et al. in [174], Ryan et al. in [237] and Chan et al. in [63]). This methodology differs from the 'optical flow analysis' because the exploited camera focuses on the area to be analyzed while a software counts the people in the framed area.

Table 2.4: population density data refreshing methodologies and average rate

Source	Average rate of refreshing
statistical data provided by national entities	5 Years
Mobile Phone Location Data	5 min
Optical Flow Analysis	10^{-2}s
Crowd Counting People	5s

It results that the only possible methodology to evaluate the population density is via the national entities' statistical data.

Population density evaluation for real missions

In this thesis two missions are simulated; one in Italy and the other in the USA. The author has exploited the data made available by ISTAT [146], for the Italian mission and the data available from the United States Census Bureau [272] for the American mission. The data exploited, related to the Italian mission, 'Medaglie D'oro' square in Naples, Italy, are presented in Fig.2.11b. The data refer to the 2011 census, the most recent one.

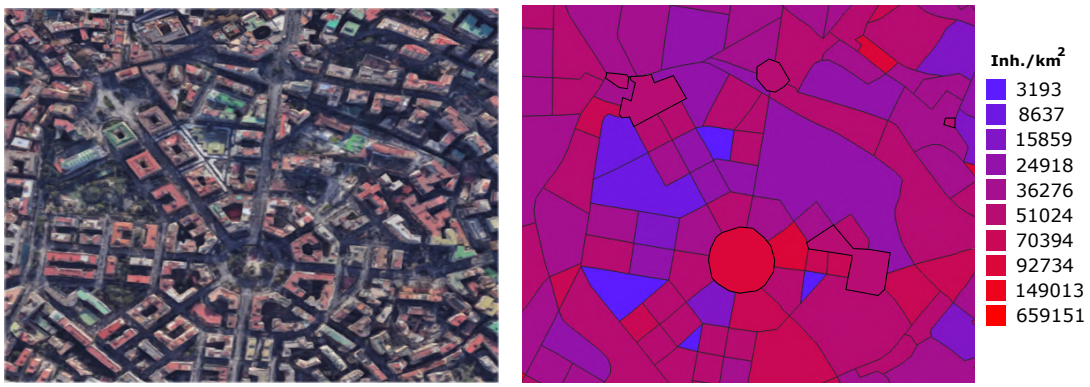

(a) (b)

Figure 2.11: figure 2.11b shows the population density (subdivision into *cadastral cell*) of the area represented in Fig.2.11a, near 'Medaglie D'oro' square, in Naples, Italy.

Fig.2.12b shows the population density map for the American mission, based in New York City (NY), in the East Village; data refer to the 2018 census. The areas part of Figs.2.11b and 2.12b correspond to the *cadastral cells,* different shape and size areas, which can also be 100 square meters large; they are colored according to the relative population density, in inhabitant per square kilometer. The data visualization was possible through the Quantum GIS program [229]. The author used Matlab to create a population density matrix, useful for evaluating the *risk map*, detailed in section 2.3.5. For the cells where there are not apartments -as the squares or parks- the author exploited the highest value of the surrounding cells.

(a) (b)

Figure 2.12: figure 2.12b shows the population density (subdivision into *cadastral cell*) of the area represented in Fig.2.12a, in the East Village, New York City (NY).

2.3.4 Casualty area methodology

An element present in the risk assessments is the number of possible involved people in the crash, equal to the product of the population density and an area. According to the various authors, this last magnitude assumes different names like *casualty area* or *hazardous area*. Its evaluation is a determining factor in assessing the risk associated with flying vehicles. The *casualty area* formulas available in the literature are unsuitable for small drone risk-related scenarios, most substantially overestimating the associated risk. In the event of a fall with a ground impact, using the formulae in the literature, a drone and a heavy airliner produce comparable lethality levels. In this thesis, the term *casualty area*, A_C, is used, and an attempt is made to offer a suitable formula for small drones, falling under the C2 EASA category [100] (MTOW up to 4 kg).
The *casualty area* formulae available in the literature are different; Tab. 2.5 shows how some authors have defined the *casualty area* scientifically. Myers was the first to study the *casualty area* problem. In [205], he lists some of the A_C's sizing factors; fall-off velocity, number of obstacles on the ground area, fragment mass distribution and density, initial fragment velocity, etc.. Since the random nature of the overall dynamics, evaluating Myers's factors is challenging. Myers also provides his *casualty area* formulation, whose problem is that it is not practically applicable to any case. Other authors have provided equations for the casualty area evaluation that are practical.
Montgomery in [196] provides a formal definition and a formula of the *casualty area*. He stated that A_C is *'the region on the ground within which 100 % casualties occur and outside of which no one is injured.'* Montgomery also enunciated his requirements about the *casualty area*, saying that it must consider the *'size of the person, of the falling debris, and the angle on impact'*. These requirements invalidate various original *casualty area* formulae, constant to these factors.
Weibel and Hansman in [286] proposed the simplest A_C definition. They state that the *casualty area* equals the drone's frontal area (Tab. 2.5). This definition does not consider essential factors, such as the glide angle γ (Fig.2.14c); not respecting Montgomery's requirements, it cannot be used in this thesis's applications. EASA in [105] associates the *casualty area* to the reference area (S_{ref}, not better explained) and the Maximum Take-Off Weight (MTOW) via a k factor, to be evaluated for each drone, as shown in Tab. 2.5. The EASA formula does not respect Montgomery's requirements and is not analyzed in this thesis.
In [196], Montgomery introduces the idealization of both the affected person (Fig.2.14a) and the falling debris (Fig.2.14b). Many authors proposing an original *casualty area* definition, have exploited these idealizations. In [125], Grimsley, uses Montgomery's idealizations in his *casualty area* formula, including the distance that the vehicle needs to come to a stop, a parameter hard to find out (equation in Table 2.5, shown in Fig.2.13a). Grimsley's equation fulfills Montgomery's requirements but does not fit this thesis's needs (better explained below) and, therefore, will not be exploited. Dalamagkidis in [81] proposes a version of the *casualty area* that fulfills Montgomery's requirements

(formula in Table 2.5 shown in Fig.2.13b). Dalamagkidis's formula respects Montgomery's requirements, but like Grimsley's formula, it presents problems (explained further below) that make it unsuitable for this thesis's purposes. Montgomery also introduced his *casualty area* formula, in Table 2.5 and Fig.2.13c; Ranger Commanders Council (in [75] and [76]), and the FAA in [107] refers to this formulation while EASA used to exploit it. Montgomery's formula fulfills his requirements, but, as will be analyzed below, it has limitations (the same as Grimsley's and Dalamagkidis's formulae) that do not make it suitable for the thesis. Montgomery's procedure was the basis for Grimsley's and Dalamagkidis's formulas; they tried to lessen Montgomery's equation's limitations but failed. The present paper tries to tailor Montgomery's formulation to small-sized drones belonging to the C2 EASA category [105].

Original casualty area methodology

The *casualty area* formulae available in the literature meeting Montgomery requirements are the Grimsley formulas, Fig.2.13a, the Dalamagkidis formula, Fig.2.13b, and the Montgomery one Fig.2.13c, all in Table 2.5. These formulas show the same problem; the A_C diverges for γ approaches zero. Since the risk is proportional to the *casualty area*, according to the most accreditated risk assessment (the one of Dalamagkidis et al. [82], Eq.2.4), an infinite *casualty area* implies an absolute risk that precludes any use of drones in an urban environment. Grimsley and Dalamagkidis modified Montgomery's formula trying to decrease the γ range where the casualty area formula returns extreme values. Their results, however, are not satisfactory. This thesis proposes a new *casualty area* formulation, respecting Montgomery's requirements, not presenting its cons. The introduction of a *casualty area* always finite and fulfilling the Montgomery's requirements, would make using drones easier even in the environments that now ban their use, as it would not lead to infinite risk.

The thesis's original *casualty area* formulation fulfills the requirements that Montgomery identified in [196], i.e., taking into account the size of the person on the ground (Fig.2.14a), of the falling debris (Fig.2.14b), and the angle of impact γ (Fig.2.14c).
Both the human body and the falling debris are idealized in this thesis, as suggested by Montgomery. This thesis assumes each person as a vertically-oriented right circular cylinder h_p high, and with radius r_p, set to 6.0 ft (1.8 m) and 1 ft (0.3 m) respectively [75], as shown in Fig.2.14a. An r_f-radius sphere simulates the falling debris; the debris's most massive cross-sectional length is its diagonal (Fig.2.14b). Fig.2.14c shows the *glide angle* γ, the angle between the horizontal plane and the drone impact velocity. This thesis uses the same variables. The only different hypothesis from Montgomery's ones is about the falling debris kinetic energy; Montgomery considers the kinetic energy of the debris so high that any obstacle found on the trajectory keeps the path unchanged, stopping only on the ground [107]. In contrast the author of this thesis considers the energy of the debris to be such as to prevent its fall at the first object encountered.

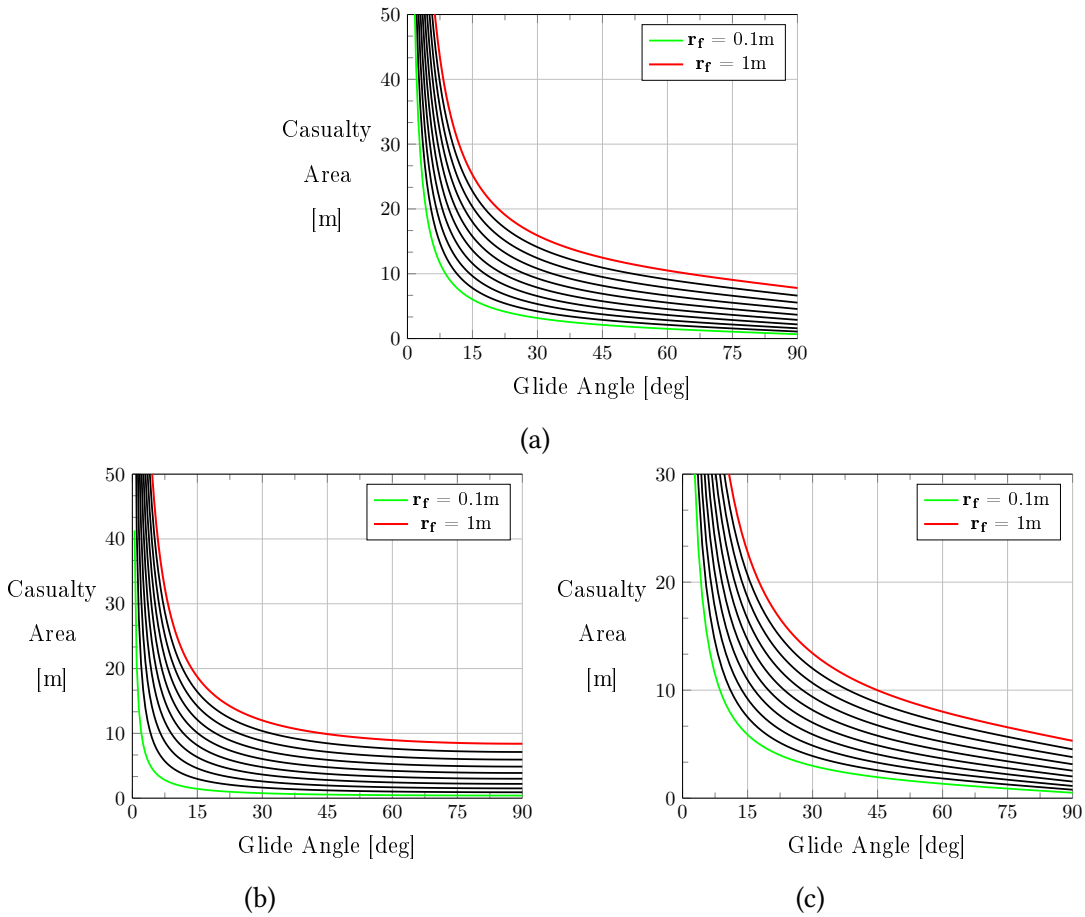

Figure 2.13: *casualty area* vs. glide angles proposed by Grimsley in 2.13a, Dalamagkidis in 2.13b and Montgomery in 2.13c. Formulae in Table 2.5.

.

Table 2.5: comparison of the *casualty area* models.

Authors	Casualty area formula
Myers [205]	$\int_{-\infty}^{\infty}\int_{-\infty}^{\infty} P_k(x,y)dxdy$
Weibel [286]	Falling Object Frontal Area
EASA [90]	$k \cdot \left(\frac{MTOW^2}{S_{ref}}\right)^{\frac{2}{3}}$
Grimsley [125]	$(L_f + h_p/\tan(\gamma) + 2r_p)2(r_f + r_p)$
Dalamagkidis [82]	$2r_f\left[L_f + \frac{h_p}{\sin(\gamma)}\right]$
Montgomery [196]	$\begin{cases} 2(r_p + r_f)h_p/\tan(\gamma) + \pi(r_p + r_f)^2 & \gamma < \pi/2 \\ \pi(r_p + r_f)^2 & \gamma = \pi/2 \end{cases}$

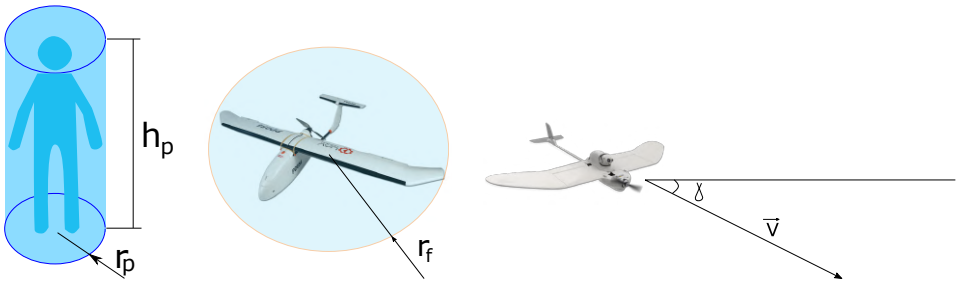

(a) (b) (c)

Figure 2.14: 2.14a shows the right cylinder representing a human, including the variables h_p and r_p. The r_f-radius sphere in Fig.2.14b represents the debris. Fig.2.14c shows the glide angle γ, the angle between the horizontal plane and the fragment velocity.

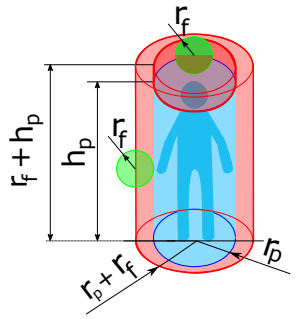

Figure 2.15: buffer cylinder, exploited by Montgomery in [196] and the author of the present thesis.

To make things more straightforward, the author introduces a right cylinder called *buffer cylinder*. It is created by adding the debris radius r_f to the right-man cylinder

dimensions r_p and h_p, Fig.2.15. Montgomery and the author of the present thesis exploit the *buffer cylinder* for the A_C formulation.
Since later on the paper will compare the Montgomery and the author's A_C equations, we will adopt a particular symbology. We will refer to Montgomery's A_C with $A_{C_{old}}$ and to this thesis author's one as $A_{C_{new}}$.
The *casualty area*, according to Montgomery, $A_{C_{old}}$, equation 2.6, equals the area that the *buffer cylinder* illuminated by γ-inclined lines projects on the floor, as more clear in Fig.2.16a.

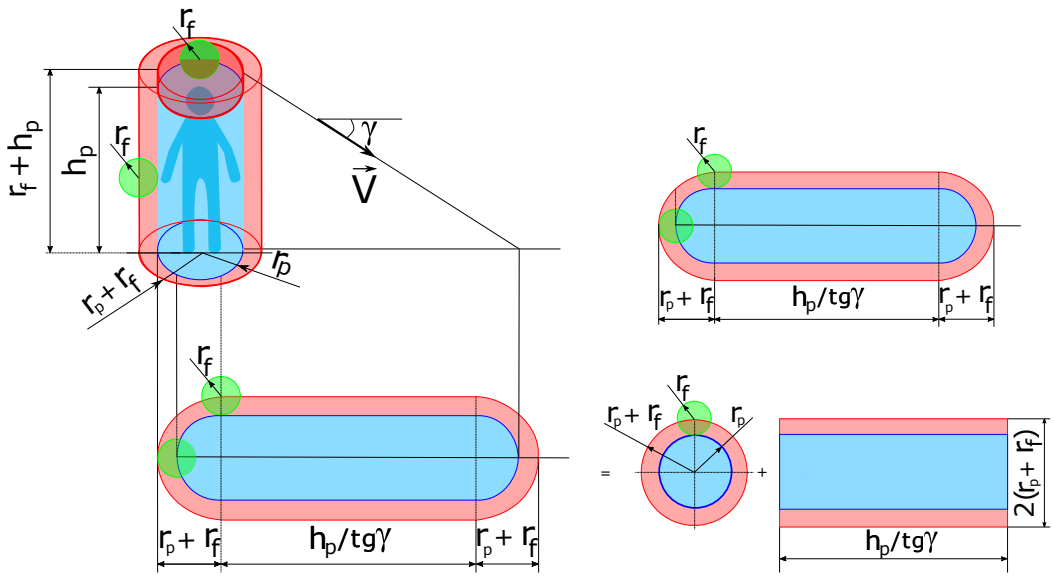

Figure 2.16: in Fig.2.16a definition of the *casualty area*, according to Montgomery [74]. In Fig.2.16b breakdown into circle and rectangle of the Montgomery's *casualty area*

.

$$\begin{cases} A_{C_{old}}(\gamma, r_f) = 2(r_p + r_f)h_p/\tan(\gamma) + \pi(r_p + r_f)^2 & \gamma < \pi/2 \\ A_{C_{old}}(\gamma, r_f) = \pi(r_p + r_f)^2 & \gamma = \pi/2 \end{cases} \tag{2.6}$$

Figure 2.16b shows Montgomery's *casualty area* breakdown into a rectangle and a circle. In $A_{C_{old}}$, the share due to the circle remains constant while the portion relating to the rectangle varies as $\tan^{-1}(\gamma)$; for this reason, the latter share tends to infinity when γ tends to zero leading to the large values of the casualty area when γ is small. $A_{C_{old}}$ is correct in representing the high kinetic energy debris crash case, but it doesn't mean the small kinetic energy debris one, as the C2 EASA category [100] drone crash. In this last case, the most realistic hypothesis excludes an infinite *casualty area* (as for Montgomery,' Grimsley,' or Dalamagkisid's formulae in the γ null case). The buffer cylinder's projection, on an inclined plane, Fig.2.15, represents a suitable low-kinetic energy debris *casualty area* modeling; the author of this thesis exploited this modeling to develop

the $A_{C_{new}}$. In the original modeling, the buffer cylinder is illuminated by γ-inclined rays while the projection plane is normal to them (see Fig.2.17a). Fig.2.17b clarifies the breakdown of the original *casualty area* model into an ellipse and a rectangle. Since

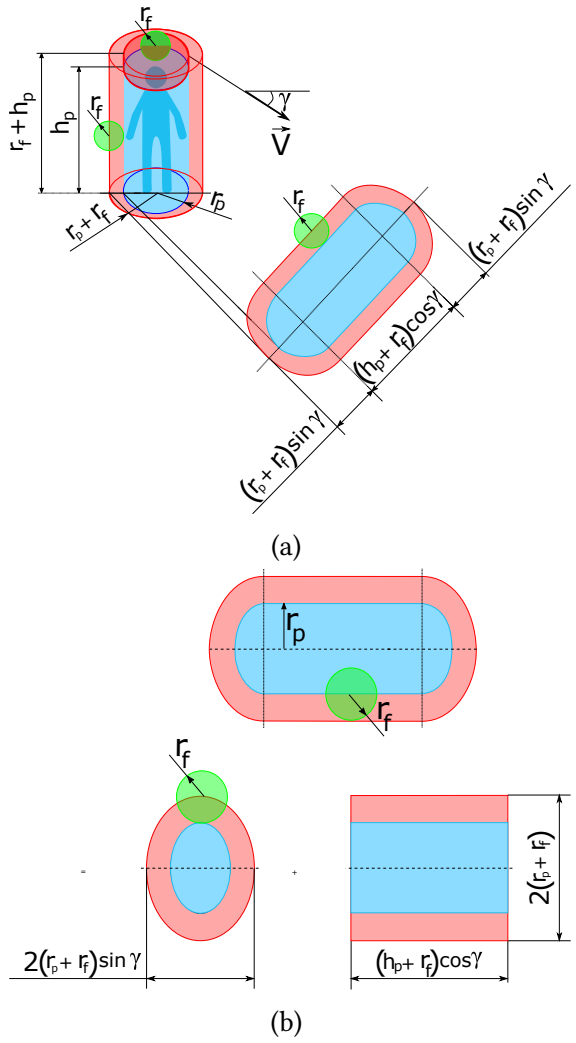

Figure 2.17: figure 2.17a shows the *casualty area* explanation according to the thesis's author. In Fig.2.16b breakdown into an ellipse and a rectangle of the authors *casualty area*

.

the projection plane is not parallel to the rays that illuminate the buffer cylinder, as for Montgomery in the null γ case, the projection, that is, the *casualty area*, never tends to infinite.

$A_{C_{old}}$ equals $A_{C_{new}}$ in the 90 deg γ case, as the horizontal section area of the buffer cylinder in both cases, i.e., an r_p plus r_f radius circle. In the γ null case, $A_{C_{new}}$ is the area of the buffer cylinder main vertical section, i.e., $2(r_p + r_f)$ by $(h_p + r_f)$ rectangle-sized

surface. Eq.2.7 shows these two extreme cases.

$$\begin{cases} A_{C_{new}}(\gamma = 0) = 2(r_p + r_f)(h_p + r_f) \\ A_{C_{new}}(\gamma = \pi/2) = \pi(r_p + r_f)^2 \end{cases} \tag{2.7}$$

In the intermediate γ range, $A_{C_{new}}$ has both a contribution deriving from the circle -that becomes null if γ is null and the only contribution when γ equals 90 deg- and one emanating from the rectangle -that becomes null if γ equals 90 deg while it is the only contribution when γ is null. These contributions show a γ-trigonometric trend. The circle-related share varies as the sine of γ (becoming an ellipse), and the one connected to the rectangle runs as the cosine of γ. The original *casualty area* formula is, then, the following:

$$A_{C_{new}}(\gamma, r_f) = \pi(r_p + r_f)^2 \sin(\gamma) + 2(r_p + r_f)(h_p + r_f)\cos(\gamma) \tag{2.8}$$

Fig.2.18a shows the graph of Eq.2.8, the original *casualty area* formulation as a function of γ for several debris' sizes r_f. At the same time, Fig.2.18b overlaps Montgomery's and the thesis author's *casualty area* formulations, highlighting the differences for small γ where Montgomery's formula, Eq.2.6, diverges while Eq.2.8 is still defined.

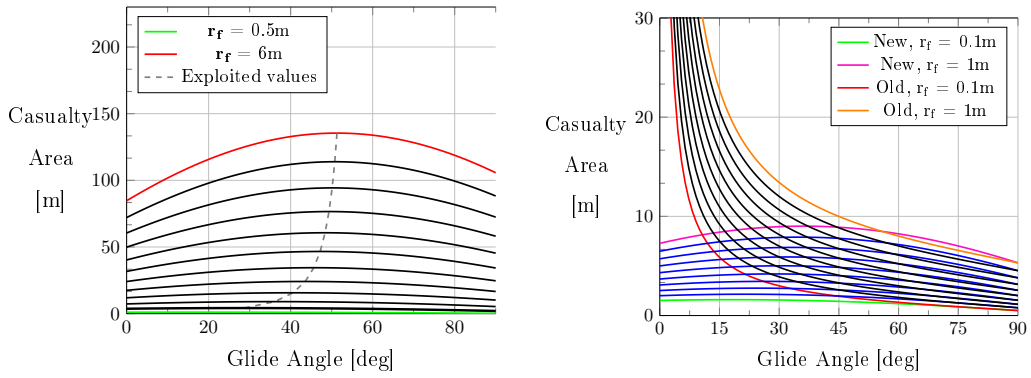

(a) (b)

Figure 2.18: figure 2.18a shows the $A_{C_{new}}$ graphical representation as γ function, according to Eq.2.8. Fig.2.18b shows the overlap of Eq.2.6 [196], subscript *'Old,'* and the original formulation as Eq.2.8, subscript *'New.'* The graphs are parametrized for debris radius, r_f.

The $A_{C_{new}}$ pros are several. Eq.2.8 results continuous and finite for $\gamma \in [0, \pi/2]$, then it admits a relative maximum for each debris size r_f.
Given the uncertainty about the angle at impact, the maximum of each curve assumes a significant value. The dotted line in Fig.2.18a and Fig.2.19 show this value, called *'exploitable casualty area,'* $A_{c_{exp}}$. This last value is not a function of both γ and r_f, but just of r_f. The *'exploitable casualty area'* $A_{c_{exp}}$ is the *casualty area's* value when γ fulfills

the following condition:

$$\left.\frac{\partial A_{C_{new}}(\gamma, r_f)}{\partial \gamma}\right|_{r_f} = 0 \tag{2.9}$$

this condition occurs if

$$\gamma_{exp}(r_f) = \arctan\left[\frac{\pi(r_P + r_f)}{2(r_f + r_f)}\right] \tag{2.10}$$

where $\gamma_{exp}(r_f)$ represents the glide angle that fulfills the Eq. 2.9. Therefore:

$$A_{C_{new}}(\gamma_{exp}(r_f), r_f) = A_{C_{exp}}(r_f) \tag{2.11}$$

From equation 2.9. it follows that the *casualty area* is only dependent on r_f, an easily measurable parameter. This change in formulation turns out to be necessary considering the random nature of γ; a precise value of the *'casualty area'* can be assigned for each drone, i.e., its *'exploitable casualty area'* $A_{C_{exp}}$, Fig.2.19.

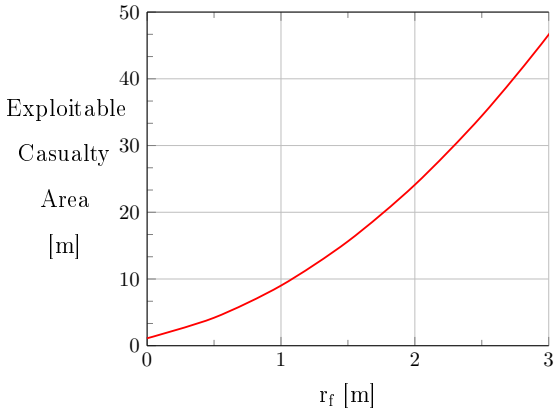

Figure 2.19: *exploitable casualty area* as a function of r_f.

The introduction and then the use of the *exploitable casualty area* are steps essential to create a risk map. Associating a casualty area, which still respects Montgomery's requirements, with each drone size, solves a problem regarding the uncertainty given by the unknown γ at the impact. Furthermore, using the *exploitable casualty area*, the actual *casualty area* at impact is almost always overestimated, making the risk evaluation more conservative. Evaluating the *casualty area* in advance makes assessing a risk map (deepened in section 2.3.5) possible. The adoption of the original formulation for the casualty area then produces exciting and practical implications.
The validation of the original *casualty area* formulation is considerable. However, this thesis did not verify it, having based only on a different assumption and following the same reasoning carried out by all the other analyzed *casualty area* formulations. The

different hypothesis the original assessment is based on, as mentioned introduction above, better fulfills the lightweight drone fall case. The validity of the original hypothesis should be tested in actual experiments to understand if the first hit object absorbs all the energy of the fall in a case in point.

2.3.5 Risk map

This chapter shows the final result of the risk assessment, i.e., the risk map. The risk map is an indispensable input for the path planner acting as a gain map. Figures in this section show the *risk maps* for different drone sizes and different kinetic energies at impact related to the two areas analyzed in this thesis. These figures help the reader to understand how the various involved parameters influence the risk and the most impacting ones. The two analyzed scenarios represent two classical urban environments, and the conclusion obtained are valid for all the possible urban environments.
As said, the drone size influences the number of the people potentially affected by a drone -via A_C- while drone kinetic energy conditions the probability of fatality of the affected people -via P(F|E)-. As expected, the larger the drone, and the more energy on the impact it carries, the more dangerous it is. Each figure from 2.20 to 2.23 (Naples area), and from 2.29 to 2.32 (New York area), is related to a specific drone maximum length, varying the kinetic energy at the impact. On the contrary, figures from 2.24 to 2.28, and from 2.33 to 2.37, refer to risk maps for different drone sizes but at the same kinetic energy at the impact. The analysis of these figures leads to some critical conclusions that will be better explained.
The first conclusion is that the increase of E_{imp} does raise the risk but not very incisively. Within each figure from 2.20 to 2.23 (Naples area), and from 2.29 to 2.32 (New York area), with a constant maximum drone length, and then a constant exploited casualty area, the E_{imp} switches from 100J to 1000J, thus multiplying the value by ten. However, this significant increase in the energy at the impact does not translate into an evident boost in risk that remains nearly the same.
More noticeable is the risk change related to the drone size, Figs.2.24 to 2.28, and from 2.33 to 2.37. The drone size analyzed in this thesis ranges from r_f equal to 0.25 meters to 3.5 meters (representing the LTE drone case). The following empirical law appears to be clear; tripling the maximum size of the drone leads to virtually doubling the related risk. So the second conclusion of this section is that among the parameters that most influence the risk, according to formulas used in this thesis, Equation 2.4, the size of the drone turns out to be the fundamental one. The reason appears to be the role that drone size plays in risk assessment. The kinetic energy at impact affects P(F|E) in a less than linear way, while the maximum size of the drone has a quadratic influence on the *casualty area*. It derives that the kinetic energy influences the risk in a less than linear way while the maximum drone dimension influences the risk quadratically. The analysis of the risk maps leads to a fundamental empirical law: to reduce the drone-related risk, it is more advantageous to use small drones than lightweight ones. From this perspective, it is clear that rotary-wing drones are a less risky choice than fixed-wing ones as the former are typically more compact and slower than the latter, as clear from Table 1.1. For these very reasons, LTA drones turn out to be the most dangerous choice among the possible drone choices being the biggest ones (as well as impractical for the reasons mentioned in section 1.3.3).

(a) 'Medaglie d'oro' square, aerial view

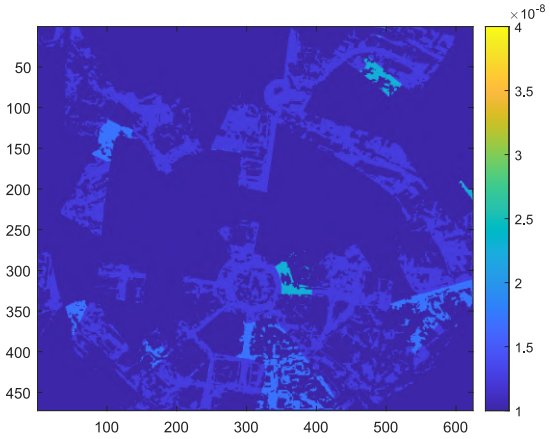

(b) Risk map, r_f =0.25 m, E_{imp}=100 J

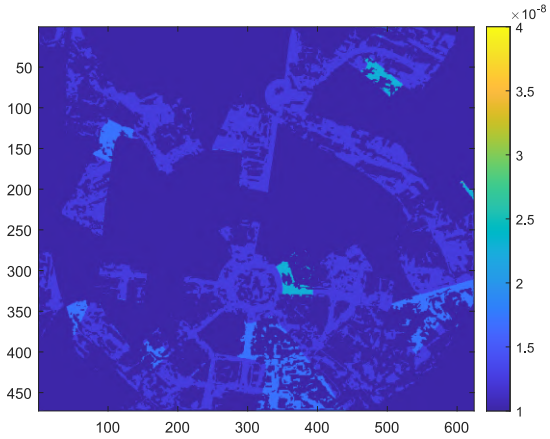

(c) Risk map, r_f =0.25 m, E_{imp}=150 J

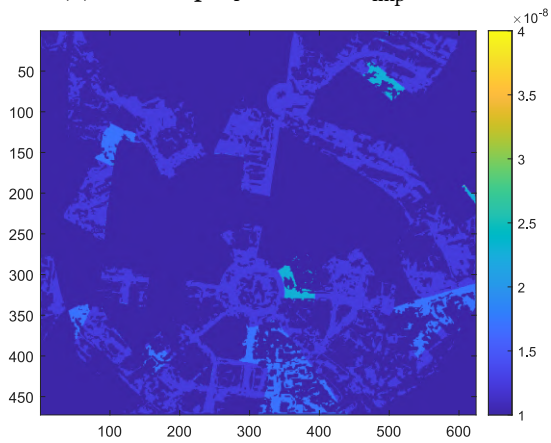

(d) Risk map, r_f =0.25 m, E_{imp}=300 J

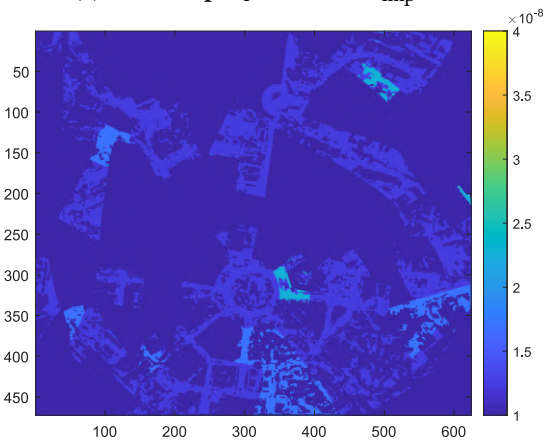

(e) Risk map, r_f =0.25 m, E_{imp}=600 J

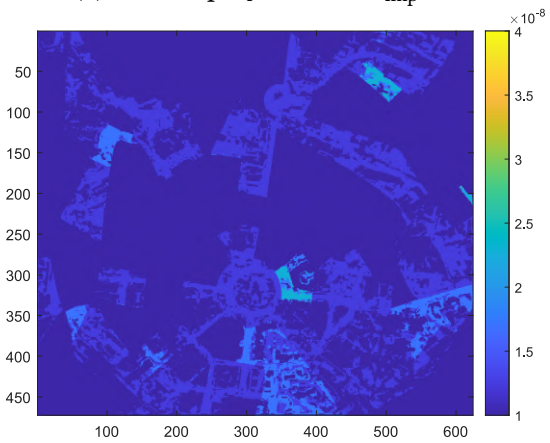

(f) Risk map, r_f =0.25 m, E_{imp}=1000 J

Figure 2.20: figures 2.20b - 2.20f show the *'risk maps'* related to the 'Medaglie d'oro' square, in Naples, Italy, for a drone 0.5 m wide ($A_{C_{exp}}$=2.4 m^2) and different drones kinetic energy.

(a) 'Medaglie d'oro' square, aerial view

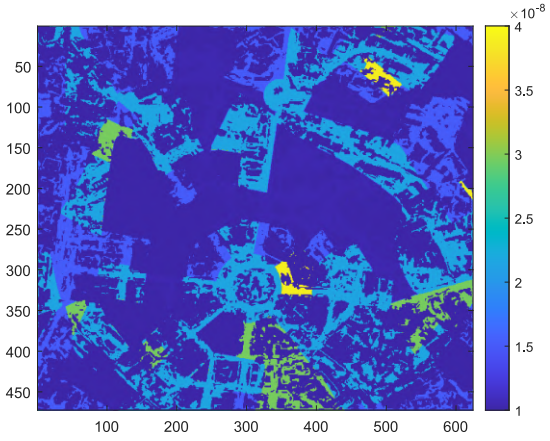

(b) Risk map, r_f =0.5 m, E_{imp}=100 J

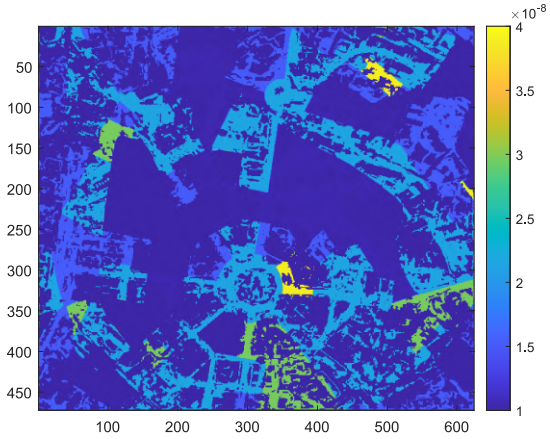

(c) Risk map, r_f =0.5 m, E_{imp}=150 J

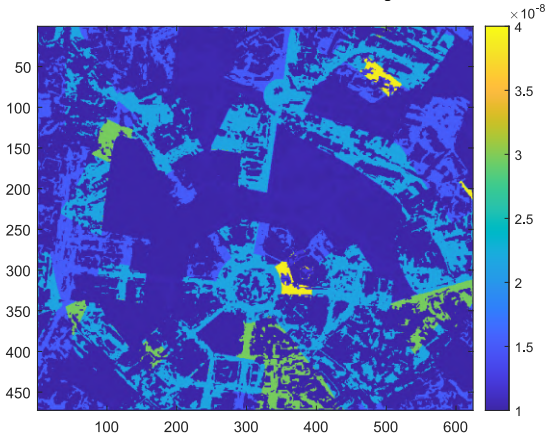

(d) Risk map, r_f =0.5 m, E_{imp}=300 J

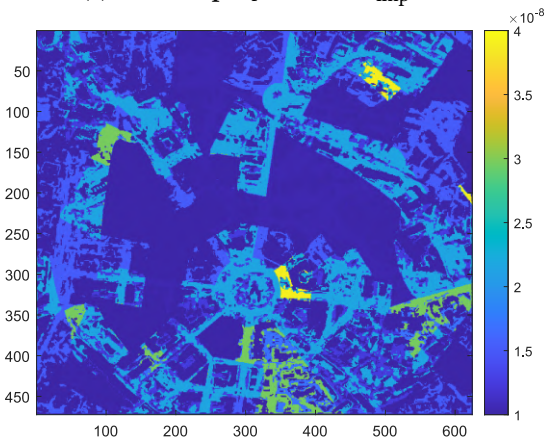

(e) Risk map, r_f =0.5 m, E_{imp}=600 J

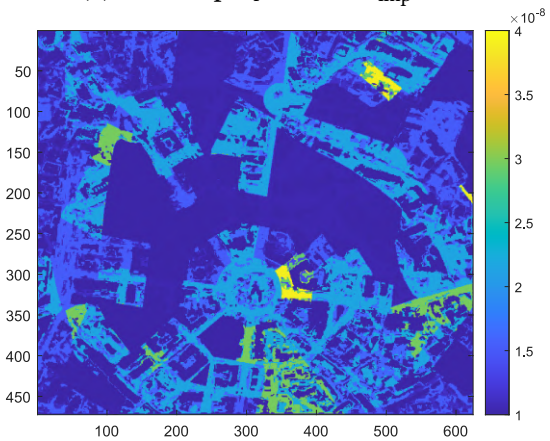

(f) Risk map, r_f =0.5 m, E_{imp}=1000 J

Figure 2.21: figures 2.21b - 2.21f show the *'risk maps'* related to the 'Medaglie d'oro' square, in Naples, Italy, for a drone 1 m wide ($A_{C_{exp}}$=4.2 m^2) and different drones kinetic energy.

(a) 'Medaglie d'oro' square, aerial view

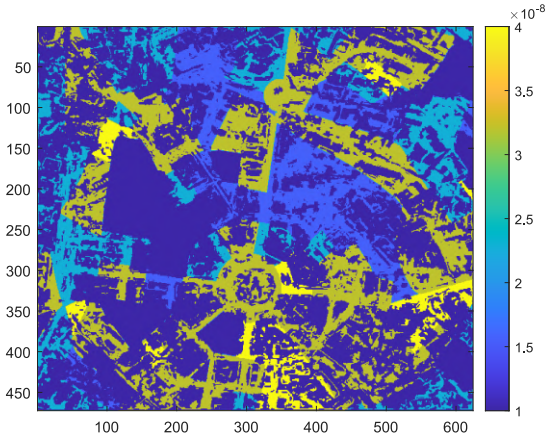

(b) Risk map, r_f =0.75 m, E_{imp}=100 J

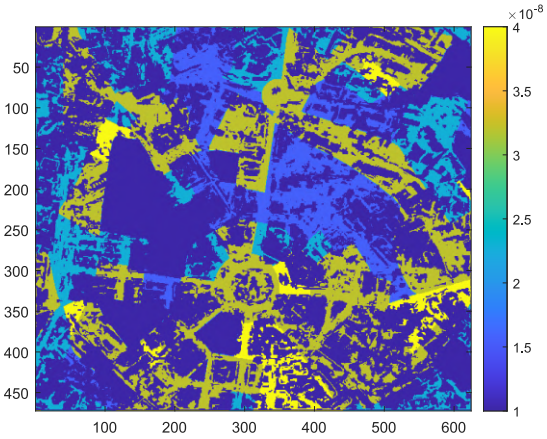

(c) Risk map, r_f =0.75 m, E_{imp}=150 J

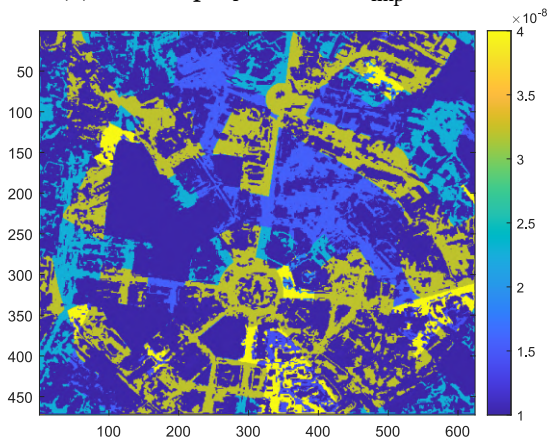

(d) Risk map, r_f =0.75 m, E_{imp}=300 J

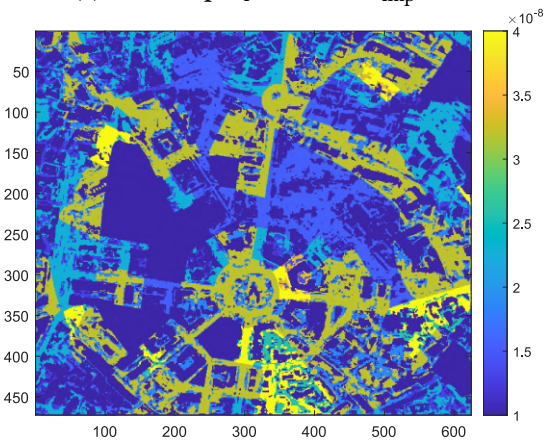

(e) Risk map, r_f =0.75 m, E_{imp}=600 J

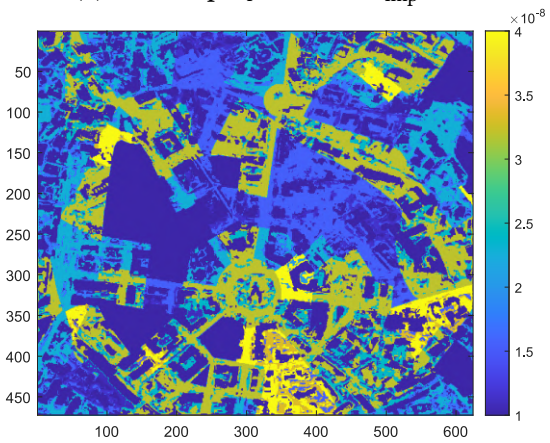

(f) Risk map, r_f =0.75 m, E_{imp}=1000 J

Figure 2.22: figures 2.22b - 2.22f show the *'risk maps'* related to the 'Medaglie d'oro' square, in Naples, Italy, for a drone 1.5 m wide ($A_{C_{exp}}$=6.3 m^2) and different drones kinetic energy.

(a) 'Medaglie d'oro' square, aerial view

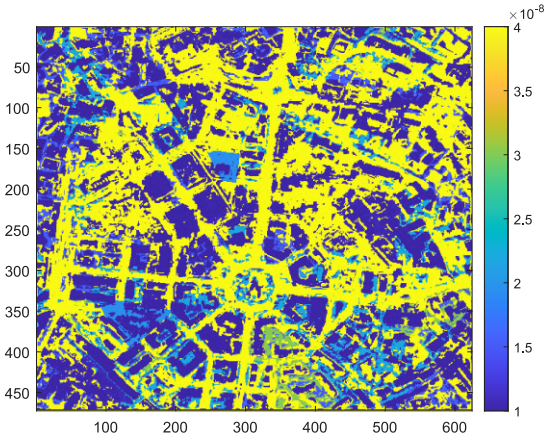

(b) Risk map, r_f =3.5 m, E_{imp}=100 J

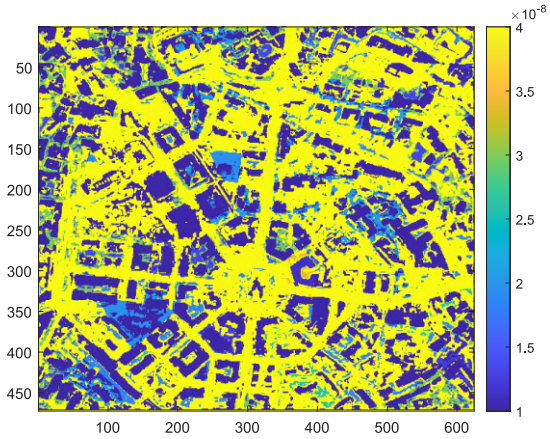

(c) Risk map, r_f =3.5 m, E_{imp}=150 J

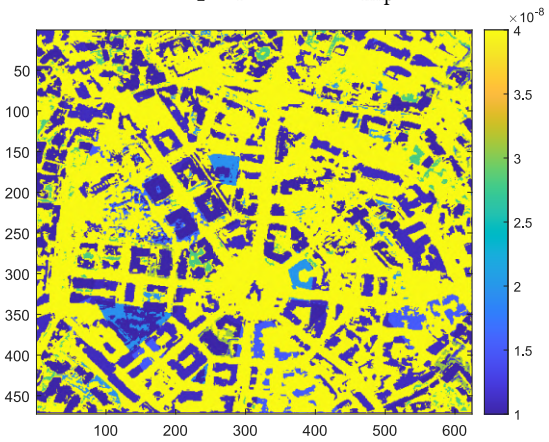

(d) Risk map, r_f =3.5 m, E_{imp}=300 J

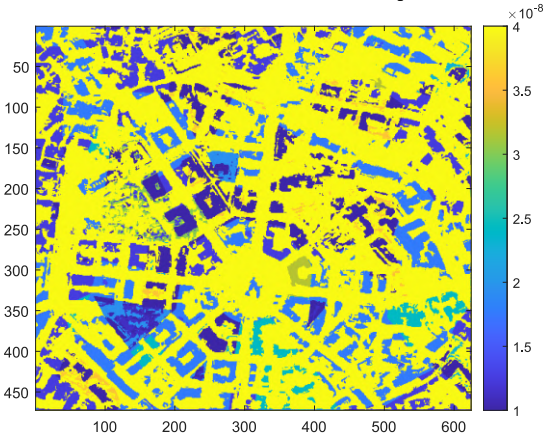

(e) Risk map, r_f =3.5 m, E_{imp}=600 J

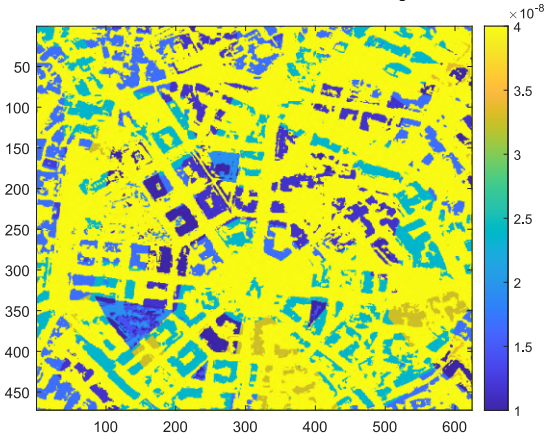

(f) Risk map, r_f =3.5 m, E_{imp}=1000 J

Figure 2.23: figures 2.23b - 2.23f show the *'risk maps'* related to the 'Medaglie d'oro' square, in Naples, Italy, for a 7 m long LTA drone ($A_{C_{exp}}$=60.64 m^2) and different drones kinetic energy. Most of the risk-map is out of scale; the risk value is about 10 times that of figure 2.22.

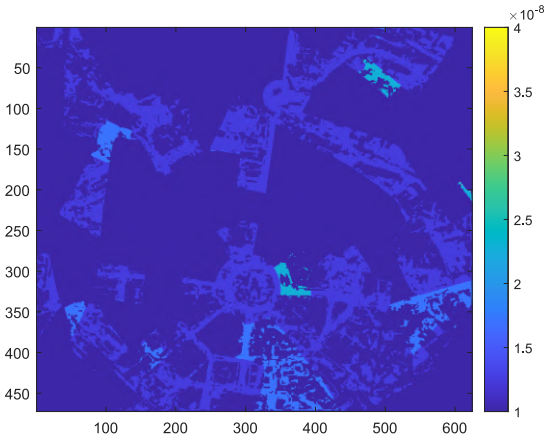

(a) Risk map, r_f =0.25 m, E_{imp}=100 J

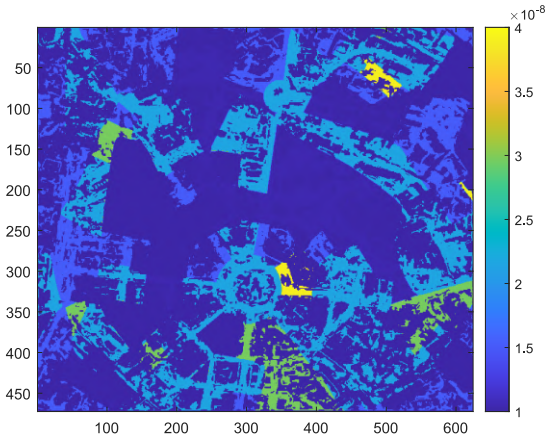

(b) Risk map, r_f =0.5 m, E_{imp}=100 J

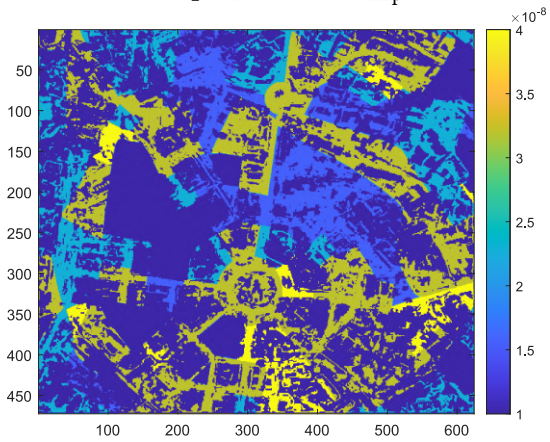

(c) Risk map, r_f =0.75 m, E_{imp}=100 J

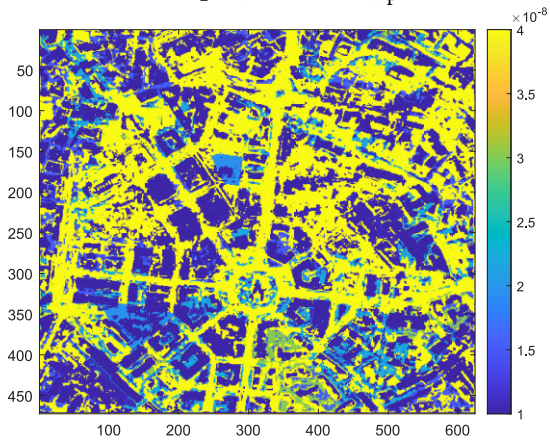

(d) Risk map, r_f =3.5 m, E_{imp}=100 J

Figure 2.24: figures 2.24a - 2.24d show the *'risk maps'* related to the 'Medaglie d'oro' square, in Naples, Italy, for different drone lengths at the same drones kinetic energy at the impact, 100 N. It is is clear how the maximum drone length, and then the casualty area, plays an essential role in the risk evaluation.

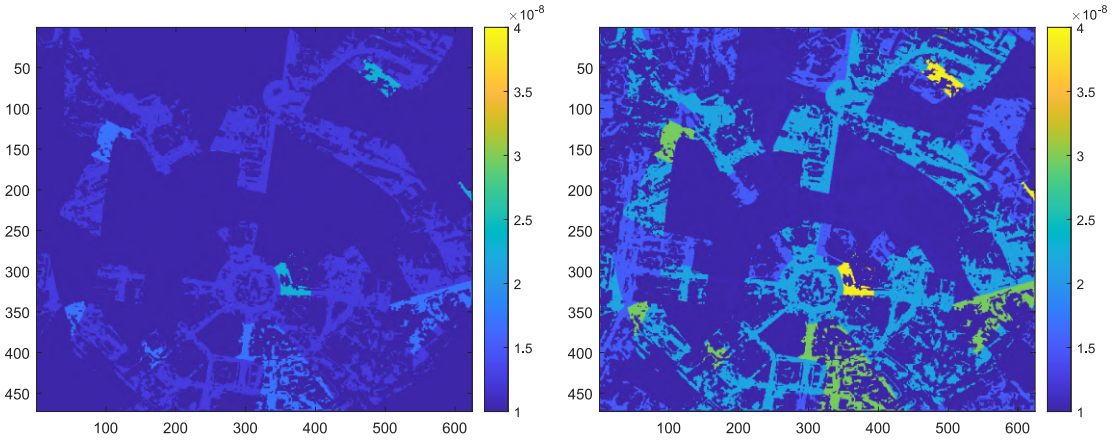

(a) Risk map, r_f =0.25 m, E_{imp}=150 J

(b) Risk map, r_f =0.5 m, E_{imp}=150 J

(c) Risk map, r_f =0.75 m, E_{imp}=150 J

(d) Risk map, r_f =3.5 m, E_{imp}=150 J

Figure 2.25: figures 2.25a - 2.25d show the *'risk maps'* related to the 'Medaglie d'oro' square, in Naples, Italy, for different drone lengths at the same drones kinetic energy at the impact, 150 N. It is is clear how the maximum drone length, and then the casualty area, plays an essential role in the risk evaluation.

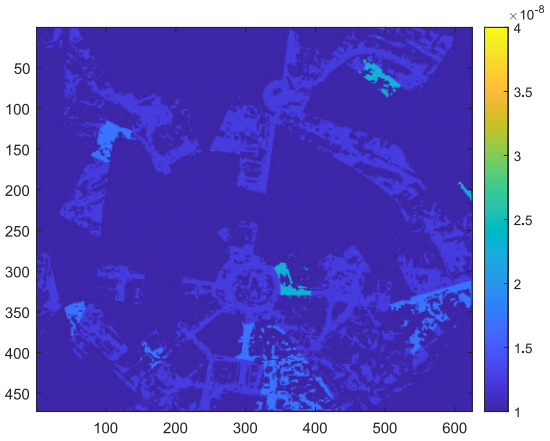

(a) Risk map, r_f =0.25 m, E_{imp}=300 J

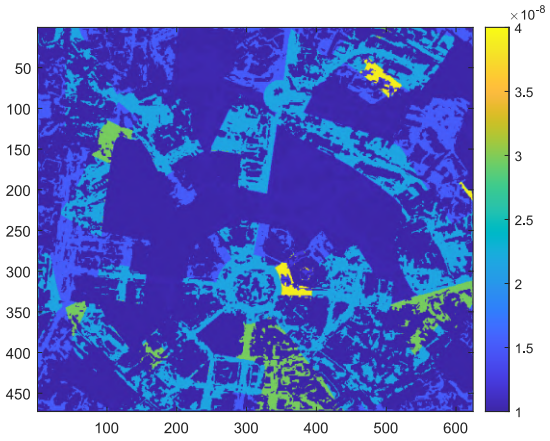

(b) Risk map, r_f =0.5 m, E_{imp}=300 J

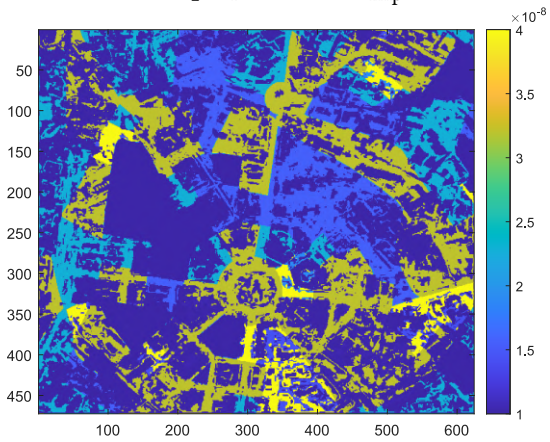

(c) Risk map, r_f =0.75 m, E_{imp}=300 J

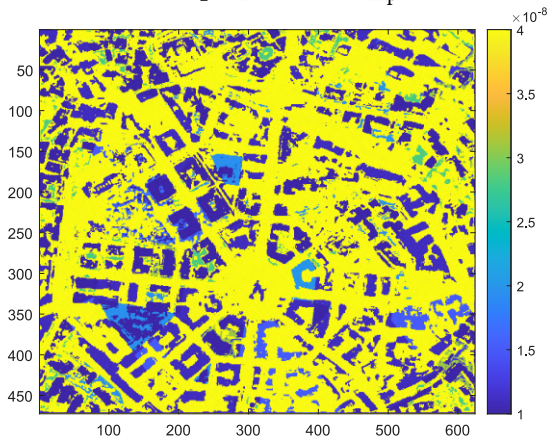

(d) Risk map, r_f =3.5 m, E_{imp}=300 J

Figure 2.26: figures 2.26a - 2.26d show the *'risk maps'* related to the 'Medaglie d'oro' square, in Naples, Italy, for different drone lengths at the same drones kinetic energy at the impact, 300 N. It is is clear how the maximum drone length, and then the casualty area, plays an essential role in the risk evaluation.

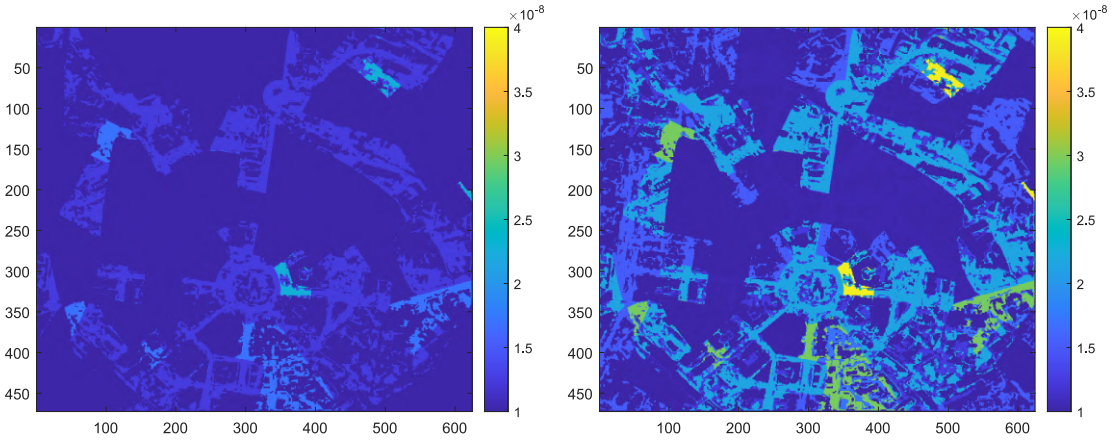

(a) Risk map, r_f =0.25 m, E_{imp}=600 J

(b) Risk map, r_f =0.5 m, E_{imp}=600 J

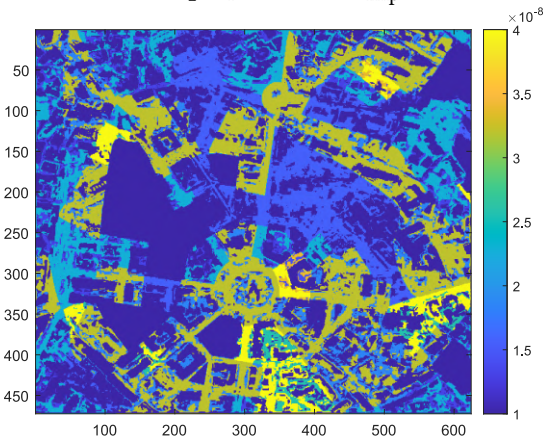

(c) Risk map, r_f =0.75 m, E_{imp}=600 J

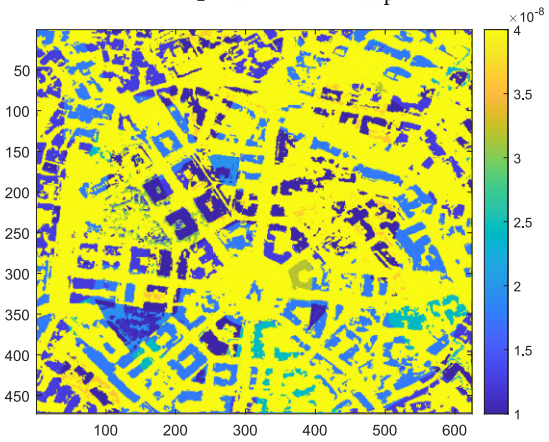

(d) Risk map, r_f =3.5 m, E_{imp}=600 J

Figure 2.27: figures 2.27a - 2.27d show the *'risk maps'* related to the 'Medaglie d'oro' square, in Naples, Italy, for different drone lengths at the same drones kinetic energy at the impact, 600 N. It is is clear how the maximum drone length, and then the casualty area, plays an essential role in the risk evaluation.

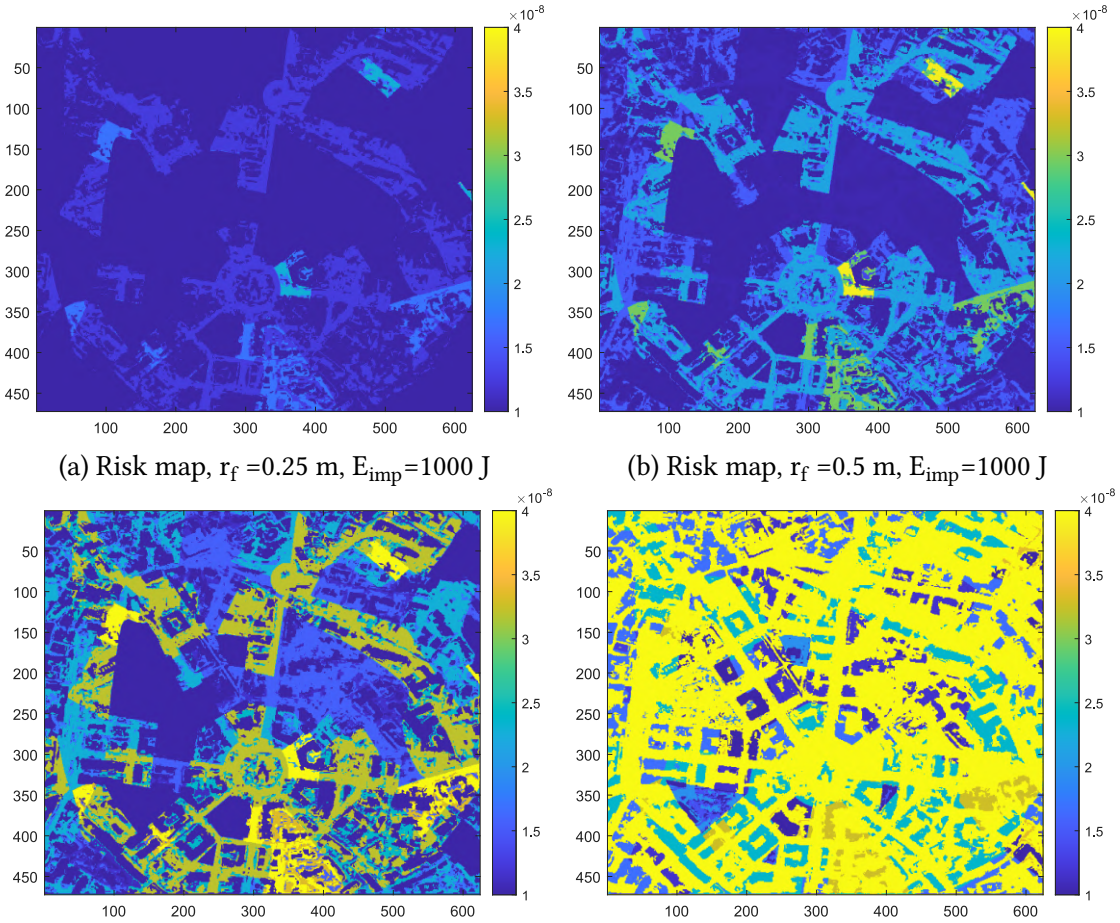

(a) Risk map, r_f =0.25 m, E_{imp}=1000 J

(b) Risk map, r_f =0.5 m, E_{imp}=1000 J

(c) Risk map, r_f =0.75 m, E_{imp}=1000 J

(d) Risk map, r_f =3.5 m, E_{imp}=1000 J

Figure 2.28: figures 2.28a - 2.28d show the *'risk maps'* related to the 'Medaglie d'oro' square, in Naples, Italy, for different drone lengths at the same drones kinetic energy at the impact, 1000 N. It is is clear how the maximum drone length, and then the casualty area, plays an essential role in the risk evaluation.

(a) New York City, aerial view.

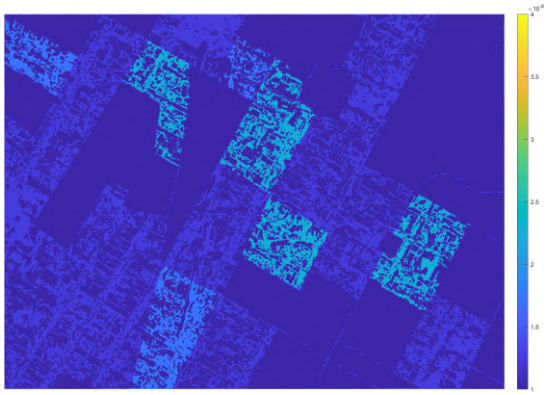

(b) Risk map, r_f =0.25 m, E_{imp}=100 J

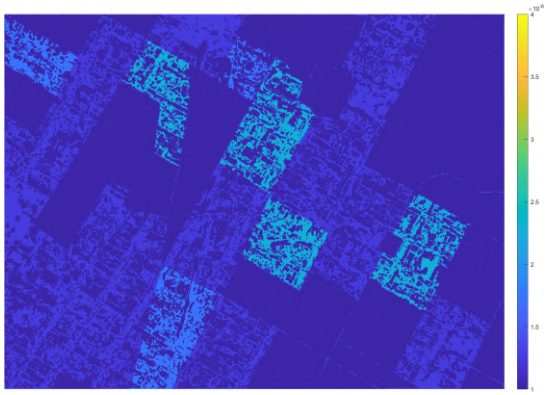

(c) Risk map, r_f =0.25 m, E_{imp}=150 J

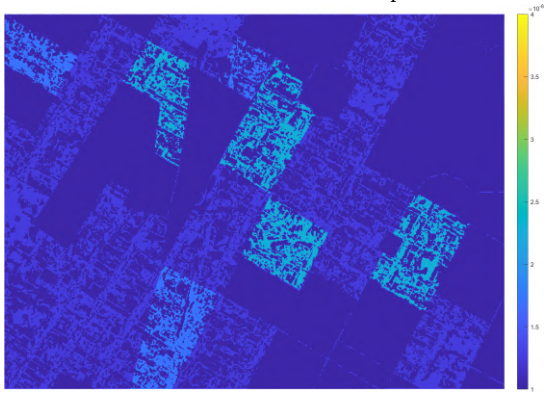

(d) Risk map, r_f =0.25 m, E_{imp}=300 J

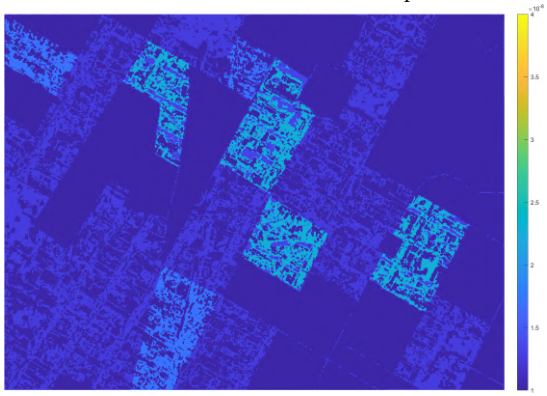

(e) Risk map, r_f =0.25 m, E_{imp}=600 J

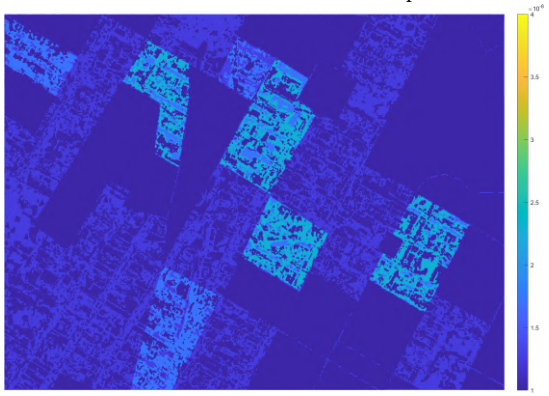

(f) Risk map, r_f =0.25 m, E_{imp}=1000 J

Figure 2.29: figures 2.29b - 2.29f show the *'risk maps'* related to the East Village, part of New York City (NY), for a drone 0.5 m wide ($A_{C_{exp}}$=2.4 m^2) and different drones kinetic energy.

(a) New York City, aerial view.

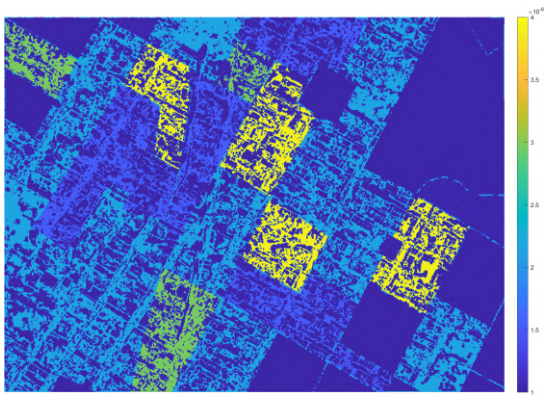

(b) Risk map, r_f =0.5 m, E_{imp}=100 J

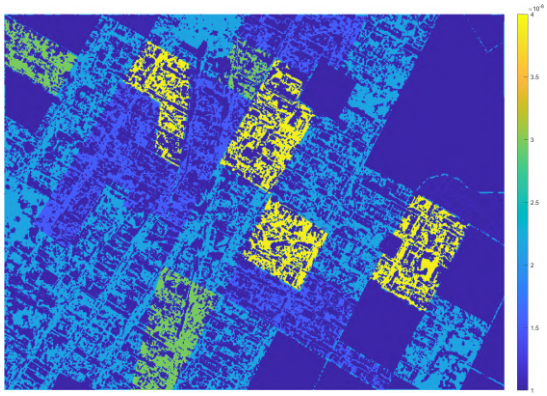

(c) Risk map, r_f =0.5 m, E_{imp}=150 J

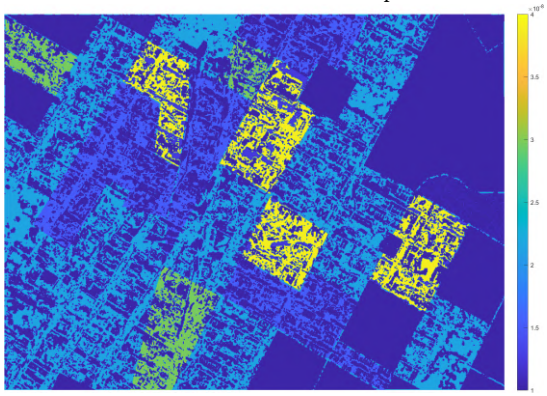

(d) Risk map, r_f =0.5 m, E_{imp}=300 J

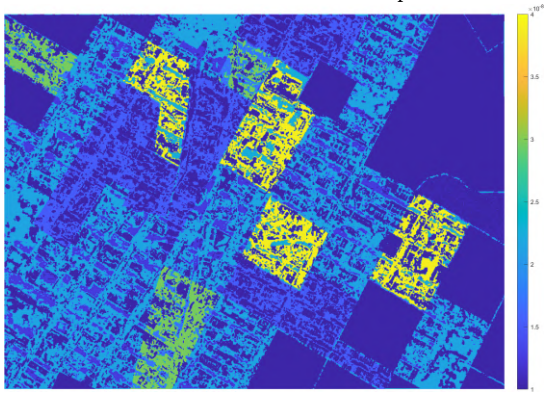

(e) Risk map, r_f =0.5 m, E_{imp}=600 J

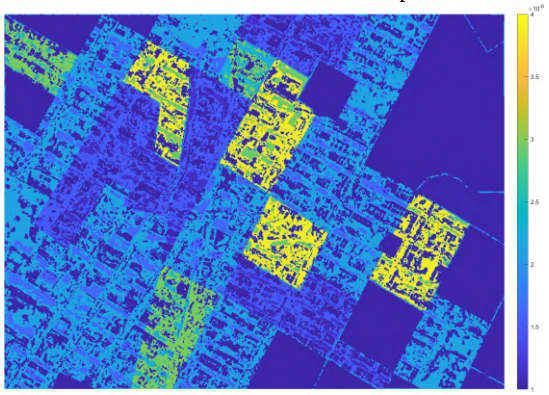

(f) Risk map, r_f =0.5 m, E_{imp}=1000 J

Figure 2.30: figures 2.30b - 2.30f show the *'risk maps'* related to the East Village, part of New York City (NY), for a drone 1 m wide ($A_{C_{exp}}$=4.2 m^2) and different drones kinetic energy.

(a) New York City, aerial view.

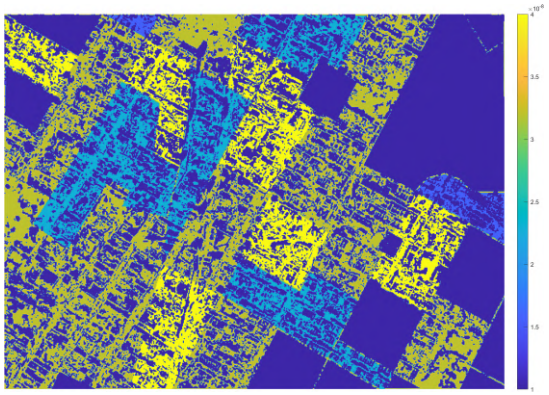

(b) Risk map, r_f =0.75 m, E_{imp}=100 J

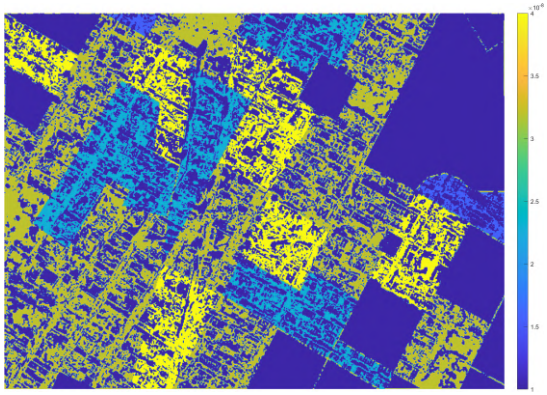

(c) Risk map, r_f =0.75 m, E_{imp}=150 J

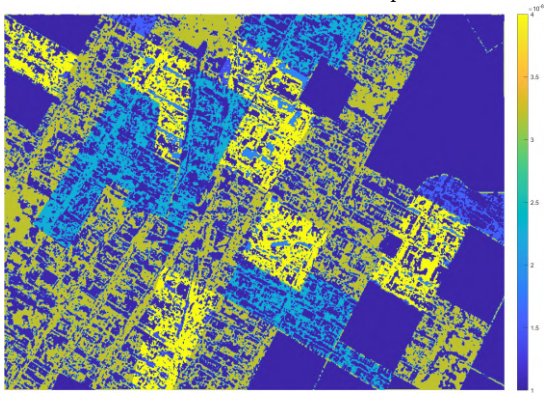

(d) Risk map, r_f =0.75 m, E_{imp}=300 J

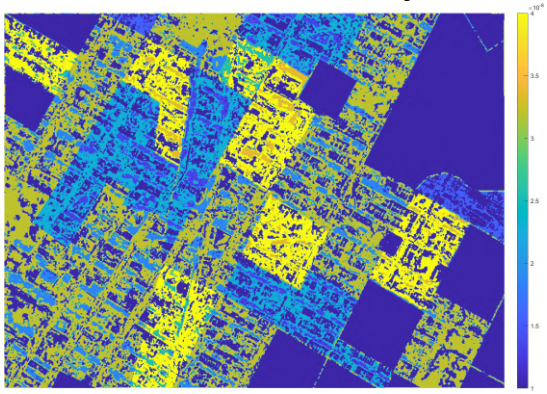

(e) Risk map, r_f =0.75 m, E_{imp}=600 J

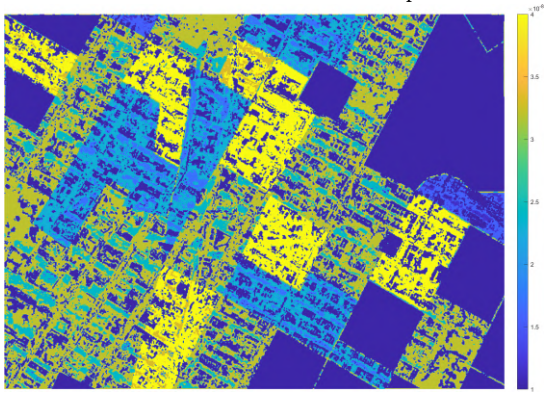

(f) Risk map, r_f =0.75 m, E_{imp}=1000 J

Figure 2.31: figures 2.31b - 2.31f show the *'risk maps'* related to the East Village, part of New York City (NY), for a drone 1.5 m wide ($A_{C_{exp}}$=6.3 m^2) and different drones kinetic energy.

(a) New York City, aerial view.

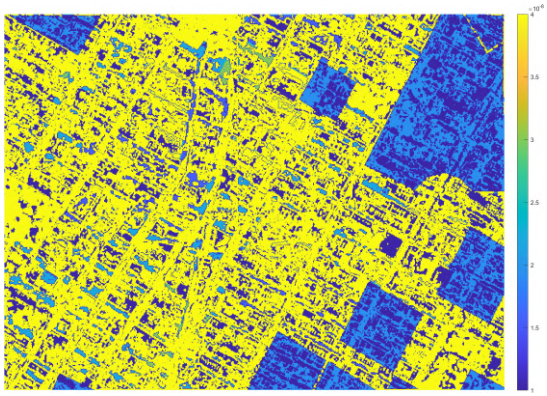

(b) Risk map, r_f =3.5 m, E_{imp}=100 J

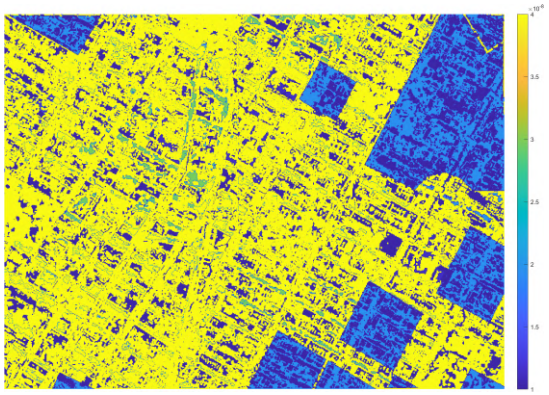

(c) Risk map, r_f =3.5 m, E_{imp}=150 J

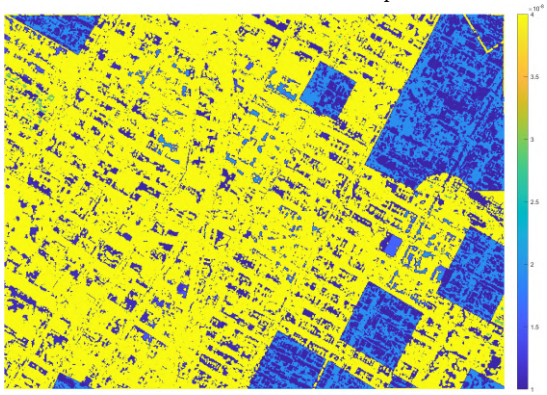

(d) Risk map, r_f =3.5 m, E_{imp}=300 J

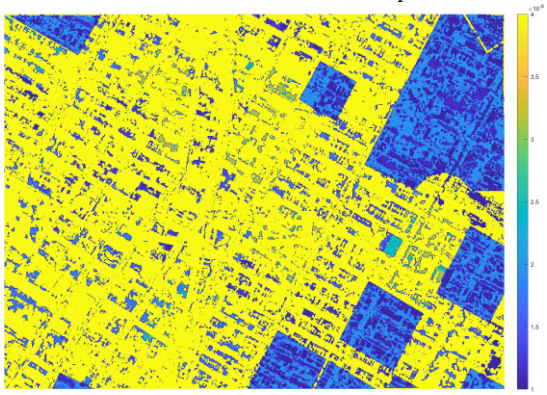

(e) Risk map, r_f =3.5 m, E_{imp}=600 J

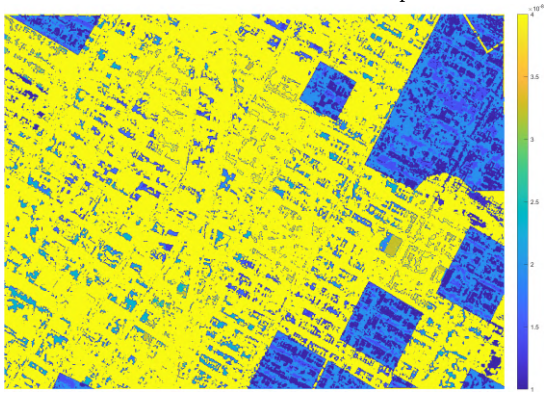

(f) Risk map, r_f =3.5 m, E_{imp}=1000 J

Figure 2.32: figures 2.32b - 2.32f show the *'risk maps'* related to the East Village, part of New York City (NY), for a 7 m long LTA drone ($A_{C_{exp}}$=60.64 m^2) and different drones kinetic energy. Most of the risk-map is out of scale; the risk value is about 10 times that of figure 2.31.

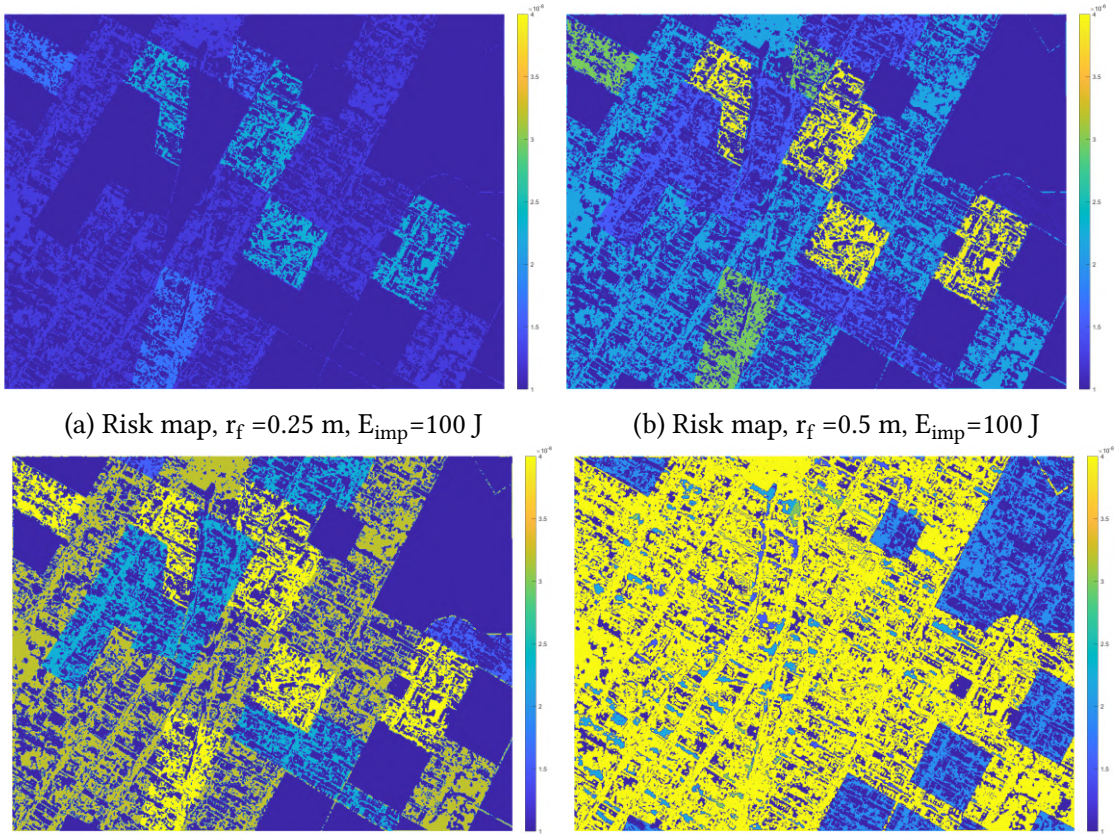

(a) Risk map, r_f =0.25 m, E_{imp}=100 J

(b) Risk map, r_f =0.5 m, E_{imp}=100 J

(c) Risk map, r_f =0.75 m, E_{imp}=100 J

(d) Risk map, r_f =3.5 m, E_{imp}=100 J

Figure 2.33: figures 2.33a - 2.33d show the *'risk maps'* related to the East Village, part of New York City (NY), for different drone lengths at the same drones kinetic energy at the impact, 100 N. It is is clear how the maximum drone length, and then the casualty area, plays an essential role in the risk evaluation.

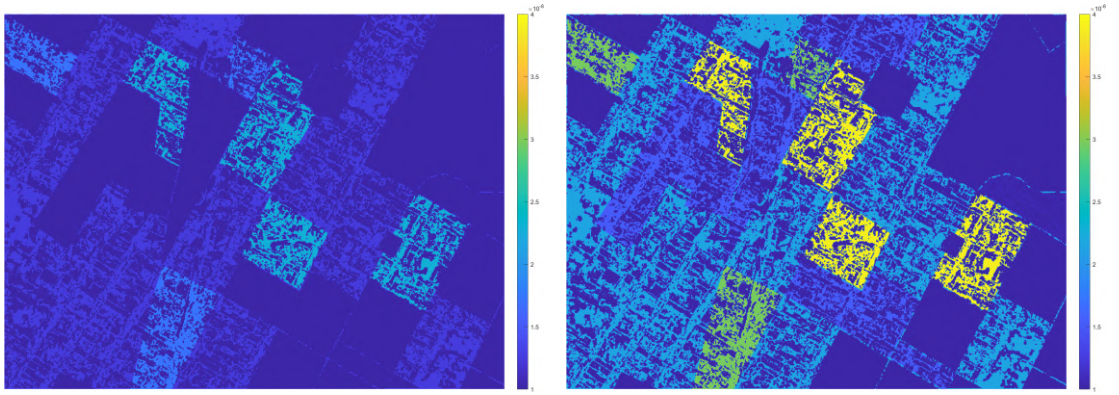

(a) Risk map, r_f =0.25 m, E_{imp}=150 J

(b) Risk map, r_f =0.5 m, E_{imp}=150 J

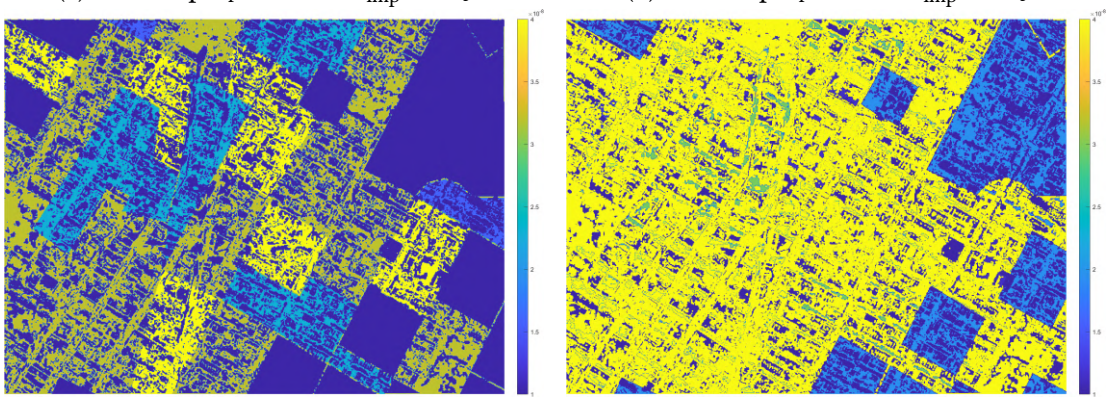

(c) Risk map, r_f =0.75 m, E_{imp}=150 J

(d) Risk map, r_f =3.5 m, E_{imp}=150 J

Figure 2.34: figures 2.34a - 2.34d show the *'risk maps'* related to the East Village, part of New York City (NY), for different drone lengths at the same drones kinetic energy at the impact, 150 N. It is is clear how the maximum drone length, and then the casualty area, plays an essential role in the risk evaluation.

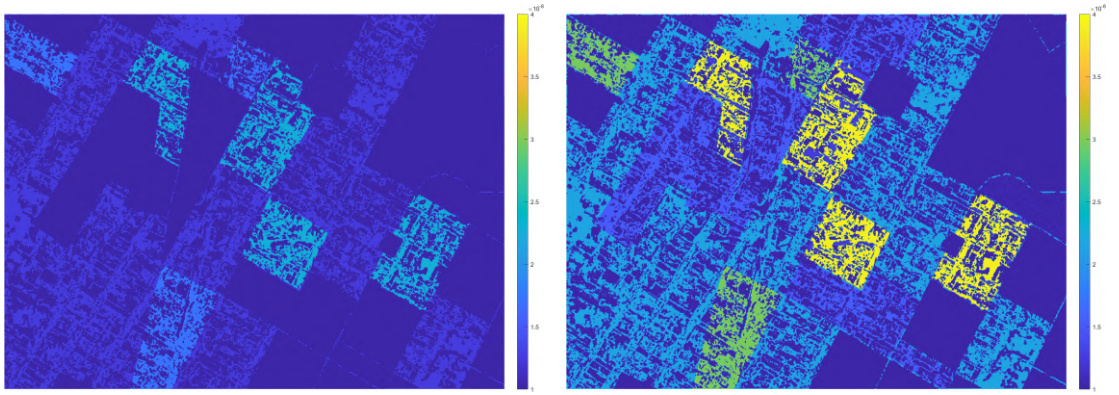

(a) Risk map, r_f =0.25 m, E_{imp}=300 J

(b) Risk map, r_f =0.5 m, E_{imp}=300 J

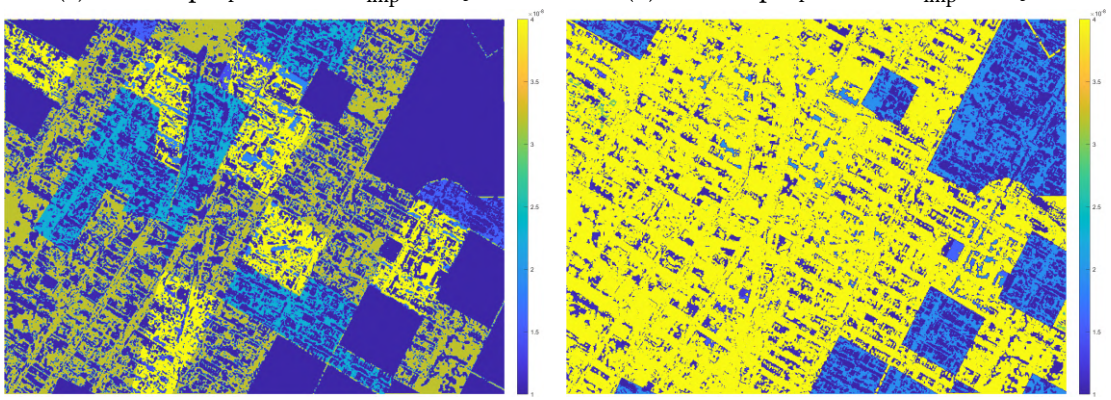

(c) Risk map, r_f =0.75 m, E_{imp}=300 J

(d) Risk map, r_f =3.5 m, E_{imp}=300 J

Figure 2.35: figures 2.35a - 2.35d show the *'risk maps'* related to the East Village, part of New York City (NY), for different drone lengths at the same drones kinetic energy at the impact, 300 N. It is is clear how the maximum drone length, and then the casualty area, plays an essential role in the risk evaluation.

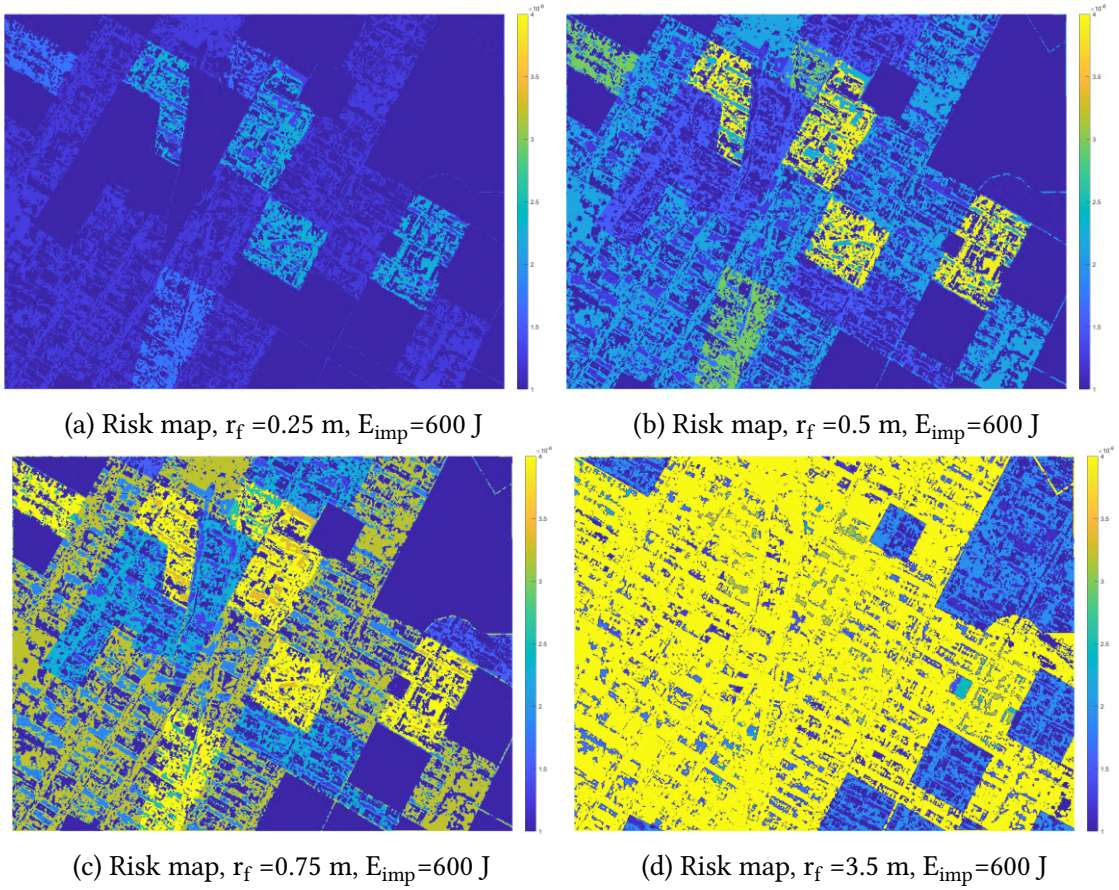

(a) Risk map, r_f =0.25 m, E_{imp}=600 J

(b) Risk map, r_f =0.5 m, E_{imp}=600 J

(c) Risk map, r_f =0.75 m, E_{imp}=600 J

(d) Risk map, r_f =3.5 m, E_{imp}=600 J

Figure 2.36: figures 2.36a - 2.36d show the *'risk maps'* related to the East Village, part of New York City (NY), for different drone lengths at the same drones kinetic energy at the impact, 600 N. It is is clear how the maximum drone length, and then the casualty area, plays an essential role in the risk evaluation.

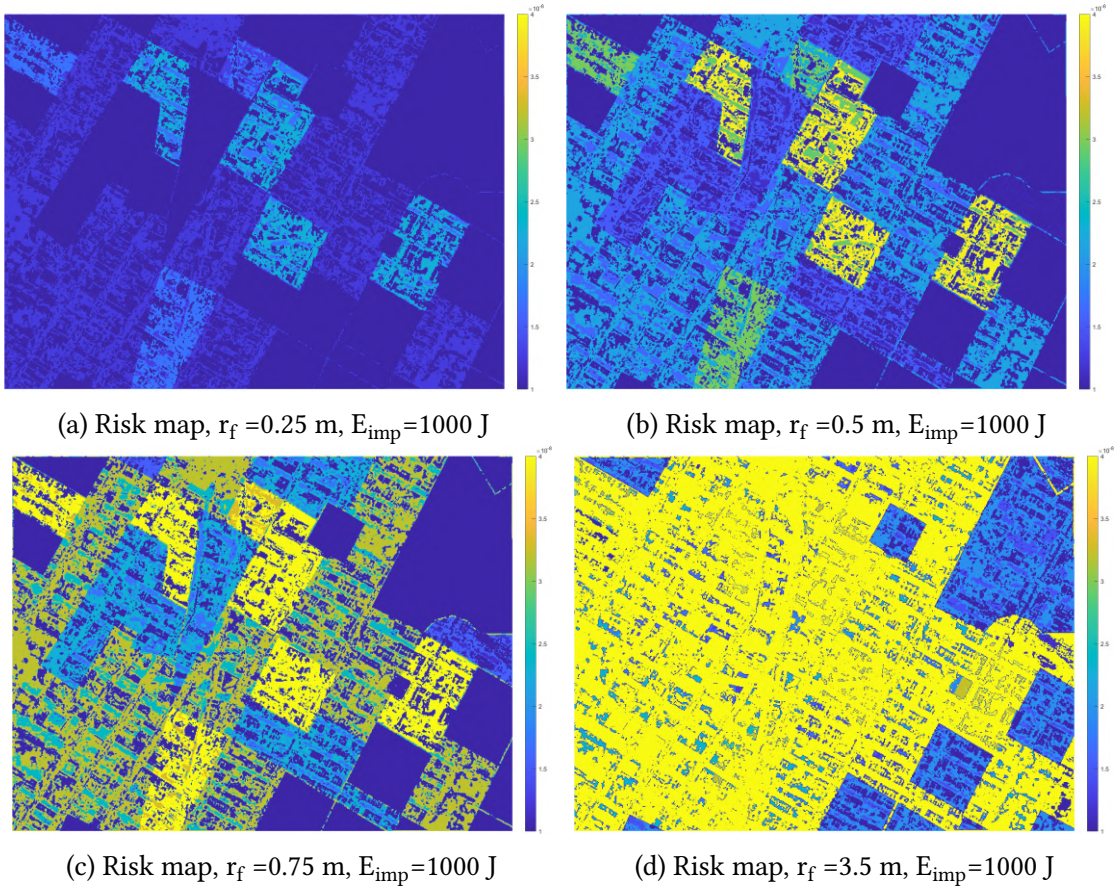

(a) Risk map, r_f =0.25 m, E_{imp}=1000 J

(b) Risk map, r_f =0.5 m, E_{imp}=1000 J

(c) Risk map, r_f =0.75 m, E_{imp}=1000 J

(d) Risk map, r_f =3.5 m, E_{imp}=1000 J

Figure 2.37: figures 2.37a - 2.37d show the *'risk maps'* related to the East Village, part of New York City (NY), for different drone lengths at the same drones kinetic energy at the impact, 1000 N. It is is clear how the maximum drone length, and then the casualty area, plays an essential role in the risk evaluation.

2.4 Flight allowed map

This section shows the map's evaluation in which the drone can fly, relative to the area of interest, called the *flight-allowed* map. This map is a fundamental input for the path planner and is the union of the *occupancy* and the *no-fly zone* maps introduced below. The flight allowed map is represented as a matrix consisting of '1' -the drone can't fly- and '0' -the drone can fly-. Each number represents a 1x1 square meter. The author made great use of open-source tools, which therefore allow wide repeatability of the exercises.

2.4.1 Occupancy map

The *'occupancy map'* provides information about an area drones cannot overfly at the 'operating height' due to obstacles. The output is a 2-D matrix containing just two values, as in the *'no-fly zone'* map, which is deepened in section 2.4.2. The value '0' indicates an area drones can fly over, while the value '1' indicates an obstacle at the given height. These numbers are compatible with those used in the *'no-fly zone'* map, where '0' shows a flyover allowed area and '1,' forbidden airspace. Each number refers to a square, typically (as also happens in this thesis) 1x1 square meter.
The generation of such a map requires a 3D map of the area of interest and the UAV *operating height*. A web mapping service could provide the former information; this thesis exploits OpenStreetMap [248]. Mission purposes determine the latter information. The process to obtain the *occupancy* map adopted in this thesis is shown in Figs.2.38 and 2.39. Once the area of interest has been identified, its CAD is extracted through *OpenStreetMap* [248] provided data, Fig.2.38b and 2.39b. The writer of this thesis has chosen the areas near 'Medaglie D'oro' square in Naples, Italy, Fig.2.38a, and a part of New York City (NY), Fig.2.39a. The intersections of these CADs and a horizontal plane positioned at the *operating height* are represented in figures 2.38c and 2.39c, respectively. The intersection data are stored in a matrix, as discussed above, whose representations are the Figs.2.38d of 2.39d, where black dots (value 1) represent obstacles. The whole process that derives the *occupancy* map matrix uses a Matlab script optimized to handle *.osm OpenStreetMap* provided files.

(a) 'Medaglie d'oro' square, aerial view.

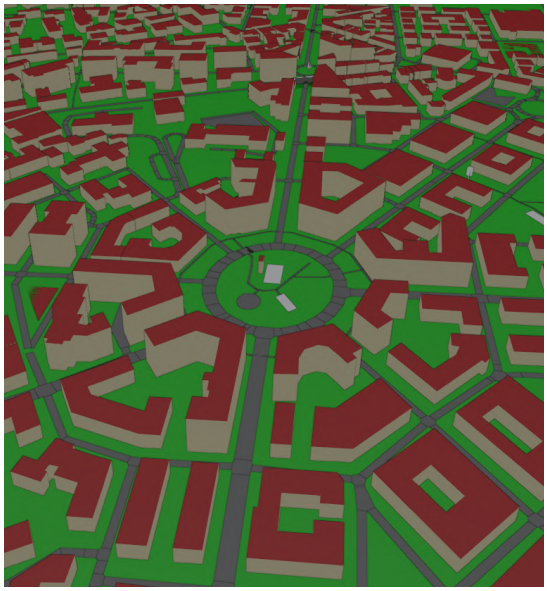

(b) The CAD of the area in Fig.2.38a.

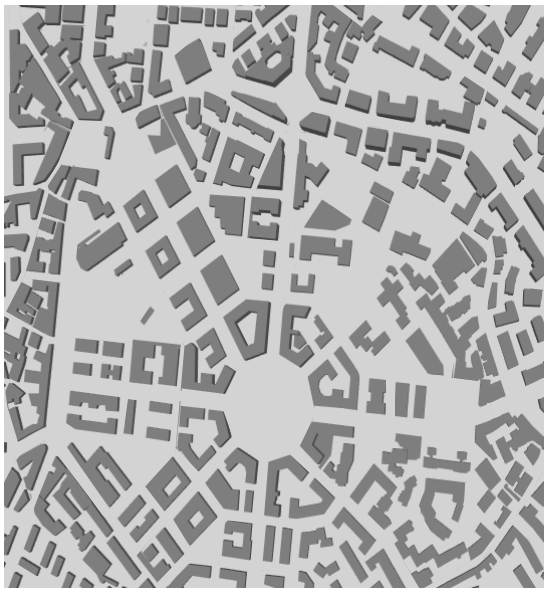

(c) Section of the CAD of figure 2.38b with an horizontal plane.

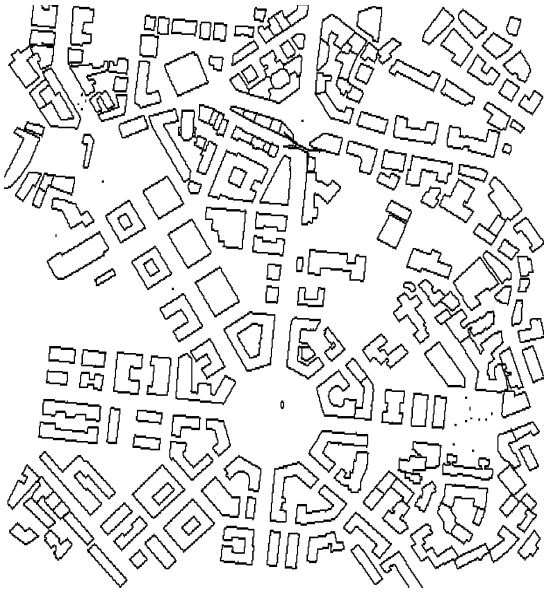

(d) Representation of the Occupancy map matrix of the area in Fig.2.38a.

Figure 2.38: maps relating to an area near Medaglie d'Oro square, Naples, Italy. Picture 2.38a is an aerial view, Fig.2.38b shows the CAD obtained through OpenStreetMap [248], Fig.2.38c is a section of the CAD of figure 2.38b and a 5 meters height horizontal plane, while Fig.2.38d shows the Occupancy map of the area of interest, represented in binary terms: '1' (black) represents the obstacle and '0' (white) free airspace.

(a) New York, aerial view.

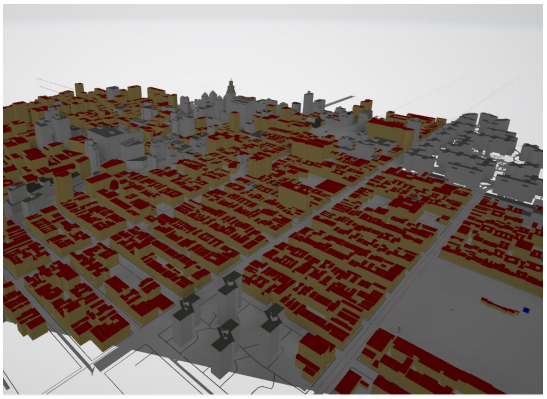

(b) The CAD of the area in Fig.2.39a.

(c) Section of the CAD of figure 2.39b with an horizontal plane.

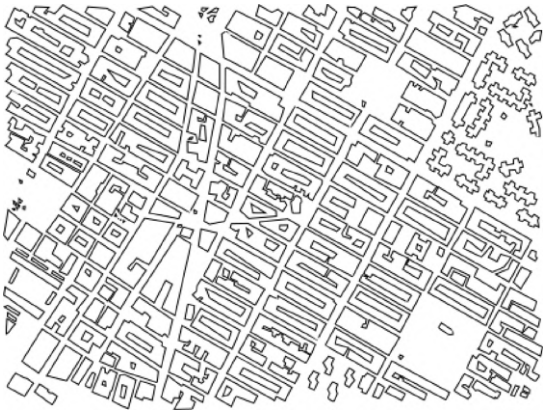

(d) Representation of the Occupancy map matrix of the area in Fig.2.39a.

Figure 2.39: maps relating to an area in New York City (NY). Picture 2.39a is an aerial view, Fig.2.39b shows the CAD obtained through OpenStreetMap [248], Fig.2.39c is a section of the CAD of figure 2.39b and a 5 meters height horizontal plane and 2.39d is the rapresentation of the occupancy map of the area of interest, represented in binary terms: '1' (black) represents the obstacle and'0' (white) free airspace.

2.4.2 No-Fly zone map evaluation

This section deals with the generation of the *no-fly zone* map that, together with the *occupancy map* discussed in the previous section, forms the 2D *flight allowed map*, one of the inputs that the path planner will exploit. The *'no-fly zone'* map is a two-dimensional location-based map showing the places, called the *no-fly zone*, where UAV flight is not allowed due to legal reasons. The *no-fly zone* areas are particular areas that, for safety reasons, cannot be flown over by any drone or for which a special authorization, not possessed at the time of overflight, is required. These bans can be permanent or event-based. The restricted airspace in Washington D.C. [108], Fig.2.40d, or the area within five miles of any airport, Fig.2.40b, represent examples of permanent bans. The temporary flight restrictions that authorities set up when they foresee an enormous influx of people or a VIP, represent event-based ban examples. The governing bodies or dedicated websites (for example, [29] or [96]) indicate these areas. The *'no-fly zone'* map information can only assume two values, as in the *occupancy map*. The value '0' indicates a flyover allowed area, while the value '1' indicates forbidden airspace. These numbers are compatible with those used in the *occupancy* map, where '0' shows a flyover allowed area and '1,' an obstacle. Each number refers to a square, typically (as also happens in this thesis) 1x1 square meter. Obtaining this map is relatively simple, as the air traffic authorities provide this information updated daily. Figure 2.40 shows some *no-fly zones*; data are provided by the DJI drone company [96]. Different colors indicate different types of restrictions;

- restricted zones: overflight is never allowed;
- altitude zones: overflight is allowed at an altitude below 300 meters;
- regulatory restricted zones: overflight is prohibited due to local regulations and policies.

Figures 2.41b and 2.42b show the areas the author has chosen for the thesis purposes and relative prohibitions. The airspace above the analyzed regions is crossed by the *altitude zone* connected to the Capodichino airport, serving Naples, and the New York Skyports Seaplane Base in New York. This restrictions turn not significant as the thesis will simulate low-flying drones, especially rotary-wing ones. This map can be modified mainly by introducing *temporary flight restrictions*, which the competent authorities can communicate in advance.

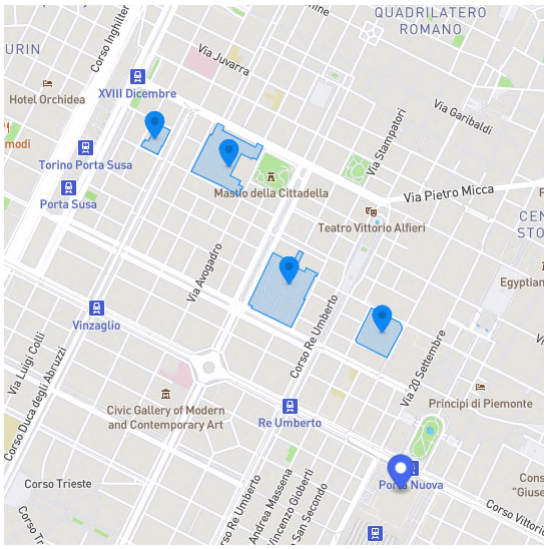

(a) *'no-fly zone'* map in the city of Turin, Italy. The ban is due to local regulations.

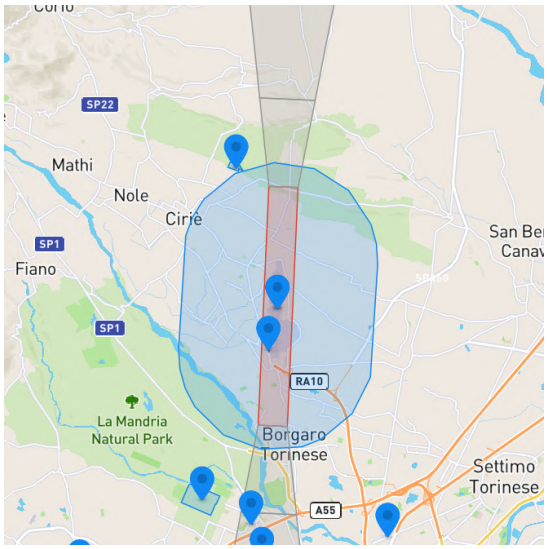

(b) *'no-fly zone'* map related to Caselle (TO) airport.

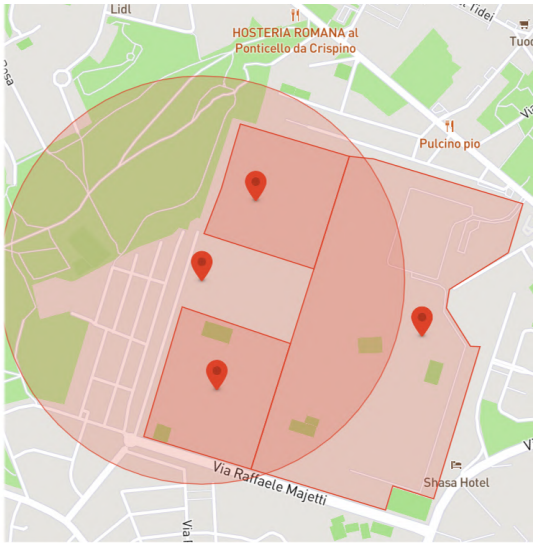

(c) Permanent *'no-fly zone'* related to Rebibbia prison, Rome, Italy.

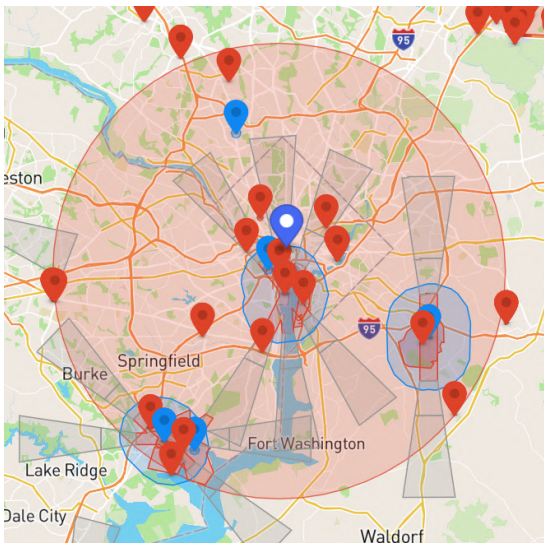

(d) Permanent *'no-fly zone'* related to District of Columbia, U.S.A.

Figure 2.40: different no-fly zones areas, data are provided by the drone company DJI [96].

(a) *'Medaglie d'oro'* square, Naples, Italy, aerial view.

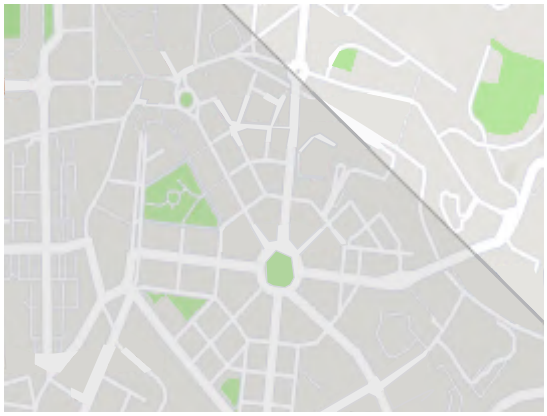

(b) Drone flight restriction related to the area in Fig.2.41a.

Figure 2.41: aerial view of one of the areas analyzed in this section, near piazza 'Medaglie d'Oro,' Naples, Italy in Fig.2.41a and the related *'no-fly zone,'* obtained through DJI [96] in Fig.2.41b. There is a darker area indicating an *altitude zone*.

(a) Part of New York City, NY aerial view.

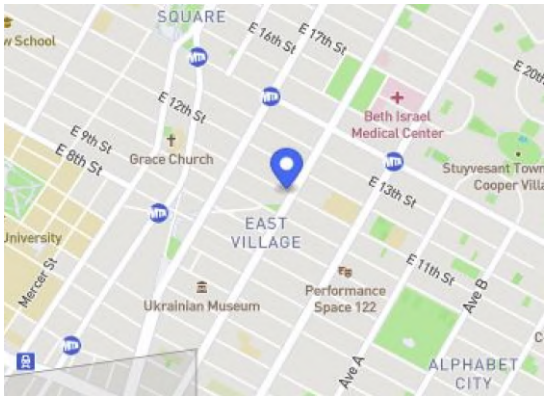

(b) Drone flight restriction related to the area in Fig.2.42a.

Figure 2.42: aerial view of one of the areas analyzed in this section, part of New York City (NY), in Fig.2.42a and the related *'no-fly zone,'* obtained through DJI [96] in Fig.2.42b; the analyzed area is affected by the altitude zone.

2.4.3 Buffer zone

Once obtained the *flight allowed* map the drone operates in (a map formed by the union of the *occupancy* and *no-fly zone* maps), it is necessary to enlarge the obstacles or forbidden areas to take into account the drone turning radius. The amount an obstacle is enlarged is called *buffer zone*, i.e., an area that enlarges the obstacle in all directions by an amount called *inflation radius*, as in figures 2.43 and 2.44. This step is essential as the path planner does not foresee the drone's trajectory; it only provides ordered way-points whose connecting segments do not touch the obstacles, Fig.2.45a. The path planner, then, could generate paths that the drone could hardly follow without hitting anything. The drone turning radius represents the smallest circular turn radius the drone is capable of. It takes into account some structural and aerodynamic characteristics. In this work, the turning radius is taken as *inflation radius*, as standard in the literature. By their nature, quadrotors have a zero minimum turning radius; they can also stop and hover while changing direction. The direction change requires a turn maneuver at cruise speed, and the turn radius can never be zero. The following formula expresses the minimum turning radius at a given rate [207] for drones using thrust to stay in the air, i.e., fixed-wing and rotary-wing drones:

$$R = \frac{V^2}{g\sqrt{n^2_{max} - 1}} \tag{2.12}$$

where

R [m] turning radius;

V [m/s] turning speed;

g [m/s^2] acceleration of gravity;

n_{max} maximum load factor.

The maximum load factor n_{max} is the maximum ratio between inertia forces and aircraft weight in the direction normal to the wing plane. The load factor is equal to 1 when the aircraft is static on the ground. The user can set the autopilot to decrease the drone speed when it expects a turn to reach a smaller R. According to graph 1.4c, the most likely cruising speed for a commercial fixed-wing drone is between 15 and 20 m/s. The 15 m/s value turns out to be the 80 percentile for fixed-wing models' speed, the same value that Table 1.1 provides. Rotating wing models have a lower cruising speed; according to graph 1.6c, 7 m/s represents the 90th percentile for the rotary-wing analyzed models speed, the same value Table 1.1 presents. The author of the thesis used these values to estimate the most probable speed for both types of drones and then the related turning radius or the *inflation radius*. [176] and [116] studied some drones' structural characteristics, including the load factor. As Tables 2.7 and 2.8 show, n_{max} is approximately 3.8 for both studies, equal to the classic maximum load factor in general aviation

aircraft. In the calculations, this paper suggests a very conservative n_{max} value equal to 2.

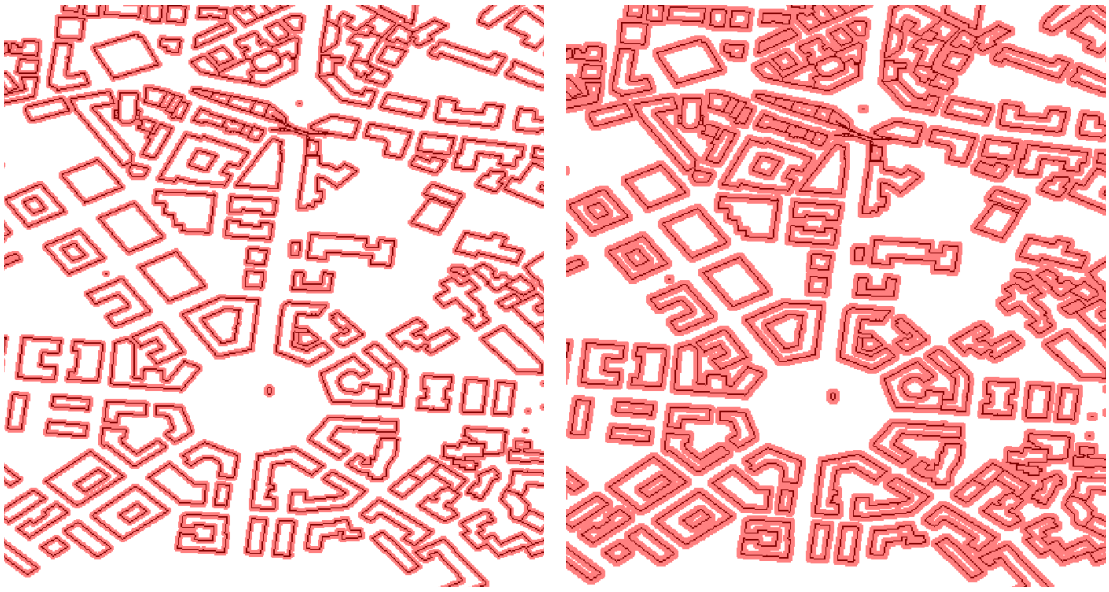

(a) *Inflation Radius* 2 meters. (b) *Inflation Radius* 3 meters.

Figure 2.43: *occupancy map* of the area near Medaglie d'Oro square, Naples, Italy. In red the *buffer zone* with a different *inflation radius* for each figure.

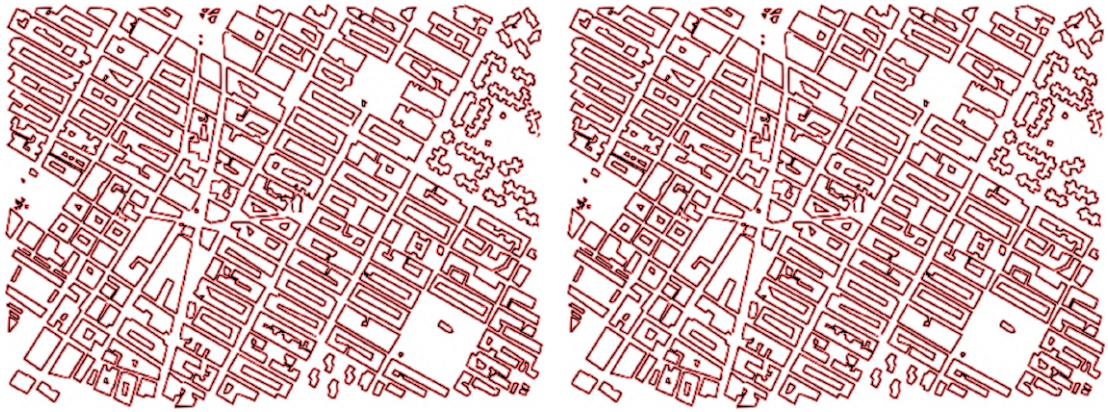

(a) *Inflation Radius* 2 meters. (b) *Inflation Radius* 3 meters.

Figure 2.44: *occupancy map* of the area in the East Village in New York City (NY). In red the *buffer zone* with a different *inflation radius* for each figure.

Figure 2.45b shows that the turning radius associated with the typical fixed-wing drones speed is too high to make them usable at building height. At 15 m/s, classical fixed-wing speed value, and n_{max} equal to 2, we obtain a turning radius of about 13

meters. At the same time, we obtain 3 meters as a turning radius for rotary-wing drones when flying at 7 m/s, typical cruise speed, and n_{max} equal to 2. It turns out that the rotary-wing drones are more appropriate to flight at buildings altitudes while fixed-wing drones do not.

Table 2.6

Table 2.7: data from Majka et al. [176].

Parameter	Value
Wing area	0.86 m^2
Gross weight	9.69 kg
Cruise speed	29.40 m/s
Stall speed	12.67 m/s
n_{max}	3.8

Table 2.8: data from Glizde et al. [116].

Parameter	Value
Wing area	0.98 m^2
Gross weight	7 kg
Cruise speed	26 m/s
Stall speed	8.5 m/s
n_{max}	3.75

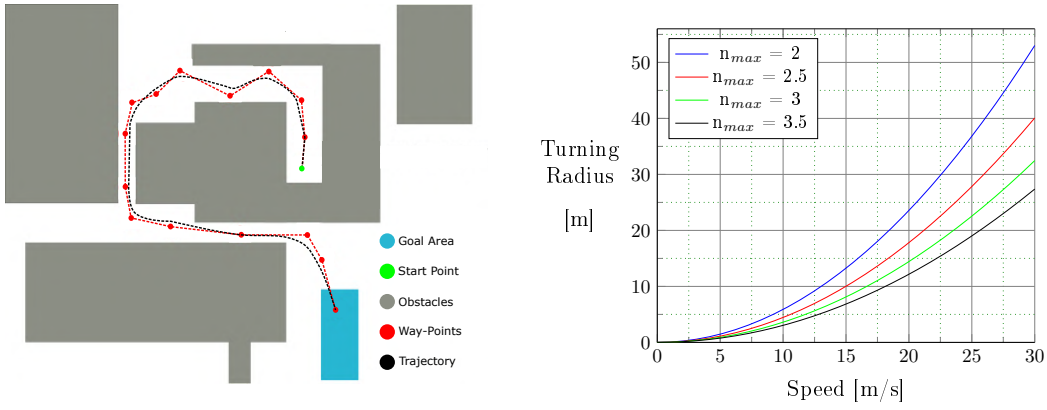

(a) (b)

Figure 2.45: 2.45a shows the path planner provided way-points and drone trajectory while 2.45b shows the fixed-wing drone turning radius as a speed function parameterized for different load factors, formula 2.12.

The evaluation of the turning radius for the airships is not well thorough in the literature. The US War Department in [88] provides an empirical LTA turning radius formula, valid for the classical configuration LTAs, with an engine configuration more suited for forwarding flight; the formula is the following:

$$R = \frac{L_b}{sin(2\gamma)} \tag{2.13}$$

where

- R = minimum turning radius [m];
- L_b = airship length [m];
- γ = angle of yaw [rad];

According to Table 1.1, the most common LTA drone length is 7 meters while the yaw angle is in the order of 10 degrees; using these values, Formula 2.13 returns a turning radius value of about 23 meters. This value, combined with their great inertia and wind sensibility, makes it possible to use these devices only at much higher than buildings altitudes. Rotary-wings drones can successfully deliver goods and fly at buildings height, but their low flight endurance and speed force them to operate on small distances.
Fixed-wing drones can fly faster and longer but can't perform at buildings height because of their excessive turning radius. They can't hover and then can not deliver almost anything. Airship drones have few practical uses; they can carry phone antennas simulating phone towers due to their long flight endurance. They find few applications in the urban environment, but rural-based missions can successfully exploit them.

2.5 Findings

This section analyzes the results of a series of simulations carried out using all the methodologies introduced in this chapter for two different scenarios. The aim is to show the practical slant of these introductions and, therefore, use them in realistic missions.
We analyzed the case of two rotary-wing drones with the same characteristics, Table 1.1, which operate in the areas examined in this chapter, namely 'Medaglie d'oro' in Naples, Italy, shown in Fig.2.38 and a part of New York City, NY, Fig.2.39. The mission the drones accomplish is traveling between the same two points. The author of the thesis has chosen the start and goal points to have high the two drones' chances to cross each other's path in the central part of the map, but this never happened. The missions concern four different risk levels, each relating to a different r_f, namely 0.25, 0.5, 0.75, and 3.5 (hypothetical LTA drone case) meters, with impact energy E_{imp} always equal to 1 kN. For each risk map, the author of the thesis has analyzed six cases of flight above buildings height, so the buildings are not obstacles, and only the risk is taken into account, and six at building height, so considering the risk and the building as obstacles. When flying at building height, the *inflation radius* introduced during the way-points generation phase was equal to 3 meters, as images 2.43b and 2.44b show.

As anticipated in section 2.1.1, the path planner has exploited a risk weight coefficient equal to 50 for all the missions analyzed. We can state the following: a risk weight increasing has the same effect as a risk increasing, so the images in this section can also represent the behavior of the path planner as the risk weight coefficient increases.
In the images of this section, the red and green lines represent realistic drones' trajectories, not the lines connecting the various way-points. The dynamic of the drones follows the 6 DOF autopilot model offered by the physical engine Gazebo [209], to which the path planner communicates the way-points.

Figure 2.62 shows the way-points output calculation time using an I5 6200 2.3 GHz processor for the two analyzed scenarios; the figure shows that the calculation time for the generation of way-points increases with increasing risk and introducing obstacles.

Now let's see how the path planner varies the generation of way-points as the boundary conditions vary.
In the former part of this section, we are going to analyze the missions related to the Naples area, figures 2.46 to 2.53, while in the latter one, we are going to analyze the missions related to New York area, figures 2.54 to 2.61.
Figure 2.46 shows a higher than buildings and very low-risk situation (Fig. 2.20f provides the risk map). The result is the generation of almost straight trajectories from the start to the goal points, within the RRT* algorithm limits, which does not produce an exact solution. Figure 2.47, which introduces the obstacles for the same risk map,

shows similar path planner behavior; it provides the shortest path. In these two images, the effect of risk is almost absent. As the risk increases (or the risk weight coefficient) increases, the drones' trajectory tends to lie more often in the less dangerous areas, becoming, in this mission, longer and longer. Figs.2.48 (higher than buildings mission) and 2.49 (buildings height mission) are related to the risk map that Fig.2.21f provides. The reader can see that the drone trajectories pass less often through the center of the square, preferring the surrounding areas at a lower risk. This trend is higher in Figs.2.50 (higher than buildings mission) and 2.51 (buildings height mission), whose risk map is provided by Fig.2.22f.
Figures 2.52 (higher than buildings mission) and 2.53 (buildings height mission), whose Fig.2.23f provides the risk map, represent the case of a particularly dangerous rotary-wing drone, with a risk level equal to that of a 7 meters long airship at one kJ energy at impact. It seems that the trajectory returns straight, but you can see how it passes over the low-risk areas deriving from the presence of the buildings; this passage, obviously, dramatically lowers the total risk of the trajectory.

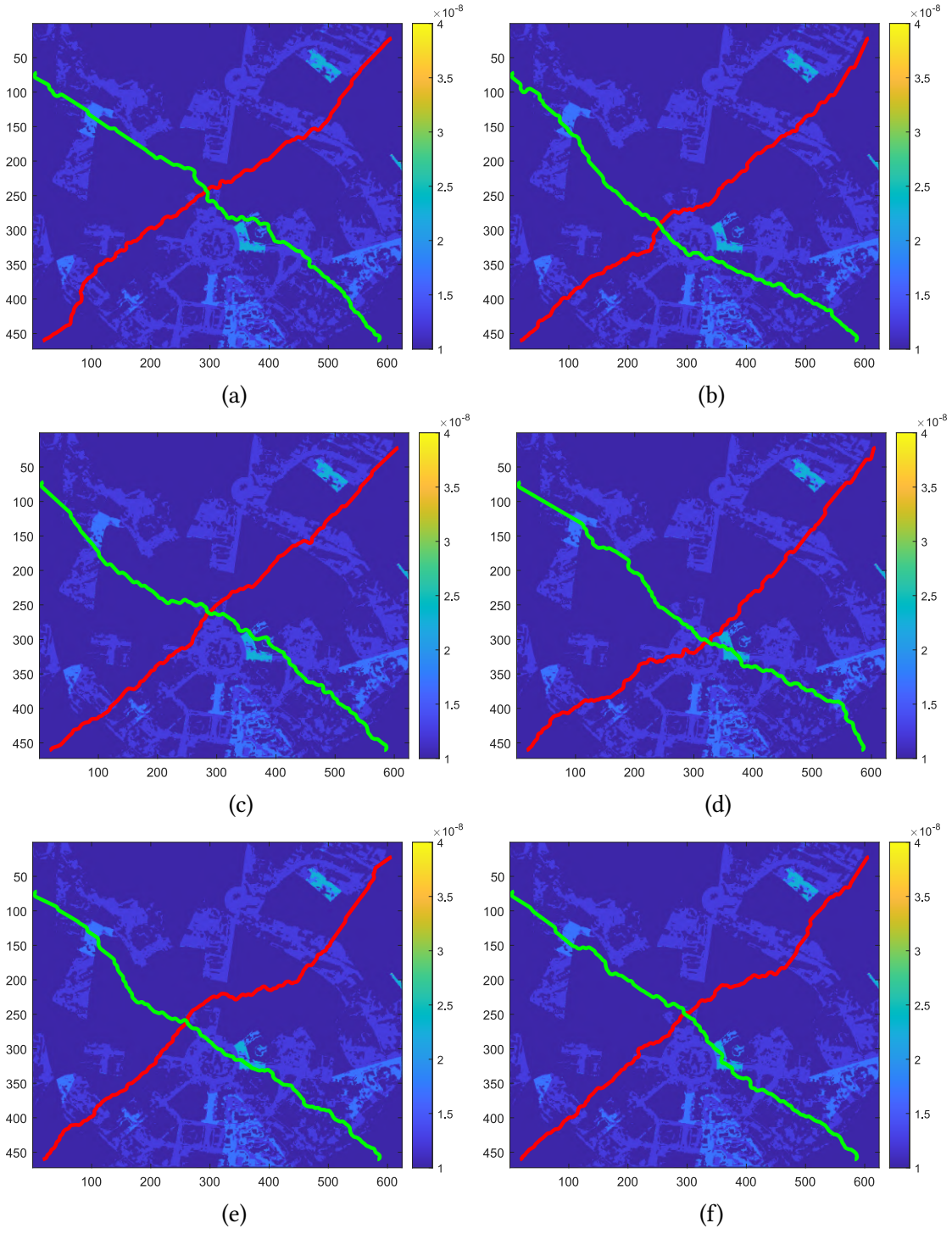

Figure 2.46: figures 2.46a - 2.46f represent simulations related to the case r_f=0.25 m, E_{imp}=1000 N, in the Naples area, with no obstacles.

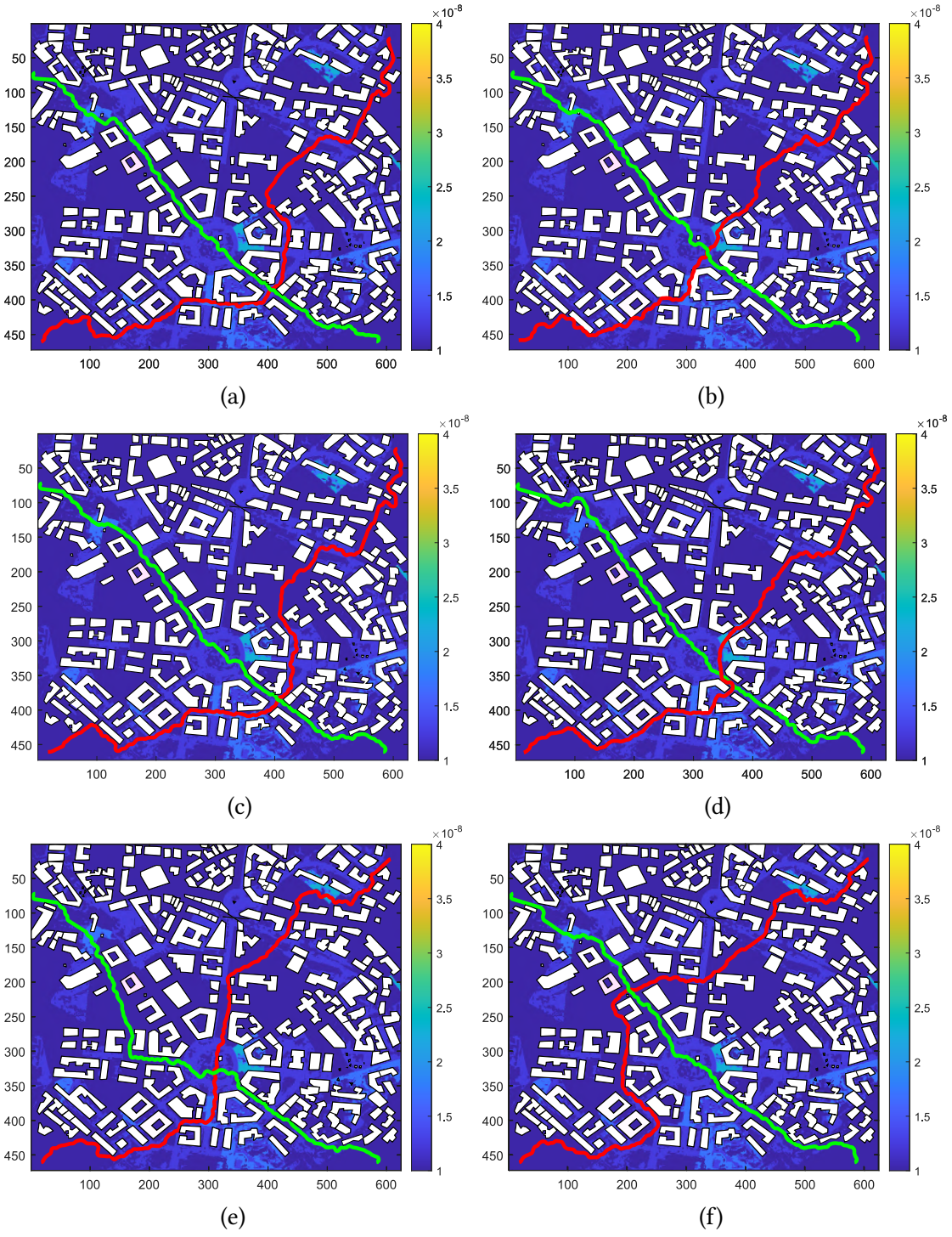

Figure 2.47: figures 2.47a - 2.47f represent simulations related to the case r_f=0.25 m, E_{imp}=1000 N, in the Naples area, obstacles at 15 m height considered.

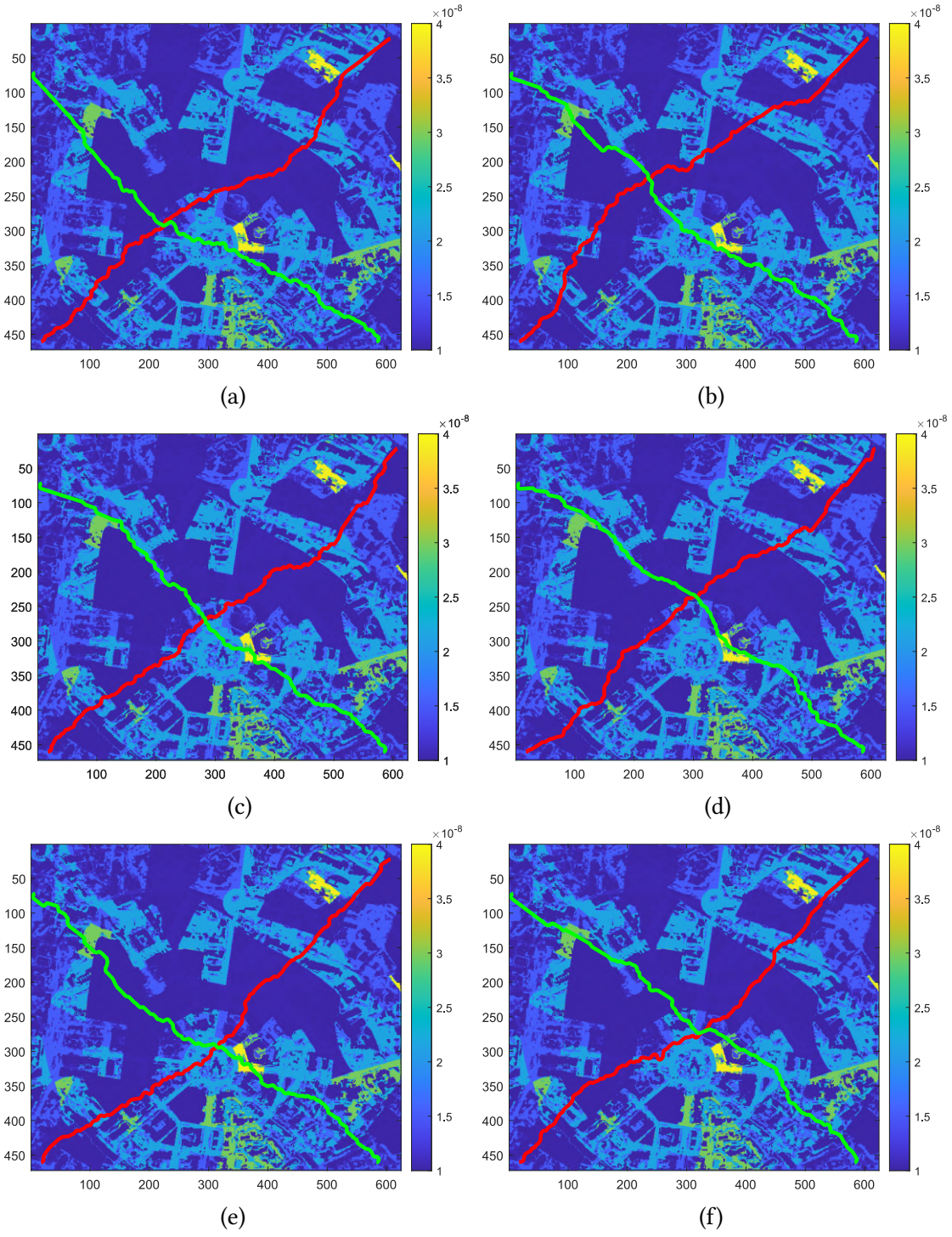

Figure 2.48: figures 2.48a - 2.48f represent simulations related to the case r_f=0.5 m, E_{imp}=1000 N, in the Naples area, with no obstacles.

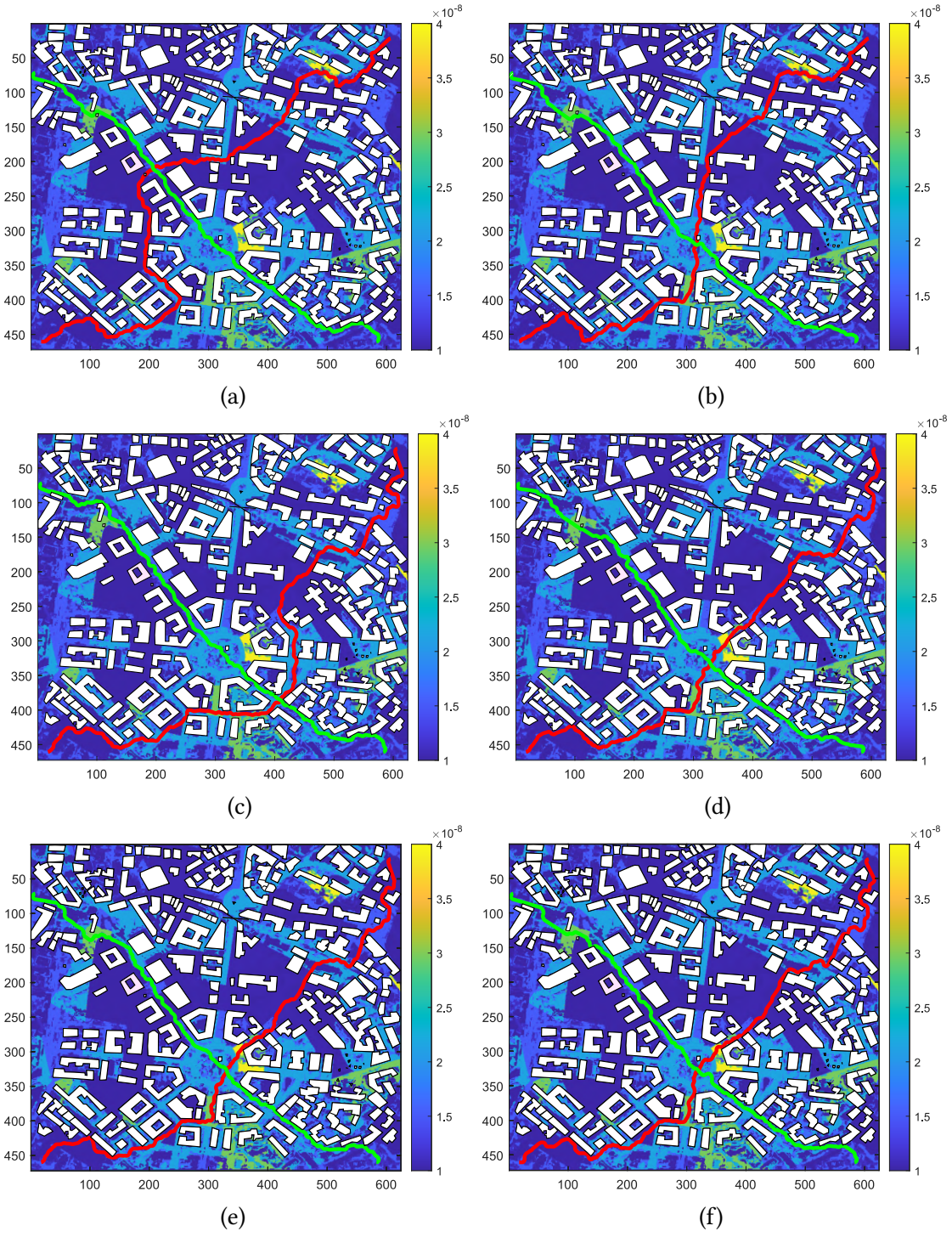

Figure 2.49: figures 2.49a - 2.49f represent simulations related to the case r_f=0.5 m, E_{imp}=1000 N, in the Naples area, obstacles at 15 m height considered.

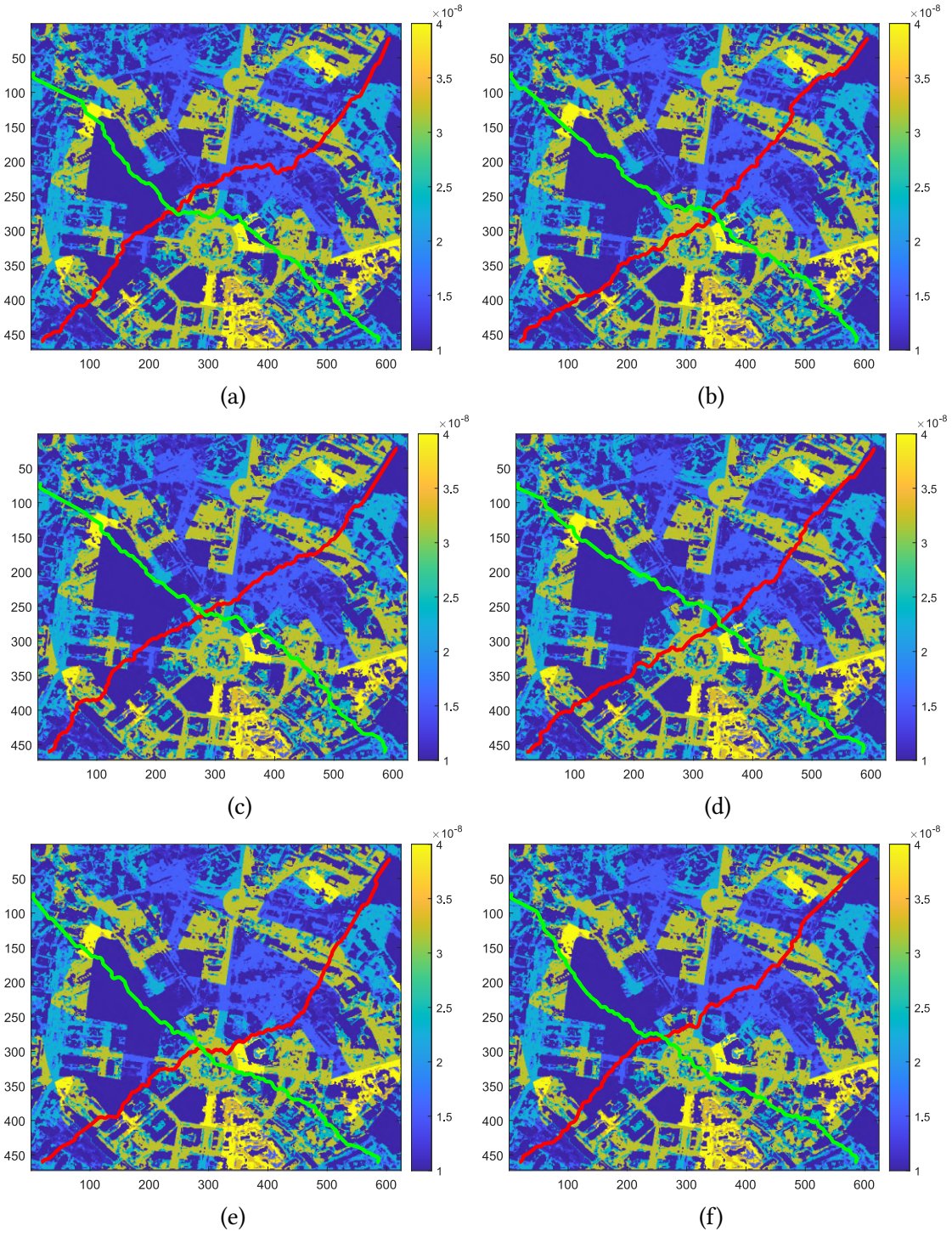

Figure 2.50: figures 2.50a - 2.50f represent simulations related to the case r_f=0.75 m, E_{imp}=1000 N, in the Naples area, with no obstacles.

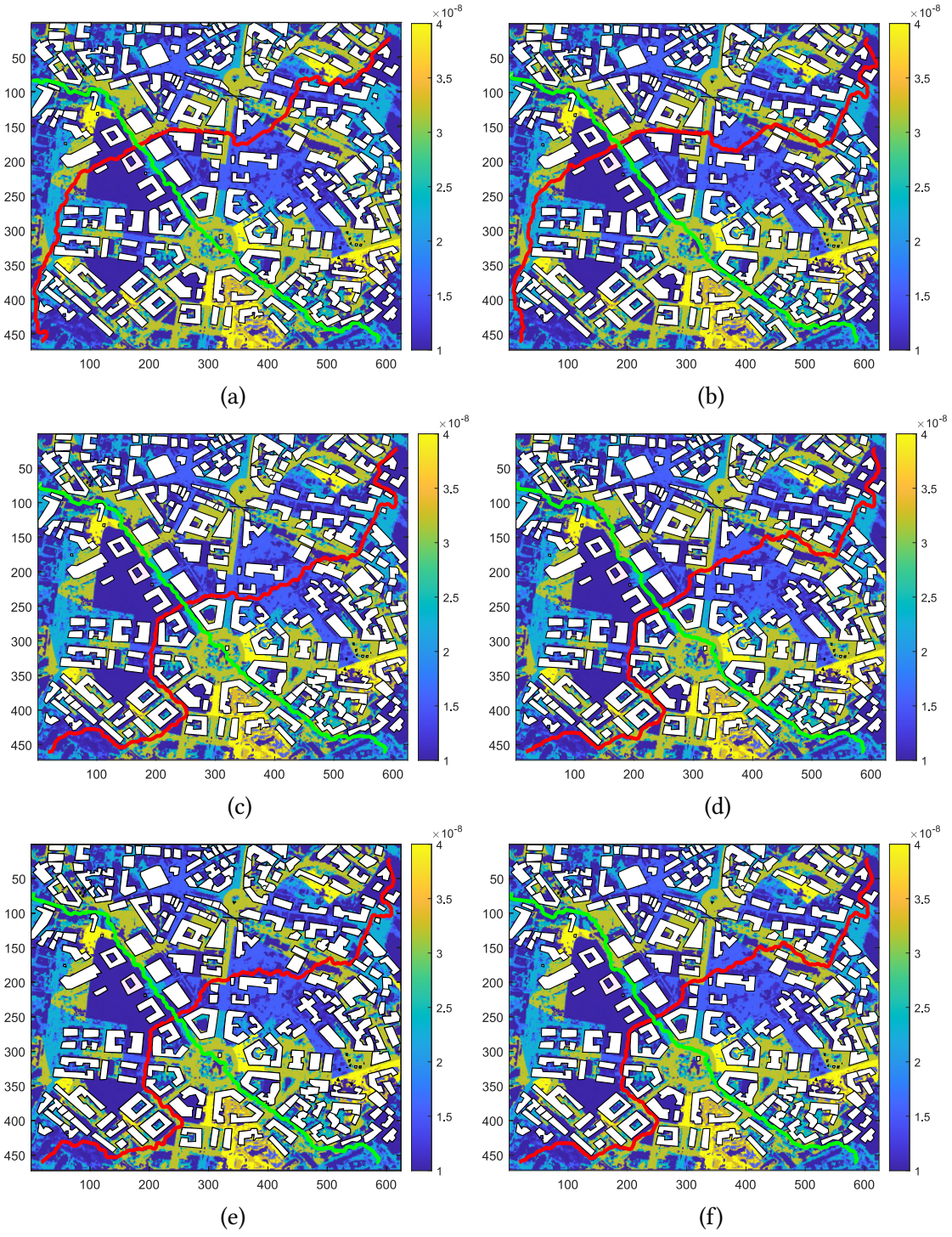

Figure 2.51: figures 2.51a - 2.51f represent simulations related to the case r_f=0.75 m, E_{imp}=1000 N, in the Naples area, obstacles at 15 m height considered.

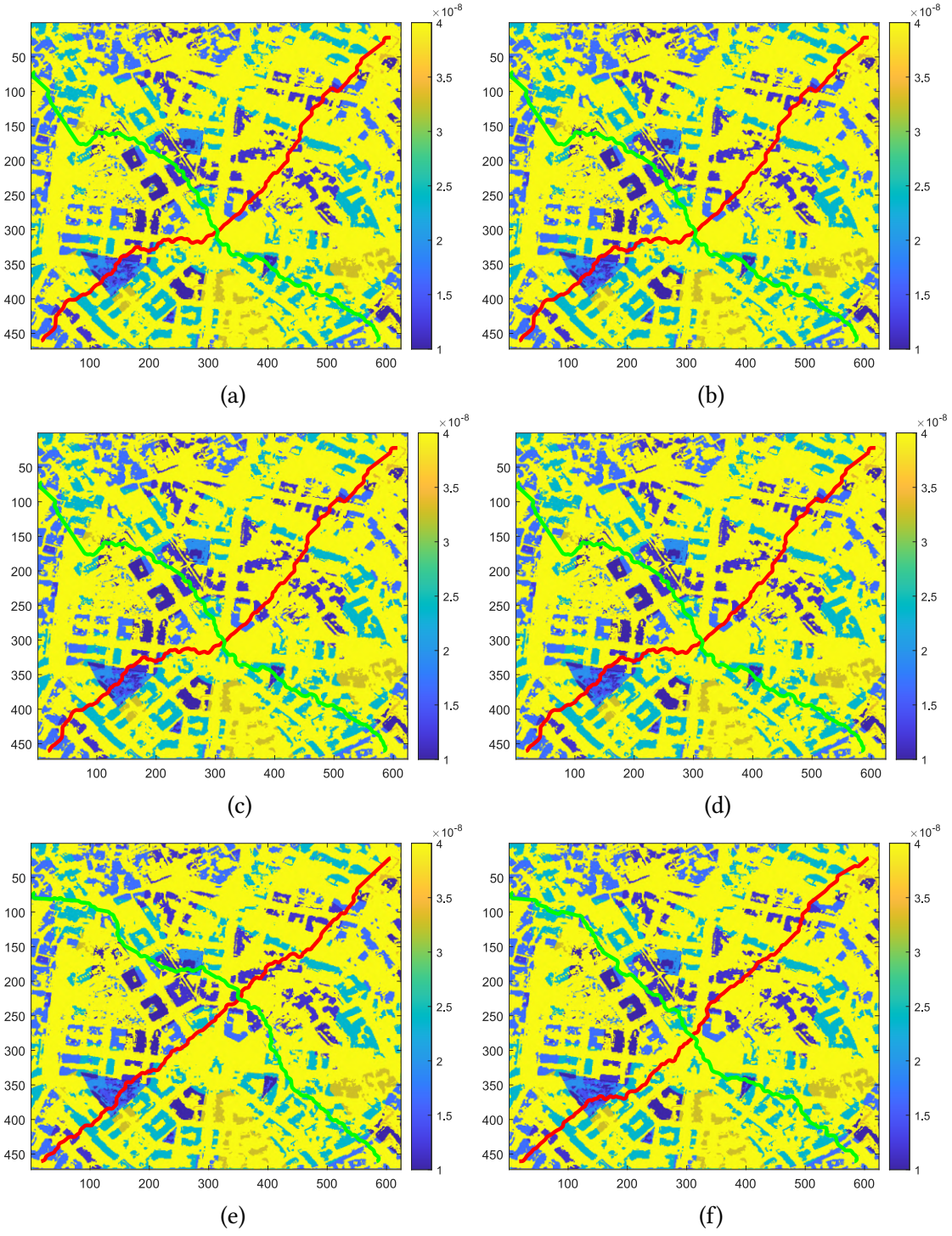

Figure 2.52: figures 2.52a - 2.52f represent simulations related to the case r_f=3.5 m, E_{imp}=1000 N, in the Naples area, with no obstacles.

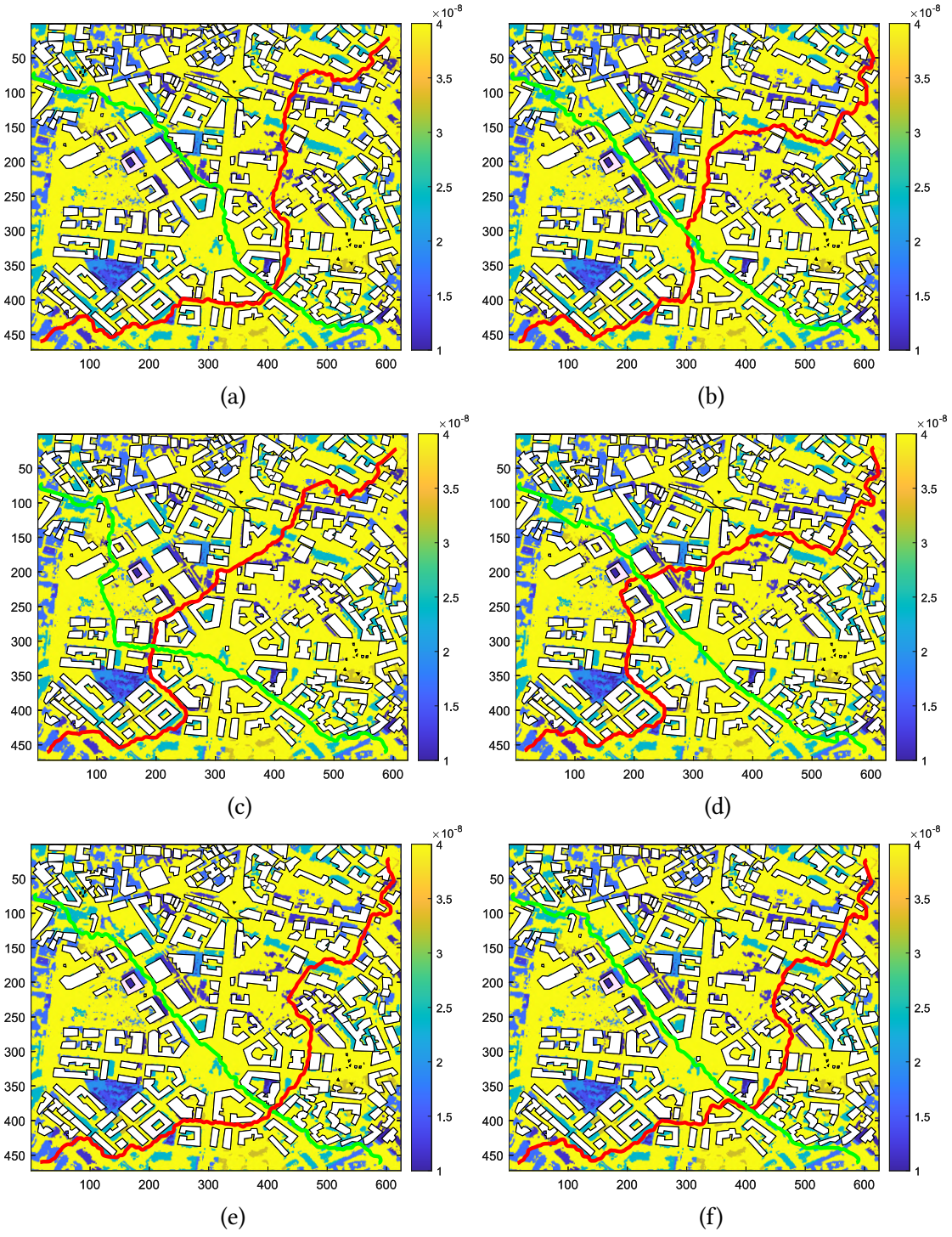

Figure 2.53: figures 2.53a - 2.53f represent simulations related to the case r_f=3.5 m, E_{imp}=1000 N, in the Naples area, obstacles at 15 m height considered.

In this part of the section, we are going to analyze the results of the missions based in the East Village of New York City (NY). In these missions, we can see a more uniform distribution of the risk, and this fact leads to the different behavior of the paths compared to the missions in the Naples area.

Figure 2.54 shows a higher than buildings and very low-risk situation (Fig.2.29f provides the risk map). Even in this case, the result is the generation of almost straight trajectories from the start to the goal points, within the RRT* algorithm limits, which does not produce an exact solution. Figure 2.55, which introduces the obstacles for the same risk map, provides the shortest path. In these two images, the effect of risk is almost absent. As the risk increases, the drones' trajectory should tend to lie more often in the less dangerous areas.

Figs.2.56 (higher than buildings mission) and 2.57 (buildings height mission) are related to the risk map that Fig.2.30f provides. Due to the particular risk map, the behavior of these two figures is very similar to the conduct of the previous ones. This behavior is because the risk map doesn't show significant areas of high risk; even the mainly higher risk zones have smaller low-risk areas. For this reason, the path planner provides paths that seem to go through the higher risk zones but actually cross all the tiny low-risk areas. The results are almost straight trajectories. The reader can see the same behavior in all the paths in New York area, figures 2.58 to 2.32f; the path planner provides an almost straight path that actually crosses the small low-risk areas. For this reason, all the paths related to New York area, seem to not take into account the different risk levels.

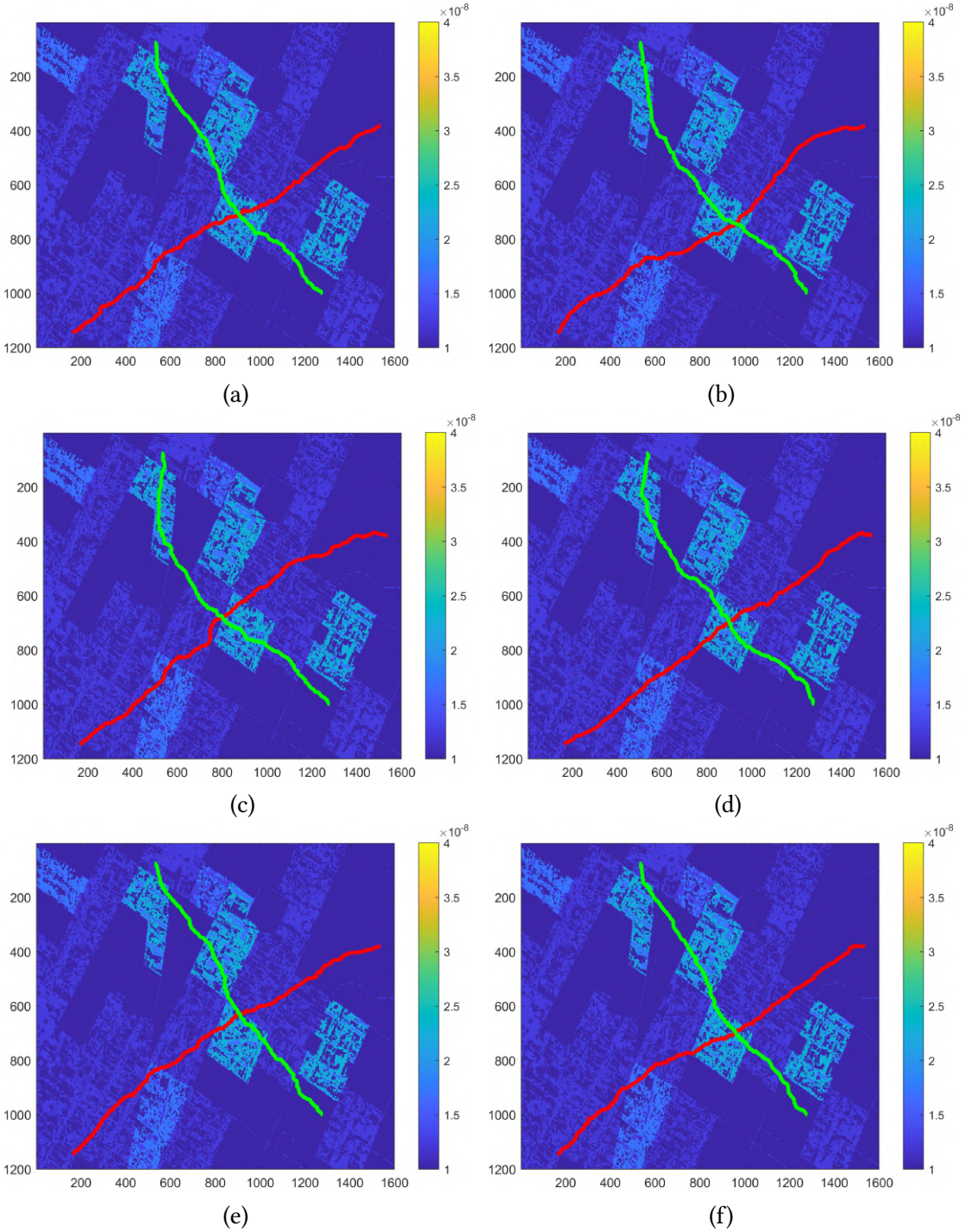

Figure 2.54: figures 2.54a - 2.54f represent simulations related to the case r_f=0.25 m, E_{imp}=1000 N, in New York area, with no obstacles.

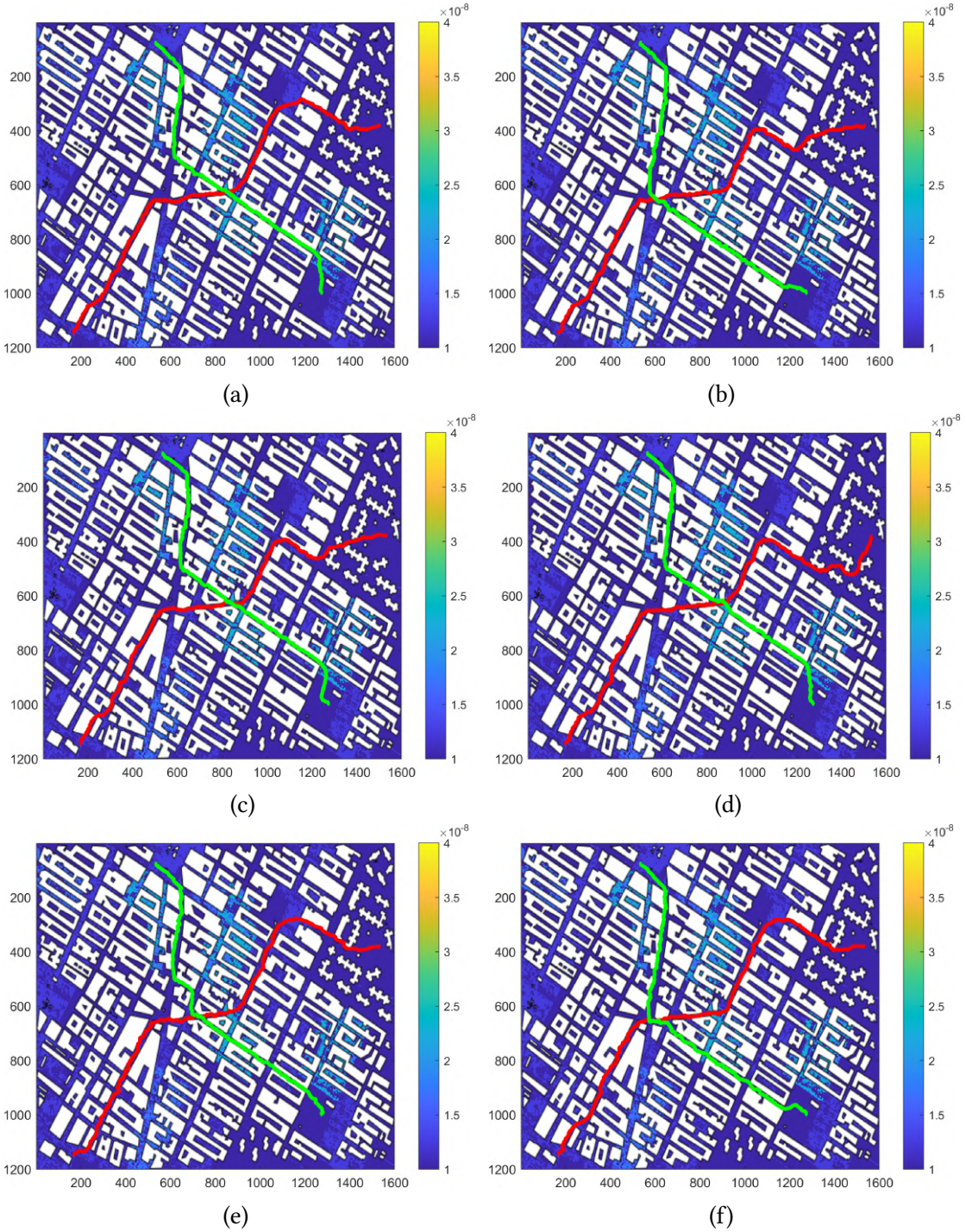

Figure 2.55: figures 2.55a - 2.55f represent simulations related to the case r_f=0.25 m, E_{imp}=1000 N, in New York area, obstacles at 15 m height considered.

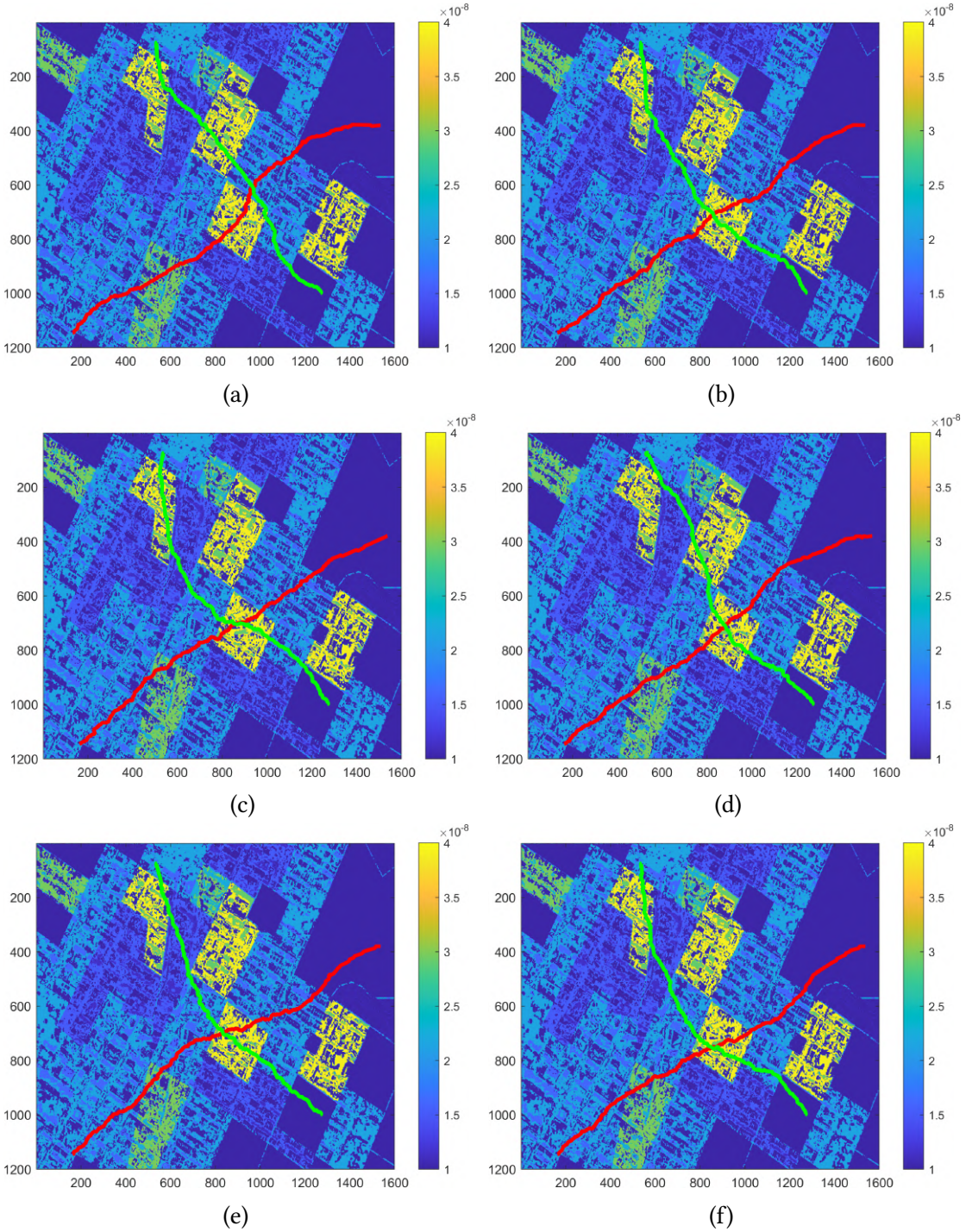

Figure 2.56: figures 2.56a - 2.56f represent simulations related to the case r_f=0.5 m, E_{imp}=1000 N, in New York area, with no obstacles.

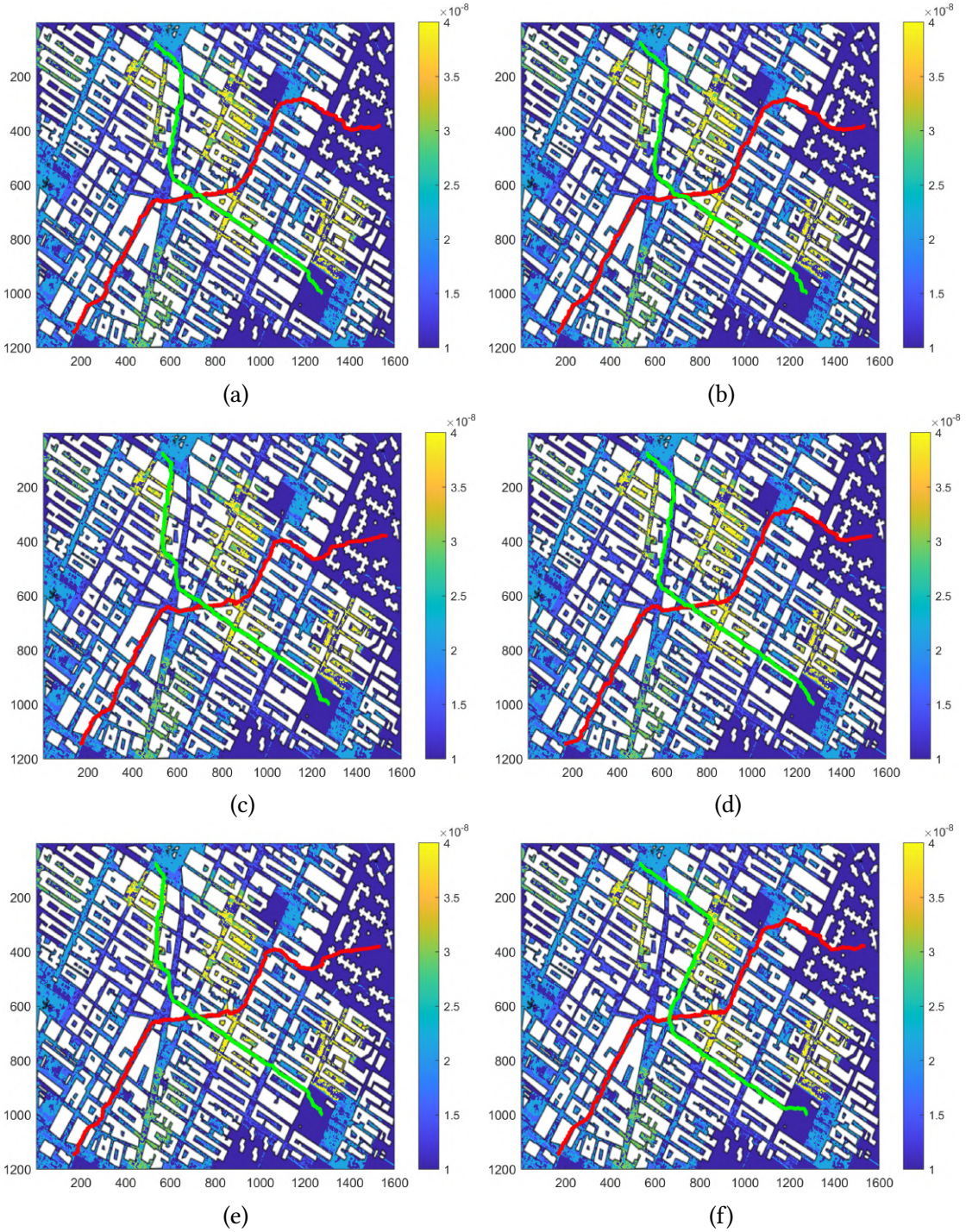

Figure 2.57: figures 2.57a - 2.57f represent simulations related to the case r_f=0.5 m, E_{imp}=1000 N, in New York area, obstacles at 15 m height considered.

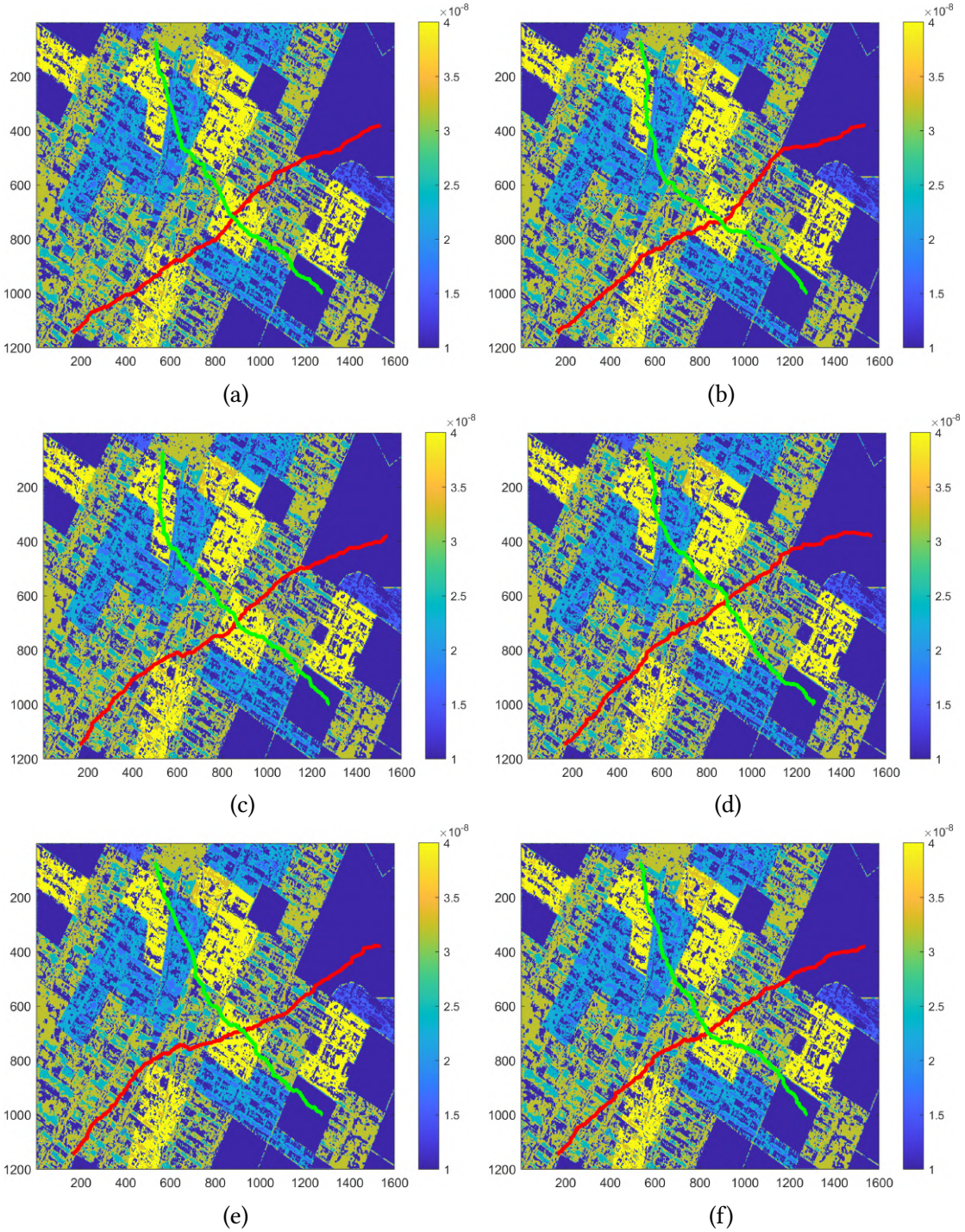

Figure 2.58: figures 2.58a - 2.58f represent simulations related to the case r_f=0.75 m, E_{imp}=1000 N, in New York area, with no obstacles.

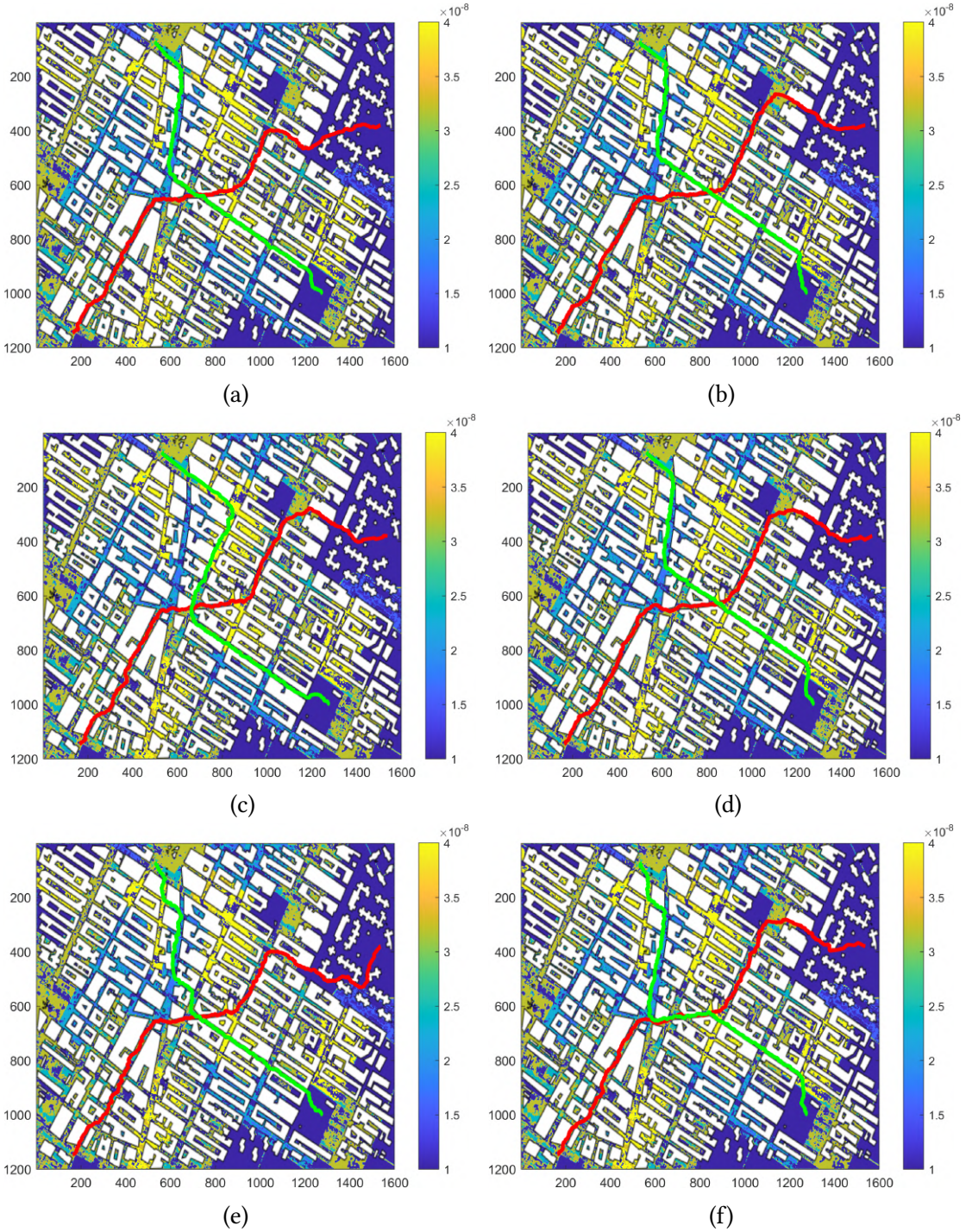

Figure 2.59: figures 2.59a - 2.59f represent simulations related to the case r_f=0.75 m, E_{imp}=1000 N, in New York area, obstacles at 15 m height considered.

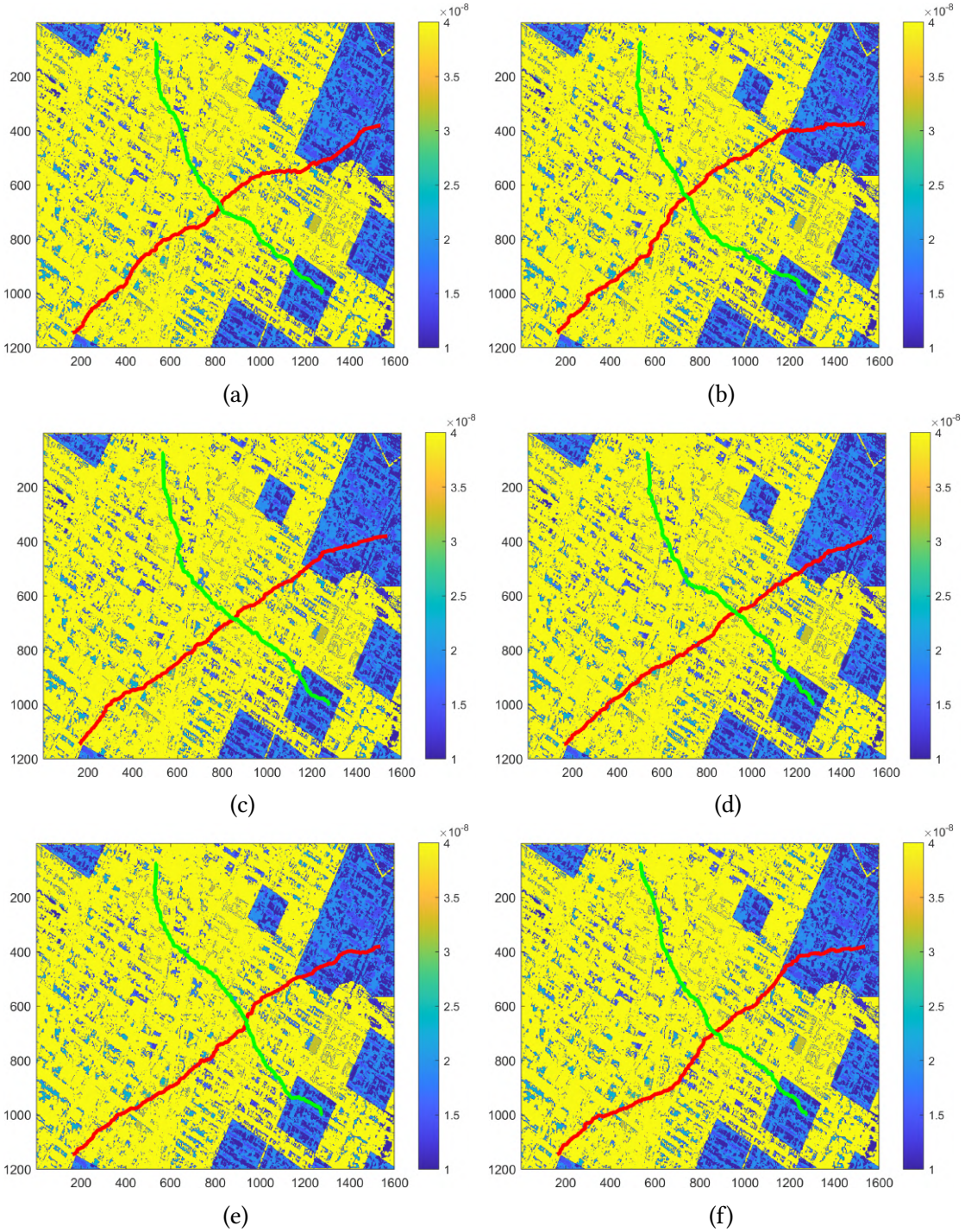

Figure 2.60: figures 2.60a - 2.60f represent simulations related to the case r_f=3.5 m, E_{imp}=1000 N, in New York area, with no obstacles.

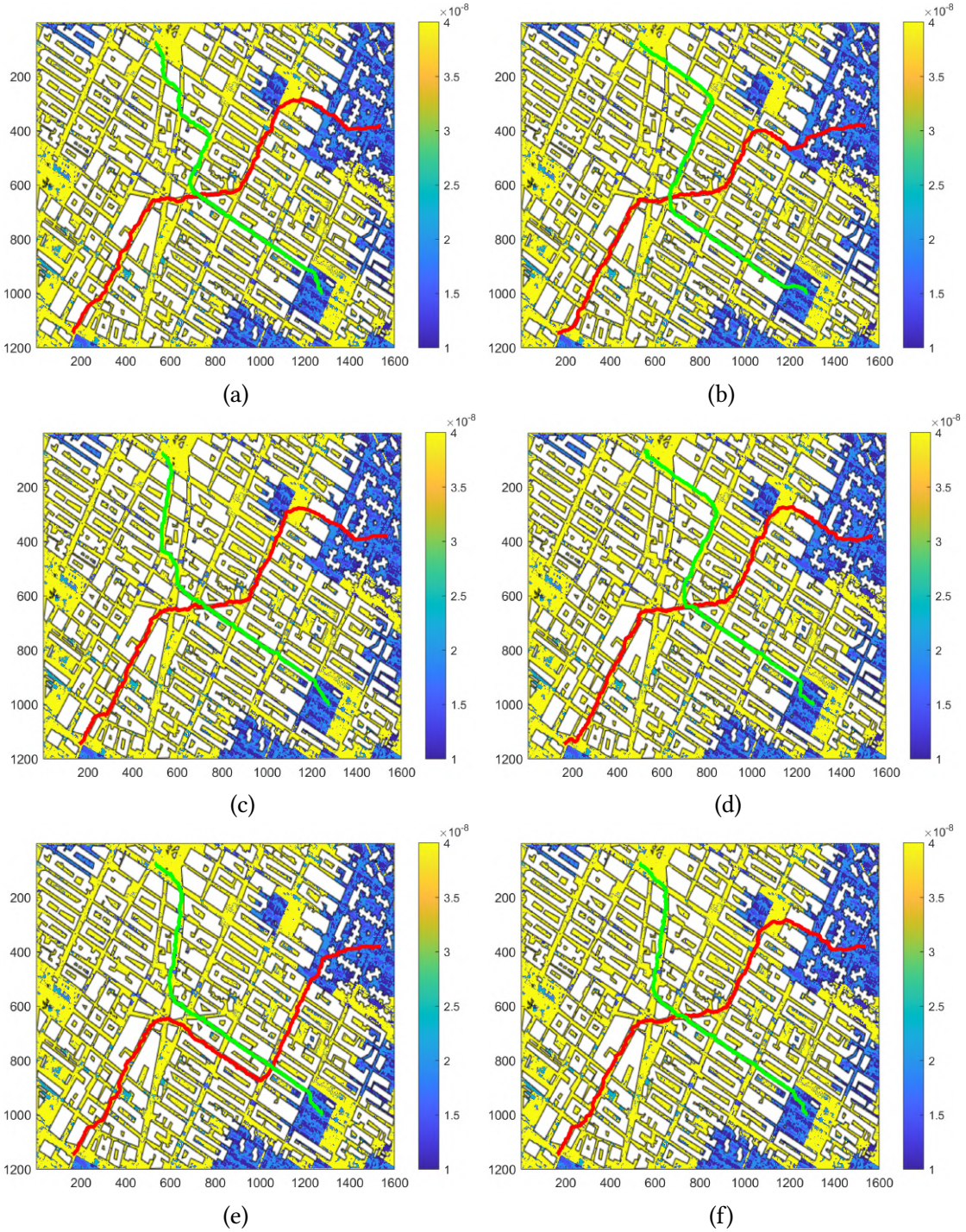

Figure 2.61: figures 2.61a - 2.61f represent simulations related to the case r_f=3.5 m, E_{imp}=1000 N, in New York area, obstacles at 15 m height considered.

Fig.2.62 shows the time the computer used in this thesis (characteristics in Table 3.3) needed to produce the results of this section. More performing computers can significantly reduce the calculation time and, therefore, not represent a real mission's bottleneck problem. Thus, the real-time path planning parameter would be maintained at any level of risk introduced. The scenarios analyzed in this thesis were chosen on a purely random basis. Therefore, they do not represent a more straightforward scenario than others. The size of the scenario surface was dictated by the hardware available; the maximum manageable size was chosen.

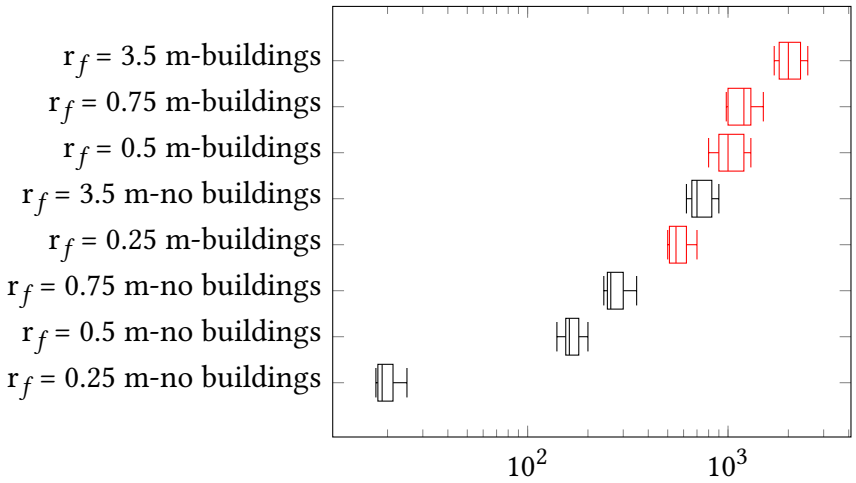

(a) computational time needed for the simulation related to Naples area.

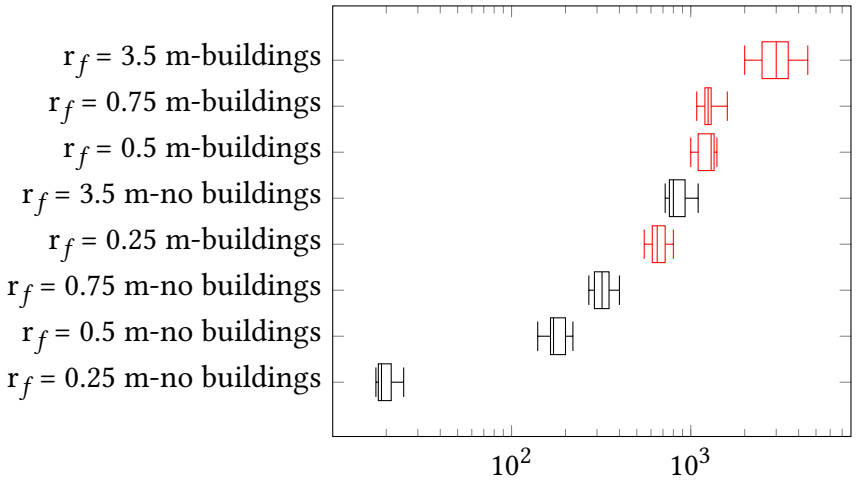

(b) computational time needed for the simulation in New York (NY) area.

Figure 2.62: Average computational time needed for the RRT* simulations related to the two scenarios analyzed in this thesis.

Chapter 3

Setup of the simulation environment

This chapter represents the final part of the thesis and is divided into two parts. The first analyzes the reliability of the libraries used to simulate the drone's battery and propulsion system, while the second part will introduce and simulate the architecture that for the author could lead the drones to perform a commercially reasonable service in an urban environment, taking advantage of the innovations introduced in the previous chapter. Table 3.1 briefly recaps the major specifications of the drones exploited in this chapter.

Table 3.1: drone type and their characteristics exploited in the simulation.

Type	Maximum Length	Speed	Weight	Flight Endurance	Turning Radius
Fixed wing	1.5 m	15 m/s	2 kg	45 min	13 m (n_{max}=2)
Rotary wing	0.5 m	7 m/s	2 kg	25 min	3 m (n_{max}=2)

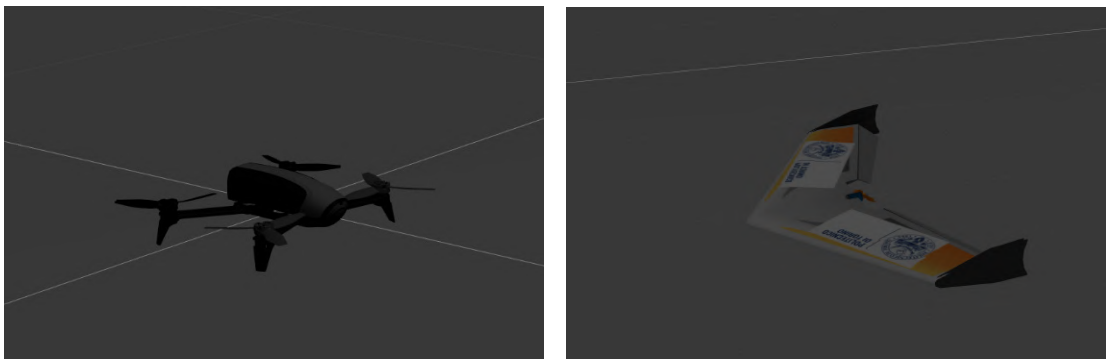

Figure 3.1: rotary-wing, Fig.3.1a, and a fixed-wing drone model, Fig.3.1b exploited in the simulation.

3.1 Drone Propulsion System simulation

This paragraph analyzes the mathematical model exploited by the software simulating the drone's propulsion system. This analysis turned out necessary to evaluate the degree of reliability of the whole simulation, which has led to inevitable simplifications. The author will show if the simplifications adopted for the propulsive part of the drone -composed of the battery, ESC, and propeller- are acceptable or not. This analysis will use experimental data and formulas widely shared by the scientific community. The adopted methodology is to verify the relative magnitude of the energy losses not considered in the mathematical adopted model. Two Gazebo libraries have been analyzed and compared with other alternatives; '*brass_gazebo_battery.cpp*' [150] (section 3.1.2) for the battery simulation and *'gazebo_motor_model.cpp'* [106] for the simulation of propulsive drone system (section 3.1.3).

3.1.1 Exploited software

As already mentioned, this thesis uses the open-source Gazebo [209] and the proprietary Matlab [177] programs. Gazebo libraries make it suitable for unmanned systems, simulating complex 3D environments as well. It can use a list of different physical libraries see Table 3.2; they are slightly different and better suit different scenarios. The ODE library [242] is the default one, and offers a good trade-off between computational time and quality of the results. Gazebo exploits CAD models obtained through a vast series of tools (open-source as well as Blender [50], used in this thesis). This section uses data from the manufacturer, obtained statistically or via sample analysis (Tables 3.4 and 3.6).

Table 3.2: physical simulation engines used by Gazebo programs [209].

	Contact	Joint Damping	Coordinates	Obj Stacking
ODE [242]	Rigid/Impulse	Implicit or Explicit	Maximal	0.4
DART[163]	Rigid/Impulse	Implicit	Generalized	1.1
Bullet [73]	Rigid/Impulse	Explicit	Maximal	0.5
Simbody [280]	Rigid/Force	Implicit	Generalized	>100

Table 3.3 summarizes the primary data of the exploited desktop. The machine is assembled to obtain reliable performance, following the guidelines of both Matlab [178] and Gazebo [69].

Table 3.3: characteristics of the desktop used in this work.

CPU Model	Intel i5-3470 @ 3.20GHz	Ram	4 Gb DDR3 @ 1330 MHz
OS	Ubuntu 16.04.6 LTS	GPU	Mining-p104-4g @ 1.6 GHz

The following sections are going to analyze the error made using some of the most common physical available propulsion-related Gazebo libraries. In particular, the author examined the models of the Li-Po battery (section 3.1.2) and the propulsive drone system (section 3.1.3), comparing the results with more reliable models or sources. The purpose of this paragraph is to validate the Gazebo exploited models, evaluating that the error is acceptable.

3.1.2 Li-Po Battery Simulation

The battery is the energy source for the propulsion system, payloads, and systems onboard the drone. The analysis of the drone flight duration is essential in order to design the missions correctly. Being clear about the battery characteristics is necessary for this purpose, and this is the goal of this section. The battery management system is tasked with controlling the charging and discharging phase of the battery and estimating the energy stored in the battery at any given time accurately. The available capacity is called the State Of Charge (SOC). The estimation of the SOC is vital when managing drones.
For the Li-Po batteries, it turns out that the *'open circuit battery'* model, the one Gazebo library uses, is both accurate and straightforward to use [164]. The literature shows that this model reflects very well the conditions within regular use of the battery ([130] and [274]), even without taking into account the aging (mainly the decreasing of the maximum capacity [42]), self-discharging and thermal effects (higher battery capacity at higher temperatures [175]). This section evaluates the error committed and the advantage in the computational time obtained using the open circuit battery based library proposed by Gazebo. The focus was only on the typically used onboard drones Li-Po batteries whose characteristics Table 3.4 summarizes.

Table 3.4: the main data of the batteries exploited for the comparison of the battery model by Matlab [187] and Gazebo [150] programs.

Battery Model	Nominal Voltage	Lin. Coeff.	Discharge Current	Batt. Resistance
A123 Li-ion [172]	3.22 V	6Ω	1.95 A	2mΩ
CGR18650AF [215]	3.6 V	12 Ω	1.95 A	10mΩ
CGR17500 [216]	3.7 V	11.7 Ω	2.15 A	1.5mΩ
Lumier 205 [115]	3.7 V	5 Ω	2.15A	1mΩ
SR674361P [190]	3.7 V	13 Ω	2 A	160 mΩ
803048 [188]	3.7 V	6 Ω	2A	130 mΩ
LP523040 [171]	3.7 V	13 Ω	2.9 A	200 mΩ
LP523040 [171]	3.7 V	15 Ω	2.75 A	200 mΩ

Gazebo Battery Model

UAV field widely uses the *lithium polymer* (Li-Po) battery [253]. Compared to the other civil grade ones, higher capacity per unit mass characterizes those batteries [283]; moreover, the literature has deeply analyzed them. This section examines the package Gazebo uses the most to simulate a Li-Po battery comparing the results with a more complex and reliable Matlab function.
The Gazebo package is called '*brass_gazebo_battery.cpp*' [150], based on the *open-circuit battery model*. The Matlab function *"power converter-based electrochemical battery emulator"* [187] provides a valid model for a comparison (see Fig.3.2). The duration of

the battery discharge phase is both a power demanded and the battery capacity function. A battery has to be suitable for the required operating current. The C-rate number is significant in evaluating the maximum safety battery discharge rate [112]. The '*brass_gazebo_battery.cpp*' package always supposes a battery suitable for the onboard payload, with appropriate C-rate. The following equation bonds the instantaneous required current to the actual battery capacity:

$$\mathrm{Q} = \text{Battery Nominal Capacity} - \sum_{n=1}^{N} \mathrm{I}(n)\Delta t \tag{3.1}$$

The instantaneous required current depends on both the instantaneous power needed and battery voltage, while the battery state of charge (the level of charge of an electric battery relative to its capacity, indicated as SOC) determines the battery voltage (Eq.3.2). The '*brass_gazebo_battery.cpp*' package uses the system of equations 3.2, shown in Fig.3.2 for this purpose.

$$\begin{cases} \mathrm{I}(n+1) = \dfrac{\mathrm{P}(n)}{\mathrm{V}(\mathrm{SOC}(n))} \\ \mathrm{SOC}(n+1) = 1 - \sum_{0}^{n} \dfrac{\mathrm{I}(n)\Delta t}{\text{Battery Nominal Capacity}} \\ \mathrm{V}(n+1) = \mathrm{V}_0 - \dfrac{\mathrm{K}\cdot\mathrm{Q}(\mathrm{n})}{\mathrm{Q}(\mathrm{n}) - \mathrm{i}^*}\mathrm{i}(\mathrm{n}) - \mathrm{R}\cdot\mathrm{i}(\mathrm{n}) \end{cases} \tag{3.2}$$

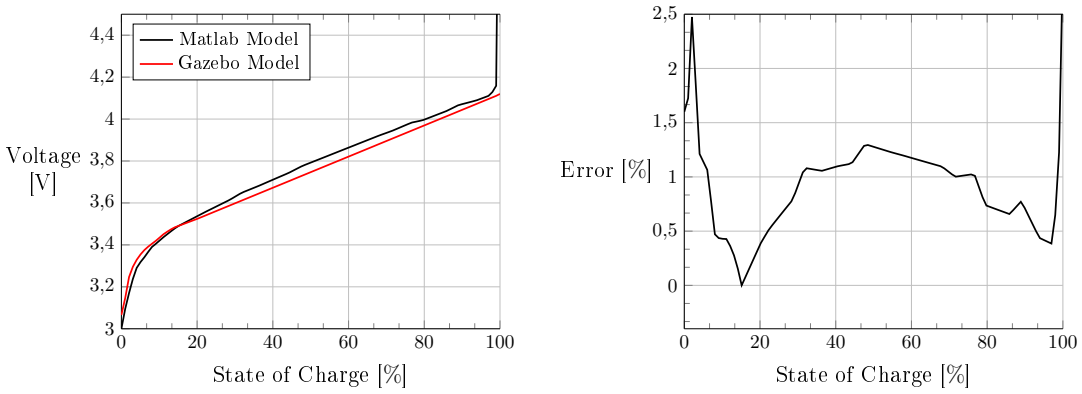

(a) (b)

Figure 3.2: Fig.3.2a shows the battery voltage vs. SOC for the Gazebo and Matlab model related to the battery SR674361P [190], working very far from critical conditions and at room temperature. Fig.3.2b shows the mean error between the two models.

The Matlab-based *"power converter-based electrochemical battery emulator"* is a more complex tool; it also considers the surface battery temperature and the required amperage via an empirical model. In the analyzed case, the battery is supposed at room temperature, and the needed current is much lower than the maximum sustainable one.

Yet the deviation turns out to be minor, as Fig.3.2b and Table 3.5 point out, less than 5%. Only in a small area close to SOC 100%, the difference becomes significant. From the comparison, the author considers using the Gazebo battery library suitable for a reasonable simulation. Table 3.5 shows that the time required by these two packages is different. The difference arises from the diverse nature of the two programs and is in line with similar other comparisons [138].

Table 3.5: comparison of the battery analysis time performance offered by Matlab [187] and Gazebo [150], based libraries on the desktop described in Table 3.3.

N_{cells}	State of Charge (SOC)	Required Power [W]	$\frac{Matlab_{Time}}{Gazebo_{Time}}$	Max Error
2	100%	35	30%	2%
2	85%	35	29%	4%
2	70%	35	29%	3%
2	50%	35	31%	3%
2	30%	35	31%	4%
2	20%	35	31%	5%
3	100%	60	30%	3%
3	85%	60	30%	5%
3	70%	60	28%	5%
3	50%	60	29%	4%
3	30%	60	29%	4%
3	20%	60	29%	6%
4	100%	100	31%	5%
4	85%	100	25%	7%
4	70%	100	25%	7%
4	50%	100	31%	5%
4	30%	100	31%	8%
4	20%	100	31%	6%

3.1.3 Motor and propulsion system simulation

The propulsion system represents the primary drone energy expenditure [260]. It is necessary to pay close attention to the propulsion system modeling and its energy demand to have good SOC reliability. A dedicated but numerically costly model could not be an advantage. The ideal is a reliable model (around 5% of error [139]), which guarantees little calculation time. The '*gazebo_motor_model.cpp*' [106] is the most used package in simulating the drone propulsion system in Gazebo environment, Fig.3.3. This section analyzes its accuracy and time saving compared to another solution. *gazebo_motor_model.cpp* simulates a system composed of a motor, ESC (Electronic Speed Control), and propeller. The system accepts as input the required RPM (Revolutions Per Minute) and the battery's main characteristics (voltage and current). It outputs the thrust, the motor RPM, and the required electric power. The company datasheets (Table 3.6) helped evaluate losses due to the motor windings Joule effect, while an analysis of a sample was necessary to determine the other losses. The analyzed motor was the A20-20L [128], whose data are summarized in Table 3.7.

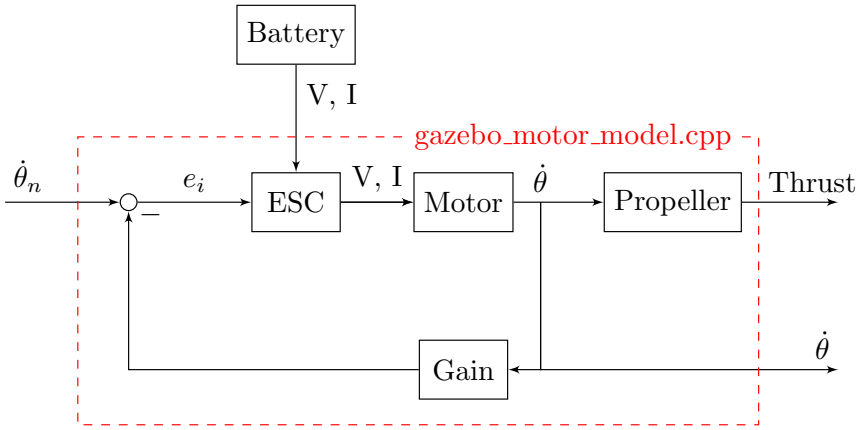

Figure 3.3: block diagram of the drone propulsion system simulated by the package *'gazebo_motor_model.cpp.'* The system consists of ESC, motor, and propeller.

Electromechanical motor system

The '*gazebo_motor_model.cpp*' package describes the propulsion system of a classic drone. As Fig.3.3 shows, it simulates a system composed of ESC, motor, and propeller. The fundamental part is the mechanical motor-propeller coupling modeled via system 3.3; ESC only affects total efficiency, acting as an electrical loss.

$$\begin{cases} J\ddot{\theta} + b\dot{\theta} + K_Q\dot{\theta}^2 = \frac{60}{2\pi K_v} i \\ V_{motor} = \dot{\theta}/K_v \end{cases} \tag{3.3}$$

This section investigates whether the hypotheses behind the mathematical model adopted by this Gazebo package are acceptable. The non-linear system 3.3 looks basic and does not introduce any inductance or delay due to electrical effects. The motor inductance increases the rotational inertia, playing as an oscillating factor as well. On one extreme, the motor inductance consumes voltage, reducing peak motor speed. On the other extreme, the motor inductance produces torque, decreasing the measured motor current. The central hypothesis leading to this system is that the dissipated power appears small compared to the mechanical generated one, i.e., the motor has very high efficiency. To verify this hypothesis, the author exploited the most common UAV brushless motors data.
Table 3.6 reports some data regarding drone brushless motor and helps in deriving the maximum dissipated-supplied power ratio $\left(\frac{P_{Joule}}{P_{max}}\right)$; this ratio is relatively small for the most analyzed motors. If the other forms of efficiency losses, analyzed in the following, are small compared to the P_{Joule}, system 3.3 can be considered suitable.

It should be noted that even if the model adopted is valid in the case of small losses, i.e., the efficiency of the propulsive apparatus not unitary, in order to calculate the consumption of the battery correctly, all losses must be considered. In the gazebo package, these losses are considered in the term *'max motor efficiency'*.

Table 3.6: main parameter of some brushless drone motors.

Model	$K_v\left[\frac{rad}{(V \cdot s)}\right]$	I_{max}[A]	P_{max} [W]	R_{int}[mΩ]	$\frac{P_{Joule}}{P_{max}}$
F60 Pro III [198]	2700	53	800	37	13%
3B-R 2207 3Bhobby [137]	2200	30	730	52	6%
HGLRC FLAME 1104 [136]	7500	11.8	131	190	20%
BeeMotor 1108 [254]	5500	15.4	246	203	19%
XING X5215 X [255]	170	48	2300	134	13%
U3 KV700 [199]	700	60	3000	99	12%
U12 KV90 [200]	90	50	2500	47	4%
U8 KV170 [201]	170	35	1300	89	8%
A20-20L[128]	1022	17.5	180	89	15%

Practical example: A20-20L motor

To test the magnitude of all the drone brushless motor losses, the author has analyzed the motor A20-20L [128] by Hacker, Fig.3.4; Table 3.7 shows its characteristics. Figure 3.6a helps to understand the layout of the windings, while figure 3.6b supplies the pole magnet size. The possibility of analyzing the motor turned out decisive since the lack of data to assess the whole motor losses. In particular, in this section, the author is going to evaluate the iron, eddy current in permanent magnet, and skin losses belonging to the model above. Widely validated formulas helped in the assessment.

Table 3.7: main parameters of the A20-20L brushless drone motor.

N_p	14	N_w	12	I	17.5 [A]
P_{max} [W]	180	R_{int}	89 [mΩ]	$\frac{P_{Joule}}{P_{max}}$	15%
$\frac{P_{Iron}}{P_{max}}$	$\approx 10^{-8}$	$\frac{P_{eddy}}{P_{max}}$	$\approx 10^{-14}$	η_{motor}	≈85%
f	875 [Hz]	σ	$2.5{\cdot}10^{6}$ [(Ω·m)$^{-1}$]	d	$3.5{\cdot}10^{-4}$ [m]
μ	$1.3{\cdot}10^{-6}$ [H/m]	n_{coil}	200	d_{mag}	$2{\cdot}10^{-3}$ [m]
ρ	9.7 [Ω·m]	V_{mag}	$1.4{\cdot}10^{-6}$ [m^3]	d_c	$\approx 10^{-4}$[m]
k_e	2.6	k_h	143 [A/m^3]	V_{induct}	$\approx 1.5{\cdot}10^{-11}$

(a) (b)

Figure 3.4: visual representation of the motor A20-20L [128] used as sample.

The author has exploited formula 3.4 by Bertotti [49], approved in literature, to evaluate the inductance iron losses.

$$P_{Iron} = \left[k_h f {B_{max}}^2 + \sigma \frac{d^2}{12} \left(\frac{dB(t)}{dt} \right)^2 + k_e \left(\frac{dB(t)}{dt} \right)^{\frac{3}{2}} \right] V_{induct} \approx 10^{-6} W \tag{3.4}$$

Graph 3.5 shows that P_{Iron} remains in the order of magnitude 10^{-6} W. Since $\frac{P_{Iron}}{P_{max}} \approx 10^{-8}$ or $\frac{P_{Iron}}{P_{Joule}} \approx 10^{-7}$, P_{Iron} turns out to be negligible.

A variable magnetic field passing through a permanent magnet generates the eddy current; the author exploited the Ishak's formula 3.5 [145] for its evaluation.

$$P_{eddy} = \frac{(\pi \cdot B_{max} \cdot d_{mag} \cdot f)^2}{6\rho} V_{mag} \approx 10^{-12}\,W \tag{3.5}$$

Hence $\frac{P_{eddy}}{P_{max}} \approx 10^{-14}$ or $\frac{P_{eddy}}{P_{Joule}} \approx 10^{-12}$; ignoring P_{eddy} in evaluating the motor efficiency looks allowed.

Engineers overlook the skin effect in the copper windings of a motor. The skin effect represents the apparent resistance increase in a conductor when crossed by an alternating current. The hypothesis 'skin depth (δ) much larger than the conductor diameter

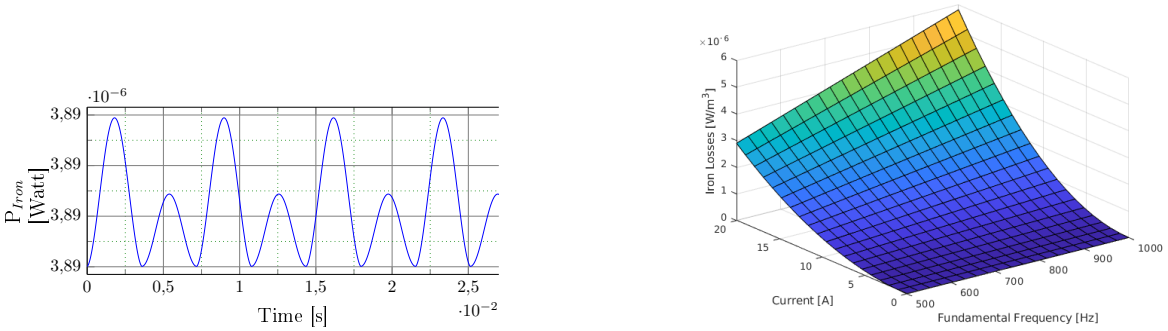

(a) (b)

Figure 3.5: Fig.3.5a represents P_{Iron} vs time. Fig.3.5b represents the maximum P_{Iron} vs current vs the fundamental frequency.

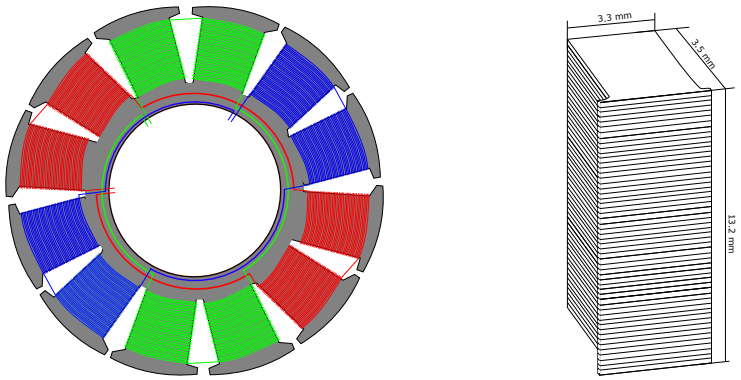

(a) (b)

Figure 3.6: representation of the inductances in Fig.3.6a and size of the inductance magnet in Fig.3.6b both related to the motor A20-20L [128].

(d_c)' allows the omittance of the skin effect. To verify this hypothesis, the author has exploited Eq.3.6, by Jordan et al. in [154], that confirmes such a hypothesis; the skin effect can be neglected for the purposes of this thesis.

$$\delta = \sqrt{\frac{2\rho}{\omega\mu}} = 54 \gg\approx 10^{-4}m = d_c \tag{3.6}$$

Since all the losses calculated in this section are small, the system of equation 3.3 is suitable. The author suggests the same behavior to all the motors belonging to the same category.

3.1.4 Propeller

The propellers are a fundamental part of the propulsion system. Their role is well described by the system of equation 3.3, but their efficiency (indicated as the ratio between thrust developed and power absorbed) affects the efficiency of the entire propulsion system and then actual battery consumption. This section will briefly explore the differences of drone-grade with respect to the civil-grade propellers and the consequences they entail on efficiency. This section exploits publications found in the literature and will draw some general considerations. When talking about propellers, an essential factor to mention is the advance ratio J, that indicates the ratio of the freestream fluid speed to the propeller tip speed. For the same propeller and working at the same flow regime, the efficiency varies with the advance ratio, as in Fig.3.7. Fig.3.7 represents the efficiency vs. J for both drone (solid line) and civil (dashed line) grade propellers (data from [126] and [249], Table 3.8). Fig.3.7 shows the propellers used in the drone environment and the NACA6409-airfoil-based propellers used in civil environment working at different twist angles, data from [126] and [249]. Figure 3.7 and Table 3.8 refer to propellers in cruise conditions.

Table 3.8: characteristics of the both drones and civil propeller analyzed in Fig.3.7 for cuise conditions.

	V_∞	D	c_{max}	n	$Re_{\frac{3}{4}}$
Civil	150 m/s	1.6 m	0.32 m	230 rad/s	$5.2{\cdot}10^6$
Drone	12 m/s	0.22 m	0.025 m	785 rad/s	$3{\cdot}10^4$

The study of Fig.3.7 shows that the maximum civil grade propellers' efficiency is about 50% higher than the drone's grade ones.
The main reason the drone propellers are less efficient is the lower Reynolds number (Re) they operate. The Reynolds number is defined as the ratio between inertial forces and viscous forces within a fluid. It depends on the chemical characteristics of the fluid, its relative speed, and the characteristic length of the problem to be analyzed that for a propeller, is the chord at a three-quarters of the radius. The Reynolds number at three-quarters of the radius, $Re_{\frac{3}{4}}$, typically indicates the flow regime at which the propeller operates. Table 3.8 shows that $Re_{\frac{3}{4}}$ for drone propellers results in virtually two magnitudes smaller than the civil grade propellers. Working at a low Reynolds number regime, as for the drone-grade propellers, decreases the efficiency of the airfoil and then the propeller. The top drone's propeller efficiency typically remains around 0.55, the value that the package *'gazebo_motor_model.cpp'* exploits by default.
It is important to note that the propellers of drones have constant pitch; their efficiency degrades very quickly outside the best operating advance ratio. Since the drone we analyze the most always work at cruise speed, it is reasonable to assume that drones move in a relatively small range of advance ratios, and therefore, their propellers always work at their maximum efficiency.

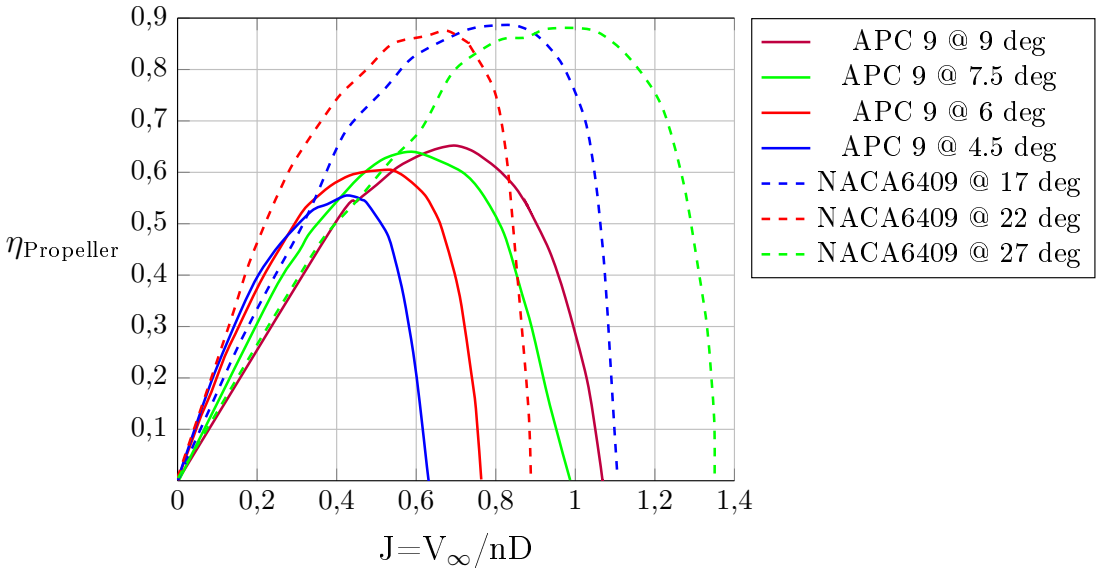

Figure 3.7: propeller efficiency vs. advance ratio for drone (solid line) and civil propellers (dashed lines) in cruise conditions, data from [126] and [249]. The two types of propellers work at different operating regimes, determined by the airfoil Reynolds number.

3.1.5 Electronic Speed Control

The Electronic Speed Control (ESC) is an essential device in controlling the brushless motors, widely used on drones. This section analyzes how the ESC influences the drone propulsion system by analyzing the ESC efficiency, η_{ESC}, related work, available in the literature. Some publications (including Gong et al. in [120]) have pointed out that the ESC efficiency, η_{ESC}, is not unitary and depends on the RPM of the motor. In their work, Gong analyzes the efficiency vs. motor RPM of some ESCs divided by construction quality at different amperages and voltages; this section draws conclusions from that work. The efficiency of an ESC also depends on the operating temperature, but this variation is slight (less than 5% of the total value) and is not considered in this thesis work. The battery amperage and motor's RPM and torque (combined with the budget) determine the choice of the best ESC. Fig.3.8, from [120], reveals the same behavior for all the analyzed ESCs. Within an RPM range, η_{ESC} waves around the maximum, called $\eta_{ESC|max}$, determined by the construction quality as well. If wisely chosen, an ESC will work in its maximum efficiency range. In the Gazebo program, the ESC only influences, linearly, the efficiency of the propulsive apparatus via the ESC efficiency η_{ESC}. The top drone grade ESC efficiency oscillates around 85%, the value recommended, in the design phase, by the author of this work. The exploited Gazebo library does not take explicitly into account the ESC value, assuming the ESC efficiency as unitary, but the author of this thesis considered it by modifying the library.

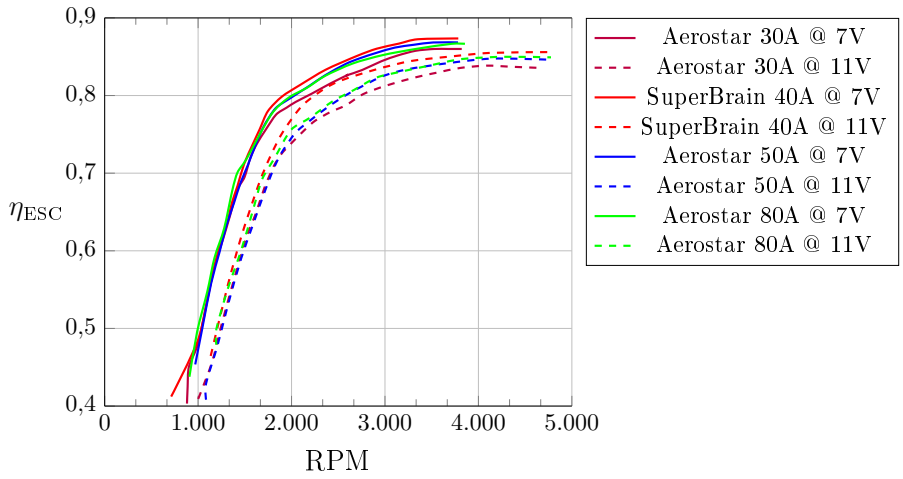

Figure 3.8: ESC efficiency vs. motor RPM, at different amperage and voltage data from Gong et al. in [120]. The behavior is similar to each other; after a certain RPM, the efficiency tends to $\eta_{ESC|max}$.

3.1.6 Motor and propulsion system simulation conclusion

The work carried out in this paragraph has concerned the analysis of the different parts of the propulsion system. At first, the paragraph has analyzed the electric motor losses not considered in the gazebo model, particularly the iron, eddy, and the due skin effect losses. Several sources have been used, including the analysis of the actual drone grade motor A20-20L [128]; the conclusion is that these losses, combined with each other, are small, and therefore the mathematical model used to describe the engine turns out to be faithful. Indeed, even if relatively small, the inefficiencies, even if justifying the Gazebo library adopted model, are considered in the Gazebo library.
The author of the thesis evaluated, in the second part of the paragraph, the influence of the propeller on the propulsive apparatus and verified that it only introduces inefficiencies due to the small size of the civil drone grade propellers. The author analyzed publications about the propellers' performance in the civil and in the drone field; the drone propellers have an efficiency of about half compared to the civil ones. The propeller efficiency is explicitly taken into account in the Gazebo model. We then studied the influence of the ESC on the propulsive system, an effect that has not been analyzed in the literature. The only effect introduced by this device is a loss of efficiency of the propulsion system. This term is not explicitly taken into account in the distributed version of the analyzed Gazebo library. Still, it can, as happens for the propeller, be taken into account in the term *'Max Motor Efficiency.'*

3.2 Environment, payload and autopilot simulation

A 3D simulation of an actual mission, allowing to visualize obstacles, taking into account the physics, can significantly help evaluate the goodness of the adopted solutions. Any problem that has not been investigated in the preliminary phase becomes, with the simulation of a real 3D scenario, clearer, and the mission designers can think about possible solutions. This paragraph shows all the steps taken for the simulation of the building, drones, payloads and the most common obstacles, in order to simulate a realistic mission. For these simulations, the author of the thesis has exploited a vast series of tools, introduced below. This paragraph doens't want to be comprehensive but just offer an overview of the simulation.

Gazebo is both a graphics and physics engine, which has lately become among the most used software involving drone simulations. This success is due to multiple factors, whose the most important is its compatibility with the Robot Operating System (ROS [159]) program. ROS makes easy the interaction with control systems and payloads of the drone (simulated or not); the interaction with external programs is possible through *'nodes'* and *'topic.'* The scenario the drones are set is the urban one, and it has been generated using *OpenStreetMap* [248] data, Figs.3.9a and 3.9b, in the same way analyzed in section 2.4.1. *OpenStreetMap* is a widespread web mapping free and open-source service. It provides reliable data about the buildings and the green in the cities. The process of creating the CAD of the environment involves finding the area to analyze, Fig. 3.9a, and importing its related *'.osm'* data, Fig. 3.9b; the author of this thesis has chosen, for the simulation environment, the area near Medaglia d'Oro square in Naples, Italy. Data from OpenStreetMap can be manipulated in Blender [203] environment, where the modification of the CAD is a quick operation. Blender is exclusively a CAD program, unlike Gazebo where modifying the CAD could be much more difficult. Fig. 3.9c shows the CAD from OpenStreetMap loaded in Blender; there is a long black shape representing the metropolitan tunnel that passes under the area to be analyzed, but at street level, not below as it should be. Figure 3.9d shows the same area where the tunnel is removed through Blender. The obtained CAD, as it is possible to see, accurately offers representations of every part that typically makes up a city, such as buildings, roads, railway lines, and bridges. The exploited data are reliable as based on actual cadastral data. Figures 3.9e and 3.9f show the CAD of the area analyzed in the thesis, loaded into the Gazebo program. As said, Gazebo makes simulating a vast series of payload and all drone equipment such as engines or GPS systems easy and Figure 3.9f represents a drone using a camera and a LIDAR in a Gazebo environment. Note how the obstacles in the Gazebo have a dual nature. The former is called *visual*, the latter is called *collision*. The *visual* nature derives from the CAD model and allows the visualization of the model. Instead, the *collision* nature is used for physics within the Gazebo program, more precisely for collision with other elements within the simulation or for

data relating to sensors such as SONAR or LIDAR. While the degree of detail of the *visual* part can be high, the degree of detail of the *collision* part is low. The *collision* part of each element can be represented as a combination of rectangular parallelepipeds. Figure 3.9f shows the difference between these two nature of an object; the *visual* part is very accurate while the *collision* part is represented by the parallelepiped whose edges are white. Payload simulation represents an essential part of the overall simulation.

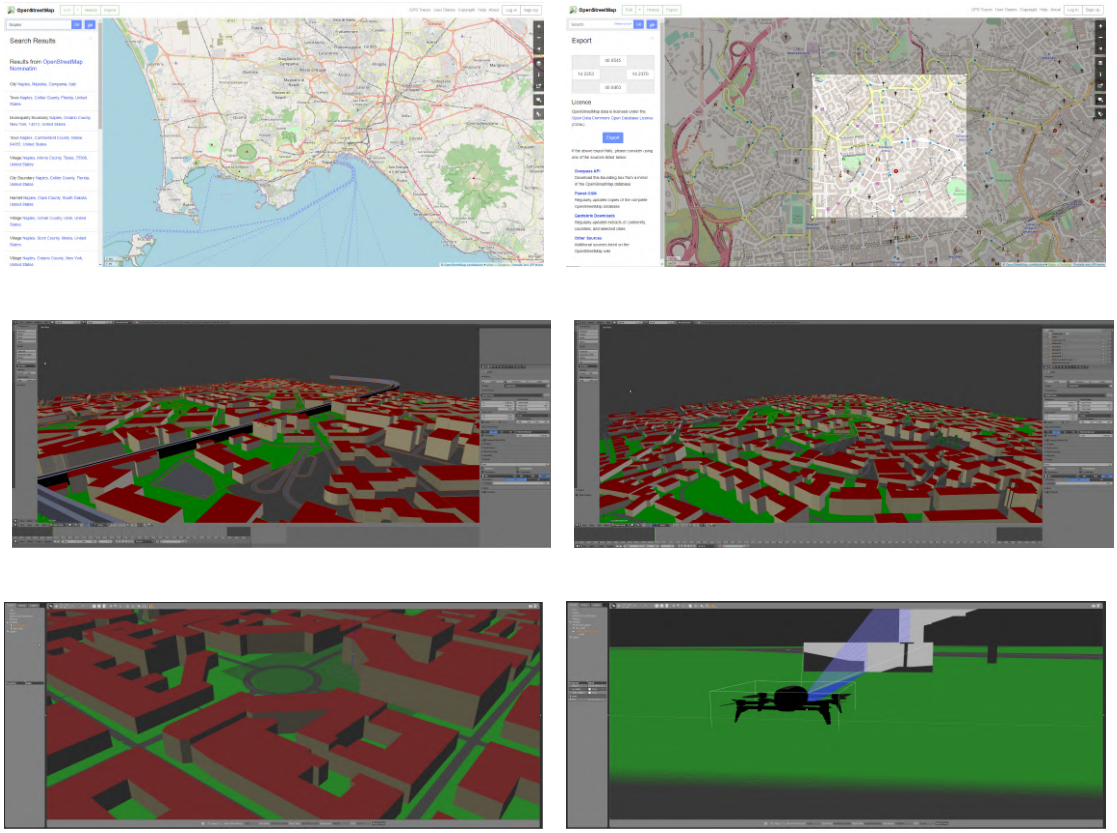

Figure 3.9: figures 3.9a and 3.9b show the site www.OpenStreetMap.com [248] where it is possible to download the analyzed area CAD data. Figs.3.9c and 3.9d show the Blender program [203] before and after the CAD manipulation. Fig.3.9e shows the Gazebo environment with the CAD of the city. Fig.3.9f shows, in the Gazebo environment, a CAD of a drone and some of its payloads; the figure shows also the difference between the collision and visual elements.

These accessories allow the drone to carry out its task or orient itself towards the surrounding environment, and their data coming is vital for the autopilot. The simulation carried out in this thesis exploits some packages offered by 'Gazebo' [209]. These packages simulate the various payloads used onboard the drone. The mathematical model

characterizing them is easily editable, and therefore more accurate models can be implemented. Payload simulation is an exciting aspect to analyze. Still, this thesis has not investigated the accuracy of the offered outputs, and the payload adopted libraries have been used as a black box. The output data of the simulated payloads were transferred to an external PC (through the architecture shown in figure 3.10) which used them as input for the autopilot.
The autopilot is a device used to control the trajectory of the drone, allowing the drone to fly without constant human intervention. An autopilot must work in conjunction with other sensors to understand the position and orientation of the drone in the environment. For this reason, INS and GPS receivers are usually mounted onboard the drone.
The autopilot acts, depending on the specifications, on the flight control system. A quadrotor drone can only control the number of revolutions per minute of each motor (small drones use fixed-pitch propellers) to vary both the attitude and the displacement. A fixed-wing drone can typically control many more parts: rpm of the motor, ailerons, and tail organs.
The author of this thesis has opted for an architecture composed of an off-board high-level autopilot and a low-level on-board autopilot, as shown in figure 3.10. A computer on the ground acts as an upper-level autopilot, a path-planner, and analyzes the payload data. It performs most of the calculations remotely to free the drone as much as possible from the calculation burden. To simulate this architecture, the author exploited two PCs; the upper-level autopilot runs on a PC different from where the simulation and the low-level on-board autopilot run. The PCs communicate via the internet using the ROS program. The author has developed the Matlab script that acts as an upper-level autopilot while he has exploited the Gazebo library *'gazebo-ros-control,'* via the topic *'cmd_vel'* to simulate the low-level on-board autopilot. The upper-level Matlab-based autopilot needs the path planner waypoints (discussed in chapter 2) and some drone-related data, as cruising speed and the turning radius. The autopilot produces a trajectory taking into account the drone constraints. The difference between the waypoints and the autopilot trajectory is evident in Fig.3.11a where the black dashed line represents the trajectory the autopilot wants the drone to follow. The Matlab-based autopilot is a fly-by-waypoints one, the most popular type; the airplane or drone moves toward the (n + 1)-th waypoint when it is close enough to the n-th waypoint.

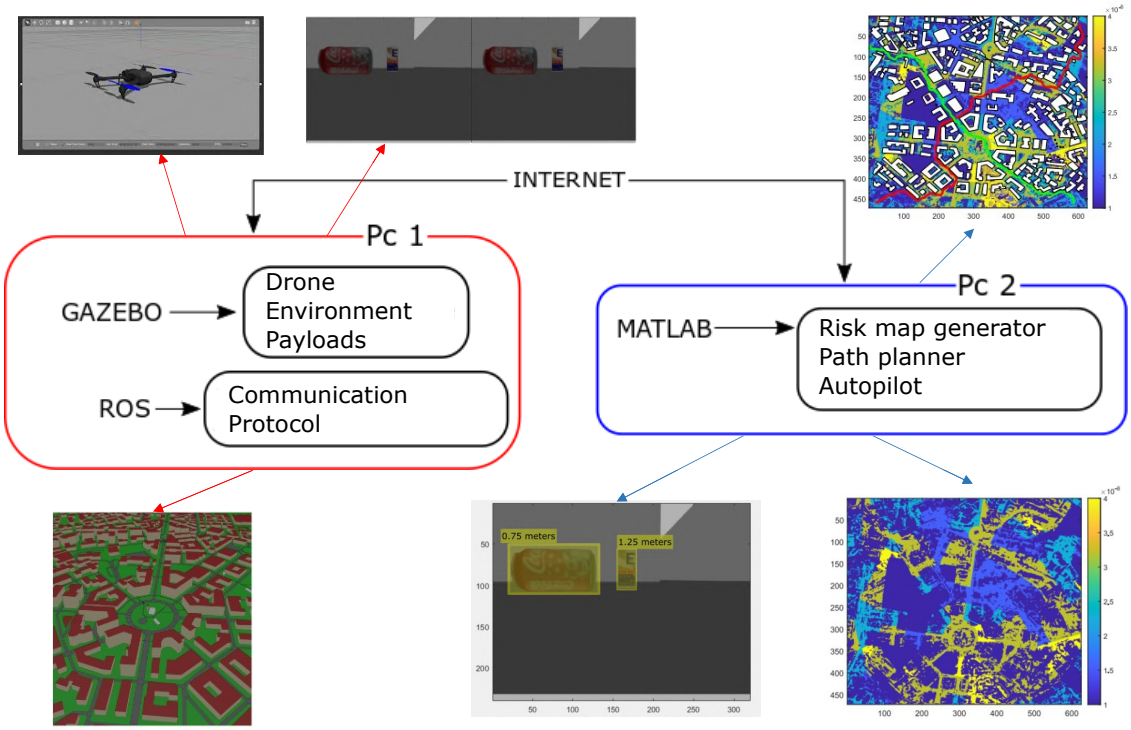

Figure 3.10: architecture simulated in this thesis.

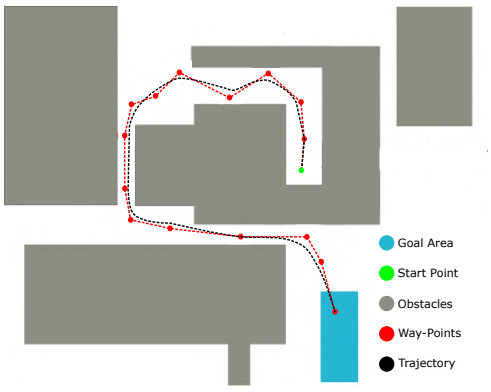

(a)

Figure 3.11: differences between the waypoints and the trajectory developed from the high-level autopilot.

The following listing represents a pseudo-code of the upper-level autopilot.

```
Waypoint = load('WayPoint_pathplanner.txt');
Distmin = minimum distance from waypoints the aircraft searches ...
    the next waypoint;
Start_Pos = drone starting position;
Y0 = starting condition;

for j=1:number of Waypoints
   dist_aer_wa = Distance between airplane and waypoint;
    while dist_aer_wa>Distmin;
            [T,Y]=ode23(@horizontal 3D airplane equation, Y0);
            % Update of starting conditions
            Y0 = Y;
            Displacement = cartesian transformation of Y;
            % Update of the drone starting position;
            Start_Pos = Start_Pos + Displacement;
            i=i+1;
     dist_aer_wa=norm(Waypoint - Start_Pos );
    end
end
```

The high-level off-board Matlab autopilot communicates to the low-level on-board autopilot the linear or angular speed the drone has to accomplish. The task of the low-level on-board autopilot, i.e. the Gazebo library *'gazebo-ros-control'*, is to command the drone flight control system. This architecture implies a very high communication frequency between the drone (or better, its low-level autopilot) and the high-level Matlab-based autopilot that also continuously controls the onboard mounted sensors. The frequency adopted in the thesis is 50Hz.
Figure 3.12 shows the reference frame adopted in this thesis; Fig.3.12a represents the case related to a rotary-wing drone, while Fig.3.12b the fixed-wing drone one. The pseudo-code the author of the thesis used to move the drone and analyze its payloads data from Matlab, is shown in the following self-explaining listing.

```
% Loading of the commands to be given to the drone
% obtained through the high-level autopilot.
 [Velocity Theta ]= load('autopilot_control_values.txt');

% Set up the communication between Matlab and Gazebo via ROS,
% knowing the machine's Ip address where Gazebo runs.
 rosinit(Ip_value_Gazebo_pc);

% Subscribe to the ROS topic `/drone/front_camera/image_raw'
% to get the drone front camera data.
 ForwardVideo = rossubscriber('/drone/front_camera/image_raw');

% Subscribe to the ROS topic `sensor_msgs/LaserScan'
```

```
% to get Lidar data.
 scan = rossubscriber('sensor_msgs/LaserScan')

% Subscribe to the ROS topic `sensor_msgs/NavsatFix'
% to get GPS data.
 GPS = rossubscriber('sensor_msgs/NavsatFix');


%%%% Steps to take to get the drone off the ground.
% Create the ROS publisher for the topic `/drone/takeoff'.
 take_off = rospublisher('/drone/takeoff');
% Create an empty message.
 message_empty = rosmessage('std_msgs/Empty');
% Send an empty message to the topic `/drone/takeoff',
% via ROS, to the drone to take off.
 send(take_off, message_empty);



% Create the ROS publisher for the topic `cmd_vel' in order
% to move the drone sending speed-related messages
 [cmd, cmd_msg] = rospublisher('cmd_vel');

% `For' cycle used to send linear and angular speed
% messages to the drone at 50 Hz

 for i=1: length(Velocity)

% Drone camera last image data loading.
 cloud = ForwardVideo.LatestMessage;
% Loading of the last image pixel data.
 Rs = cloud.Data(1:3:end);
% Manage the image in order to be viewed from a classical screen
% and to be classified by a trained neural network.
 R = reshape(Rs, cloud.Width, cloud.Height);
 R=imrotate(R, -90); R = flipdim(R, 2);
 imshow(R, 'InitialMagnification', 200);
% Classification of the image
 label = classify(net, R);

% Display drone-based lidar scan point cloud
 plot(scan)

% Plots of the drone latitude-longitude based locations
 geoplot(GPS.latitude, GPS.longitude, 'g*')

% Create a message to set a linear speed (m/s) a
% long the drone X axis.
 cmd_msg.Linear.X = Velocity(i);
% Create a message to set a angular speed (rad/sec)
```

```
% along the drone Z axis.
 cmd_msg.Angular.Z = Theta(i);
%  Send the linear and the angular speed message to the
% topic `cmd_msg', via ROS, to the drone to rotate along its Z ...
    axis.
 send(cmd, cmd_msg) ;
% Simulation of the 50 Hz update frequency.
pause 1/50;
end


%%%% Steps to make the drone land
% Create the ROS publisher for the topic `/drone/land';
 pub_land = rospublisher('/drone/land');
% Send an empty message to the topic `/drone/land',
%via ROS, to the drone to take off;
 send(pub_land, message_empty);
```

Let's analyze the previous listing. The information about the speed the drone has to move is stored in the *autopilot_control_values.txt* file, written by an original Matlab language-based autopilot. It gives information about linear and angular speed for the drone to follow the right path the path-planner evaluated.
Matlab uses the *'rosinit'* command to better communicate to the ROS program, using the *ip4* address of the machine Gazebo is running on.
As previously mentioned, ROS uses *topic* and *nodes*, channels on which it communicates both incoming and outgoing information. Communication occurs via a particular protocol on these channels; each type of information has a specific message type that can be received or sent. *rossubscriber* is the command Matlab uses to subscribe to a ROS topic, in order to have the related information; this command is used for topic that only send information. For the topics that receive information, the Matlab command *'rospublisher'* is used. For example, for the quadrotor drone to take off, you need to connect to the *'drone/takeoff'* topic, via the Matlab command *'rospublisher,'* and send the right message, i.e., *'std_msg/Empty.'*
To move the drone, you have to connect Matlab to the topic *'cmd_vel,'* which moves the drone by a certain linear or angular speed. The message type for the topic *'cmd_vel'* differs for each direction we want the drone to move or axis we want the drone to rotate; *cmd_msg.Linear.X*, *cmd_msg.Linear.Y* and *cmd_msg.Linear.Z* indicate the linear speed value along the three drone axes (in meters per second), while *cmd_msg.Angular.X*, *cmd_msg.Angular.Y* and *cmd_msg.Angular.Z* indicate the angular speed value (radians per second) around these axes, shown in figure 3.12. The listing above also shows how to subscribe to the camera, GPS (Fig.3.13c) or LIDAR (Figs.3.13a and 3.13b) topics and analyze the related data. The author has also used a trained neural network to classify the object in the simulated camera image, Fig3.13d.

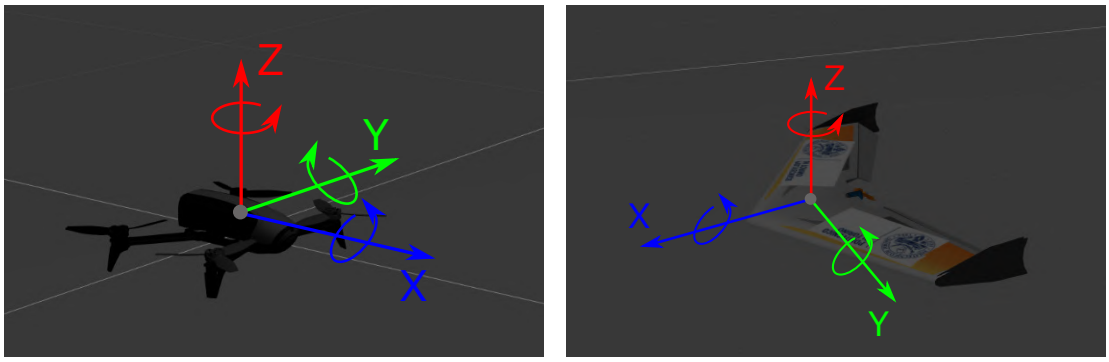

Figure 3.12: drone frame for a rotary-wing drone, Fig.3.12a and a fixed-wig drone, Fig.3.12b.

In a real drone, the autopilot is a relatively small piece of hardware with a non-negligible cost: the more the product's performance increases, the more its cost increases. The performances of an autopilot are typically linked to the error made by the sensors belonging to it [278]. The drone position is calculated by integrating the accelerometer signal twice, so the position error is proportional to the square of the sensor noise. The attitude is derived by integrating the angular rate measured by the gyros and the error results proportionate to the reset time. It is possible, within limits, to assist the position measurements with GPS measurements, but it is tough to help in the attitude measurement. Still, it is clear that the longer the mission is or the spaces are narrow, the more the autopilot and the sensors mounted on board must have high performances. The tasks hypothesized in this thesis provide, on average, a long duration of time and a relatively small room for maneuver; the quality of the onboard pieces of hardware must be high. In the simulation, it was possible to introduce an error related to the sensors belonging to the Gaussian distribution. The error has been set the same along the three axes and equal to 0.01% standard deviation value and a zero mean. In reality, the types of errors are many, such as scale factor errors, misalignments, temperature dependencies, and gyro g-sensitivity, but they are not considered in the Gazebo simulation.

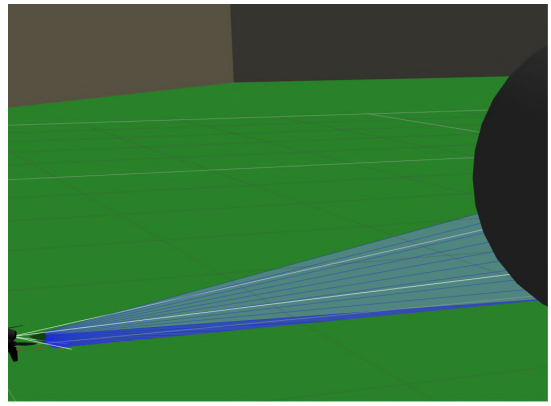

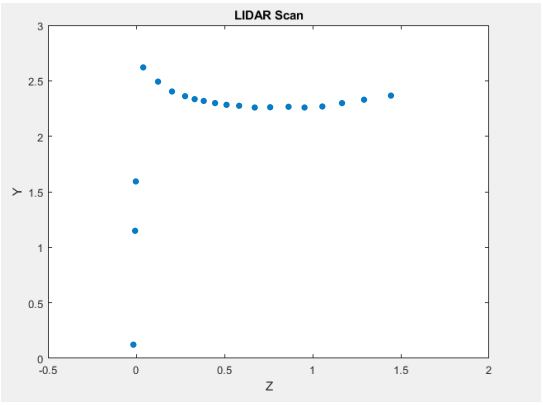

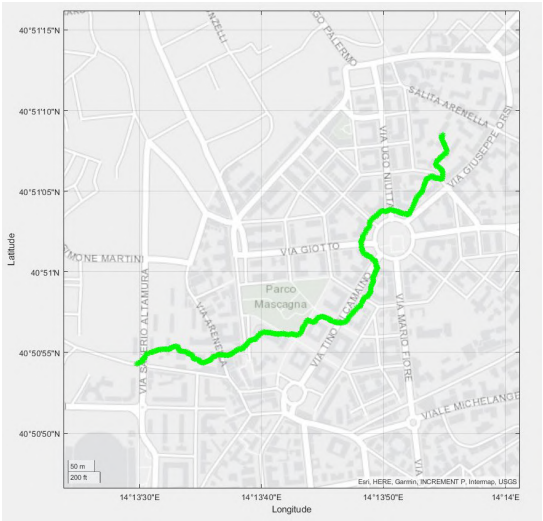

Figure 3.13: payloads and their analyis in Matlab. Fig.3.13a shows a LIDAR in Gazebo while Fig.3.13b shows the LIDAR data read in Matlab. Fig.3.13c shows the GPS data from Gazebo into Matlab while Fig.3.13d shows the neural network classification.

3.3 Conclusions

The results of the analysis of the Gazebo libraries used for the battery simulation (library *brass_gazebo_battery.cpp*), and the propulsion system (library *gazebo_motor_ model.cpp* to simulate ESC, motor, and propeller) have shown that the adopted simplifications have very little influence on the quality of the solutions. The overall error made in using the Gazebo libraries remains in the order of 15%, which according to the literature, is an permissible error, especially in a preliminary phase, as for academic use. The mathematical models Gazebo is based on have the great advantage of requiring a low computational load. Low computational load allows real-time simulation even for relatively low-performance laptops such as those used, in this thesis, with considerable advantages from the point of view of usefulness in the academic field.
Having verified the goodness of the Gazebo libraries has allowed the simulation of an implementation of the architecture, which wants to simulate cloud computing; this was the subject of the second part of the chapter. The aim of this architecture is to relieve the drone as much as possible from computational calculations; the analysis of the payloads, the generation of the path, and the high-level autopilot are tasks performed outside the drone. The author has simulated the proposed architecture with commonly available to the academic environment tools, introducing a minimum error. The author hopes that this can be a good starting point for future studies that explore the introduced themes better.

Chapter 4

Final consideration

This thesis wanted to show and overcome the difficulties currently existing in the introduction of small civil drones in an urban environment. As analyzed in the first part of the thesis, the reasons drones are almost not allowed in the urban environment are mainly legislative, and this is a situation familiar to virtually all the countries in the world. In almost all countries, the legislation judges the drones to be too dangerous to fly over people, and the drone ban in the urban environment is the solution found. The author of this thesis wanted to show that drones are actually not so dangerous as supposed, and he has proposed another solution to overcome these bans, identified in a new formulation of the risk calculation suitable for small drones that doesn't interfere with the risk assessment used for bigger drones. The original risk formulation starts from one of the most widespread and accredited risk formulations in the academic world and represents a better version of it. The justifications for the innovations introduced are well explained through the thesis. If adopted, this original risk-formulation would allow the use of small drones even where they are not allowed for risk-related problems, as it dramatically reduces the mission-associated risk. Furthermore, this original risk formulation provides results that a path planner can consider the same way a path planner considers a gain map; the original risk formulation produces a risk map. This is the first time an academic work is related to a risk minimization drone path. The result is that an autopilot can generate a drone path that either minimizes the distance or the total risk for the population. The risk assessment with this original formulation requires information on the overflown area, the drone, and the mission to accomplish. The author has developed and made available all the tools necessary for the correct evaluation of each of the needed values making the risk evaluation almost an automatic task. The author has also analyzed a series of risk maps obtained for different scenarios in two different cities. The scenarios are related to different drone maximum lengths and different drone energies at the impact covering a great range of drone types and missions. The two different cities the thesis has focused on, represent two different kinds of crowded modern occidental cities. The former is Naples in southern Italy, representing an old city with all the characteristic buildings and narrow streets, while the

other is New York, one of the most energetic and modern conglomerations of this era. Thus, the two cities pose different challenges to drone path planners. The analysis of these risk maps has revealed the factors that are important to handle in order to minimize the risk and the irrelevant factors; the author has proved how the most critical drone-related factor in the risk evaluation is the drone maximum length. Thus, in order to make drones safe, it's essential to make them small. An effort has been made to make all the exploited tools, the ones for the evaluation of the risk and the ones for the path evaluation, as friendly as possible. In the final part of the thesis, a realistic mission was also simulated in a virtual environment, making extensive use of tools available and known in the academic environment. The purpose of this simulation was twofold; to evaluate the goodness of the exploited tools and to show the practical side of the innovations introduced. The new risk assessment represents a solid basis for offering a service based on drones, even in an urban environment.

Nomenclature

Roman Symbols

δ	Skin depth
$\dot{\theta}, \ddot{\theta}$	Rotor angular speed and acceleration
μ	Permeability of the conductor
ω	Current frequency
ρ	Resistivity of the conductor
σ	Conducivity of the kernel
d_c	Diameter of the conductor
$\mathrm{N}_{\mathrm{cells}}$	Number of cells in series
$\mathrm{P}_{\mathrm{Iron}}$	Iron Losses power
Δt	Time step simulation [s]
AR	Airplane Wing Aspect Ratio
b	Motor viscous friction constant
$\mathrm{B}_{\mathrm{max}}$	Peak of the magnetic flux density
C_D	Overall Drag Coefficient
C_{D_0}	Aircraft Zero-Lift Drag Coefficient
C_L	Aircraft Lift Coefficient
D	Propeller's diameter
d	Thickness of the lamination
d_{mag}	Permanent magnets thickness

E	Aerodynamic Efficiency
e_0	Oswald Efficiency Number
f	Fundamental frequency
I	Nominal current
i^*	Discharge Capacity
I(n)	Required current at step '*n*'
J	Motor moment of inertia
K	Battery Linear Coefficient
k_e	Excess loss coefficient
k_h	Steinmetz hysteresis Coefficient
K_Q	Propeller torque constant
K_v	Motor velocity constant
LOS	Line of Sight
MTOW	Maximum Take-Off Weight
n	Integration step
n	Propeller's rotation rate
N_p	Number of Poles
N_w	Number of windings
n_{coil}	Number of coils
P_n	Success probability of the n-th part
P_{eddy}	eddy currents Power
P_{max}	Maximum motor required power
P_{System}	Whole system success proability
P(*n*)	Instantaneous required power at step '*n*'
Q	Actual Battery Capacity

R Battery Resistance

R_{int} Motor internal resistance

$Re_{\frac{3}{4}}$ Reynolds at $\frac{3}{4}$ of the radius

RPAS Remotely Piloted Aircraft System

S Wing Area

UAV Unmanned Aircraft Vehicle

V_{induct} Volume of the inductance

V_{∞} Freestream fluid velocity

V_{mag} Permanent magnets volume

V_{motor} Motor voltage

V_0 Constant Coefficient

V(SOC) Instantaneous battery voltage

VTOL Vertical Take-Off and Landing

WS Airplane Wing Span

Bibliography

[1] Acecore Technologies. *Neo Drone - Workswell GIS320*. http://www.acecoretechnologies.com/neo/. [Online; accessed 10-October-2018]. 2018.

[2] Acecore Technologies. *Zoe Portable Versatility*. http://www.acecoretechnologies.com/zoe/. [Online; accessed 10-October-2018]. 2018.

[3] Action Drone. *AD1 Drone Specifications*. http://actiondroneusa.com/systems/ad1/. [Online; accessed 10-October-2018]. 2018.

[4] Action Drone. *AD2 Drone Specifications*. http://actiondroneusa.com/systems/ad2/. [Online; accessed 10-October-2018]. 2018.

[5] Adam Satariano. *Facebook Halts Aquila, Its Internet Drone Project*. https://www.nytimes.com/2018/06/27/technology/facebook-drone-internet.html. [Online; accessed January-2021]. 2018.

[6] Miroslaw Adamski. "Analysis of propulsion systems of unmanned aerial vehicles." In: *Journal of Marine Engineering & Technology* 16.4 (2017), pp. 291–297.

[7] *Adi Arriansyah. The 6 known ways to power a drone*. https://www.techinasia.com/talk/6-known-ways-power-a-drone. [Online; accessed September-2020]. 2016.

[8] Aeraccess. *Hawker Q800X*. http://www.aeraccess.com/Product-Drones-Q800xe. [Online; accessed 10-October-2018]. 2018.

[9] *Aeraccess Airborne Engineering Research. Gosh*. http://www.c-astral.com/en/products/bramor-c4eye. [Online; accessed 24-july-2020]. 2018.

[10] Aero Drum Ltd.. *RC Blimps 10m*. http://rc-zeppelin.com/pdf_dokumentacija/10%20m%20OUTDOOR%20RC%20BLIMP.pdf. [Online; accessed 10-October-2018]. 2018.

[11] Aero Drum Ltd.. *RC Blimps 12m*. http://rc-zeppelin.com/pdf_dokumentacija/12%20m%20OUTDOOR%20RC%20BLIMP.pdf. [Online; accessed 10-October-2018]. 2018.

[12] Aero Drum Ltd.. *RC Blimps 5m*. http://rc-zeppelin.com/pdf_dokumentacija/5%20m%20OUTDOOR%20RC%20BLIMP.pdf. [Online; accessed 10-October-2018]. 2018.

[13] Aero Drum Ltd.. *RC Blimps 6m*. http://rc-zeppelin.com/pdf_dokumentacija/6%20m%20Outdoor%20RC%20Blimp.pdf. [Online; accessed 10-October-2018]. 2018.

[14] Aero Drum Ltd.. *RC Blimps 7m*. http://rc-zeppelin.com/pdf_dokumentacija/7%20m%20OUTDOOR%20RC%20BLIMP.pdf. [Online; accessed 10-October-2018]. 2018.

[15] Aerocontact. *UAV Draganflyer Guardian*. https://www.aerocontact.com/en/virtual-aviation-exhibition/product/292-uav-draganflyer-guardian. [Online; accessed 10-October-2018]. 2018.

[16] Aeroenvironment. *Vapor*. https://www.avinc.com/cis/vapor. [Online; accessed February-2021]. 2021.

[17] *Aeromapper. AVEM*. http://aeromapper.com/en/solution/avem/. [Online; accessed 24-july-2020]. 2020.

[18] *Aeronautics Ltd. Orbiter 1k*. http://aeronautics-sys.com/home-page/page-systems/page-systems-orbiter-1k-muas/. [Online; accessed 4-febr-2020]. 2020.

[19] *AeroVironment, Inc. PUMA 3 AE*. https://www.avinc.com/uas/view/puma. [Online; accessed 24-july-2020]. 2020.

[20] *AeroVironment, Inc. RAVEN B*. https://www.avinc.com/uas/view/raven. [Online; accessed 24-july-2020]. 2020.

[21] *AeroVironment, Inc. WASP AE*. https://www.avinc.com/uas/view/wasp. [Online; accessed 24-july-2020]. 2020.

[22] AeroVironmet. *Snipe™ - The Snipe Nano UAS (UAV) - AeroVironment, Inc.* https://www.avinc.com/images/uploads/product_docs/Snipe_. [Online; accessed October-2017]. 2017.

[23] *Aeryon. Scout*. https://www.aeryon.com/aeryon-scout. [Online; accessed 24-april-2018]. 2018.

[24] *Aeryon. Skyranger*. https://www.aeryon.com/aeryon-skyranger/features. [Online; accessed 24-april-2018]. 2018.

[25] *AgEagle. RX48*. http://ageagle.com/rx48-2/. [Online; accessed 4-febr-2020]. 2020.

[26] *AgEagle. RX60*. http://ageagle.com/rx60/. [Online; accessed 4-febr-2020]. 2020.

[27] *Agencia Estatal de Seguridad Aerea. Preguntas frecuentes Sobre el Real Decreto*. https://www.seguridadaerea.gob.es/langcastellano/ciase/mpresas/trabajos/rpas/faq/default.aspxr13. [Online; accessed September-2020]. 2020.

[28] *Airforce Technology. Tracker Mini Unmanned Aerial System (UAS).* http://www.airforce-technology.com/projects/tracker-mini-unmanned-aerial-system-uas/. [Online; accessed 24-july-2020]. 2018.

[29] Airmap. *Restricted Areas Evaluation, know before you fly source.* http://knowbe/foreyoufly.org/air-space-map/. [Online; accessed 30-September-2018]. 2015.

[30] Alphabet Inc.. *Google Maps.* https://www.google.com/maps. [Online; accessed 15-October-2020]. 2020.

[31] Altavian. *galaxy R8700.* https://www.unmannedsystemssource.com/shop/vehicles/altavian-galaxy-r8700/. [Online; accessed 10-October-2018]. 2018.

[32] Anabatic Aero. *Anabatic Zeppelin.* http://www.anabatic.aero/indoor_zeppelin.php. [Online; accessed 10-October-2018]. 2018.

[33] Anabatic Aero. *Single Specification.* http://www.anabatic.aero/single_specifications.php. [Online; accessed 10-October-2018]. 2018.

[34] Anabatic Aero. *Twin Specification.* http://www.anabatic.aero/twin_specifications.php. [Online; accessed 10-October-2018]. 2018.

[35] *Andreas Parsch. AeroVironment RQ-14 Dragon Eye / Swift.* http://www.designation-systems.net/dusrm/app2/q-14.html. [Online; accessed 24-july-2020]. 2007.

[36] Andrew Elefant. *Understanding Drone Regulations in National Parks, Forests and Wilderness Areas.* https://www.aloft.ai/blog/understanding-drone-regulations-in-national-parks-forests-and-wilderness-areas/. [Online; accessed 28-June-2021]. 2021.

[37] Angelo Antonio Zagaria. *Multidisciplinary Design of Rigid Airship equipped to Superyacht in Collaboration with Pininfarina.* https://webthesis.biblio.polito.it/9192/1/tesi.pdf. [Online; accessed 1-march-2021]. 2018.

[38] *Anil Chopra. Manned vd Unmanned.* http://www.sps-aviation.com/story. [Online; accessed 20-june-2020]. 2013.

[39] David Anthony et al. "On crop height estimation with UAVs." In: *2014 IEEE/RSJ International Conference on Intelligent Robots and Systems*. IEEE. 2014, pp. 4805–4812.

[40] *Australian Government, Home Bureau. Refurnishment Procedure Australia.* http://yourhome.gov.au/you-begin/renovations-and-additions. [Online; accessed December-10-2018]. 2018.

[41] *Australian Government, Local Bureau. Municipality tasks in South Australia.* https://www.australia.gov.au/about-government/how-government-works/local-government. [Online; accessed December-10-2018]. 2018.

[42] Simone Barcellona et al. "Analysis of ageing effect on Li-polymer batteries." In: *The Scientific World Journal* 2015 (2015).

[43] Jerome Barraquand, Bruno Langlois, and J-C Latombe. "Numerical potential field techniques for robot path planning." In: *IEEE transactions on systems, man, and cybernetics* 22.2 (1992), pp. 224–241.

[44] Jerome Barraquand and Jean-Claude Latombe. "Robot motion planning: A distributed representation approach." In: *The International Journal of Robotics Research* 10.6 (1991), pp. 628–649.

[45] *Battery University Team. BU-304a: Safety Concerns with Li-ion.* https://batteryuniversity.com/learn/article/safetyconcernswithlion. [Online; accessed 20-july-2020]. 2019.

[46] Yassine Benabbas et al. "Spatio-temporal optical flow analysis for people counting." In: IEEE. 2010, pp. 212–217.

[47] Maren Bennewitz and Wolfram Burgard. *An experimental comparison of path planning techniques for teams of mobile robots.* Springer, 2000, pp. 175–182.

[48] *Berthold K.P. Horn. A brief tour of the world of cellular repeater antennas.* https://people.csail.mit.edu/bkph/cellular_repeater_inside.shtml. [Online; accessed 27-November-2020].

[49] G Bertotti, F Fiorillo, and GP Soardo. "The prediction of power losses in soft magnetic materials." In: *Le Journal de Physique Colloques* 49.C8 (1988), pp. C8–1915.

[50] Blender org. *Blender.* https://www.blender.org. [Online; accessed 23-January-2020]. 2020.

[51] Blimp Guys.com. *Blimps.* http://www.blimpguys.com/electricAirships.htm. [Online; accessed 10-October-2018]. 2007.

[52] Blimp Guys.com. *Blimps.* http://www.blimpguys.com/electricAirships.htm. [Online; accessed 10-October-2018]. 2007.

[53] *BlueBird Aero System. MicroB.* http://www.bluebird-uav.com/microb/. [Online; accessed 4-febr-2020]. 2020.

[54] Irem Bor-Yaliniz et al. "Is 5G ready for drones: A look into contemporary and prospective wireless networks from a standardization perspective." In: *IEEE Wireless Communications* 26.1 (2019), pp. 18–27.

[55] Johann Borenstein and Yoram Koren. "The vector field histogram-fast obstacle avoidance for mobile robots." In: *IEEE transactions on robotics and automation* 7.3 (1991), pp. 278–288.

[56] Francesco Bullo and Kevin M Lynch. In: *Kinematic controllability and decoupled trajectory planning for underactuated mechanical systems.* Vol. 4. IEEE. 2001, pp. 3300–3307.

[57] Maren Bennewitz Wolfram Burgard. "An Experimental Comparison of Path Planning Techniques for Teams of Mobile Robots." In: *Autonome Mobile Systeme 2000: 16. Fachgesprach Karlsruhe* (2013), p. 175.

[58] bvpservice. *PRODUCTS.* http://bvpservice.by/en/products/uav/unmanned-aerial-systems-for-environmental-monitoring-installed-on-airships. [Online; accessed 10-October-2018]. 2018.

[59] *C-Astral Aerospace Ltd. Bram C.* http://www.c-astral.com/en/products/bramor-c4eye. [Online; accessed 24-july-2020]. 2018.

[60] Francesco Calabrese et al. "Understanding individual mobility patterns from urban sensing data: A mobile phone trace example." In: *Transportation research part C: emerging technologies* 26 (2013), pp. 301–313.

[61] Julián Candia et al. "Uncovering individual and collective human dynamics from mobile phone records." In: *Journal of physics A: mathematical and theoretical* 41.22 (2008), p. 224015.

[62] *CAT UAV. Atmos.* http://www.catuav.com/uav-products. [Online; accessed 24-july-2020]. 2020.

[63] Antoni B Chan and Nuno Vasconcelos. "Counting people with low-level features and Bayesian regression." In: *IEEE Transactions on Image Processing* 21.4 (2012), pp. 2160–2177.

[64] *China Internet Information Center. Municipality tasks in China.* http://www.china.org.cn/english/Political/28842.htm. [Online; accessed December-10-2018]. 2018.

[65] *Civil Aviation Authority U.K. Unmanned Aircraft System Operations in UK Airspace – The UK Recognised Assessment Entity.* https://publicapps.caa.co.uk/docs/33/CAP722B(E2)-20191204.pdf. [Online; accessed 7-july-2020]. 2019.

[66] Clearpathrobotics. *Hummingbird, Unmanned Aerial Vehicle.* https://www.clearpathrobotics.com/hummingbird-unmanned-aerial-vehicle/. [Online; accessed 10-October-2018]. 2018.

[67] Clearpathrobotics. *Pelican, Unmanned Aerial Vehicle.* https://www.clearpathrobotics.com/pelican-unmanned-aerial-vehicle/. [Online; accessed 10-October-2018]. 2018.

[68] Kimberly Dean Coder. *Falling tree leaves: leaf abscission.* University of Georgia, Daniel B. Warnell School of Forest Resources, 1999.

[69] Stack Overflow Community. *System Requirements for Gazebo.* https://robotics.stackexchange.com/questions/12325/system-requirements-for-gazebo. [Online; accessed 4-September-2019]. 2017.

[70] *Comune di Roma, ufficio municipalità. Local Planning Authorities Rome, Italy.* https://www.comune.roma.it/web/it/scheda-servizi.page?contentId=INF76709. [Online; accessed December-10-2018]. 2018.

[71] Yang Cong et al. In: *Flow mosaicking: Real-time pedestrian counting without scene-specific learning*. ieee. 2009, pp. 1093–1100.

[72] Fausto G Costa et al. "The use of unmanned aerial vehicles and wireless sensor network in agricultural applications." In: *2012 IEEE International Geoscience and Remote Sensing Symposium*. IEEE. 2012, pp. 5045–5048.

[73] Erwin Coumans. *Bullet Physics*. https://bitbucket.org/odedevs/ode/src/default/. [Online; accessed 4-September-2019]. 2019.

[74] Range Commanders Council. *Common Risk Criteria for National Test Ranges: Inert Debris*. 2002.

[75] Range Safety Group Range Commanders Council. "Common Risk Criteria for National Test Ranges Inert Debris." In: *Range Commanders Council - Range Safety Group* (2000).

[76] Range Safety Group Range Commanders Council. "Common Risk Criteria for National Test Ranges Inert Debris, Supplement." In: *Range Commanders Council - Range Safety Group* (2000).

[77] Range Safety Group Range Commanders Council. "RANGE SAFETY CRITERIA FOR UNMANNED AIR VEHICLES Document 323-99." In: *Range Commanders Council - Range Safety Group* (1999).

[78] Range Safety Group Range Commanders Council. "RANGE SAFETY CRITERIA FOR UNMANNED AIR VEHICLES Supplement 323-99." In: *Range Commanders Council - Range Safety Group* (1999).

[79] Ross Cutler and Larry S. Davis. "Robust real-time periodic motion detection, analysis, and applications." In: *IEEE Transactions on Pattern Analysis and Machine Intelligence* 22.8 (2000), pp. 781–796.

[80] Konstantinos Dalamagkidis, Kimon P Valavanis, and Les A Piegl. "Evaluating the risk of unmanned aircraft ground impacts." In: IEEE. 2008, pp. 709–716.

[81] Konstantinos Dalamagkidis, Kimon P Valavanis, and Les A Piegl. *On integrating unmanned aircraft systems into the national airspace system: issues, challenges, operational restrictions, certification, and recommendations*. Vol. 54. springer science & Business Media, 2011.

[82] Konstantinos Dalamagkidis, Kimon P Valavanis, and Les A Piegl. "On unmanned aircraft systems issues, challenges and operational restrictions preventing integration into the National Airspace System." In: *Progress in Aerospace Sciences* 44.7-8 (2008), pp. 503–519.

[83] *Dave Shafer. How Much Does Satellite Internet Cost?* SatelliteInternet.com/resources/how-much-does-satellite-internet-cost/. [Online; accessed 3-August-2020]. 2019.

[84] Guillaume De Syon. *Zeppelin!: Germany and the airship, 1900–1939*. JHU Press, 2002.

[85] *Delair France. 1st in France: Drone completes 30 miles BVLOS flight via 3G cell network.* https://delair.aero/power-utilities/drone-completes-bvlos-flight-via-3g/. [Online; accessed September-2020]. 2017.

[86] Ministero dell'ambiente. *Municipality tasks in Italy*. http://www.minambiente.it/sites/default/files/archivio/allegati. [Online; accessed December-10-2018]. 2018.

[87] Jur van Den Berg et al. In: *Centralized path planning for multiple robots: Optimal decoupling into sequential plans*. Vol. 2. 2.5. 2009, pp. 2–3.

[88] War Department. *Technical Manual of Airship Aerodynamics*. https://www.faa.gov/regulations_policies/handbooks_manuals/aviation/media/airship_aerodynamics.pdf. [Online; accessed 19-February-2021]. 1941.

[89] Jan Diekmann et al. "Potential dangers during the handling of lithium-ion batteries." In: *Recycling of Lithium-Ion Batteries*. Springer, 2018, pp. 39–51.

[90] EASA Rulemaking Directorate. "Policy Statement Airworthiness Certification of Unmanned Aircraft Systems (UAS), E." In: *Y013-01* 25 (2009).

[91] DJI. *Inspire 1 Pro, specifications*. http://www.dji.com/inspire-1-pro-and-raw. [Online; accessed 10-October-2018]. 2016.

[92] DJI. *Inspire 2, specifications*. http://www.dji.com/inspire-2/infospecs. [Online; accessed 10-October-2018]. 2016.

[93] DJI. *Mavic, specifications*. http://www.dji.com/mavic/. [Online; accessed 10-October-2018]. 2018.

[94] DJI. *P4 Multispectral*. https://www.dji.com/it/p4-multispectral. [Online; accessed 01-July-2021]. 2021.

[95] DJI. *Phantom 4, specifications*. http://www.dji.com/phantom-4-adv/. [Online; accessed 10-October-2018]. 2018.

[96] DJI. *Restricted Areas Evaluation, DJI source*. https://www.dji.com/flysafe/geo-map. [Online; accessed 30-September-2018]. 2018.

[97] *Dr Peter Harrop. Satellite or Drone Internet*. https://www.idtechex.com/en/research-article/satellite-or-drone-internet/10395. [Online; accessed September-2020]. 2016.

[98] Draganfly. *Commander Technical Specifications*. https://draganfly.com/products/draganflyer-commander/. [Online; accessed 10-October-2018]. 2018.

[99] EASA. *Easa Safety Review 2017*. 2017.

[100] *EASA, European Union Aviation Safety Agency. Easy Access Rules for Unmanned Aircraft Systems (Regulations (EU) 2019/947 and (EU) 2019/945)*. https://www.easa.europa.eu/sites/default/files/dfu/Easy$_$Access$_$Rules$_$for$_$Unmanned$_$Aircraft$_$Systems.pdf. [Online; accessed 7-july-2020]. 2019.

[101] *Easton Bevins. Refurnishment Procedure Easton, UK*. http://www.eastonbevinslimited.co.uk/refurbishment-and-renovation. [Online; accessed December-10-2018]. 2018.

[102] *Eddie Saunders. Alphabet s Wing drones get FAA approval to make deliveries in the US*. https://www.caasint.com/amazon-prime-air-drone-delivery-nearly-doubles-uk-staff/. [Online; accessed September-2020]. 2020.

[103] *ENAC, Italian Civil Aviation Authority. Progetti di ricerca e sviluppo settore SAPR*. https://www.enac.gov.it/sicurezza-aerea/droni/progetti-di-ricerca-e-sviluppo-settore-sapr. [Online; accessed 7-july-2020]. 2020.

[104] *ENAC, Italian Civil Aviation Authority. Progetti di ricerca e sviluppo settore SAPR*. https://www.enac.gov.it/sites/default/files/allegati/2019-Dic/R$_$26S$_$Elenco$_$Stakeolder$_$Progetti$_$$$_16_$dicembre$_$2019.pdf. [Online; accessed 7-july-2020]. 2020.

[105] *European Aviation Safety Agency. Civil drones (Unmanned aircraft)*. https://www.easa.europa.eu/easa-and-you/civil-drones-rpas. [Online; accessed November 2019]. 2018.

[106] Mina Kamel Fadri Furrer Michael Burri and Markus Achtelik. *gazebo_motor_model.cpp File Reference*. http://aerotrash.over-blog.com/2015/02/2-blade-vs-3-blade-and-4-blade-propellers.html. [Online; accessed 02-October-2019]. 2019.

[107] *Federal Aviation Administration. Flight Safety Analysis Handarticle, Version 1.0*. https://www.faa.gov/about/office$_$org/headquarters$_$offices/ast/media/Flight$_$Safety$_$Analysis$_$Handarticle$_$final$_$9$_$2011v1.pdf. [Online; accessed 10-December-2018]. 2011.

[108] *Federal Aviation Administration. Restricted Areas in USA*. https://www.faa.gov/uas/resources/community$_$engagement/no$_$drone$_$zone/. [Online; accessed 30-September-2018]. 2018.

[109] Dieter Fox, Wolfram Burgard, and Sebastian Thrun. "The dynamic window approach to collision avoidance." In: *IEEE Robotics & Automation Magazine* 4.1 (1997), pp. 23–33.

[110] *Franck Schrotoh. Drone Energy Sources – Pushing the Boundaries of Electric Flight.* https://dronelife.com/2017/06/06/drone-energy-sources-pushing-boundaries-electric-flight. [Online; accessed 20-july-2020]. 2017.

[111] Micheal Freilich. *Sentinel-6.* https://www.nasa.gov/sentinel-6. [Online; accessed January 2021]. 2021.

[112] Béatrice Garcia et al. "Room temperature molten salts as lithium battery electrolyte." In: *Electrochimica Acta* 49.26 (2004), pp. 4583–4588.

[113] Avinash Gautam and Sudeept Mohan. In: *A review of research in multi-robot systems.* IEEE. 2012, pp. 1–5.

[114] *GEOCENTO, intelligent earth imaging. PRICE COMPARISON FOR BASIC IMAGERY.* https://geocento.com/imagery-pricing-plans/. [Online; accessed 3-August-2020]. 2019.

[115] GETFPV. *LumierBattery Specification.* https://www.getfpv.com/lumenier-205mah-1s-25c-lipo-battery-jst-xh-2-0.html. [Online; accessed 4-September-2019]. 2017.

[116] Nikolajs Glīzde. "Plotting the Flight Envelope of an Unmanned Aircraft System Air Vehicle." In: *Transport and Aerospace Engineering* 4.1 (2017), pp. 80–87.

[117] *Global Drone Regulations Database. China, UAS Regulations.* https://droneregulations.info/China/CN.html. [Online; accessed 7-july-2020]. 2018.

[118] *Global Military Review. Bayraktar.* http://globalmilitaryreview.blogspot.it/2011/12/turkish-bayraktar-mini-uav.htm. [Online; accessed 24-april-2018]. 2018.

[119] *Global Military Review. Bayraktar Type B.* https://www.flightglobal.com/news/articles/turkish-army-orders-mini-uavs-208327/. [Online; accessed 24-april-2018]. 2018.

[120] Andrew Gong and Dries Verstraete. "Experimental testing of electronic speed controllers for UAVs." In: *53rd AIAA/SAE/ASEE Joint Propulsion Conference.* 2017, p. 4955.

[121] Marta C Gonzalez, Cesar A Hidalgo, and Albert-Laszlo Barabasi. "Understanding individual human mobility patterns." In: *nature* 453.7196 (2008), p. 779.

[122] Netherlands Government. *Municipality tasks in Netherlands.* https://www.government.nl/topics/municipalities/municipalities-tasks. [Online; accessed December-10-2018]. 2018.

[123] *Government of South Africa, Local Bureau. Municipality tasks in South Africa.* https://www.gov.za/about-government/government-system/local-government. [Online; accessed December-10-2018]. 2018.

[124] *Government of South Australia. Local Planning Authorities Australia.* https://www.sa.gov.au/topics/planning-and-property/land-and-property-development/engaging-building-industry-professionals/getting-approval-to-build. [Online; accessed December-10-2018]. 2018.

[125] Frank Grimsley. "Equivalent safety analysis using casualty expectation approach." In: (2004), p. 6428.

[126] Guillaume. *2-blade vs 3-blade and 4-blade propellers in drone field.* http://aerotrash.over-blog.com/2015/02/2-blade-vs-3-blade-and-4-blade-propellers.html. [Online; accessed 01-October-2019]. 2015.

[127] Gunter's Space Page. *Gaojing-1 01, 02, 03, 04 (SuperView 1).* https://space.skyrocket.de/doc_sdat/gaojing-1.htm. [Online; accessed Jan-2021]. 2020.

[128] Hacker. *A20-20 L EVO kv1022 sheet.* https://www.hacker-motor-shop.com/Brushless-Motors/Hacker-Outrunner/Hacker-A20/A20-20-L-EVO-kv1022.htm?shop=hacker_e&SessionId=&a=article&ProdNr=97800006&p=16&rdeocl=1&rdetpl=productpage&rdebox=box1. [Online; accessed 27-September-2019]. 2019.

[129] Richard Harwood. *Planning Permission.* Vol. 54. International Specialized article Services, 2017.

[130] Hongwen He et al. "Online model-based estimation of state-of-charge and open-circuit voltage of lithium-ion batteries in electric vehicles." In: *Energy* 39.1 (2012), pp. 310–318.

[131] Marie Heaphy et al. "UAVs for data collection-plugging the gap." In: *NZJ For* 62 (2017), pp. 23–30.

[132] *HÉLICÉO - Geomatic Innovation & Technology. Foxypro.* http://www.heliceo.com/en/produits-pour-geometres/foxypro-vtol-airplane/. [Online; accessed 4-febr-2020]. 2020.

[133] *HÉLICÉO - Geomatic Innovation & Technology. Foxyslim.* http://www.heliceo.com/en/produits-pour-geometres/foxyslim-airplane-drone/. [Online; accessed 4-febr-2020]. 2020.

[134] *HÉLICÉO - Geomatic Innovation& Technology. SuperFox4.* http://www.heliceo.com/en/produits-pour-geometres/fox4-multirotor-drone/. [Online; accessed 24-april-2018]. 2018.

[135] *HÉLICÉO - Geomatic Innovation&Technology. SuperFox6.* http://www.heliceo.com/en/produits-pour-geometres/fox6-drone-surveyor/. [Online; accessed 24-april-2018]. 2018.

[136] HGLRC. *HGLRC FLAME 1104 7500KV Micro Brushless Motor.* https://www.hglrc.com/products/hglrc-flame-1104-7500kv-micro-brushless-motor-for-xjb-75-mini-fpv-racer. [Online; accessed 24-September-2019]. 2019.

[137] Brother Hobby. *3B-R2207 spec.* https://www.brotherhobbystore.com/returner-r6-2306-rainbow_p0013.html. [Online; accessed 24-September-2019]. 2019.

[138] *How much difference is between runtime of a program in matlab and one in c++?* https://www.researchgate.net/post/How_much_difference_is_between_runtime_of_a_program_in_matlab_and_one_in_c. [Online; accessed 23-September-2019]. 2016.

[139] *How much variation between experimental and numerical results is acceptable?* https://www.researchgate.net/post/How_much_variation_between_experimental_and_numerical_results_is_acceptable2. [Online; accessed 23-September-2019]. 2014.

[140] *IAI. Micro Falcon.* http://www.iai.co.il/2013/22031-en/homepage.aspx. [Online; accessed 4-febr-2020]. 2013.

[141] IDS Corporation. *Unmanned Systems.* https://www.idscorporation.com/drones/ids-drones/item/. [Online; accessed 10-October-2018]. 2018.

[142] *Infodrone.es. SCR recibe la primera autorizacion de Espana para BVLOS.* http://www.infodron.es/id/2020/06/25/noticia-recibe-primera-autorizacion-espana-realizar-vuelos-bvlos.html. [Online; accessed September-2020]. 2020.

[143] *Innocon Ltd. Micro Falcon.* http://www.innoconltd.com/$_$CategoryID=179$&$ArticleID=104. [Online; accessed 4-febr-2020]. 2010.

[144] *Innocon Ltd. Micro Falcon.* http://www.innoconltd.com. [Online; accessed 4-febr-2020]. 2010.

[145] Dahaman Ishak, ZQ Zhu, and David Howe. "Eddy-current loss in the rotor magnets of permanent-magnet brushless machines having a fractional number of slots per pole." In: *IEEE Transactions on magnetics* 41.9 (2005), pp. 2462–2469.

[146] *Istituto Nazionale di Statistica. Popolazione e Famiglie.* https://www.istat.it. [Online; accessed 25-October-2018]. 2018.

[147] ItalDron. *Evoluzione 4HSE INSPECTOR*. https://www.italdron.com/it/droni-professionali-e-accessori/droni-professionali/titan-4hse-sicurezza. [Online; accessed 10-October-2018]. 2016.

[148] Jackson Gothe-Snape. *Google-affiliated drone delivery service found to be exceeding noise limits*. https://www.abc.net.au/news/2019-09-12/canberra-delivery-drone-noise-levels-revealed/11503262. [Online; accessed 28-June-2021]. 2019.

[149] Damien Christophe Jacques et al. "D4D Challenge 2014." In: (2014).

[150] Pooyan Jamshidi. *Battery plugin (open-circuit model) for any kinds of robot simulations in Gazebo*. https://github.com/pooyanjamshidi/brass_gazebo_battery. [Online; accessed 11-September-2019]. 2019.

[151] *Jon Porter. Alphabet s Wing drones get FAA approval to make deliveries in the US.* https://www.theverge.com/2019/4/23/18512658/google-alphabet-wing-drone-delivery-service-faa-approval-commercial-deliveries. [Online; accessed September-2020]. 2019.

[152] *Jonathan Barnes. Drones vs Manned Aircraft - Which Tool is Right for Your Project?* https://www.commercialuavnews.com/infrastructure/drones-vs-manned-aircraft. [Online; accessed 20-june-2020]. 2018.

[153] *Jonathan Barnes. Drones vs Satellites: Competitive or Complementary?* https://www.businessinsider.com/elon-musk-flying-cars-bad-idea-2017-2$_$IR=T. [Online; accessed 24-july-2020]. 2018.

[154] Edward C Jordan and Keith G Balmain. "Electromagnetic waves and radiating systems." In: (1968).

[155] Sertac Karaman and Emilio Frazzoli. "Incremental sampling-based algorithms for optimal motion planning." In: *Robotics Science and Systems VI* 104 (2010), p. 2.

[156] Maher Khatib and Raja Chatila. *An extended potential field approach for mobile robot sensor-based motions*. 1995.

[157] Ghazaleh Khodabandelou et al. "Population estimation from mobile network traffic metadata." In: IEEE. 2016, pp. 1–9.

[158] Lora Kolodny. *Fixed-wing drones not quite taking off in commercial market, a new DroneDeploy study finds*. https://techcrunch.com/2016/08/15/fixed-wing-drones-not-quite-taking-off-in-commercial-market-a-new-dronedeploy-study-finds/?guccounter=1&guce_referrer=aHR0cHM6Ly93d3cuZ29vZ2xlLmNvbS8&guce_referrer_sig=AQAAANv4Nzf9NeQjRYGTiE4MRSfL1NCx0Hdf31B-Szfhf3V_5mraymdDLTEy1FS99xTaScjzb5fFrz5Cfa7Pcxaru3zFZ4V2LPN9MGxkYw-l2gRzn2rzMqg17-9hOzhkGtsZsSfywvEYHWhBsLXwUI1t3. [Online; accessed January-2021]. 2016.

[159] Anis Koubâa et al. *Robot Operating System (ROS)*. Vol. 1. Springer, 2017.

[160] JC Latombe. "Robot motion planning Kluwer Academic Publishers Boston Google Scholar." In: (1991).

[161] Jean-Claude Latombe. *Robot motion planning*. Vol. 124. Springer Science & Business Media, 2012.

[162] Jean-Claude Latombe. *Robot Motion Planning (the Kluwer international series in engineering and computer science)*. 1990.

[163] Jeongseok Lee et al. "Dart: Dynamic animation and robotics toolkit." In: *Journal of Open Source Software* 3.22 (2018), p. 500.

[164] Seongjun Lee et al. "State-of-charge and capacity estimation of lithium-ion battery using a new open-circuit voltage versus state-of-charge." In: *Journal of power sources* 185.2 (2008), pp. 1367–1373.

[165] *Lehman Aviation. Zala 16*. http://zala.aero/zala-421-16em/. [Online; accessed 24-april-2018]. 2018.

[166] *Lehman Aviation. Zala 8*. http://zala.aero/zala-421-08/. [Online; accessed 24-april-2018]. 2018.

[167] *Lehmann Aviation. LA 500*. http://www.lehmannaviation.com/assets/downloads/Tech$_$Specs$_$LA500-AG.pdf. [Online; accessed 24-april-2018]. 2018.

[168] Thomas Lemaire, Rachid Alami, Simon Lacroix, et al. "A distributed tasks allocation scheme in multi-UAV context." In: *ICRA* 2004 (2004).

[169] Jingwen Li, Lei Huang, and Changping Liu. "Robust people counting in video surveillance: Dataset and system." In: IEEE. 2011, pp. 54–59.

[170] David Liben-Nowell et al. "Geographic routing in social networks." In: *Proceedings of the National Academy of Sciences* 102.33 (2005), pp. 11623–11628.

[171] LipolBattery. *LP523040 Specification*. https://www.lipolbattery.com/LiPo-Battery-Datahseet/LiPo_Battery_LP226693_3.7V_1350mAh_Cell.pdf. [Online; accessed 25-January-2020]. 2019.

[172] A123 System LLC. *A123 System LLC*. http://www.a123systems.com. [Online; accessed 4-September-2019]. 2019.

[173] *Looked Martin. Desert Hawk III*. http://www.lockheedmartin.com/content/dam/lockheed/data/ms2/documents/Desert$_$Hawk$_$Brochure.pdf. [Online; accessed 24-april-2018]. 2018.

[174] Chen Change Loy et al. "Crowd counting and profiling: Methodology and evaluation." In: Springer, 2013, pp. 347–382.

[175] Shuai Ma et al. "Temperature effect and thermal impact in lithium-ion batteries: A review." In: *Progress in Natural Science: Materials International* 28.6 (2018), pp. 653–666.

[176] Andrzej Majka. "Flight loads of mini UAV." In: *Solid State Phenomena*. Vol. 198. Trans Tech Publ. 2013, pp. 194–199.

[177] MathWorks. *MATLAB*. https://it.mathworks.com/products/matlab.html. [Online; accessed 23-January-2020]. 2020.

[178] Mathworks. *System Requirements - Release 2019a*. https://www.mathworks.com/content/dam/mathworks/mathworks-dot-com/support/sysreq/files/system-requirements-release-2019a-windows.pdf. [Online; accessed 4-September-2019]. 2019.

[179] *Mavinci. Sirius UAS*. http://www.mavinci.de/downloads/mavinci$_$sirius$_$uas.pdf. [Online; accessed 24-april-2018]. 2018.

[180] *MAVTech. Agri 1900*. http://www.mavtech.eu/site/assets/files/1313/agri1900.pdf. [Online; accessed 24-april-2018]. 2018.

[181] *MAVTech. Agri 2000*. http://www.mavtech.eu/site/assets/files/1168/agri2000.pdf. [Online; accessed 24-april-2018]. 2018.

[182] *MAVTech. MH 850*. http://www.c-astral.com/en/products/bramor-c4eye. [Online; accessed 24-april-2018]. 2018.

[183] *MAVTech. Q4L*. http://www.mavtech.eu/site/assets/files/1150/q4l-rotor$_$-$_$v3.pdf. [Online; accessed 24-april-2018]. 2018.

[184] mavtech. *Q4P DRONE - OVERVIEW*. http://www.mavtech.eu/site/assets/files/1158/q4p-rotor.pdf. [Online; accessed 10-October-2018]. 2016.

[185] *MicaSense Team. Satellite vs. Drone Imagery in Vegetation Mapping*. https://blog.micasense.com/satellite-vs-drone-imagery-in-vegetation-mapping-59b928a37a11. [Online; accessed September-2020]. 2019.

[186] *Michael Huerta. Speech – "Unmanned Aircraft Systems Symposium Opening Remarks"*. [Online; accessed September-2020]. 2017.

[187] Marek Michalczuk et al. "Power converter-based electrochemical battery emulator." In: *Przeglad Elektrotechniczny* 90.7 (2014), pp. 18–22.

[188] Microchip. *803048 Li-Po battery Report*. http://ww1.microchip.com/downloads/en/devicedoc/acc-rn-220xp-battery-ds.pdf. [Online; accessed 4-September-2019]. 2013.

[189] Microdrones. *WORK SMARTER WITH MICRODRONES INTEGRATED SYSTEMS*. . [Online; accessed October-2018]. 2018.

[190] MikriElektronika. *Li-Po battery datasheet*. https://download.mikroe.com/documents/datasheets/battery-datasheet.pdf. [Online; accessed 4-September-2019]. 2013.

[191] MikroKopter. *MK8, multicopter*. http://www.mikrokopter.de/en/products/nmk8stden/nmk8ueberen. [Online; accessed 10-October-2018]. 2018.

[192] Javier Minguez and Luis Montano. "Nearness diagram navigation (nd): A new real time collision avoidance approach." In: *Intelligent Robots and Systems, 2000.(IROS 2000). Proceedings. 2000 IEEE/RSJ International Conference on* 3 (2000), pp. 2094–2100.

[193] *Minisyère De La Transition Ecologique. Drones - Usages professionnels*. https://www.ecologie.gouv.fr. [Online; accessed September-2020]. 2020.

[194] Miriam McNabb. *New Texas Bill Restricts Drone Flight Over Farms*. https://dronelife.com/2017/06/01/new-texas-bill-restricts-drone-flight-farms/. [Online; accessed 28-June-2021]. 2017.

[195] Morteza Montazeri-Gh, Seyed Alireza Miran Fashandi, and Soheil Jafari. "Theoretical and Experimental Study of a Micro Jet Engine Start-Up Behaviour." In: *Tehnički vjesnik* 25.3 (2018), pp. 839–845.

[196] Robert M Montgomery and James A Ward. "Casualty areas from impacting inert debris for people in the open." In: (1995).

[197] Yves-Alexandre de Montjoye et al. "D4D-Senegal: the second mobile phone data for development challenge." In: *arXiv preprint arXiv:1407.4885* (2014).

[198] T Motor. *T-Motor F60 PRO III1750 KV brushless motor spec*. https://www.amazon.com/stores/node/7647078011?_encoding=UTF8&field-lbr_brands_browse-bin=T-Motor&ref_=bl_dp_s_web_7647078011. [Online; accessed 24-September-2019]. 2019.

[199] T Motor. *U3 KV700 spec*. http://store-en.tmotor.com/goods.php?id=317. [Online; accessed 24-September-2019]. 2019.

[200] T Motor. *U3 KV700 spec*. http://store-en.tmotor.com/goods.php?id=330. [Online; accessed 24-September-2019]. 2019.

[201] T Motor. *U8 KV170 spec*. http://store-en.tmotor.com/goods.php?id=324. [Online; accessed 24-September-2019]. 2019.

[202] Thomas J Mueller. *Aerodynamic measurements at low raynolds numbers for fixed wing micro-air vehicles*. Tech. rep. NOTRE DAME UNIV IN DEPT OF AEROSPACE and MECHANICAL ENGINEERING, 2000.

[203] Tony Mullen. *Mastering blender*. John Wiley & Sons, 2011.

[204] O Mustafa et al. "Pilot study on monitoring climate-induced changes in penguin colonies in the Antarctic using satellite images." In: *Project FKZ* 3711.85 (2012), p. 199.

[205] KA Myers. *Lethal Area Description*. Tech. rep. ARMY BALLISTIC RESEARCH LAB ABERDEEN PROVING GROUND MD, 1963.

[206] *New York State, Department of State. Refurnishment Procedure Albanym, NY, USA*. https://www.schuylercounty.us/DocumentCenter/View/1517/Village-of-Watkins-Glen-updated-Zoning-Law?bidId=. [Online; accessed December-10-2018]. 2018.

[207] Fabrizio Nicolosi. *Airplane Turning Characteristics*. http://wpage.unina.it/fabrnico/DIDATTICA/PGV_2012/MECC_VOLO/PPT/MV_7_Virata.pdf. [Online; accessed 19-February-2021]. 2008.

[208] Anibal Ollero et al. "AWARE: Platform for Autonomous self-deploying and operation of Wireless sensor-actuator networks cooperating with unmanned AeRial vehiclEs." In: *2007 IEEE International Workshop on Safety, Security and Rescue Robotics*. IEEE. 2007, pp. 1–6.

[209] Open Source Robotics Foundation. *Gazebo Open Source*. http://gazebosim.org. [Online; accessed 14-February-2017]. 2014.

[210] *Orange Cousin. Refurnishment Procedure South Africa*. https://www.justlanded.com/english/South-Africa/South-Africa-Guide/Property/Renovation-Restoration. [Online; accessed December-10-2018]. 2018.

[211] Origin Hobby. *Model 6068, Datasheet*. http://www.originhobby.com/en/product/OH6086.html. [Online; accessed 10-October-2018]. 2018.

[212] Origin Hobby. *Model 6160, Datasheet*. http://www.originhobby.com/en/product/OH6160.html. [Online; accessed 10-October-2018]. 2018.

[213] Origin Hobby. *Model 8200, Datasheet*. http://www.originhobby.com/en/product/OH8200.html. [Online; accessed 10-October-2018]. 2018.

[214] Original Hobby. *Model 4100, Datasheet*. http://www.originhobby.com/en/product/OH-4100.html. [Online; accessed 10-October-2018]. 2018.

[215] Panasonic. *CGR18650AF*. https://www.datasheetarchive.com/pdf/download.php?id=1fba0476dbf72936a88cde4c94c9b19d803011&type=P&term=CGR18650. [Online; accessed 4-September-2019]. 2007.

[216] Panasonic. *Panasonic Battery Handbook*. https://www.datasheetarchive.com/pdf/download.php?id=58a2bf21b460244920d1f7010a6a12be07a071&type=P&term=CGR18650. [Online; accessed 4-September-2019]. 2000.

[217] Lynne E Parker. "Multiple mobile robot systems." In: Springer, 2008, pp. 921–941.

[218] Lynne E Parker. *Multiple mobile robot teams, path planning and motion coordination in*. Springer, 2009, pp. 5783–5800.

[219] Judea Pearl. "Heuristics: intelligent search strategies for computer problem solving." In: (1984).

[220] Tao Pei et al. "A new insight into land use classification based on aggregated mobile phone data." In: *International Journal of Geographical Information Science* 28.9 (2014), pp. 1988–2007.

[221] *People's Republic of China. Local Planning China.* http://www.npc.gov.cn/englishnpc/Law/2007-12/12/content$_$1383918.htm. [Online; accessed December-10-2018]. 2018.

[222] Mohammad Pessarakli. *Handarticle of photosynthesis.* CRC press, 2005.

[223] Enrico Petritoli, Fabio Leccese, and Lorenzo Ciani. "Reliability and maintenance analysis of unmanned aerial vehicles." In: *Sensors* 18.9 (2018), p. 3171.

[224] Melissa Petruzzello. *Trees leaves cycle.* https://www.britannica.com/story/why-do-leaves-fall-in-autumn. [Online; accessed 15-Febbraio-2019]. 2019.

[225] Juan Plaza. *What is the Value of the European Drone Market?* https://www.commercialuavnews.com/europe/value-european-drone-market. [Online; accessed 7-December-2020]. 2019.

[226] *Powermag Team. Five Inspections Made Easier with Drone Technology.* https://www.powermag.com/five-inspections-made-easier-with-drone-technology/. [Online; accessed September-2020]. 2019.

[227] *Press SUAS NEWS. FAA approves another groundbreaking BVLOS flight.* https://www.suasnews.com/2019/08/faa-approves-another-groundbreaking-bvlos-flight/. [Online; accessed 7-july-2020]. 2019.

[228] *Public Affair Bureau. Local Planning Authorities South Africa.* https://www.thedti.gov.za/business$_$regulation/acts/building_standards$_$act.pdf. [Online; accessed December-10-2018]. 2018.

[229] *Qgis team. Qgis, A Free and Open Source Geographic Information System.* https://www.qgis.org/en/site/. [Online; accessed 1-November-2020]. 2020.

[230] R4 Robotics. *IMLEHPQC Specifications.* http://r4robotics.com/product/r4-industrial-model-long-endurance-high-payload-quad-configuration/. [Online; accessed 10-October-2018]. 2018.

[231] R4 Robotics. *IMSHC Specifications.* http://r4robotics.com/product/r4-industrial-model-standard-hexa-configuration/. [Online; accessed 10-October-2018]. 2018.

[232] R4 Robotics. *Model R4.* http://r4robotics.com/product/r4-large-roller/. [Online; accessed 10-October-2018]. 2018.

[233] R4 Robotics. *Model R4 small.* http://r4robotics.com/product/r4-roller-small-model/. [Online; accessed 10-October-2018]. 2018.

[234] R4 Robotics. *R4 IMSQC*. http://r4robotics.com/product/r4-industrial-model-standard-quad-configuration/. [Online; accessed 10-October-2018]. 2018.

[235] EF Roberts. *The Reform of Planning Law; Land Use and the United States*. HeinOnline, 1976.

[236] Laura Rocchio. *LandSat Information*. https://web.archive.org/web/20100501135128/http://landsat.gsfc.nasa.gov/about/L7$_$td.html. [Online; accessed 19-December-2018]. 2018.

[237] David Ryan et al. "An evaluation of crowd counting methods, features and regression models." In: *Computer Vision and Image Understanding* 130 (2015), pp. 1–17.

[238] *Safet Satara. Four Battery Technology Solutions That Could Shape Our Future*. https://www.topspeed.com/cars/warp-coils-seem-closer-to-reality-than-a-battery-with-energy-density-of-gasoline-ar185365.html. [Online; accessed 20-july-2020]. 2019.

[239] Gildardo Sanchez and J-C Latombe. "Using a PRM planner to compare centralized and decoupled planning for multi-robot systems." In: *Proceedings 2002 IEEE International Conference on Robotics and Automation (Cat. No. 02CH37292)* 2 (2002), pp. 2112–2119.

[240] R Schaufele et al. "FAA Aerospace Forecast: Fiscal Years 2018–2038." In: *Washington, DC* (2018).

[241] Ali Al-Sheary and Ali Almagbile. "Crowd monitoring system using unmanned aerial vehicle (uav)." In: *Journal of Civil Engineering and Architecture* 11 (2017), pp. 1014–1024.

[242] Russel L. Smith. *ODE - A Short Guide*. https://bitbucket.org/odedevs/ode/src/default/. [Online; accessed 4-September-2019]. 2019.

[243] Smithsonian, National Air and Space Museum. *Pioneer RQ-2A UAV*. https://airandspace.si.edu/collection-objects/pioneer-rq-2a-uav/nasm_A20000794000. [Online; accessed january-2021]. 2018.

[244] Solvelight Robotics. *DRAGANFLYER X4-P PROFESSIONAL QUADCOPTER BASE MODEL*. https://www.solvelight.com/product/draganflyer-x4-p-professional-quadcopter-base-model/. [Online; accessed 10-October-2018]. 2018.

[245] Chaoming Song et al. "Limits of predictability in human mobility." In: *Science* 327.5968 (2010), pp. 1018–1021.

[246] *Spacecraft Company. Local Planning Authorities UK*. https://www.planningportal.co.uk. [Online; accessed December-10-2018]. 2018.

[247] *Statistisches Bundesamt. German Population Statistics.* https://www.destatis.de/DE/Startseite.html. [Online; accessed 25-October-2018]. 2018.

[248] *Steve Coast. OpenstreetMap Project.* https://www.openstreetmap.org. [Online; accessed 3-Febbraio-2019]. 2019.

[249] George W Stickle and John L Crigler. *Propeller Analysis from Experimental Data.* 1941.

[250] *SunBird. SB4.* http://www.sunbirds-uas.com/en/drones/drones/sb4phoenix.html. [Online; accessed 4-febr-2020]. 2020.

[251] SwellPro. *Splashdrone 3.* http://www.swellpro.com/waterproof-splash-drone-3-auto.html. [Online; accessed October-2018]. 2018.

[252] Hannes Taubenböck and Thomas Esch. "Remote sensing—An effective data source for urban monitoring." In: *Avalable online: http://earthzine. org/2011/07/20/remote-sensing-an-effective-data-source-for-urban-monitoring/(accessed on 10 June 2015)* (2011).

[253] GetFPV Team. *All About Multirotor Drone Batteries.* https://www.getfpv.com/learn/new-to-fpv/all-about-multirotor-fpv-drone-battery/. [Online; accessed 23-September-2019]. 2018.

[254] I-Flight Team. *BeeMotor 1108 brushless motor spec.* https://www.iflight-rc.com/index.php?route=product/product&path=110_263&product_id=836. [Online; accessed 24-September-2019]. 2018.

[255] I-Flight Team. *MOTOR XING X5215 X CLASS FPV NextGen Motor.* https://www.iflight-rc.com/index.php?route=product/product&product_id=857. [Online; accessed 24-September-2019]. 2019.

[256] Microdrones Team. *DRONES HAVE CHANGED MANY INDUSTRIES – AGRICULTURE IS NO EXCEPTION.* 2018.

[257] *Team DRONEII. Drone Energy Sources – Pushing the Boundaries of Electric Flight.* https://www.droneii.com/drone-energy-sources. [Online; accessed 24-july-2020]. 2017.

[258] Thiago Teixeira and Andreas Savvides. In: *Lightweight people counting and localizing in indoor spaces using camera sensor nodes.* IEEE. 2007, pp. 36–43.

[259] Max Teodorescu. *5 of the worst drone-related accidents.* https://www.electronicproducts.com/5-of-the-worst-drone-related-accidents. [Online; accessed 10-December-2020]. 2015.

[260] Amila Thibbotuwawa et al. "Energy consumption in unmanned aerial vehicles: A review of energy consumption models and their relation to the UAV routing." In: *International Conference on Information Systems Architecture and Technology.* Springer. 2018, pp. 173–184.

[261] TI Asahi. *PAIS D-800 8 Rotor Multicopter*. http://www.jahedteb.ir/PDF/UAS-UAV/PENTAX-D800-EN.pdf. [Online; accessed October-2018]. 2018.

[262] Prashant Tiwari et al. "Wireless sensor networks: Introduction, advantages, applications and research challenges." In: *HCTL Open International Journal of Technology Innovations and Research (IJTIR)* 14 (2015), pp. 1–11.

[263] *U.S. AIR FORCE. WASP III*. http://www.af.mil/About-Us/Fact-Sheets/Display/Article/104480/wasp-iii/. [Online; accessed 24-july-2020]. 2007.

[264] *UAVER. Avian P*. http://www.uaver.com/avian-p-aerial-mapping.html. [Online; accessed 24-april-2018]. 2018.

[265] *UAVER. Avian S*. http://www.uaver.com/real-time-surveillance.html. [Online; accessed 24-april-2018]. 2018.

[266] *UAVER. Avian-RTK(PPK) High Accuracy*. http://www.uaver.com/product-Avian-RTK(PPK)-Avian-RTK.html. [Online; accessed 24-april-2018]. 2018.

[267] *UAVER. Besra Hand Thrown Launch*. http://www.uaver.com/product-Besra-Besra.html. [Online; accessed 24-april-2018]. 2018.

[268] *UAVER. Swallow*. http://www.uaver.com/swallow-p-aerial-mapping.html. [Online; accessed 24-april-2018]. 2018.

[269] Uaver Drone. *Direct Industry*. http://www.directindustry.it/prod/carbon-based-technology-inc/product-120899-1322873.html. [Online; accessed October-2018]. 2018.

[270] *UAVGlobal. WASP III*. http://www.uavglobal.com/aurora-flight-sciences-skate/. [Online; accessed 4-febr-2020]. 2012.

[271] *UCONSYSTEM. Remoeye*. http://www.uconsystem.com/english/business/business02.asp. [Online; accessed 4-febr-2020]. 2020.

[272] *United States Census Bureau. Census Data in the United States of America in 2018*. https://www.census.gov. [Online; accessed 3-October-2018]. 2018.

[273] *Unmanned Systems Source. Altavian NOVA F7200*. https://www.unmannedsystemssource.com/shop/vehicles/altavian-nova-f7200/. [Online; accessed 24-july-2020]. 2018.

[274] Christoph Unterrieder et al. "Comparative study and improvement of battery open-circuit voltage estimation methods." In: *2012 IEEE 55th International Midwest Symposium on Circuits and Systems (MWSCAS)*. IEEE. 2012, pp. 1076–1079.

[275] Upneet Singh. *Alphabet Inc. decides to abandon balloon internet company Loon*. https://thetechportal.com/2021/01/22/alphabet-inc-decides-to-abandon-balloon-internet-company-loon/. [Online; accessed January-2021]. 2021.

[276] *USLegal.com. Municipality tasks in the USA.* https://municipal.uslegal.com/powers-functions-and-duties-of-municipality/. [Online; accessed December-10-2018]. 2018.

[277] João Valente et al. "An air-ground wireless sensor network for crop monitoring." In: *Sensors* 11.6 (2011), pp. 6088–6108.

[278] Vectornav. *INS ERROR BUDGET.* https://www.vectornav.com/resources/ins-error-budget. [Online; accessed January-2021].

[279] Senem Velipasalar, Ying-Li Tian, and Arun Hampapur. In: *Automatic counting of interacting people by using a single uncalibrated camera.* IEEE. 2006, pp. 1265–1268.

[280] Yuri Vicit. *Simbody Phisics.* https://github.com/simbody/simbody. [Online; accessed 4-September-2019]. 2019.

[281] John Villasenor. ""Drones" and the future of domestic aviation [Point of View]." In: *Proceedings of the IEEE* 102.3 (2014), pp. 235–238.

[282] Andreas E Voigt, Alexander Donkels, and Kristian K Fettig. "Manned-Unmanned Teaming Cooperative Formation Flight-A Project Review." In: *The Vertical Flight Society's 75th Annual Forum and Technology* (2019).

[283] David G Vutetakis and John B Timmons. *A comparison of lithium-ion and lead-acid aircraft batteries.* Tech. rep. SAE Technical Paper, 2008.

[284] Matt Wade. *Should You Buy a Fixed Wing or Rotary Drone?* https://waypoint.sensefly.com/buy-fixed-wing-drone-or-rotary/. [Online; accessed January-2021]. 2015.

[285] Yuliang Wei et al. "Noise reduction of UAV using biomimetic propellers with varied morphologies leading-edge serration." In: *Journal of Bionic Engineering* 17.4 (2020), pp. 767–779.

[286] Roland Weibel and R John Hansman. "Safety considerations for operation of different classes of uavs in the nas." In: *AIAA 4th Aviation Technology, Integration and Operations (ATIO) Forum* (2004), p. 6244.

[287] Xamen. *Be 4000, specifications.* http://www.xamen.fr/index.php/en/products/be-4000-en. [Online; accessed 10-October-2018]. 2018.

[288] Xamen. *Le 4800 X, specifications.* http://www.xamen.fr/index.php/en/products/le-4-8-x-en. [Online; accessed 10-October-2018]. 2018.

[289] XWING. *The Future of Aviation. Closer Than You Think.* https://www.xwing.com. [Online; accessed 29-June-2021]. 2021.

[290] Yuneec. *Breeze, specifications.* http://us.yuneec.com/breeze-specs. [Online; accessed 10-October-2018]. 2018.

[291] Yuneec. *H920, specifications*. http://us.yuneec.com/h920-specs. [Online; accessed 10-October-2018]. 2018.

[292] Yuneec. *Typhoon H, specifications*. http://us.yuneec.com/typhoon-h-specs. [Online; accessed 10-October-2018]. 2018.

[293] Jun Zhang and Jiahao Xing. "Cooperative task assignment of multi-UAV system." In: *Chinese Journal of Aeronautics* (2020).

[294] Yawei Zhang et al. "A promising trend for field information collection: An air-ground multi-sensor monitoring system." In: *Information processing in agriculture* 5.2 (2018), pp. 224–233.

This Ph.D. thesis has been typeset by means of the TEX-system facilities. The typesetting engine was LuaLATEX. The document class was `toptesi`, by Claudio Beccari, with option `tipotesi=scudo`. This class is available in every up-to-date and complete TEX-system installation.